



Thèse

2013

Open Access

This version of the publication is provided by the author(s) and made available in accordance with the copyright holder(s).

Timescales and petrologic processes during incremental pluton assembly:
a case study from the Val Fredda Complex, Adamello Batholith, N. Italy

Broderick, Cindy Ann

How to cite

BRODERICK, Cindy Ann. Timescales and petrologic processes during incremental pluton assembly: a case study from the Val Fredda Complex, Adamello Batholith, N. Italy. Doctoral Thesis, 2013. doi: 10.13097/archive-ouverte/unige:34411

This publication URL: <https://archive-ouverte.unige.ch/unige:34411>

Publication DOI: [10.13097/archive-ouverte/unige:34411](https://doi.org/10.13097/archive-ouverte/unige:34411)

**Timescales and petrologic processes during incremental pluton
assembly: a case study from the Val Fredda Complex, Adamello
Batholith, N. Italy**

THÈSE

présentée à la Faculté des sciences de l'Université de Genève
pour obtenir le grade de Docteur ès sciences,
mention sciences de la Terre

par
Cindy Broderick
de
Stockton (État-Unis)

Thèse No 4612

Genève
Atelier de reprographie ReproMail
2013



**UNIVERSITÉ
DE GENÈVE**

FACULTÉ DES SCIENCES

**Doctorat ès sciences
Mention Sciences de la Terre**

Thèse de *Madame Cindy Ann BRODERICK*

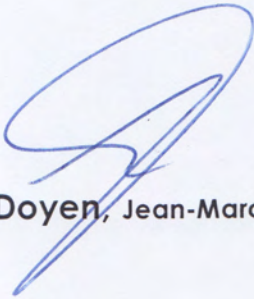
intitulée :

**" Timescales and Petrologic Processes during Incremental
Pluton Assembly : a Case Study from the Val Fredda Complex,
Adamello Batholith, N. Italy "**

La Faculté des sciences, sur le préavis de Messieurs U. SCHALTEGGER, professeur ordinaire et directeur de thèse (Département de minéralogie), P. ULMER, professeur (Institute of Geochemistry and Petrology, Swiss Federal Institute of Technology (ETH), Zurich, Switzerland) et O. MÜNTENER, professeur (Institut des sciences de la Terre, Université de Lausanne, Suisse), autorise l'impression de la présente thèse, sans exprimer d'opinion sur les propositions qui y sont énoncées.

Genève, le 12 novembre 2013

Thèse - 4612 -


Le Doyen, Jean-Marc TRISCONE

N.B. - La thèse doit porter la déclaration précédente et remplir les conditions énumérées dans les "Informations relatives aux thèses de doctorat à l'Université de Genève".

TIMESCALES AND PETROLOGIC PROCESSES DURING INCREMENTAL PLUTON ASSEMBLY: A CASE STUDY FROM THE VAL FREDDA COMPLEX, ADAMELLO BATHOLITH, N. ITALY

Thesis abstract

This thesis investigates the emplacement and magmatic evolution of the Val Fredda Complex (VFC), located in the southern tip of the Adamello batholith, N. Italy. The VFC provides insights into the history of a pluton that was constructed by multiple injections of compositionally diverse magmas, where we can observe complex relationships among mafic sheets injected into solidifying felsic magmas. We present an isotopic and geochemical data set which utilizes high precision ID-TIMS geochronology, trace element analyses from zircon and titanite combined with Hf isotopic compositions of zircon, all from the same mineral volume. This data set is integrated with in situ trace element analyses, field observations and data published in the literature.

The first chapter provides an introduction and overview of the objectives of this thesis, which investigates complex zircon populations between co-magmatic felsic and mafic lithologies during the incremental assembly of a pluton.

The second chapter investigates complex zircon populations and how they relate to magma emplacement. Using high precision U-Pb zircon geochronology we demonstrate that during 100 – 200 ka periods of protracted zircon growth, multiple periods of enhanced zircon crystallization can be identified. Coinciding periods of zircon crystallization from the different units between 42.54 Ma to 42.50 Ma and 42.48 Ma to 42.40 Ma are the result of rejuvenation of the felsic crystal mushes that reflect thermal fluctuations due to repeated mafic injections. Thermal fluctuations kept the felsic magmas above solidus conditions in a “crystal mush state” through most of their history.

Zircon trace element compositions record non-systematic inter- and intra-grain trace element variations which reflect chemical variability within different isolated magma batches that formed from the remelting and rejuvenation of the initial felsic intrusions by the mafic melt injections. The existence of multiple magma batches is supported by our zircon Hf isotopic compositions that record large variations in ϵ_{Hf} ranging from +2 to +8, during the remobilization of the felsic crystal mushes, and point to increased mixing with the Cadino gabbro ($\epsilon_{\text{Hf}} = +9$) through time. This study highlights

the difficulty to relate zircon dates to physical processes such as magma emplacement.

Chapter 3 presents ID-TIMS U-Pb dates for zircons that were extracted from thin sections in order to evaluate whether periods of enhanced zircon growth are related to specific crystallizing mineral assemblages within the paragenetic sequence of a magma.

Back scatter electron (BSE) and cathodoluminescence (CL) images reveal that zircon saturated early in the VFC felsic magmas and crystallized throughout the paragenetic sequence. However, many grains reveal the presence of cores. The remaining “core-free” grains are typically less than 100 μm in length and contain low amounts of radiogenic lead ($\text{Pb}^* = 0.62 - 0.86$ picograms) resulting in low analytical precision, up to 1% (2σ) on single $^{206}\text{Pb}/^{238}\text{U}$ dates. In contrast to the felsic samples, BSE and CL images reveal that zircon saturated late in the Mattoni gabbro (MG) and crystallized with the late matrix forming minerals quartz and plagioclase. High precision (0.08 – 0.18 %) single, texturally controlled $^{206}\text{Pb}/^{238}\text{U}$ dates were obtained as a result of large zircon grains ($< 100\ \mu\text{m}$) and high Pb^* . Our investigation of the VFC felsic and mafic samples highlights the limitations of our texturally controlled ID-TIMS dating method, which requires “core-free” zircons with sufficient amounts of radiogenic lead to achieve the necessary precision of 0.1% on single $^{206}\text{Pb}/^{238}\text{U}$ dates and early zircon saturation is required in order to resolve the timing of crystallization of distinct mineral assemblages. Based upon this, we were unable to link periods of zircon crystallization within the VFC magmas to the stage at which they crystallized in the paragenetic sequence. However, the range in ages for the MG recorded by our high precision texturally controlled zircon dates (42.451 ± 0.077 Ma to 42.546 ± 0.061 Ma) is consistent with the previous age dispersion recorded by conventional separation techniques (42.426 ± 0.039 Ma to 42.539 ± 0.033 Ma), thus providing evidence that the U-Pb zircon dates obtained through conventional separation represent the span of zircon crystallization in the MG.

In the fourth chapter we present equilibrium the rare earth element (REE) melt compositions calculated from trace element concentrations in crystallizing mineral assemblages from the VFC, in order to track the magmatic evolution during incremental pluton assembly. Trace element analyses of titanite and zircon, acquired from the same mineral volume used for high precision U-Pb dating, allows us to track changes in the melt compositions as a function of time. Titanite occurs as a major host phase for REE budget during crystallization of the VFC and records trace element compositions that are distinct for

each magma composition. Calculated mineral equilibrium melt compositions, combined with the Zr-in-titanite thermometer reveals coeval titanite and amphibole crystallization at temperatures ranging from $\sim 700^{\circ}\text{C}$ to 750°C in the felsic melts and coeval titanite and zircon crystallization at $\sim 800^{\circ}\text{C}$ in the mafic melts. The melt compositions in equilibrium with titanite provide insights into melt compositions at low crystallization temperatures; however these melts cannot be related to titanite U-Pb dates which reflect cooling below the 650°C closure temperature.

In contrast to titanite, zircon contains only small percentages ($< 10\%$) of the REE budget, despite recording prolonged periods of zircon growth over 100 – 200 ka timescales. Calculated equilibrium melt compositions for zircon reflect coeval crystallization with plagioclase and to a lesser extent amphibole. However, large variations are observed in zircon equilibrium melt compositions which show no coherent trends through time. We interpret the non-systematic melt variations to represent chemically distinct magma batches. During periods of rejuvenation, zircon equilibrium melt batches require $\sim 50\%$ crystallization of varying proportions of plagioclase and amphibole, from starting melt compositions in equilibrium with initial zircons, while other zircon equilibrium melt batches appear to reflect different degrees of mixing with mafic melts. This study illustrates the power of applying trace element compositions from crystallizing mineral assemblages in combination with zircon, to obtain a detailed record of magmatic evolution which is not evident in whole rock studies.

Finally, in Chapter 5, we present the general conclusions of this thesis which pertain to emplacement and magmatic evolution of the VFC.

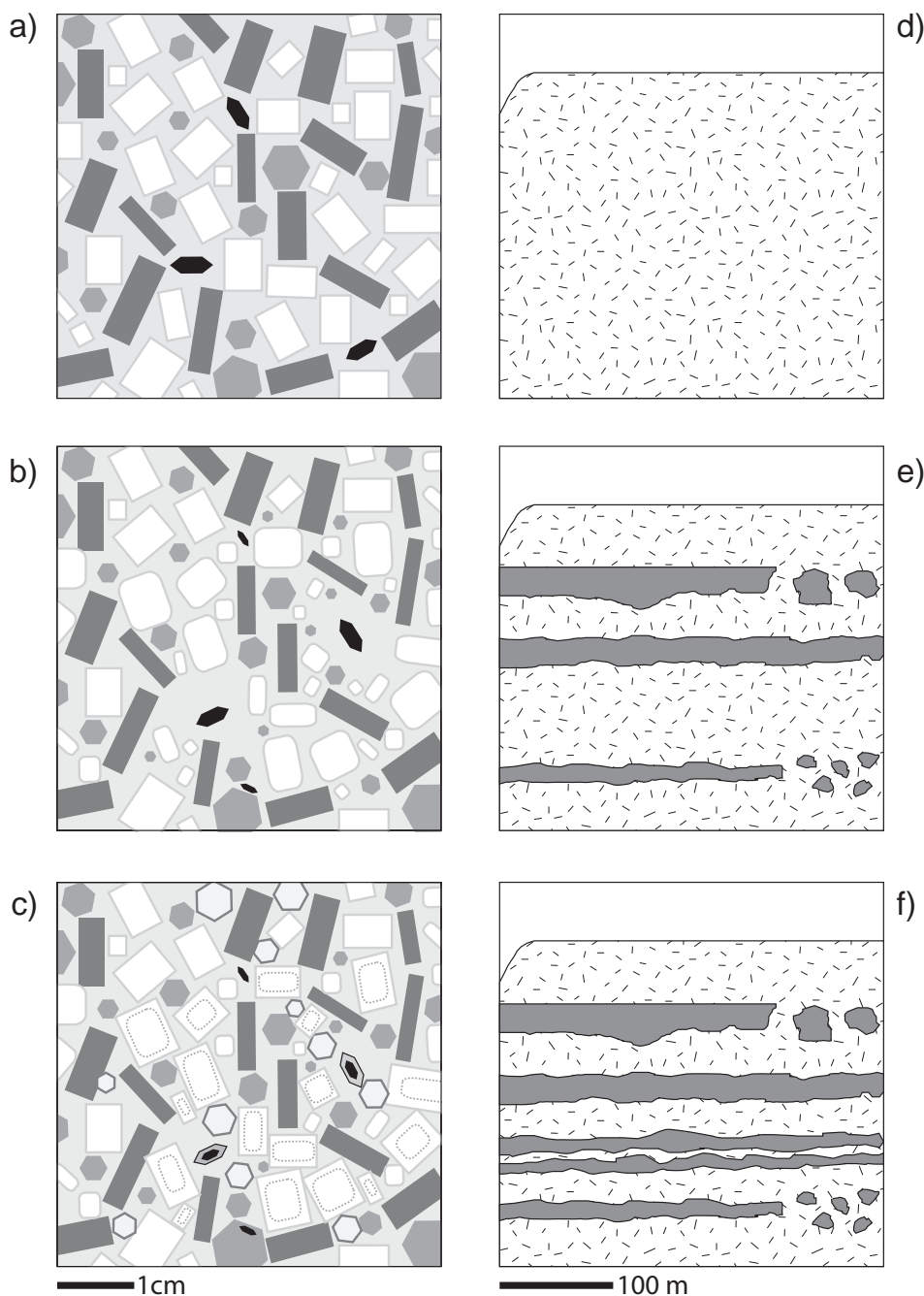


Figure 1: A conceptual model for zircon crystallization at the crystal scale (a-c) and at the outcrop scale (d-f) for VFC emplacement. a) initial felsic intrusions record subsequent cooling and crystallization (~60 - 70% crystals); b) felsic crystal mushes during periods of rejuvenation become reheated causing melting and a decrease in crystal content (~ 50%) due to resorption and dissolution; c) crystal mushes further crystallized (~ 80 – 90%) upon cooling; d) initial emplacement of the felsic intrusions; e) during the onset of mafic sheet injections the mafic sheets break up into enclave swarms and the felsic units become remobilized; f) continued smaller volume of mafic injections.

Figure 1 : Un modèle conceptuel pour la cristallisation de zircons à l'échelle d'un cristal (a-c) et à l'échelle de l'affleurement (d-f) pour l'emplacement du Complexe du Val Fredda. a) des intrusions felsiques initiales enregistrent subséquemment un refroidissement et un rajeunissement ; b) pendant les périodes de rajeunissement, des « crystal mush » felsiques se réchauffent et fondent, provoquant une diminution de la teneur en cristaux (~50 %) à cause de la resorption et la dissolution ; c) les « crystal mush » plus cristallisés par le refroidissement ; d) emplacement initial des intrusions felsiques ; e) lors du début des injections de dikes mafiques les dikes se désintègrent en essaims d'enclaves et les unités felsiques se remobilisent ; f) des injections mafiques continuent à plus faible volume.

ECHELLES DE TEMPS ET PROCESSUS PÉTROLOGIQUES LORS DE LA CONSTRUCTION SÉQUENTIELLE D'UN PLUTON: UNE ÉTUDE DE CAS DU COMPLEXE DE VAL FREDDA, BATHOLITE DE L'ADAMELLO, ITALIE DU NORD.

Résumé de thèse

Cette thèse étudie l'emplacement et l'évolution magmatique du Complexe de Val Fredda (CVF), qui se trouve dans l'extrémité Sud du Batholite d'Adamello, dans le Nord de l'Italie. Le CVF donne un aperçu de l'histoire d'un pluton qui fut construit par de multiples injections de magmas de compositions variées, où l'on peut observer des relations complexes entre des dikes mafiques qui intrudent des magmas felsiques pendant la solidification de ces derniers. Cette thèse présente des données isotopiques et géochimiques qui incluent des méthodes de géochronologie de haute précision par spectrométrie de masse à thermo-ionisation (ID-TIMS), des analyses d'éléments traces sur des titanites et zircons, et des compositions isotopiques de Hf sur zircons, tous obtenus sur les mêmes volumes minérales. Ces données sont intégrées avec des analyses d'éléments traces in situ, des observations de terrain, et des données publiées précédemment.

Le premier chapitre présente l'introduction et un aperçu des objectifs de cette thèse.

Le deuxième chapitre étudie les relations entre de complexes populations d'âge et de chimie de zircons, et comment elles reflètent l'emplacement magmatique. En utilisant la géochronologie U-Pb de haute précision sur zircon, nous démontrons que lors de périodes de croissance de zircons de 100 ka – 200 ka, de multiples périodes de croissance accentuée peuvent être identifiées. Des périodes coïncidentes de cristallisation de zircons entre les différentes unités, entre 42.54 Ma et 42.50 Ma, et entre 42.48 Ma et 42.40 Ma, sont le résultat d'un rajeunissement des suspensions de cristaux dans liquide felsique « crystal mush » à cause de fluctuations thermiques pendant l'injection répétée de magmas mafiques. Ces fluctuations thermiques maintinrent les magmas felsiques au-dessus de leur solidus dans un « état de crystal mush » pendant la majorité de leur histoire.

Les compositions en éléments traces des zircons enregistrent des variations inter- et intra-grains, qui reflètent la variabilité chimique entre des lots de magmas distincts qui se sont formés par la fusion et

le rajeunissement des magmas felsiques initiaux par des injections de magmas mafiques. L'existence de multiples lots de magmas distincts est indiquée par les données isotopiques Hf dans les zircons, qui enregistrèrent de grandes variations en ϵ_{Hf} entre +2 et +8 lors de la remobilisation des crystal mush felsiques, et indiquent un mélange accroissant avec le gabbro de Cadino ($\epsilon_{\text{Hf}} = +9$) au fil du temps. Cette étude surligne la difficulté à lier des datations U-Pb sur zircon avec des processus physiques, tels que l'emplacement magmatique.

Le chapitre 3 présente des datations U-Pb ID-TIMS obtenues à partir de zircons extraits de lames minces, afin de déterminer si des périodes de croissance accentuées de zircon sont liées à la cristallisation d'assemblages minérales spécifiques dans la séquence paragénétique d'un magma.

Des images de diffraction d'électrons rétrodiffusées (back scattered electrons; BSE) et de cathodoluminescence (CL) révèlent que le zircon satura tôt dans les magmas du CVF et cristallisa tout au long de la séquence paragénétique. Cependant, de nombreux grains possèdent des noyaux hérités. Les grains sans noyau ont une longueur typique inférieure à 100 μm et contiennent peu de plomb radiogénique ($\text{Pb}^* = 0.62 - 0.86$ picogrammes) résultant en une faible précision analytique, de l'ordre de jusqu'à 1% sur des âges $^{206}\text{Pb}/^{238}\text{U}$. Par contre, dans le gabbro de Mattoni, les images BSE et CL montrent que les zircons saturèrent tardivement et cristallisèrent dans les minéraux formant la matrice tardive, notamment le quartz et le plagioclase. Des datations $^{206}\text{Pb}/^{238}\text{U}$ de haute précision (0.08 – 0.18 %), ainsi que leur contexte textural, furent obtenus grâce à la grande taille des zircons ($< 100 \mu\text{m}$) et la teneur élevée en Pb^* .

L'étude d'échantillons mafiques et felsiques du CVF met en évidence les limitations de notre méthode de datation ID-TIMS dans le contexte textural, qui nécessite des zircons sans noyau avec suffisamment de plomb radiogénique pour atteindre la précision requise de 0.1% sur des datations $^{206}\text{Pb}/^{238}\text{U}$, et la saturation précoce du zircon est requise pour pouvoir résoudre la chronologie de cristallisation d'assemblages minéraux distincts. En conséquence, il fut impossible de lier les périodes de cristallisation de zircon dans les magmas du CVF avec l'étape dans laquelle ils se sont cristallisés dans la séquence paragénétique. Cependant, la gamme d'âges du gabbro de Mattoni obtenues avec nos datations de haute précision et leur contexte textural ($42.451 \pm 0.077 \text{ Ma}$ to $42.546 \pm 0.061 \text{ Ma}$) est en accord avec la dispersion d'âges précédemment obtenue avec des moyens conventionnels ($42.426 \pm 0.039 \text{ Ma}$ to $42.539 \pm 0.033 \text{ Ma}$), ce qui suggère que les âges U-Pb sur zircon obtenus avec les moyens conventionnels sont représentatifs de la durée de cristallisation du gabbro de Mattoni.

Le quatrième chapitre présente des compositions à l'équilibre de terres rares dans les liquides magmatiques, calculées à partir de concentrations en éléments traces mesurées dans les assemblages minérales du CVF, afin d'étudier l'évolution magmatique pendant l'amalgamation incrémentale du pluton. Les analyses en éléments traces dans les titanites et zircons, acquis sur les mêmes volumes minérales qui furent utilisées pour les datations U-Pb de haute précision, nous permettent de reconstruire les variations de composition magmatique en fonction du temps. La titanite est un hôte majeur pour le budget en terres rares lors de la cristallisation fractionnée du CVF, et enregistre des compositions en éléments traces qui sont distincts pour chaque composition magmatique. Les calculs de compositions d'équilibre en éléments traces des magmas avec les minéraux, combinés avec la thermométrie de Zr en titanite, suggèrent une cristallisation simultanée de titanite et amphibole à des températures qui se situent entre $\sim 700^{\circ}\text{C}$ et 750°C dans les magmas felsiques, et une cristallisation simultanée de titanite et zircon à $\sim 800^{\circ}\text{C}$ dans les magmas mafiques. Les compositions des magmas à l'équilibre avec la titanite permettent un aperçu des compositions magmatiques de faible température ; cependant ces magmas ne peuvent être corrélés avec des datations U-Pb sur titanite car ces dernières reflètent le refroidissement de la roche sous la température de fermeture de 650°C .

Contrairement à la titanite, le zircon ne contient que des pourcentages faibles ($< 10\%$) du budget total en terres rares, en dépit de leur enregistrement de la croissance de zircon prolongée sur des durées de 100 – 200 ka. Les compositions magmatiques calculées à l'équilibre avec le zircon reflètent une cristallisation simultanée avec le plagioclase, et dans une moindre mesure, l'amphibole. Néanmoins, de grandes variations sont observées dans les compositions magmatiques à l'équilibre avec le zircon, qui ne montrent pas de tendances temporelles cohérentes. Les variations non-systématiques de composition magmatique sont interprétées ici comme le reflet de lots de magmas de chimies distinctes. Lors de périodes de rajeunissement, le magma en équilibre avec le zircon nécessite $\sim 50\%$ de cristallisation en proportions variables de plagioclase et d'amphibole à partir de compositions à l'équilibre avec les zircons initiaux, tandis que d'autres compositions magmatiques calculées semblent refléter des degrés variables de mélange avec des magmas mafiques. Cette étude démontre la pertinence de l'utilisation de compositions en éléments traces sur des minéraux à l'équilibre avec le zircon, pour obtenir un enregistrement détaillé de l'évolution magmatique, qui n'est pas mise en évidence par l'étude de roches totales.

Finalement, dans le chapitre 5, nous présentons les conclusions générales de cette thèse.

Acknowledgements

First and foremost I would like to thank my supervisor Urs Schaltegger for his continued support, advice, patience and persistence which has made this PhD thesis possible. I would also like to thank my thesis committee, Othmar Müntener and Peter Ulmer for their encouragement and constructive comments. I am very grateful to have been a part of the 4D Adamello Pro-doctoral School and I would like to thank the Professors and students for sharing in such an amazing experience! I would like to thank Othmar, Peter Brack, Lucas and Benita for organizing great field excursions over the last four years! A special thanks to Peter Ulmer for always hiking with me at the back of the line and always making me laugh during the field excursions!

In addition, I am grateful to have been a part of the Isotope Geochemistry and Geochronology group at the University of Geneva, thanks for all of the discussions and advice over the years. I would like to thank the ID-TIMS U-Pb group, Maria Ovtcharova, Bryan Sell, Jörn Wotzlav and Björn Baresel, for their patience in teaching me about high precision U-Pb dating of zircon and still allowing me to work in the clean lab even when I had high blanks. I am grateful for all of my field assistants, especially Mickael Heiniger, because without you there would be no rocks! I would like to thank Axel Gerdes for his assistance with my Hf isotope analyses, Daniel Frick and Detlef Günther for their assistance with the TIMS-TEA measurements, and Alexey Ulianov for his assistance with LA-ICP-MS trace element analyses. I am also very grateful for all of the people that have provided technical support throughout my PhD: Richard Spikings, Kalin Kouzmanov, Rossana Martini, Susanne Schmidt, Sofia Saldana, Elizabeth Lagut, Jean-Marie Boccard and Fred Arlaud.

Thanks to all of the people I have met while at the University of Geneva, it has been a truly great experience! I would like to thank Flora for being a fantastic office mate (707 rocks!!) but also for being a great friend who introduced me to some awesome office theme songs! I would like to thank Roelant for teaching me about all things Swiss, for appreciating my celebrity knowledge at pub quiz, but mainly for being a great friend over the last four years. Ryan, you hooligan, thanks for the good times and teaching me that one more for the road usually means two or three! Also, Ryan thanks so much for coming back to Geneva for my defense and the magnum Champagne you are truly awesome! I would like to thank the ProSoc, David, Roel, Nik, Katha, Toby, Rohit, Alex, Sylvia and Anina for the great times on our field excursions and outside of working hours! I would like to thank Katha for always making me laugh when we have to climb with these outdoor guys in the snow! To the members of the ProSoc I hope our next excursion is on a sunny beach with fruity drinks. I would like to thank my family for their love and continued support throughout my PhD. I especially want to thank Yannick for all of his love and support and for being so amazing, especially at the end!

TABLE OF CONTENTS

Thesis abstract	i
Résumé en Français	v
Acknowledgements	ix
1 Introduction and outline of thesis	1
2 Repetitive rejuvenation of tonalitic crystal mush by injections of mafic melts (southern Adamello batholith, northern Italy)	7
2.1 Introduction	8
2.2 Geologic setting	9
2.3 Analytical procedures	13
2.3.1 ID-TIMS	13
2.3.2 Trace element analysis in zircon	15
2.3.3 Zircon Hf isotope analysis	16
2.4 Results	17
2.4.1 Zircon U-Pb geochronology	17
2.4.2 Titanite U-Pb geochronology	21
2.4.3 Trace element composition of zircon	25
2.4.4 Hf isotopes of zircon	39
2.5 Discussion	39
2.5.1 Interpretation of zircon ages	39
2.5.2 VFC thermal modeling	42
2.5.3 A conceptual model part 1: zircon crystallization	42
2.5.4 A conceptual model part 2: emplacement of the VFC	46
2.6 Conclusions and Outlook	48
References	48
3 Texturally controlled ID-TIMS U-Pb dating of zircon from thin sections: An example from the Val Fredda Complex, N. Italy	55
3.1 Introduction	56
3.2 Geologic setting	57
3.3 Petrography	59
3.3 Analytical techniques	61

3.4.1	Locating zircons in thin section	61
3.4.2	LA-ICP-MS zircon trace element analysis	62
3.4.3	Texturally controlled ID-TIMS zircon dating	62
3.5	Results	63
3.5.1	Zircon occurrence and textural relationships	63
3.5.2	In situ zircon trace element composition	72
3.5.3	Texturally controlled ID-TIMS U-Pb zircon dating	74
3.6	Discussion	77
3.6.1	Dating small zircons from thin section	77
3.6.2	Texturally controlled ID-TIMS dating: an example from the Mattoni gabbro	79
3.7	Conclusions	82
	References	83
4	Tracking REE variations in melt compositions during the rejuvenation of felsic crystal mushes using trace element compositions of titanite and zircon	87
4.1	Introduction	88
4.2	Geological setting	89
4.3	Petrography	91
4.4	Analytical methods	93
4.4.1	Whole-rock geochemistry and modal abundances	93
4.4.2	TIMS-TEA (titanite trace element analyses)	95
4.4.3	Trace element analysis in apatite by LA-ICP-MS	97
4.5	Results	100
4.5.1	Whole-rock compositions	100
4.5.2	Titanite aliquots	102
4.5.3	Trace element composition of titanite	102
4.6	Discussion	103
4.6.1	Mineral contributions to whole-rock REE budget	103
4.6.2	Calculated melt compositions	107
4.7	Conclusions	118

References	119
5 Conclusions and Outlook	125
Appendix	
Appendix A: Chapter 2	129
Appendix B: Chapter 3	143
Appendix C: Chapter 4	153
Appendix D: ID-TIMS U-Pb zircon dates for WAT	155
Appendix E: ID-TIMS U-Pb zircon dates for the Listino Suite	159
Appendix F: ID-TIMS U-Pb zircon dates for the Bruffione	165

Thesis Introduction

This thesis is part of the 4D Adamello Pro-Doctoral school which is an interdisciplinary approach to contribute to the understanding of the generation and emplacement of batholiths in space and time. The goal of the doctoral school is to integrate disciplines such as numerical modeling, experimental petrology, geochemistry, geochronology, geophysics and rheology in order to address pertinent questions related to batholith formation, such as melt generation and extraction in the upper mantle; physical models of magma propagation through the upper mantle and crust; crystallization processes during ascent and emplacement; thermal evolution of magma bodies and contact aureoles; and time-scales of magma generation and crystallization.

This thesis is part of the fourth dimension which focuses on resolving timescales of magma evolution. Using high precision U-Pb zircon geochronology it is possible to resolve individual magma pulses and to determine the time intervals of high magma flux in a magmatic system (Matzel et al., 2006; Michel et al., 2008; Leuthold et al., 2012; Schoene et al., 2012). The data obtained from this thesis will be used to address magma evolution during incremental pluton assembly through time. This thesis will discuss zircon growth within the paragenetic sequence of a magma and use chemical variations in zircon to discuss different processes (e.g. fractional crystallization, mixing, melting, etc.) during magma emplacement. In addition our high precision U-Pb zircon dates will provide input parameters for time-resolved thermo-mechanical models for batholith emplacement.

Current Knowledge

U-Pb zircon geochronology is commonly used for determining timescales of batholith formation and has revealed that plutons are incrementally assembled by repeated magma injections (Michel et al., 2008; Miller et al., 2011; Leuthold et al., 2012) and eventually build up batholiths over extended periods of time. Timescales of pluton construction may vary over thousands to few millions of years (Glazner et al., 2004; Coleman et al., 2004; Matzel et al., 2006; Michel et al., 2008; Schaltegger et al., 2009; Leuthold et al., 2012; Schoene et al., 2012).

Recent advances in ID-TIMS U-Pb zircon geochronology such as chemical abrasion to reduce Pb loss (Mattinson, 2005) and reduction in laboratory analytical blanks have resulted in analytical uncertainties at the permil level on single $^{206}\text{Pb}/^{238}\text{U}$ zircon dates (Schmitz and Schoene, 2007; Schoene et al., 2010). Increased precision now often results in zircon age dispersions over 100 ka

timescales within single samples (Schaltegger et al., 2009; Memeti et al., 2010; Schoene et al., 2012; Wotzlaw et al., 2013). Complex zircon populations may reflect prolonged growth of autocrystic zircon and potentially the incorporation of antecrystic and xenocrystic zircon (Miller et al., 2007). In this thesis, using the terminology of Miller et al. (2007), we consider autocrystic zircon as zircons which have crystallized from the last intrusive pulse, whereas antecrystic zircons are considered to be zircons which are recycled from an earlier pulse of magma within the same magmatic system, and xenocrystic zircons are zircons which are incorporated from the surrounding host rock. Therefore our ability to reconstruct processes of interest is dependent on what zircon dates are actually recording. Geochemical and isotopic analyses of zircon are often employed to track magmatic processes such as changes in magma composition, crystallinity and temperature during magma evolution (Claiborne et al., 2010; Reid et al., 2011; Schoene et al., 2012; Wotzlaw et al., 2013).

Aims of the Thesis

In order to resolve timescales of magmatic processes, such as duration and evolution during emplacement, we carried out a detailed investigation of the Val Fredda Complex (VFC) in the southern tip of the Adamello batholith, N. Italy. The VFC provides insights into an incrementally assembled pluton that was constructed by compositionally diverse magmas from which individual magma pulses can be identified. In this thesis we investigate complex zircon populations between co-magmatic felsic and mafic lithologies using state of the art techniques, which allow us to obtain high precision ID-TIMS U-Pb zircon dates, trace element concentrations obtained from TIMS-TEA analysis (Schoene et al., 2010) and Hf isotope compositions, all from the same volume of zircon, combined with LA-ICP-MS trace element data.

It is the aims of this thesis establish a quantitative dataset to address the following questions:

- Among complex zircon populations that record prolonged growth, what do zircon dates record? And how do they relate to the emplacement of a magma?
- By combining high precision U-Pb dates with geochemical and isotopic data, can we make distinctions between autocrystic and antecrystic zircon growth?
- Can we use autocrystic zircon growth to quantify timescales of individual magma pulses? For example, does the date recorded by zircon reflect prolonged residence times in a magma or do zircon U-Pb dates reflect periods in which magmas are saturated in zircon?
- Can we relate periods of protracted zircon growth to the paragenetic sequence of a magma?

- Can accessory minerals provide insights into the processes affecting the chemical variability of a magma such as melt rejuvenation and mixing through time?

Outline of the Thesis

This thesis is presented in three chapters within the framework of the main aims outlined above.

Chapter 2 presents a state of the art approach for the analysis of complex zircon populations by using high precision U-Pb dates, Hf isotopic compositions and trace element analysis all from the same volume of zircon. In addition we integrate in situ trace element analysis combined with CL imaging, in attempt to link multiple periods of zircon growth, observed in CL images, to the age dispersion recorded by high precision zircon dates. This data set was used to determine a detailed history for the evolution of the Val Fredda Complex by documenting changes in magma composition, crystallinity and temperature fluctuations during 100 – 200 ka periods of protracted zircon growth.

Chapter 3 establishes a new technique to obtain texturally controlled ID-TIMS zircon dates from thin sections. This data was used to determine if the observed age dispersions recorded by zircons could be related to specific minerals within the paragenetic sequence of a magma. In addition we will test the results from Chapter 2 to determine if the age dispersion recorded by zircons selected from conventional separation techniques are representative of zircon crystallization or if the observed age dispersion is biased by grain selection. Advantages and drawbacks of this technique are presented for felsic and mafic lithologies.

Chapter 4 presents equilibrium REE melt compositions calculated from trace element concentrations in crystallizing mineral assemblages. We utilize trace element concentrations in titanite and zircon, obtained by TIMS-TEA (Schoene et al., 2010), in order to evaluate variations in melt compositions as a function of time. This data was used to determine the processes affecting the chemical variability in melt compositions during periods of magma rejuvenation recorded by zircon.

Chapter 5 presents the main conclusions of this thesis and outlooks.

References

- Claiborne, L.L., Miller, C.F., and Wooden, J.L., 2010, Trace element composition of igneous zircon: a thermal and compositional record of the accumulation and evolution of a large silicic batholith, Spirit Mountain, Nevada: *Contributions to Mineralogy and Petrology*, v. 160, p. 511-531.
- Coleman, D.S., Gray, W., and Glazner, A.F., 2004, Rethinking the emplacement and evolution of zoned plutons: Geochronologic evidence for incremental assembly of the Tuolumne Intrusive Suite, California: *Geology*, v. 32, p. 433-436.
- Glazner, A.F., Bartley, J.M., Coleman, D.S., Gray, W., and Taylor, R.Z., 2004, Are plutons assembled over millions of years by amalgamation from small magma chambers?: *GSA today*, v. 14, p. 4-12.
- Leuthold, J., Müntener, O., Baumgartner, L.P., Putlitz, B., Ovtcharova, M., and Schaltegger, U., 2012, Time resolved construction of a bimodal laccolith (Torres del Paine, Patagonia): *Earth and Planetary Science Letters*, v. 325, p. 85-92.
- Mattinson, J.M., 2005, Zircon U-Pb chemical abrasion ("CA-TIMS") method: combined annealing and multi-step partial dissolution analysis for improved precision and accuracy of zircon ages: *Chemical Geology*, v. 220, p. 47-66.
- Matzel, J.E.P., Bowring, S.A., and Miller, R.B., 2006, Time scales of pluton construction at differing crustal levels: Examples from the Mount Stuart and Tenpeak intrusions, North Cascades, Washington: *Geological Society of America Bulletin*, v. 118, p. 1412-1430.
- Memeti, V., Paterson, S., Matzel, J., Mundil, R., and Okaya, D., 2010, Magmatic lobes as "snapshots" of magma chamber growth and evolution in large, composite batholiths: An example from the Tuolumne intrusion, Sierra Nevada, California: *Geological Society of America Bulletin*, v. 122, p. 1912-1931.
- Michel, J., Baumgartner, L., Putlitz, B., Schaltegger, U., and Ovtcharova, M., 2008, Incremental growth of the Patagonian Torres del Paine laccolith over 90 ky: *Geology*, v. 36, p. 459-462.
- Miller, C.F., Furbish, D.J., Walker, B.A., Claiborne, L.L., Koteas, G.C., Bleick, H.A., and Miller, J.S., 2011, Growth of plutons by incremental emplacement of sheets in crystal-rich host: Evidence from Miocene intrusions of the Colorado River region, Nevada, USA: *Tectonophysics*, v. 500, p. 65-77.
- Miller, J.S., Matzel, J.E.P., Miller, C.F., Burgess, S.D., and Miller, R.B., 2007, Zircon growth and recycling during the assembly of large, composite arc plutons: *Journal of Volcanology and Geothermal Research*, v. 167, p. 282-299.
- Reid, M.R., Vazquez, J.A., and Schmitt, A.K., 2010, Zircon-scale insights into the history of a Supervolcano, Bishop Tuff, Long Valley, California, with implications for the Ti-in-zircon geothermometer: *Contributions to Mineralogy and Petrology*, v. 161, p. 293-311.
- Schaltegger, U., Brack, P., Ovtcharova, M., Peytcheva, I., Schoene, B., Stracke, A., Marocchi, M., and Bargossi, G.M., 2009, Zircon and titanite recording 1.5 million years of magma accretion, crystallization and initial cooling in a composite pluton (southern Adamello batholith, northern Italy): *Earth and Planetary Science Letters*, v. 286, p. 208-218.
- Schmitz, M. D., and Schoene, B., 2007, Derivation of isotope ratios, errors, and error correlations for U-Pb geochronology using ^{205}Pb - ^{235}U -(^{233}U)-spiked isotope dilution thermal ionization mass spectrometric data: *Geochemistry, Geophysics, Geosystems*, v. 8, no. 8.
- Schoene, B., Latkoczy, C., Schaltegger, U., and Günther, D., 2010, A new method integrating high-precision U-Pb geochronology with zircon trace element analysis (U-Pb TIMS-TEA): *Geochimica et Cosmochimica Acta*, v. 74, p. 7144-7159.
- Schoene, B., Schaltegger, U., Brack, P.,

- Latkoczy, C., Stracke, A., and Günther, D., 2012, Rates of magma differentiation and emplacement in a ballooning pluton recorded by U-Pb TIMS-TEA, Adamello batholith, Italy: *Earth and Planetary Science Letters*, v. 355, p. 162-173.
- Wotzlaw, J.-F., Schaltegger, U., Frick, D. A., Dungan, M. A., Gerdes, A., and Günther, D., 2013, Tracking the evolution of large-volume silicic magma reservoirs from assembly to supereruption: *Geology*.

Chapter 2

REPETITIVE REJUVENATION OF TONALITIC CRYSTAL MUSH BY INJECTIONS OF MAFIC MELTS (SOUTHERN ADAMELLO BATHOLITH, NORTHERN ITALY)*

Cindy Broderick¹, U. Schaltegger¹, D. Frick², D. Günther², A. Gerdes³, G. Simpson¹

¹ University of Geneva, Section of Earth and Environmental Sciences, Switzerland

² ETH Zürich, Laboratory of Inorganic Chemistry, Switzerland

³ Goethe-University Frankfurt, Institute of Geosciences, Germany

Abstract

The Val Fredda Complex in the southern tip of the Adamello Batholith, N. Italy, is a pluton that has been constructed by multiple injections of mafic melts that were injected as sills into solidifying felsic magmas. High precision U-Pb dating of single zircons reveal 100 – 200 ka periods of protracted zircon growth during the history of the VFC and individual units have zircon dates that record multiple periods of enhanced zircon crystallization. Coinciding periods of zircon crystallization from the different units between 42.54 Ma to 42.50 Ma and 42.48 Ma to 42.40 Ma, indicates that zircons from the different VFC units are recording a common thermal evolution, providing evidence for the rejuvenation of the felsic crystal mushes as the result of thermal fluctuations due to repeated mafic injections. These thermal cycles kept the felsic magmas above solidus conditions, in a “crystal mush state” consistent with calculated Ti-in-zircon temperatures of $\leq 750^{\circ}\text{C}$.

Growth textures visible in CL images confirm complex histories of multiple periods of zircon growth and dissolution. In order to link this information to the precisely dated periods of enhanced zircon crystallization, we combine CL-controlled in-situ (laser ablation) trace elements with whole grain trace elements (TIMS-TEA) and Hf isotopic compositions, from the same volume of dated zircon. Whole grain trace element ratios of Th/U, Y/Hf and $(\text{Lu/Gd})_{\text{N}}$ vary by two orders of magnitude, and record non-systematic trace element correlations with time. In-situ analyses of zircon indicate that initial magma conditions recorded by zircon cores record similar variations, whereas zircon rims appear to be more restricted in their compositions. However, these changes do not record monotonic trends between cores and rims typical for crystallization within a cooling magma. We therefore interpret the non-systematic inter- and intra-grain trace element variations in zircon to represent the chemical variability within different isolated magma batches that coexisted among the remobilized

* Manuscript to be submitted to *Lithos* or *Contributions to Mineralogy and Petrology*

felsic crystal mushes that formed from the remelting and rejuvenation of the initial felsic intrusions by the mafic melt injections. Zircon Hf isotopic compositions record large variations in ϵ_{Hf} ranging from +2 to +8, among the felsic units, and point to increased mixing with the Cadino gabbro (ϵ_{Hf} +9) through time. The lack of chemical homogenization is the result of the VFC never reaching the thermally mature stage of an eruptible convecting magma chamber, thus leading to stalling of the felsic crystal mushes in the upper crust and subsequent solidification.

2.1 Introduction

A growing body of evidence supports the notion that plutons are incrementally assembled by repeated magma injections forming sills or dykes during periods of high magma flux (Michel et al., 2008; Annen et al., 2006; Annen, 2011; Miller et al., 2011; de Saint-Blanquat et al., 2011; Leuthold et al., 2012) and eventually build up batholiths over extended periods of time. Timescales of pluton construction may vary over thousands to few millions of years (Glazner et al., 2004; Coleman et al., 2004; Matzel et al., 2006; Michel et al., 2008; Schaltegger et al., 2009; de Saint-Blanquat et al., 2011; Leuthold et al., 2012; Schoene et al., 2012), depending on their size and the integrated flux rate. Using high precision U-Pb zircon geochronology it is possible to resolve the individual magma pulses and to determine the time intervals of high magma flux in a magmatic system (Matzel et al., 2006; Michel et al., 2008; Leuthold et al., 2012; Schoene et al., 2012).

During periods of repeated magma injections, temperatures, crystal content and composition

will fluctuate within magma batches, and conditions potentially alternate between zircon saturation and undersaturation, leading to crystallization and dissolution. Following episodes of reheating and rejuvenation, magma batches will record periods of enhanced zircon crystallization associated with cooling below zircon saturation temperatures (Watson and Harrison, 1983; Hanchar and Watson, 2003). Therefore zircon has the potential to record periods of fluctuating ambient conditions during the crystallization interval (“mush state”) of a magmatic system. However, our ability to reconstruct the processes of interest depends on the survival of zircon within a crystallized magma batch during the subsequent injections in the course of pluton construction. In addition, our high precision ID-TIMS U-Pb zircon dates are obtained from whole zircon grains, integrating and thus masking a potentially complex multi-episodic growth history. Spatially resolved U-Pb dates would be the perfect analytical choice, but they do not offer the necessary 10 to 100 ka precision for resolving the timing of magmatic

processes. Finally, another big concern remains, whether and how we can eventually relate the high-precision U-Pb zircon crystallization ages to the physical state of a magmatic system such as, e.g., its crystal fraction, temperature, or viscosity at a given moment, and deduce the age of physical emplacement of a magma.

In this study, we utilize high precision CA-ID-TIMS (chemical abrasion, isotope-dilution, thermal ionization mass spectrometry) zircon geochronology, trace element concentrations obtained from TIMS-TEA analysis (Schoene et al., 2010) and initial Hf isotope composition, all from the same volume of zircon, to document changes in the magma composition, from which zircon is crystallizing, as a function of time. Combined with in situ trace element analyses and CL images, we attempt to link multiple periods of zircon growth, observed in CL, to high precision ages which reveal multiple periods of enhanced zircon crystallization.

The Val Fredda Complex in the southern tip of the Adamello Batholith, N. Italy, provides insights into the history of melt accretion in the roof of a growing and crystallizing, small pluton, which never arrived at the thermally mature stage of a convecting magma chamber. It has been constructed by multiple injections of compositionally diverse magmas, ranging from gabbro to granodiorite. Field observations reveal complex relationships among mafic magmas

injected into solidifying felsic magmas, where both magma mingling and hybridization can be observed. The zircon results presented here highlight 100 – 200 ka periods of protracted zircon growth, recording multiple periods of enhanced zircon crystallization with associated cooling after episodes of rejuvenation of the felsic crystal mush by repeated mafic injections. Zircon U-Pb dates are therefore not reflecting physical processes such as emplacement of magma, but are a measure for the variations of intensive parameters during the mush state of a magmatic system.

2.2 Geologic setting

The Tertiary Adamello Batholith is exposed over an area of ~670 km² with ~2 km of vertical relief, in the Southern Alps, Northern Italy (Fig.1a; Brack, 1983; Callegari and Brack, 2002). The Adamello batholith is mainly composed of tonalites, thondjemites and granodiorites with minor mafic units in the southern most part of the batholith (Brack, 1983; Callegari and Brack, 2002). Geochronological data indicate that the Adamello batholith was constructed sequentially from 43-42 Ma in southern and eastern marginal units and then progressively decreases in age towards the northeast to 33 Ma (Del Moro et al., 1983; Hansmann and Oberli, 1991; Skopelitis et al., in prep.). Sr and O isotopic studies also

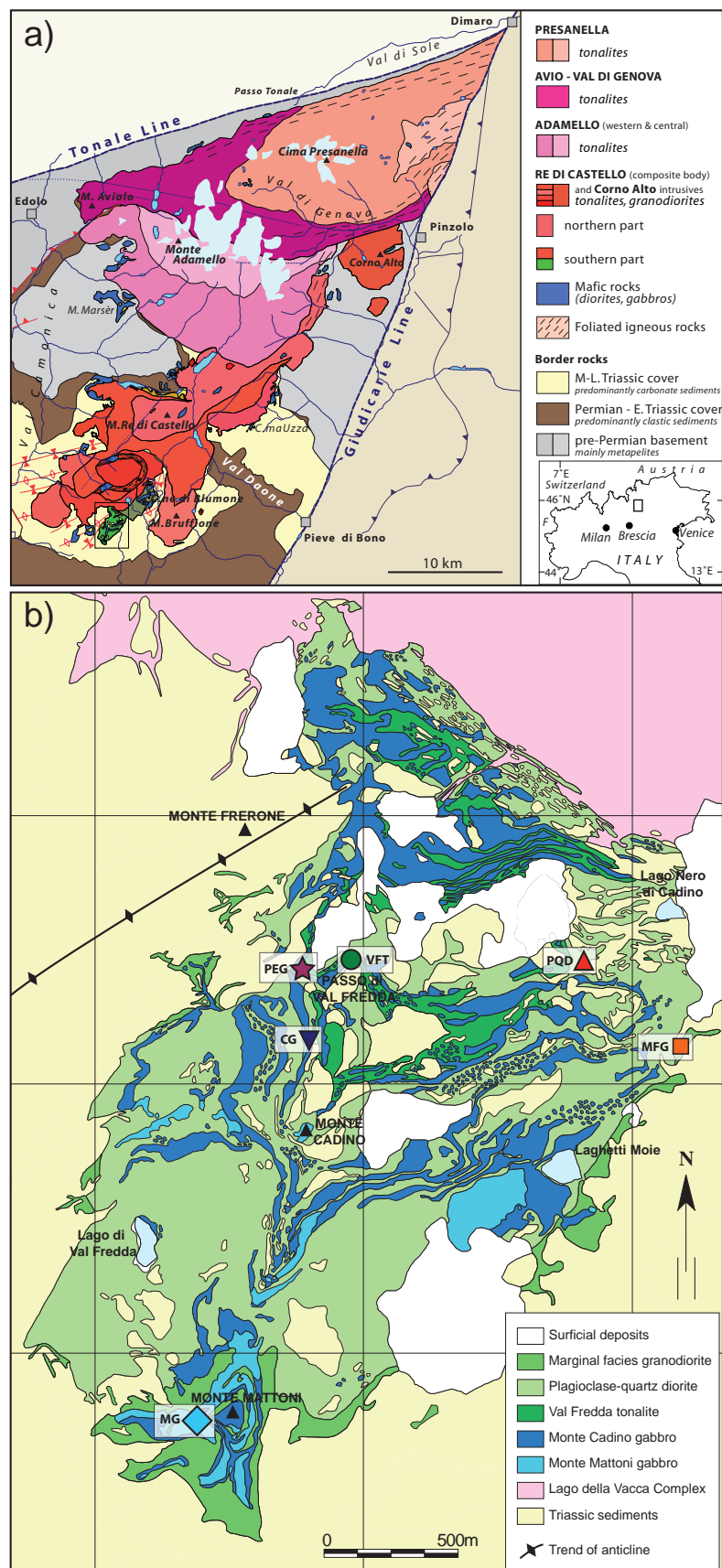


Figure 1: a) Simplified geologic map of the Adamello batholith after Schaltegger et al. (2009) showing the four super-units and corresponding lithologies. Location of field area in Fig. 1b is outlined by the black box. b) Simplified geologic map of the Val Fredda Complex modified after Blundy and Sparks (1992). Sample locations are indicated by symbols: CG = Cadino gabbro; MFG = marginal facies granodiorite; MG = Mattoni gabbro; Peg = pegmatite; PQD = plagioclase quartz diorite; VFT = Val Fredda tonalite.

reflect the sequential nature of emplacement, indicating increasing amounts of crustal assimilation during the emplacement of the batholith (Cortecci et al., 1979; Del Moro et al., 1983; Skopelitis et al., in prep.). The batholith has been divided into four so-called super-units (Callegari and Brack, 2002), with the apparent size of the intrusions and degree of homogeneity increasing northwards (Fig.1a). The oldest rocks of the Adamello batholith are recorded in the Corno Alto and the southernmost Re di Castello units, including the ~43 Ma Corno Alto granodiorites (Del Moro et al., 1983; Skopelitis et al., in prep.), the 42.43 Ma Monte Frerone granite dykes (Schaltegger et al., 2009) and the ~42 - 40 Ma Val Fredda Complex (Hansmann and Oberli, 1991; Tiepolo et al., 2011). In addition to representing the oldest part of the Adamello batholith, the Re di Castello super-unit shows the most compositional diversity with ultramafic to mafic units spatially associated with tonalites and granodiorites. The mafic rocks occur mainly in the periphery and are best exposed in the Val Fredda Complex and the Blumone Complex (Ulmer et al., 1983; Blundy and Sparks, 1992; Tiepolo et al., 2005, 2011).

This study focuses on the Val Fredda Complex (VFC), a small marginal intrusion exposed over ~6 km² in the southern most part of the batholith (Fig.1b). The VFC is bordered in the east, west and south by Triassic dolomite country rocks,

which exhibit pre-intrusive ENE-WSW striking large-scale folds (Brack, 1983; Callegari and Brack, 2002) and is itself located within a broad syncline and bound to the west by the steep sub-vertical eastern limb of the Frerone anticline, suggesting that the pre-intrusive folds in the Triassic country rocks influenced the emplacement of the VFC. Roof pendants and stoped blocks up to 300 m across of the dolomite country rocks are abundant throughout the VFC (Fig. 1b) and suggest that the VFC is presently exposed near the roof of its intrusion (Brack, 1983; Blundy and Sparks, 1992). The VFC is bordered in the north by the 42.07 - 41.76 Ma old Lago della Vacca Complex (LVC; Schoene et al., 2012). The “forceful” emplacement of the LVC caused north-south shortening in the VFC close to the contact, leading to flattening of mafic enclaves and stoped dolomite blocks in the plane parallel to the contact (Fig. 1b; John and Blundy, 1993). The ductile deformation of the VFC suggests that it had not cooled fully below its solidus when the LVC was emplaced. Based on detailed fieldwork (Brack, 1983; Ulmer et al., 1983; Blundy and Sparks, 1992) the VFC intrusion was described as a complex system that was constructed by a series of felsic magmas that show vertical accretion by horizontal injections of mafic sills, of variable thickness ~0.5 m up to 100 m, into the crystallizing roof of a larger magmatic system. We observe complex

relationships between the mafic sheets and felsic units, including hybridization, mingling and back-veining at the mafic-felsic contacts, and mafic enclave swarms, which formed by the breakup of the mafic sheets during their injection into the tonalitic magma due to the inversion of the rheology contrast during cooling (Appendix A in Fig. A1; Blundy and Sparks, 1992).

The VFC consists of five distinct, lithological units, displayed in Fig. 1b: (1) the marginal facies granodiorite (MFG) is porphyric and contains quartz, plagioclase, biotite, magnetite and accessory apatite, zircon and titanite. The MFG outcrops mainly along the southern and eastern margins; (2) the plagioclase quartz diorite (PQD) is equigranular and contains quartz, plagioclase, amphibole, biotite, magnetite and accessory apatite, zircon and titanite, which outcrops mainly in the central and northern parts; (3) the Val Fredda tonalite (VFT) is equigranular and contains quartz, plagioclase, amphibole, biotite, magnetite and accessory apatite, ilmenite, zircon and titanite, which outcrops mainly in the north of the complex; (4) the Cadino gabbro (CG) occurs through out the pluton as a series of horizontal sheets separated by felsic units (PQD, VFT) of variable thickness (mm to m scale) depending on the locality but outcrops most abundantly at Monte Cadino. The Cadino mafic rocks range from hornblende gabbros to quartz-diorites that are characterized texturally by elongate

prismatic to acicular hornblendes in a matrix of plagioclase, quartz and accessory apatite, zircon and titanite; (5) the Mattoni gabbro (MG) occurs mainly in the southern most part of the pluton near Monte Mattoni, and consists of hornblende-phyric, pyroxene-bearing gabbros that are characterized texturally by prismatic euhedral hornblendes in a matrix of plagioclase, quartz and accessory apatite, zircon, titanite and calcite. Ultramafic cumulates (hornblendite) occur at the base of the Mattoni gabbro and consists of amphiboles that contain olivine, cpx, opx and Cr-spinel inclusions (Ulmer et al., 1983; Blundy and Sparks, 1992; Tiepolo et al., 2002, 2005, 2011). Both gabbros (MG, CG) are spatially associated with coarse gabbro pegmatites which occur throughout the mafic sheets as veins and pods cross-cutting the Mattoni and Cadino gabbroic units (Ulmer et al., 1983; Blundy and Sparks, 1992). The pegmatites often contain large skeletal hornblendes, which suggest high growth rates from supersaturated solutions and because they typically occur layer-parallel near the top of the mafic sheets, the pegmatites are considered to represent the residual melts of the gabbros (Ulmer et al., 1983).

Due to the unique occurrence of ultramafic to gabbroic units, which are confined to the oldest parts of the Re di Castello super unit, they have been the focus of many studies (Ulmer et al., 1983; Blundy and Sparks, 1992; Tiepolo et al., 2002,

2005, 2011) which provide us with additional information for understanding how the VFC was emplaced. Experimental work by Ulmer et al., (1983) show that the crystallization sequence for the Mattoni gabbro is olivine + spinel \rightarrow clinopyroxene \rightarrow hornblende + orthopyroxene \rightarrow plagioclase + clinopyroxene. These results indicate early hornblende crystallization and delayed plagioclase crystallization, and combined with geothermometry and geobarometry indicate that the Mattoni gabbro formed from a deep, hot magma 1000-1100°C at 0.8 -1 GPa, which was subsequently emplaced in the shallow crust (0.2-0.3 GPa) at ~900°C (Ulmer et al., 1983; Blundy and Sparks, 1992; Nimis and Ulmer, 1998; Tiepolo et al., 2011). The shallow emplacement is consistent with Al-in-hornblende geobarometry of 0.2-0.3 GPa obtained for the felsic units (Stauffer, 2012). Experimental work by Blundy and Sparks (1992) show that the crystallization sequence for the Cadino gabbro is hornblende + plagioclase + magnetite and the lack of olivine and clinopyroxene is the result of rapid cooling of a magma from super-liquidus conditions at 1000-1050°C down to ~ 950°C. These results are consistent with chilled margins observed along Cadino sheet edges and that the acicular hornblendes are the result of rapid cooling and crystallization.

2.3 Analytical procedures

2.3.1 ID-TIMS

Zircon and titanite were separated using standard magnetic and heavy liquid mineral separation techniques, and were handpicked under a binocular microscope. Inclusion-free zircons were selected from populations of various morphologies and sizes. Titanite grains were selected from populations of euhedral honey colored grains that were free of inclusions and cracks. Zircon grains were thermally annealed and chemically abraded (Mattinson 2005), in order to minimize lead loss, due to the effects of radioactive decay damage, which is essential for the interpretation of our zircon ages. A total of 60 zircon grains and 17 titanite grains were analyzed for their U-Pb isotopic composition using high precision ID-TIMS techniques (see Appendix A for full analytical details). Zircon and titanite grains were spiked using the EARTHTIME (<http://www.earth-time.org>) ^{202}Pb - ^{205}Pb - ^{233}U - ^{235}U -tracer solution and dissolved following procedures modified after Krogh (1973). All measurements were performed at the University of Geneva on a Thermo-Scientific TRITON thermal ionization mass spectrometer equipped with a MasCom discrete dynode electron multiplier operated in ion counting mode. The initial statistical analysis was done using the TRIPOLI program followed by data reduction and age calculation using the

U-Pb Redux software (Bowring et al., 2011), using the algorithms of McLean et al. (2011). The data were corrected for mass fractionation with the ET2535 tracer composition using a $^{202}\text{Pb}/^{205}\text{Pb}$ ratio of 0.99924 and a U-Pb ratios and dates were calculated relative to $^{235}\text{U}/^{205}\text{Pb}$ ratio of 100.23. $^{206}\text{Pb}/^{238}\text{U}$ age ranked data and probability density distributions are plotted using the ISOPLOT/Ex v.3 program of Ludwig (2005). All uncertainties are reported at the two-sigma level. Data are presented in Table 1 (zircons) and Table 2 (titanites).

Initial ^{230}Th disequilibrium correction

In the $^{238}\text{U} - ^{206}\text{Pb}$ decay chain, the long lived intermediate daughter product ^{230}Th is preferentially excluded from the zircon lattice, resulting in a final ^{206}Pb deficit, and therefore yielding a younger measured $^{206}\text{Pb}/^{238}\text{U}$ date. Minerals, such as titanite, that preferentially incorporate Th (including ^{230}Th) relative to U will have a final ^{206}Pb excess yielding an older measured $^{206}\text{Pb}/^{238}\text{U}$ date. Therefore a correction for initial ^{230}Th disequilibrium is applied to all U-Pb data.

The initial ^{230}Th correction is relying on an estimated value for the Th/U of the magma at the time of mineral crystallization (Schärer, 1984). The Th/U of the magma can be estimated using one of the following approaches: 1) using the measured Th/U from volcanic glass that

is assumed to represent the melt composition (Schmitz and Bowring, 2001; Rioux et al., 2012); 2) measured Th/U from the whole rock (Blackburn et al., 2013); or 3) measured Th/U from melt inclusions in zircons (Thomas et al., 2003); or 4) use the ratio of the partition coefficients ($D_{\text{Th/U}}$) in combination with the model Th/U ratio of the zircon, calculated from the measured $^{208}\text{Pb}/^{206}\text{Pb}$ of the dated mineral assuming concordance between the $^{232}\text{Th} - ^{208}\text{Pb}$ and the $^{238}\text{U} - ^{206}\text{Pb}$ systems, to estimate the Th/U of the magma. For plutonic rocks, using the whole rock Th/U composition may lead to an erroneous correction, because the latter does not reflect the composition of the liquid at the time of zircon and titanite crystallization. Therefore we prefer to estimate the Th/U of the magma adopting, the experimentally determined $D_{\text{Th/U}} = 0.25 \pm 0.1$ from Rubatto and Hermann (2007) which is consistent with the $D_{\text{Th/U}} = 0.26 \pm 0.16$ determined for igneous zircons from intermediate rocks (55 - 65% SiO_2) (Bindeman et al., 2006). Using a constant $D_{\text{Th/U}}$ results in variable Th/U ratios for the magma at the time of zircon crystallization. Because we can demonstrate that VFC zircons are not strictly contemporaneous, but crystallize over a protracted time period, we envisage variable Th/U of the host melt due to the fractionation of accessory minerals, and therefore consider our approach for estimating the Th/U in the magma as most appropriate for

the initial ^{230}Th disequilibrium correction. The ^{230}Th correction applied to VFC zircons results in calculated dates that are older by ~ 80 ka.

For titanite the partitioning behavior between Th and U is not as well understood as for zircon, with $D_{\text{Th/U}}$ varying over an order of magnitude within single experimental studies (Prowatke and Klemme, 2005). Therefore we can not estimate the Th/U in the magma in the same way as with zircon. Because our data reveal that zircon and titanite crystallization is coeval, our best estimation for the Th/U of the magma during titanite crystallization is to use the mean Th/U of the magma calculated from the zircons of the same sample (See Appendix A for details).

Titanite common Pb correction

Titanite can incorporate a significant amount of Pb at the time of crystallization, resulting in low measured radiogenic Pb/ common Pb ratios ($^{206}\text{Pb}/^{204}\text{Pb} < 300$). As a result, titanite U-Pb dates are dependant on the accuracy of the initial common Pb isotope composition used for the correction. It is essential that a robust common Pb correction is applied to all titanite U-Pb data and that associated uncertainties are correctly propagated onto the final result. The composition of initial common Pb was estimated using the three-dimensional (3-D) concordia approach (Ludwig, 2005) in which a third axis ($^{204}\text{Pb}/^{206}\text{Pb}$) is projected onto the

Tera-Wasserburg (1972) concordia plane, the intersection yielding an estimate for both $^{206}\text{Pb}/^{204}\text{Pb}$ and $^{207}\text{Pb}/^{204}\text{Pb}$ ratios of the common Pb component and their respective uncertainties (Ludwig 2005). The estimated initial common Pb composition and associated error of the 3-D isochron intercept, calculated by ISOPLOT/Ex v.3 program (Ludwig, 2005), was used for data reduction and age calculation in the U-Pb Redux software (Bowring et al., 2011). Reported titanite U-Pb dates have been corrected for initial ^{230}Th disequilibrium, described above, and for initial common Pb composition and all uncertainties are reported at the two-sigma level. Uncertainties shown in Fig. 2 and in Table 2 are reported using the notation $\pm X/Y$ where X represents the analytical uncertainty only (dark gray bars in Fig. 2) and Y the analytical uncertainty enhanced by the uncertainty of the common Pb isotope composition (light gray bars in Fig. 2).

2.3.2 Trace element analysis in zircon

The trace element fraction, including Zr and Hf, was collected after zircon ion exchange chemistry and trace elements analyzed following the TIMS-TEA method described in Schoene et al. (2010) and summarized in Supplementary information. Trace element concentrations were analyzed using an Element 2 SF-ICP-MS in solution mode at ETH Zürich.

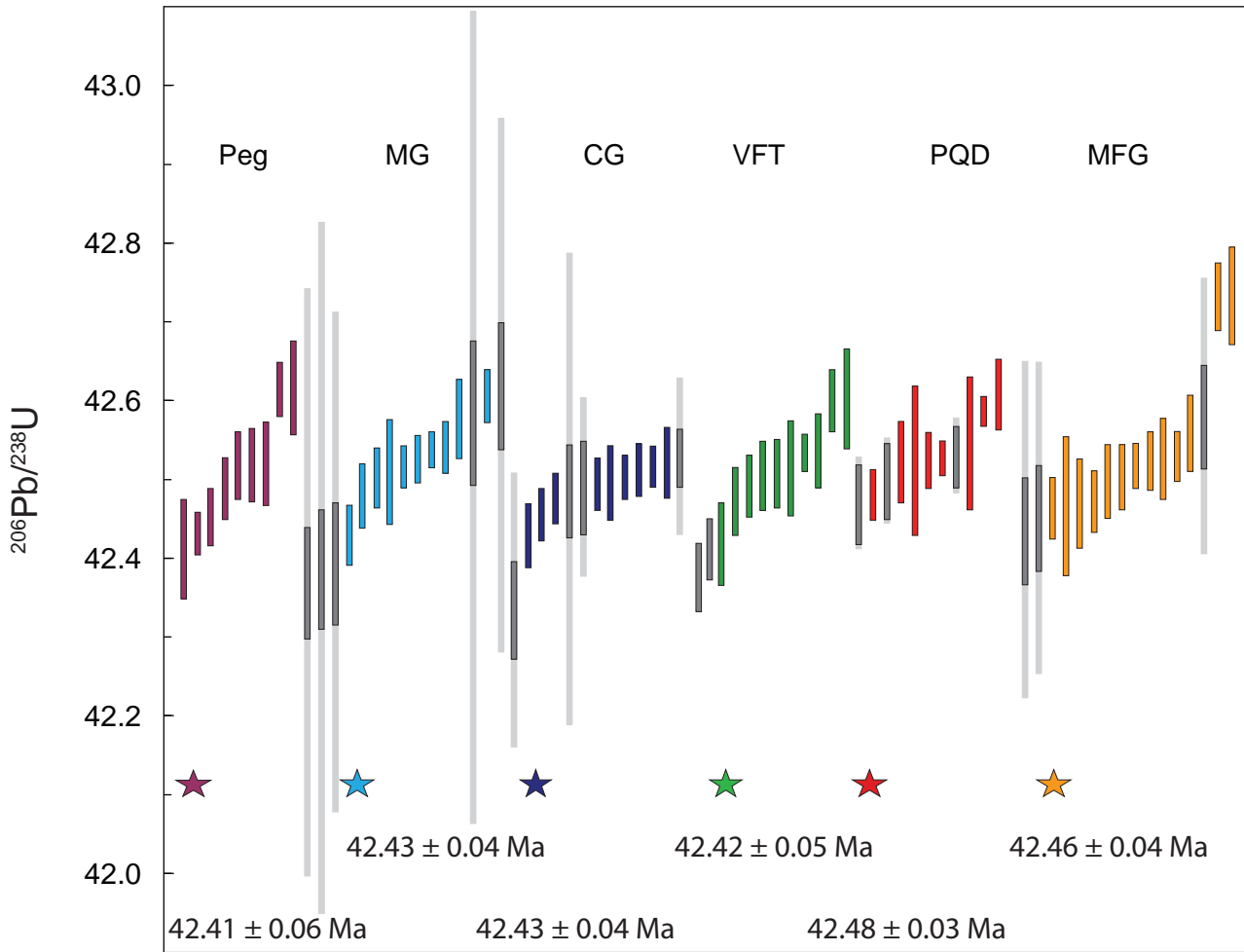


Figure 2: Age ranked plot showing $^{206}\text{Pb}/^{238}\text{U}$ dates for individual zircons and titanites. All titanite dates are plotted in gray, with extended errors (light gray bars) for propagated uncertainty of common Pb isotopic composition (see text for discussion). Stars indicate youngest zircon ages for each sample.

In situ trace element analyses of zircon were carried out on representative zircons of the same zircon population as dated by U-Pb techniques. Zircons were mounted in epoxy resin, polished and trace element concentrations analyzed by LA-ICP-MS using a Thermo Scientific Element XR mass spectrometer coupled to a New Wave Research ArF 193 nm laser ablation system at the University of Lausanne. The analytical conditions are summarized in Appendix A.

2.3.3 Zircon Hf isotope analysis

Hafnium isotopic compositions were analyzed from the same solution used for trace element analysis collected from zircon anion exchange column separation, using a Thermo-Fisher NEPTUNE multi collector inductively coupled plasma mass spectrometer (MC-ICP-MS) at Johann Wolfgang Goethe University Frankfurt in solution mode. The analytical conditions are summarized in Appendix A.

2.4 Results

2.4.1 Zircon U-Pb geochronology

Individual zircon grains from representative samples of each lithology were selected for U-Pb ID-TIMS analysis. Sample locations are shown in Figure 1b and details are given in Fig. A2 (Appendix A). Zircon U-Pb results are summarized in Table 1 and Figure 2.

ID-TIMS analysis of thirteen individual zircon grains from the MFG sample indicates the existence of two zircon groups within the MFG population. The older cluster consists of two zircons with $^{206}\text{Pb}/^{238}\text{U}$ dates of 42.73 Ma (z3, z9) and based on age alone they are considered to be antecrysts, zircons which were recycled from an earlier pulse within the same magmatic system (Miller et al., 2007). The younger cluster of eleven zircon grains scatter over 100 ka and have $^{206}\text{Pb}/^{238}\text{U}$ dates that range 42.46 ± 0.04 Ma to 42.56 ± 0.05 Ma (Fig. 2). The dates do not overlap at the two sigma level (MSWD = 2) thus excluding a calculated weighted mean age for the younger zircon cluster. The data are also presented as probability density distribution (PDD) curves for each sample (Fig. 3). The PDD curves of zircon dates contain several maxima, usually one more prominent peak representing a period of major zircon crystallization, and one or two smaller peaks interpreted as periods of minor zircon growth (Fig. 3). For the MFG age spectra,

the PDD curve reveals three periods of enhanced zircon crystallization (Fig. 3a). The younger zircon cluster shows a bimodal distribution indicating predominant zircon crystallization 42.53 Ma and a minor crystallization peak at 42.47 Ma.

$^{206}\text{Pb}/^{238}\text{U}$ dates of eight zircon grains from the PQD range from 42.48 ± 0.03 Ma to 42.61 ± 0.04 Ma (Fig. 2). The PQD zircon dates scatter over 130 ka and do not overlap at the two sigma level (MSWD = 7) therefore excluding a calculated weighted mean age. The PDD curve for the PQD zircon population indicates three phases of enhanced zircon crystallization, with two prominent peaks at 42.59 Ma and 42.53 Ma (Fig. 3a).

Ten zircon grains from the VFT sample have $^{206}\text{Pb}/^{238}\text{U}$ dates that scatter over 180 ka from 42.42 ± 0.05 Ma to 42.60 ± 0.06 Ma (Fig. 2) and do not overlap at the two sigma level (MSWD = 5.4), thus again excluding a calculated weighted mean age. The PDD curve for the VFT zircon population indicates that maximum zircon crystallization occurred between 42.53 Ma to 42.48 Ma with minor zircon crystallization preceding and postdating the main peak (Fig. 3a).

$^{206}\text{Pb}/^{238}\text{U}$ dates of nine zircon grains from the CG sample range from 42.43 ± 0.04 Ma to 42.52 ± 0.05 Ma (Fig. 2). The CG zircon grains record scatter over 90 ka and have dates that do not

Table 1:
Zircon U-Pb results for samples from the Val Fredda Complex

Fraction	Composition		Isotopic Ratios										Dates (Ma)						
	Th/U ^a	Pb* (pg) ^b	Pbc (pg) ^c	Pb*/Pbc ^d	Th/U (magma) ^e	²⁰⁶ Pb/ ²⁰⁴ Pb ^f	²⁰⁶ Pb/ ²³⁸ U ^g	±2σ %	²⁰⁷ Pb/ ²³⁵ U ^g	±2σ %	²⁰⁷ Pb/ ²⁰⁶ Pb ^g	Corr. coef.	²⁰⁶ Pb/ ²³⁸ U ^h	±2σ abs	²⁰⁷ Pb/ ²³⁵ U ⁱ	±2σ abs	²⁰⁷ Pb/ ²⁰⁶ Pb ^h	±2σ abs	
Marginal Facies granodiorite																			
MFG-z1	0.66	30.1	0.95	31.7	2.66	1861	0.006601	0.11	0.04312	0.41	0.0474	0.38	0.385	42.496	0.047	42.86	0.17	63.6	9.0
MFG-z2	0.75	9.36	1.32	7.1	2.98	424	0.006597	0.13	0.04292	1.3	0.0472	1.3	0.231	42.468	0.057	42.67	0.55	54	31
MFG-z3	0.7	18.3	1.86	9.8	2.78	586	0.006638	0.10	0.04365	0.93	0.04772	0.91	0.229	42.729	0.043	43.38	0.39	80	22
MFG-z4	0.58	52.5	0.96	55	2.31	3285	0.006611	0.11	0.04286	0.27	0.04704	0.25	0.286	42.557	0.048	42.61	0.11	45.7	6.1
MFG-z5	0.57	23.3	1.02	22.9	2.28	1381	0.006604	0.07	0.04302	0.51	0.04726	0.5	0.123	42.515	0.029	42.77	0.21	57	12
MFG-z6	0.65	14.4	1.41	10.2	2.62	616	0.006606	0.07	0.04276	0.89	0.04696	0.9	0.045	42.528	0.031	42.51	0.37	42	21
MFG-z7	0.45	4.01	0.83	4.8	1.81	314	0.006596	0.21	0.04418	2.4	0.046	2.4	0.431	42.464	0.089	41.6	1.0	57	57
MFG-z8	0.58	13.7	1.66	8.3	2.33	509	0.006597	0.09	0.04287	1.1	0.04715	1.1	0.148	42.470	0.039	42.62	0.47	51	27
MFG-z9	0.59	23.0	2.26	10.2	2.37	623	0.006638	0.14	0.04296	1.0	0.04696	0.97	0.351	42.730	0.062	42.71	0.42	41	23
MFG-z10	0.42	18.0	1.65	10.9	1.69	696	0.006606	0.12	0.04289	1.0	0.04711	1.0	0.007	42.525	0.051	42.64	0.42	49	24
MFG-z11	0.56	36.2	3.26	11.1	2.23	682	0.006605	0.09	0.04255	1.0	0.04674	1.1	0.518	42.522	0.037	42.31	0.43	30	26
MFG-z12	0.49	42	1.5	28	1.97	1721	0.006596	0.09	0.04287	0.32	0.04716	0.3	0.347	42.461	0.039	42.62	0.13	51.8	7.1
MFG-z13	0.53	15.8	1.13	13.9	2.14	857	0.006602	0.10	0.0428	0.65	0.04704	0.63	0.231	42.501	0.042	42.56	0.27	46	15
Mattoni gabbro																			
MG-z1	1.02	112	1.92	58.5	4.08	3136	0.006602	0.09	0.04287	0.29	0.04711	0.27	0.311	42.500	0.038	42.62	0.12	49.4	6.5
MG-z2	0.97	42.7	2.36	18.1	3.89	994	0.006606	0.07	0.04297	0.53	0.0472	0.53	0.058	42.523	0.030	42.72	0.22	54	13
MG-z3	1.33	50.5	2.7	18.7	5.32	947	0.006598	0.10	0.04272	0.63	0.04698	0.61	0.298	42.477	0.041	42.47	0.26	42	15
MG-z4	1.27	36.1	0.86	42.2	5.08	2142	0.006604	0.06	0.04298	0.32	0.04723	0.3	0.405	42.515	0.027	42.73	0.13	55.0	7.2
MG-z5	1.36	71.4	1.09	65.8	5.43	3267	0.006608	0.05	0.042765	0.21	0.046962	0.2	0.104	42.536	0.023	42.520	0.086	41.6	5.0
MG-z6	1.10	41.2	2.40	17.20	4.42	917	0.006603	0.16	0.04271	0.62	0.04693	0.59	0.285	42.507	0.066	42.46	0.26	40	14
MG-z7	1.22	112	1.83	60.9	4.89	3117	0.006608	0.08	0.04283	0.27	0.04703	0.25	0.43	42.539	0.033	42.58	0.11	45.0	6.0
MG-z8	1.38	40.8	1.78	23	5.51	1148	0.006618	0.08	0.04303	0.47	0.04718	0.47	0.121	42.603	0.033	42.78	0.2	53	11
MG-z9	2.49	152	1.69	90.2	9.96	3594	0.006614	0.12	0.042775	0.22	0.046929	0.18	0.508	42.575	0.050	42.529	0.09	39.9	4.5
MG-z10	1.34	21.0	1.45	14.5	5.37	736	0.006590	0.09	0.04214	1.0	0.04639	1.1	0.734	42.426	0.039	41.91	0.41	12	26
Cadino gabbro																			
CG-z1	0.88	202	1.46	138	3.52	7634	0.006590	0.10	0.042695	0.16	0.047007	0.12	0.611	42.426	0.041	42.452	0.066	43.9	3.0
CG-z2	0.71	49.9	0.66	75.6	2.83	4366	0.006604	0.08	0.0428	0.26	0.04702	0.23	0.383	42.510	0.034	42.55	0.11	44.7	5.6
CG-z3	0.93	56.6	0.70	81.3	3.74	4440	0.006605	0.11	0.042767	0.2	0.046982	0.17	0.552	42.519	0.045	42.522	0.084	42.7	4.0
CG-z4	0.91	207	1.17	177	3.63	9714	0.006601	0.08	0.042747	0.14	0.046992	0.1	0.643	42.492	0.033	42.503	0.059	43.1	2.6
CG-z5	0.83	164	0.85	194	3.3	10832	0.006598	0.08	0.042767	0.13	0.047033	0.092	0.671	42.474	0.032	42.522	0.055	45.2	2.4
CG-z6	0.90	107	0.89	119	3.59	6567	0.006602	0.06	0.042864	0.15	0.04711	0.13	0.501	42.501	0.027	42.617	0.064	49.2	3.2
CG-z7	0.82	148	0.57	257	3.29	14403	0.006595	0.08	0.042818	0.16	0.047112	0.12	0.645	42.453	0.033	42.572	0.068	49.2	3.1
CG-z8	0.76	120	0.7	172	3.02	9802	0.006601	0.11	0.042814	0.23	0.047062	0.18	0.617	42.494	0.047	42.568	0.094	46.7	4.3
CG-z9	0.84	104	0.57	182	3.35	10174	0.006604	0.06	0.042795	0.15	0.047019	0.16	0.07	42.514	0.025	42.549	0.064	44.5	3.8
Val Fredda Tonalite																			
VFT-z1	0.68	5.2	0.82	6.3	2.72	384	0.006607	0.11	0.0429	1.5	0.04712	1.5	0.081	42.533	0.047	42.65	0.61	49	35
VFT-z2	0.62	30.8	1.94	15.9	2.49	953	0.006589	0.12	0.04245	0.85	0.04675	0.87	0.095	42.416	0.053	42.21	0.35	31	21
VFT-z3	0.5	10.4	1.61	6.5	2.01	411	0.006604	0.14	0.04262	1.4	0.04683	1.4	0.409	42.512	0.060	42.38	0.59	35	33
VFT-z4	0.65	20.3	1.48	13.7	2.59	821	0.006603	0.10	0.04334	0.83	0.04763	0.78	0.504	42.505	0.043	43.08	0.35	75	19
VFT-z5	0.49	18.9	1.15	16.5	1.95	1023	0.006618	0.15	0.04303	0.73	0.04718	0.69	0.345	42.600	0.064	42.78	0.31	53	17
VFT-z6	0.65	19.7	2.37	8.30	2.61	504	0.006602	0.10	0.0428	1.2	0.04704	1.2	0.342	42.503	0.044	42.56	0.50	46	28
VFT-z7	0.54	221	4.84	45.6	2.15	2760	0.006617	0.09	0.042903	0.21	0.047044	0.18	0.505	42.598	0.039	42.654	0.088	45.8	4.4
VFT-z8	0.85	87.6	11.71	7.5	3.41	433	0.006600	0.09	0.04274	1.1	0.04699	1.1	0.046	42.490	0.040	42.5	0.46	43	27
VFT-z9	0.51	28.3	1.06	26.6	2.05	1628	0.006597	0.10	0.04277	0.37	0.04704	0.35	0.295	42.470	0.043	42.52	0.15	45.4	8.5
VFT-z10	0.54	65.1	1.43	45.5	2.18	2748	0.006607	0.05	0.04284	0.25	0.04705	0.23	0.462	42.532	0.023	42.59	0.10	46	5.5

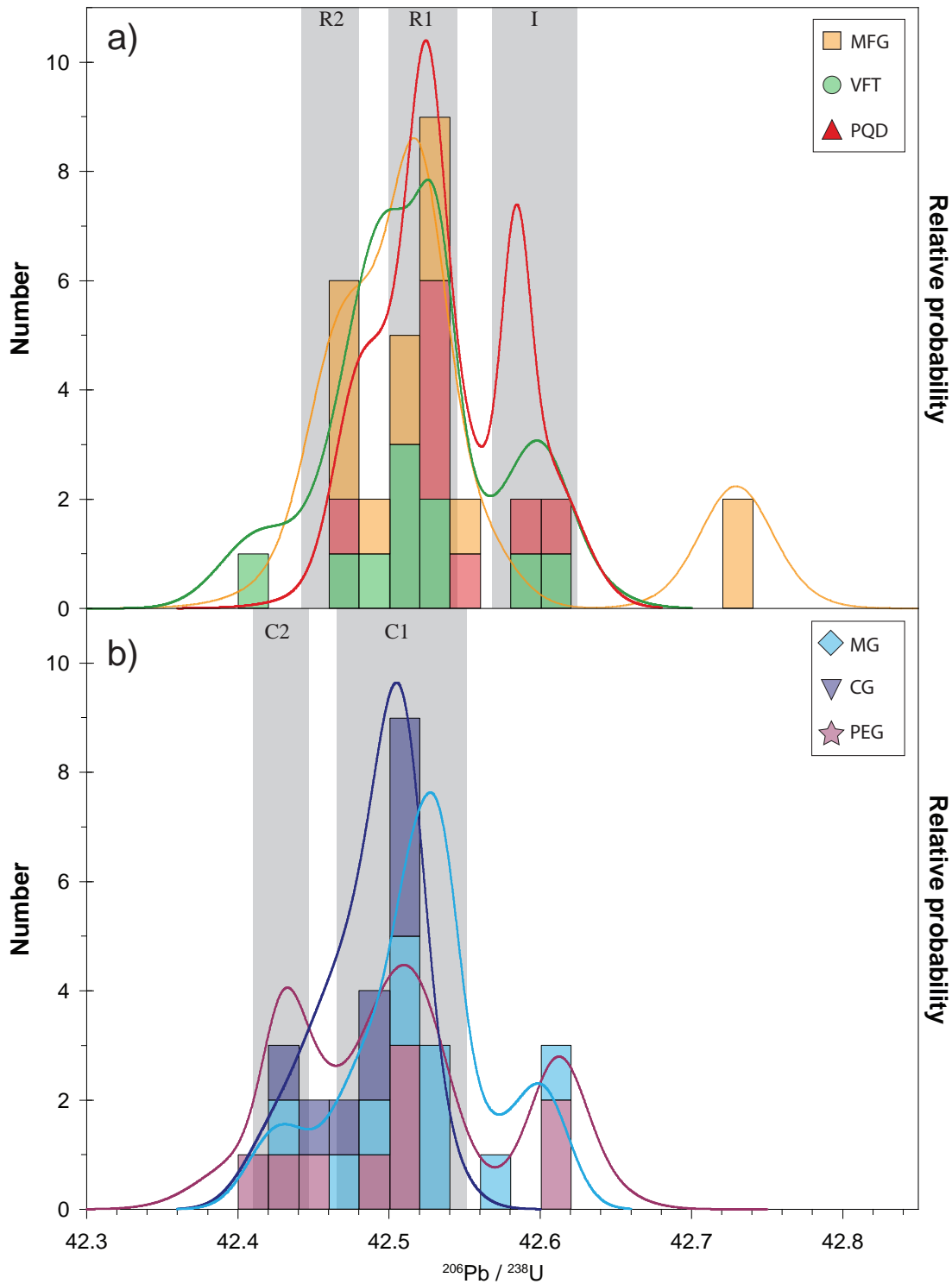


Figure 3: Histograms with probability density distribution curves from $^{206}\text{Pb}/^{238}\text{U}$ zircon dates for a) felsic samples and b) mafic samples. Peaks represent periods of enhanced zircon crystallization associated with: I = initial felsic intrusions; R1, R2 = periods of rejuvenation of felsic crystal mushes; C1, C2 = periods of zircon crystallization associated with cooling in the mafic lithologies. (See text for discussion)

overlap at the two sigma level (MSWD = 2.9) therefore excluding calculation of a weighted mean age. The PDD curve for the CG zircon population indicates main crystallization at 42.52 Ma and a minor period of zircon crystallization

at 42.44 Ma (Fig. 3b).

ID-TIMS analysis of ten individual zircon grains from the MG sample indicates two zircon clusters within the MG population. The older cluster consists of two zircons with $^{206}\text{Pb}/^{238}\text{U}$

dates of 42.58 Ma (z9) and 42.61 Ma (z8) and they are considered to be antecrysts. The younger cluster of eight zircon grains has $^{206}\text{Pb}/^{238}\text{U}$ dates that range from 42.43 ± 0.04 Ma to 42.54 ± 0.03 Ma (Fig. 2). Zircon grains have U-Pb dates that scatter over 110 ka and do not overlap at the two sigma level (MSWD = 4.4) thus excluding a calculated weighted mean age for the younger zircon cluster. The PDD curve for the MG age spectra reveals three periods of enhanced zircon crystallization. The younger zircon cluster reflects two periods of crystallization, with more important zircon crystallization occurring at 42.53 Ma and minor zircon crystallization at 42.43 Ma (Fig. 3b). However, our data are in disagreement with previous U-Pb determinations, obtained by LA-ICP-MS, which indicate the presence of xenocrystic cores that range from 51.0 ± 1.1 Ma to 43.9 ± 1.2 Ma, and record ages of 40.3 ± 1.0 Ma for zircon rims and euhedral grains (Tiepolo et al., 2011). A further detailed investigation is required in order to fully understand the reason behind the age inconsistency between both studies.

ID-TIMS analysis of nine individual zircon grains from the PEG sample indicates two zircon clusters within the PEG population. The older cluster consists of two zircons with $^{206}\text{Pb}/^{238}\text{U}$ dates of 42.61 Ma (z4, z6), considered to be antecrysts, which demonstrates that even in the case of late-stage residual melt we have to

anticipate the existence of recycled zircon from previous magma batches. The younger cluster of seven zircon grains scatter 110 ka and have $^{206}\text{Pb}/^{238}\text{U}$ dates that range from 42.41 ± 0.06 Ma to 42.52 ± 0.05 Ma (Fig. 2). Zircon grains have U-Pb dates that do not overlap at the two sigma level (MSWD = 4.8) thus excluding a calculated weighted mean age for the younger zircon cluster. The PDD curve for the PEG age spectra reveals three periods of enhanced zircon crystallization. The younger zircon cluster contains two periods crystallization, with maximum zircon crystallization occurring at 42.51 Ma and minor zircon crystallization at 42.44 Ma.

2.4.2 Titanite U-Pb geochronology

Titanite is an ubiquitous accessory mineral in igneous rocks and has been recognized as an important mineral for U-Pb geochronology (Frost et al., 2000; Storey et al., 2005; Schaltegger et al., 2009; Schoene et al., 2012). For the U-Pb system a closure temperature of $650 \pm 50^\circ\text{C}$ was determined (Cherniak, 1993), thus titanite can provide important information on the timing and duration of crystallization of low temperature magmas. Therefore individual titanite grains were selected from the same samples as zircon (MFG, PQD, VFT, CG and MG), for U-Pb ID-TIMS analysis. Titanite U-Pb results, corrected for initial ^{230}Th disequilibrium and initial

Table 2:
Titanite U-Pb results for samples from the Val Fredda Complex

Fraction	Composition				Isotopic Ratios				Dates (Ma)										
	Th/U ^a	Pb* (pg) ^b	Pbc (pg) ^c	Pb*/Pbc ^d	Th/U (magma) ^e	²⁰⁶ Pb/ ²⁰⁴ Pb ^f	²⁰⁶ Pb/ ²³⁸ U ^g	±2σ %	²⁰⁷ Pb/ ²³⁵ U ^g	±2σ %	²⁰⁷ Pb/ ²⁰⁶ Pb ^g	±2σ %	Corr. coef.	²⁰⁶ Pb/ ²³⁸ U ^h	±2σ abs	²⁰⁷ Pb/ ²³⁵ U ⁱ	±2σ abs	²⁰⁷ Pb/ ²⁰⁶ Pb ^h	±2σ abs
Marginal Facies granodiorite																			
MFG-t1	1.07	33.56	68.00	0.49	2.32	45	0.006617	0.15	0.04326	2.3	0.04743	2.2	0.914	42.577	0.065	43.00	0.98	67	52
MFG-t2	1.39	94.38	220.89	0.43	2.32	40	0.006597	0.16	0.04375	2.6	0.04812	2.5	0.967	42.433	0.069	43.5	1.1	102	59
MFG-t3	1.50	32.21	68.01	0.47	2.32	41	0.006601	0.15	0.04350	2.5	0.04782	2.4	0.971	42.448	0.066	43.2	1.1	87	56
Mattoni gabbro																			
MG-t1	6.82	37.91	22.93	1.65	4.93	56	0.006639	0.16	0.04386	2.1	0.04793	2.0	0.776	42.616	0.081	43.58	0.90	97	47
MG-t2	6.39	17.84	17.85	1.00	4.93	42	0.006632	0.19	0.04538	2.8	0.04964	2.6	0.844	42.582	0.091	45.1	1.2	179	61
MG-t3	4.78	64.85	53.83	1.20	4.93	53	0.006593	0.15	0.04423	2.0	0.04867	1.9	0.908	42.365	0.070	43.94	0.87	131	45
MG-t4	5.26	97.85	89.70	1.09	4.93	48	0.006598	0.16	0.04332	2.3	0.04764	2.2	0.910	42.384	0.076	43.06	0.99	81	52
MG-t5	6.30	44.19	26.32	1.68	4.93	59	0.006602	0.16	0.04359	2.5	0.04791	2.4	0.892	42.391	0.079	43.3	1.1	95	56
Cadino gabbro																			
CG-t1	1.26	143.79	55.81	2.58	3.36	149	0.006602	0.14	0.04310	0.6	0.04736	0.5	0.668	42.487	0.059	42.84	0.23	63	11
CG-t2	3.12	59.42	28.08	2.12	3.36	94	0.006587	0.14	0.04352	1.0	0.04794	0.9	0.630	42.331	0.062	43.26	0.42	95	21
CG-t3	2.64	78.96	71.16	1.11	3.36	61	0.006609	0.14	0.04355	1.9	0.04782	1.8	0.837	42.484	0.059	43.29	0.81	88	42
CG-t4	1.62	182.77	62.30	2.93	3.36	156	0.006610	0.09	0.04312	0.6	0.04734	0.5	0.838	42.526	0.038	42.87	0.25	62	13
Val Fredda Tonalite																			
VFT-t1	0.48	46.44	9.35	4.97	2.42	323	0.006587	0.09	0.04204	0.6	0.04632	0.6	0.614	42.408	0.039	41.82	0.26	8	14
VFT-t2	0.54	75.57	30.61	2.47	2.42	167	0.006582	0.10	0.04228	1.1	0.04661	1.0	0.347	42.373	0.043	42.05	0.44	23	25
Plagioclase quartz diorite																			
PQD-t1	0.73	26.13	10.13	2.58	2.80	166	0.006606	0.09	0.04254	0.9	0.04673	0.8	0.745	42.527	0.039	42.30	0.36	30	19
PQD-t2	0.91	50.79	19.59	2.59	2.80	161	0.006598	0.12	0.04261	0.8	0.04686	0.7	0.721	42.467	0.051	42.37	0.32	37	16
PQD-t3	0.80	85.09	29.66	2.87	2.80	180	0.006602	0.11	0.04284	0.6	0.04708	0.5	0.658	42.496	0.048	42.59	0.23	48	12

^a Th contents calculated from radiogenic ²⁰⁸Pb and the ²⁰⁷Pb/²⁰⁶Pb date of the sample, assuming concordance between U-Th and Pb systems.

^b Total mass of radiogenic Pb.

^c Total mass of common Pb.

^d Ratio of radiogenic Pb (including ²⁰⁸Pb) to common Pb.

^e Th/U ratio of magma from which mineral crystallized calculated using the mean Th/U of magma calculated from zircons of the same sample.

^g Measured ratios corrected for fractionation, tracer and blank.

^h Corrected for initial Th/U disequilibrium using radiogenic ²⁰⁸Pb and Th/U[magma] specified by ^e.

ⁱ Isotopic dates calculated using the decay constants $\lambda_{238} = 1.55125\text{E-}10$ and $\lambda_{235} = 9.8485\text{E-}10$ (Jaffey et al. 1971).

common Pb composition, are summarized in Table 2 and Figure 2. Titanite $^{206}\text{Pb}/^{238}\text{U}$ dates are plotted in Fig. 2 with analytical uncertainty only (dark gray bars) and with the propagated uncertainty derived from the common Pb correction (light gray bars).

ID-TIMS analyses of three individual titanite grains from the MFG sample have $^{206}\text{Pb}/^{238}\text{U}$ dates that range from $42.43 \pm 0.07/0.21$ Ma to $42.58 \pm 0.06/0.17$ (analytical uncertainty / common Pb correction uncertainty added) Ma and were corrected using $\text{Th}/\text{U}_{\text{magma}} = 2.32 \pm 0.37$, derived from zircon data (see above). The measured Th/U ratios in the MFG titanites range from 1.1 to 1.5, indicating that the MFG titanites have an initial ^{230}Th deficiency. The ^{230}Th correction applied to the MFG titanites results in calculated dates that are older by $\sim 40 - 60$ ka (Table 2). MFG titanites have low $^{206}\text{Pb}/^{204}\text{Pb}$ ratios (< 45), indicating a higher proportion of common Pb, resulting in their sensitivity to the common Pb correction. This is reflected in the uncertainty of the initial Pb composition corresponding to $\sim 0.5\%$ uncertainty on single $^{206}\text{Pb}/^{238}\text{U}$ titanite dates. Within the enhanced uncertainty, the titanites overlap with the entire set of zircon data, except for the two antecrystic grains.

$^{206}\text{Pb}/^{238}\text{U}$ dates of three titanite grains from the PQD range from $42.47 \pm 0.05/0.06$ Ma to $42.53 \pm 0.04/0.05$ Ma (Fig. 2) and have been corrected

using $\text{Th}/\text{U}_{\text{magma}} = 2.80 \pm 0.47$. Measured Th/U ratios between 0.6 and 0.9, indicate an initial ^{230}Th deficiency leading to an increase of the $^{206}\text{Pb}/^{238}\text{U}$ dates by $\sim 70 - 80$ ka (Table 2). The high measured $^{206}\text{Pb}/^{204}\text{Pb}$ ratios (160 – 180) makes the results less sensitive to the uncertainty on the initial Pb composition, but the titanite dates never the less overlap with the whole cluster of the five younger zircons.

$^{206}\text{Pb}/^{238}\text{U}$ dates of two titanite grains from the VFT range from $42.37 \pm 0.04/0.04$ Ma to $42.41 \pm 0.04/0.04$ Ma (Fig. 2) and have been corrected using $\text{Th}/\text{U}_{\text{magma}} = 2.42 \pm 0.45$. Both VFT titanite grains have a Th/U ratio of 0.5, indicating an initial ^{230}Th deficiency and rendering the Th corrected $^{206}\text{Pb}/^{238}\text{U}$ dates to be older by ~ 90 ka (Table 2). VFT titanites have high $^{206}\text{Pb}/^{204}\text{Pb}$ ratios (160, 320) making them less sensitive to the uncertainty on the initial Pb composition. The titanite dates are at the lower end of all results from the VFT, overlapping with the two youngest zircon dates only.

Four titanite grains from the CG sample have $^{206}\text{Pb}/^{238}\text{U}$ dates that range from $42.33 \pm 0.06/0.17$ Ma to $42.53 \pm 0.04/0.10$ Ma (Fig. 2) and have been corrected using $\text{Th}/\text{U}_{\text{magma}} = 3.36 \pm 0.30$. CG titanite grains have Th/U ratios that range from 1.2 to 3.0 and when corrected for initial ^{230}Th disequilibrium the calculated $^{206}\text{Pb}/^{238}\text{U}$ dates are older by $\sim 10 - 60$ ka (Table 2). Titanites from the CG sample have $^{206}\text{Pb}/^{204}\text{Pb}$ ratios that vary from

Table 3:
TIMS-TEA zircon trace element results for samples from the Val Fredda Complex

	Zr wt%	± 2s	Y	± 2s	Nb	± 2s	La	± 2s	Ce	± 2s	Pr	± 2s	Nd	± 2s	Sm	± 2s	Eu	± 2s	Gd	± 2s
MFG-z1	65.8	1.1	2161	75	7.1	1.2	0.53	0.22	37.5	2.2	0.39	0.11	1.6	0.9	4.4	1.6	1.7	0.6	30.5	5.8
MFG-z2	65.8	9.3	1798	219	1.4	0.9	0.88	0.65	22.8	3.2	0.62	0.55	1.0	0.8	3.3	2.3	2.0	1.1	22.0	4.4
MFG-z3	66.1	2.0	1830	113	6.8	2.3	0.83	0.67	39.0	4.8	0.43	0.26	1.0	0.8	3.1	2.0	2.3	1.0	24.1	4.3
MFG-z4	65.9	3.1	2110	52	5.9	0.8	0.57	0.28	96.4	6.1	0.28	0.13	1.6	0.8	4.3	1.7	1.4	0.5	26.6	7.8
MFG-z5	65.8	5.5	2030	169	8.2	1.3	0.12	0.08	39.1	3.1	0.14	0.07	0.9	0.5	3.6	0.9	1.3	0.5	25.5	3.7
MFG-z6	65.9	2.4	1908	79	4.9	1.1	0.15	0.08	30.3	2.3	0.14	0.07	1.4	0.4	3.5	1.0	1.4	0.4	24.7	3.8
MFG-z7	65.9	3.0	1298	89	5.6	1.4	0.33	0.24	31.1	3.7	0.21	0.16	0.7	0.6	2.4	1.6	1.2	0.7	17.5	5.4
MFG-z8	66.0	6.2	1856	161	3.6	1.2	0.69	0.53	16.4	2.9	0.17	0.14	0.4	0.4	2.3	2.1	1.2	0.6	21.6	7.9
MFG-z9	65.9	2.4	2125	248	7.5	2.3	0.93	0.53	34.2	6.2	0.67	0.41	1.5	1.4	3.4	2.5	1.3	0.8	18.4	4.8
MFG-z10	66.0	8.5	1690	183	4.7	1.3	0.50	0.18	44.2	7.2	0.47	0.22	1.6	1.0	3.6	1.9	1.2	0.7	20.9	6.7
MFG-z11	65.9	17.1	2028	190	7.5	2.5	0.47	0.37	31.9	14.4	0.48	0.38	1.2	2.0	3.4	3.8	1.3	1.3	23.9	13.4
MFG-z12	65.9	10.5	1658	189	1.7	0.7	1.08	0.81	34.1	6.3	0.62	0.39	2.0	1.8	3.8	2.7	1.4	0.6	20.2	7.2
MFG-z13	65.9	9.0	2103	278	7.0	1.2	0.31	0.21	43.0	6.7	0.22	0.15	1.4	0.9	3.8	2.0	1.4	0.6	27.1	5.4
MFG-z14	66.0	18.0	1861	859	2.1	2.4	0.64	0.58	30.2	13.5	0.45	0.36	1.3	1.7	3.0	4.1	1.3	1.2	16.9	10.7
PQD-z1	65.9	5.0	1303	94	4.0	0.9	0.49	0.18	31.2	3.5	0.43	0.18	1.0	0.5	2.8	1.5	1.2	1.0	16.5	4.6
PQD-z2	66.0	5.5	1212	94	6.8	2.0	1.45	1.14	28.4	5.3	1.26	0.95	1.0	1.1	2.3	1.6	1.2	0.2	14.1	8.6
PQD-z3	65.6	6.9	1274	118	4.8	1.8	1.06	0.57	43.3	6.6	0.61	0.38	0.1	0.1	3.2	2.2	1.6	0.8	19.9	7.5
PQD-z4	65.6	7.3	1423	124	3.6	0.8	0.49	0.27	39.5	4.1	0.28	0.16	1.3	0.7	3.1	1.4	1.2	0.5	22.4	4.0
PQD-z5	65.6	7.3	1206	133	3.6	1.0	0.90	0.43	43.7	6.2	0.63	0.38	1.8	1.1	3.2	1.9	1.2	0.6	18.9	6.4
PQD-z6	65.7	7.0	1241	75	2.1	0.7	0.61	0.45	43.9	7.3	0.41	0.30	1.6	1.4	3.0	2.2	1.2	0.5	20.3	6.5
PQD-z7	65.6	6.3	1508	118	4.8	0.7	0.44	0.19	38.1	3.0	0.24	0.10	1.2	0.5	3.5	1.1	1.2	0.3	22.4	3.7
PQD-z8	65.8	8.1	1338	119	1.4	0.2	0.18	0.12	48.5	4.5	0.18	0.09	1.5	0.4	3.8	1.3	1.6	0.3	22.1	3.8
VFT-z1	66.0	3.6	1784	108	6.8	2.5	0.42	0.63	31.6	5.6	0.54	0.34	0.1	7.1	2.8	6.4	0.6	4.6	22.8	12.0
VFT-z2	65.9	5.4	1341	90	5.2	3.1	0.47	0.35	28.7	2.7	0.48	0.08	1.2	0.7	2.8	1.2	1.3	0.3	17.2	3.9
VFT-z3	65.8	3.8	1430	78	6.9	1.5	1.58	0.12	22.6	3.5	1.41	0.20	0.8	0.6	3.8	2.3	2.1	0.9	17.7	8.1
VFT-z4	65.9	7.0	1254	120	2.9	0.6	0.26	0.11	31.6	3.2	-	-	1.5	0.9	2.3	1.4	0.6	0.2	16.4	3.5
VFT-z5	65.8	5.9	1433	122	3.7	1.0	0.13	0.11	24.2	3.1	0.09	0.09	1.1	0.6	2.8	1.7	0.7	0.3	18.7	4.2
VFT-z6	65.9	9.4	1412	222	5.0	1.1	0.63	0.11	34.1	4.8	0.38	0.10	1.1	0.7	2.5	1.3	1.0	0.3	16.2	4.1
VFT-z7	66.0	7.5	2248	354	0.8	0.2	-	-	29.2	4.0	0.08	0.29	0.9	0.3	2.8	0.6	1.1	0.2	19.3	3.1
VFT-z8	65.9	14.9	1237	707	1.1	0.3	0.19	0.05	28.6	7.9	0.26	0.06	2.3	0.5	3.4	1.2	1.8	0.4	14.9	6.2
VFT-z9	66.1	7.6	1166	100	4.0	2.7	1.61	0.80	15.2	3.5	1.16	0.67	2.3	2.0	2.7	2.6	1.0	0.8	13.6	10.7
VFT-z10	65.7	5.7	2073	196	2.4	0.5	0.62	0.22	36.6	3.0	0.21	0.12	1.2	0.5	2.9	1.0	1.1	0.3	18.3	3.4
MG-z1	66.1	4.4	2555	78	4.9	0.2	0.82	0.11	74.7	1.6	1.49	0.11	14.0	0.4	13.5	0.6	7.6	0.2	53.8	1.0
MG-z2	66.1	5.1	1031	76	1.2	0.3	-	-	22.5	1.7	0.12	0.11	1.7	0.6	2.4	0.7	1.6	0.4	13.2	2.3
MG-z3	66.1	5.5	1405	109	3.2	0.5	0.01	0.11	37.9	3.4	0.39	0.15	4.2	1.1	4.8	1.3	3.0	0.6	23.2	4.7
MG-z4	66.1	4.5	1352	112	2.6	0.6	-	-	33.5	3.4	0.30	0.10	4.4	1.3	5.0	1.2	3.2	0.5	23.3	3.0
MG-z5	66.2	4.6	1527	116	2.6	0.3	0.07	0.11	44.7	3.2	0.53	0.09	5.7	1.0	5.9	1.0	3.4	0.5	25.6	2.7
MG-z6	66.2	8.5	1489	155	0.8	0.3	0.23	0.16	24.6	3.5	0.32	0.16	2.2	0.9	3.4	1.3	2.1	0.6	16.4	3.8
MG-z7	66.3	6.4	2226	279	0.8	0.2	0.18	0.12	41.6	5.8	0.34	0.12	2.8	1.0	4.5	1.2	2.7	0.3	21.8	4.6
MG-z8	66.2	7.3	2173	276	2.2	0.5	0.45	0.21	38.2	5.5	0.59	0.19	4.5	1.4	6.0	1.9	3.8	1.0	28.5	6.9
MG-z9	66.3	8.8	4006	763	1.3	0.2	0.42	0.12	95.6	14.6	2.07	0.33	18.1	2.7	20.3	2.9	11.2	2.0	74.6	9.0
MG-z10	66.3	6.7	2226	205	0.7	0.3	0.45	0.31	39.2	6.3	0.60	0.38	3.7	1.5	5.5	1.9	3.2	1.1	25.0	7.4
CG-z1	65.9	5.0	1431	125	1.9	0.3	0.08	0.05	39.6	3.3	0.25	0.06	2.2	0.6	3.3	0.7	1.9	0.3	19.0	1.8
CG-z2	66.1	4.9	843	63	0.9	0.2	0.02	0.01	16.9	1.5	0.11	0.07	1.1	0.5	1.6	0.6	1.2	0.3	9.8	2.0
CG-z3	66.0	6.0	1318	98	1.3	0.3	0.05	0.03	31.7	2.8	0.22	0.10	2.2	0.6	3.2	1.2	2.1	0.6	17.6	3.3
CG-z4	65.9	5.2	2191	137	2.2	0.3	0.07	0.04	56.0	5.0	0.29	0.10	3.3	0.9	5.3	1.4	2.9	0.6	29.4	3.8
CG-z5	65.9	3.7	1504	77	2.1	0.3	0.03	0.02	42.0	3.5	0.13	0.11	1.7	0.6	2.9	0.8	1.7	0.4	18.4	2.0
CG-z6	66.0	6.9	933	105	1.9	0.3	-	-	24.2	3.1	0.08	0.05	1.1	0.6	1.9	0.8	1.2	0.3	11.8	3.1
CG-z7	66.0	4.0	1363	81	1.6	0.3	0.02	0.01	34.6	2.2	0.11	0.06	1.8	0.7	2.7	1.0	1.9	0.4	18.4	2.6
CG-z8	65.8	4.6	1459	79	3.0	0.6	-	-	38.6	2.8	0.12	0.06	1.7	0.7	2.8	1.2	1.7	0.4	17.6	3.4
CG-z9	65.8	8.0	1768	163	4.0	0.6	2.29	0.03	54.5	4.4	0.67	0.12	9.7	1.5	4.3	2.0	2.7	0.8	24.0	5.1
Peg-z1	65.9	10.6	1504	214	2.6	0.7	0.32	0.20	69.7	11.5	0.55	0.28	5.3	1.9	8.1	3.0	4.2	1.2	43.6	8.2
Peg-z2	65.1	8.3	1191	264	5.1	1.4	0.20	0.18	67.1	15.9	0.36	0.22	3.4	2.5	5.5	2.5	3.2	1.2	37.0	9.1
Peg-z3	66.4	6.4	1482	170	2.5	0.4	0.10	0.06	52.3	5.2	0.31	0.09	4.0	0.7	6.6	1.1	3.1	0.5	38.1	4.6
Peg-z4	66.0	9.0	1528	166	3.6	0.5	0.09	0.06	56.7	7.0	0.28	0.10	4.0	1.0	6.7	1.4	3.5	0.6	41.7	4.0
Peg-z5	65.5	7.9	1314	130	3.5	0.9	0.36	0.31	77.0	11.2	0.25	0.26	2.5	2.4	5.1	3.7	2.6	1.5	30.9	11.7
Peg-z6	65.7	8.1	1020	105	6.2	1.5	0.22	0.21	57.0	8.4	0.14	0.10	1.6	1.3	3.1	1.7	1.6	0.6	21.7	6.3
Peg-z7	65.9	8.0	1202	100	2.1	0.5	0.13	0.12	43.6	5.7	0.27	0.15	3.5	1.1	5.8	1.8	2.8	0.6	34.0	4.1
Peg-z8	65.6	10.1	1261	165	4.9	1.5	0.77	0.64	75.4	11.2	0.29	0.27	2.5	1.7	3.4	3.3	2.0	1.1	28.3	9.7
Peg-z9	65.6	8.4	1211	139	5.9	1.4	0.19	0.16	78.5	9.2	0.13	0.09	1.9	1.5	3.8	2.3	2.2	1.1	27.1	8.6

~60 – 155. Therefore, titanites with the lower $^{206}\text{Pb}/^{204}\text{Pb}$ ratios (t_2 , t_3) are very sensitive to the common Pb correction, and when the uncertainty on the initial Pb composition is incorporated, it corresponds to ~0.4 – 0.7% uncertainty on single $^{206}\text{Pb}/^{238}\text{U}$ titanite dates, much too high to resolve any temporal relationship between zircon and titanite crystallization.

Five titanite grains from the MG sample have $^{206}\text{Pb}/^{238}\text{U}$ dates that range from $42.36 \pm 0.07/0.43$ Ma to $42.61 \pm 0.08/0.34$ Ma (Fig. 2), that have been corrected using $\text{Th}/\text{U}_{\text{magma}} = 4.93 \pm 0.69$. The measured Th/U ratios for the MG titanites range from 4.8 to 6.8. Correcting

Table 3:
continued

	Tb	± 2s	Dy	± 2s	Ho	± 2s	Er	± 2s	Tm	± 2s	Yb	± 2s	Lu	± 2s	Hf	± 2s	Ta	± 2s	Th	± 2s
MFG-z1	11.7	1.5	160.9	5.6	65.2	5.8	339	10	77.0	4.9	725	37	165.9	11.4	10851	303	0.8	0.3	780	55
MFG-z2	8.8	2.1	127.3	18.6	53.0	6.0	284	53	66.0	10.8	629	91	143.4	16.5	10166	756	0.3	0.1	388	36
MFG-z3	7.4	1.8	120.7	18.4	50.3	4.9	256	38	61.3	5.8	587	68	136.8	10.9	8655	592	1.8	0.7	741	63
MFG-z4	10.0	1.4	139.2	18.3	57.3	5.9	300	20	70.2	5.8	693	67	162.9	17.1	9768	961	0.1	0.0	738	44
MFG-z5	10.3	0.6	139.1	16.9	58.5	3.4	314	26	71.8	6.9	693	51	159.0	14.7	10285	1047	0.3	0.1	668	65
MFG-z6	9.2	1.3	131.5	12.7	54.9	5.5	294	14	67.0	3.1	673	30	155.6	8.0	10080	501	2.0	0.5	505	34
MFG-z7	5.9	1.2	87.4	11.8	36.9	3.5	197	13	47.5	4.8	470	43	115.2	9.5	9928	575	0.6	0.2	789	57
MFG-z8	7.8	2.5	121.0	24.0	52.9	6.1	276	34	65.2	7.9	605	71	141.8	15.9	9215	754	0.9	0.4	302	48
MFG-z9	7.4	1.7	100.2	13.7	45.1	5.3	248	33	62.1	10.7	590	68	131.1	18.9	9544	1059	2.2	1.0	558	52
MFG-z10	9.2	1.8	127.8	13.7	56.2	6.3	293	35	70.2	9.3	646	83	137.4	16.7	8941	1136	2.0	0.7	670	63
MFG-z11	10.7	3.6	153.6	27.5	69.6	12.5	366	70	85.4	18.5	769	91	160.7	33.3	9597	2272	0.8	1.3	566	126
MFG-z12	8.5	1.9	122.4	18.2	51.7	8.0	264	38	60.0	7.3	557	72	120.7	16.9	9613	1330	0.6	0.5	1021	103
MFG-z13	11.8	2.0	166.7	24.3	75.6	10.9	401	33	92.6	9.6	841	57	171.6	26.1	9596	1329	0.9	0.4	657	70
MFG-z14	6.5	4.0	91.4	48.5	40.0	21.9	210	67	48.6	19.2	354	82	106.7	52.1	9099	2658	1.1	0.8	701	139
PQD-z1	6.2	0.9	88.3	14.1	37.8	5.2	204	21	48.6	5.2	483	47	116.7	10.8	9895	787	2.6	0.6	430	53
PQD-z2	6.1	1.8	81.5	17.7	34.0	4.8	190	26	44.5	5.4	462	63	114.6	11.5	8708	458	4.8	3.5	457	47
PQD-z3	7.9	2.6	107.3	14.9	43.7	5.0	263	29	65.1	8.2	546	61	180.5	19.1	11640	1051	0.8	0.5	640	55
PQD-z4	9.2	1.4	120.3	9.5	51.0	3.1	294	24	74.0	6.1	501	36	162.9	15.0	11642	1208	1.8	0.5	565	41
PQD-z5	7.2	1.9	98.9	13.1	42.1	4.5	246	21	63.0	8.0	477	52	165.0	17.5	11640	1259	2.2	0.6	583	74
PQD-z6	7.7	1.8	102.5	14.0	42.8	4.3	255	21	64.9	6.8	505	57	171.8	18.8	11235	1002	2.6	1.3	666	100
PQD-z7	9.6	1.2	130.8	11.8	57.1	4.7	328	28	82.2	7.0	544	60	178.5	16.6	12368	1182	1.6	0.3	472	41
PQD-z8	8.5	0.9	110.7	9.1	48.1	3.5	283	34	73.0	6.1	491	43	168.8	17.4	10540	905	0.1	0.0	661	62
VFT-z1	9.8	4.1	127.5	19.3	52.4	6.3	273	22	62.5	8.1	592	44	138.6	11.7	8883	394	5.2	2.5	606	36
VFT-z2	6.5	0.9	90.0	6.7	38.8	3.9	210	19	50.5	3.2	503	38	123.8	9.3	9933	591	2.4	0.6	392	34
VFT-z3	7.5	1.1	98.0	15.2	41.8	3.8	224	26	51.2	4.8	492	35	114.7	6.9	10277	591	3.8	1.1	392	34
VFT-z4	5.1	1.1	88.7	13.8	37.7	6.4	201	25	48.7	5.3	475	57	115.2	14.9	9564	1084	0.5	0.3	385	55
VFT-z5	6.2	1.1	106.9	12.2	44.9	4.4	238	22	55.8	4.9	529	39	122.8	9.6	10694	753	0.9	0.3	286	32
VFT-z6	6.2	0.9	90.7	11.0	39.6	4.3	218	19	52.3	4.5	521	40	127.2	9.1	9610	712	1.0	0.3	409	33
VFT-z7	8.0	1.2	111.7	12.2	52.1	6.8	280	30	68.3	10.9	428	58	128.2	20.7	9052	1624	0.0	0.0	483	61
VFT-z8	5.2	2.5	64.0	24.3	26.2	13.6	146	59	37.2	21.8	255	115	90.8	41.5	9718	3248	0.1	0.0	502	122
VFT-z9	4.4	2.0	64.5	18.5	25.7	5.2	147	25	33.4	5.6	423	66	110.3	13.8	8131	658	0.9	0.4	193	25
VFT-z10	7.8	1.5	103.3	13.5	43.9	3.6	256	22	68.1	6.4	461	50	155.1	14.0	11204	1104	2.4	0.4	435	36
MG-z1	17.2	0.5	212.3	6.6	81.7	2.4	385	14	88.1	3.2	800	32	185.9	7.4	8013	576	0.8	0.1	1453	37
MG-z2	4.9	0.6	68.2	6.2	31.0	2.7	168	14	42.9	3.9	429	29	112.2	9.5	8204	665	0.4	0.1	601	61
MG-z3	7.8	0.9	105.4	13.8	43.8	5.2	227	25	56.6	5.1	554	48	138.0	16.0	8423	727	0.8	0.1	770	74
MG-z4	8.0	1.0	104.5	12.5	43.1	3.7	216	17	51.2	4.6	486	31	120.5	10.9	8436	803	0.6	0.2	806	76
MG-z5	8.4	0.7	113.8	9.8	47.6	3.3	241	17	58.6	4.5	556	43	134.5	9.9	7765	526	0.6	0.1	722	83
MG-z6	5.8	0.9	77.2	9.6	33.0	4.1	177	22	43.2	6.3	295	36	91.2	13.5	7288	735	0.0	0.0	552	59
MG-z7	7.9	0.9	105.2	13.9	48.1	6.6	263	31	63.7	9.1	429	58	137.7	19.7	7179	700	0.0	0.0	1088	128
MG-z8	10.1	1.5	122.4	14.9	51.5	5.1	266	29	63.4	8.2	427	41	134.7	19.2	7368	993	0.4	0.2	707	80
MG-z9	23.4	2.4	252.7	29.4	93.8	9.8	439	63	97.4	15.7	568	70	156.2	22.7	6617	890	0.1	0.1	1618	180
MG-z10	8.8	1.6	117.8	17.1	47.9	6.1	232	33	54.0	9.8	371	67	112.6	24.1	6481	769	0.1	0.1	1042	117
CG-z1	7.0	0.6	101.5	10.4	42.8	4.0	228	22	55.3	5.9	568	41	142.7	9.6	9624	665	1.1	0.2	1314	118
CG-z2	3.8	0.5	56.6	6.0	25.2	2.2	140	11	35.7	3.6	373	31	96.9	8.8	8667	789	0.4	0.2	422	51
CG-z3	6.6	0.8	92.8	11.7	39.6	4.4	212	21	51.7	5.0	525	49	132.7	11.3	8942	603	0.3	0.2	920	113
CG-z4	10.9	1.1	155.3	18.8	64.8	6.6	345	38	83.2	7.8	841	56	211.1	13.5	10039	850	1.3	0.3	2001	227
CG-z5	7.0	0.7	98.0	6.8	42.8	2.9	234	17	58.6	4.4	599	37	154.5	8.3	9690	542	0.8	0.2	1434	101
CG-z6	4.5	0.7	62.2	9.6	27.9	3.8	154	17	38.7	4.8	398	40	105.1	9.9	9160	1068	1.2	0.3	652	49
CG-z7	7.0	0.6	94.0	8.2	40.1	2.7	212	16	51.0	4.0	513	29	132.1	8.6	9281	522	1.5	0.3	1312	84
CG-z8	6.8	0.8	96.9	7.3	42.3	3.0	233	18	58.5	4.3	602	41	155.1	10.8	10218	657	1.8	0.3	1236	93
CG-z9	9.1	1.2	118.2	16.4	50.3	5.3	271	32	66.6	8.1	680	59	174.8	17.3	10201	1043	2.4	0.6	1523	168
Peg-z1	14.2	2.1	186.5	25.3	75.5	12.4	386	57	95.7	12.6	608	80	224.5	33.3	10097	1454	0.9	0.3	1509	247
Peg-z2	11.9	2.3	157.3	35.2	74.5	13.5	406	77	104.1	17.0	676	111	249.8	40.4	15849	2005	0.1	0.1	3711	589
Peg-z3	12.0	1.3	190.8	19.9	68.5	5.6	314	23	72.0	5.8	419	35	150.6	13.6	6411	874	0.5	0.1	546	43
Peg-z4	13.7	1.7	186.2	25.1	77.8	9.1	393	37	100.2	10.5	623	67	232.2	22.4	9192	1018	1.2	0.2	1356	164
Peg-z5	10.8	1.8	152.6	20.2	65.3	9.4	336	48	85.0	10.9	558	62	200.6	25.4	12378	1172	2.7	0.7	4437	550
Peg-z6	7.9	1.4	115.9	15.6	49.8	6.7	262	25	66.0	6.9	439	32	166.6	13.0	11625	1002	1.3	0.5	2081	242
Peg-z7	11.1	1.0	148.8	17.4	61.1	6.5	308	27	76.7	6.6	475	47	178.7	15.2	9984	848	0.4	0.2	988	94
Peg-z8	10.3	2.4	141.9	23.1	61.4	7.5	325	40	80.3	10.8	538	54	196.8	26.5	11939	1434	1.5	0.7	3177	395
Peg-z9	10.3	2.0	143.3	17.2	59.8	8.1	305	33	75.4	8.2	498	55	182.0	16.7	11888	1162	7.5	1.8	3888	397

Zirconium is reported in wt.% and elements are reported in ppm

Concentrations are normalized to Zr+Hf = 497,464 ppm in stoichiometric zircon (Hoskin and Schaltegger, 2003).

“ - “ analysis below detection limit

$^{206}\text{Pb}/^{204}\text{Pb}$ ratios (~40 – 60) render the titanite dates completely insignificant for resolving timescales of accessory mineral crystallization.

2.4.3 Trace element composition of zircon

Results from TIMS-TEA and laser ablation ICP-MS

Trace element concentrations were analyzed from the same volume of zircon used for U-Pb age determinations, described as TIMS-TEA

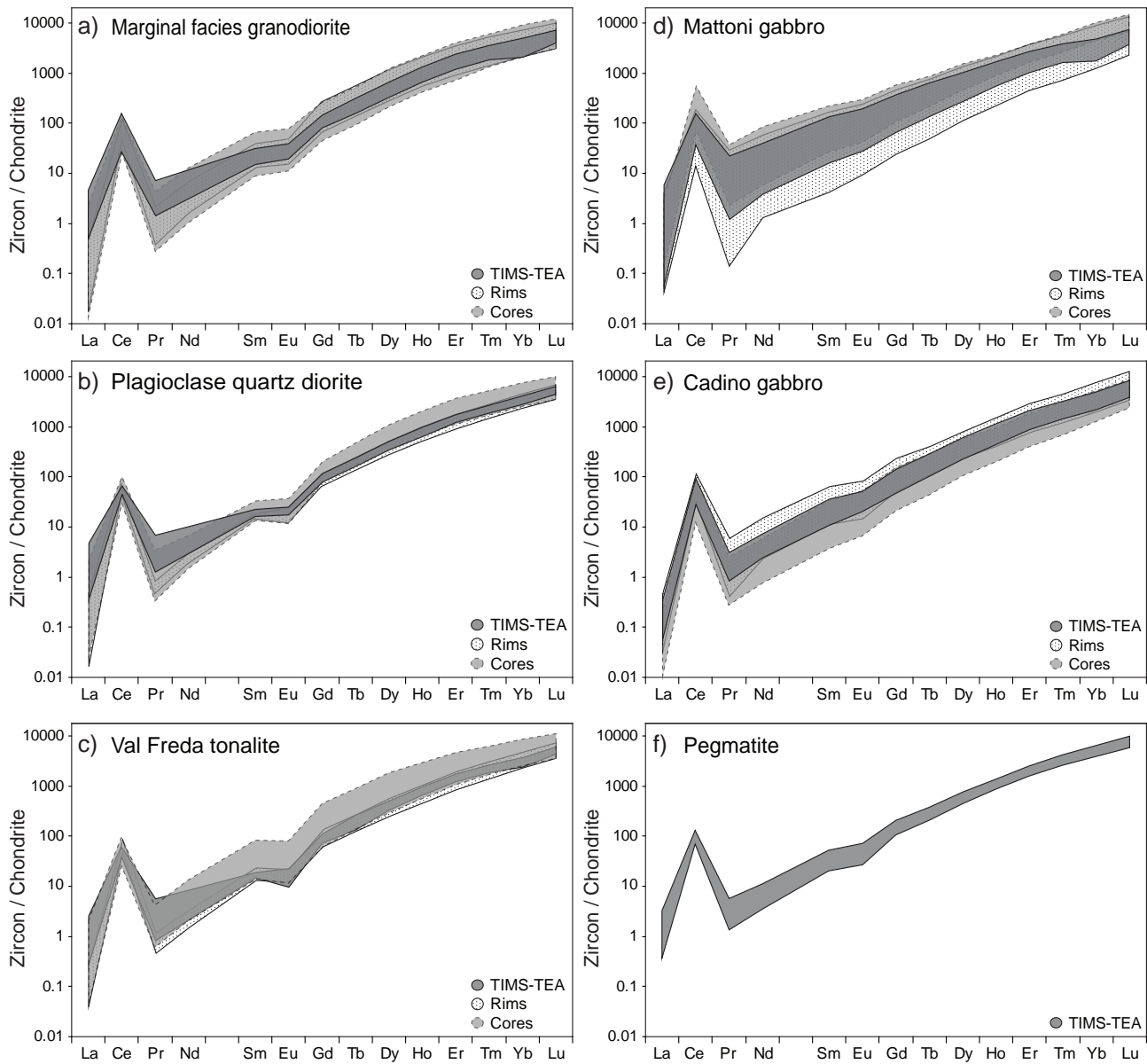


Figure 4: Chondrite normalized REE patterns for zircon, comparison between TIMS-TEA and LA-ICP-MS core and rim analyses. Zircons from the pegmatite sample were only analyzed by TIMS-TEA.

by Schoene et al. (2010). Zircon trace and rare earth element data together with the results of spatially resolved in situ analyses using LA-ICP-MS (see below) are summarized in Figures 4 & 5 and TIMS-TEA results listed in Table 3. The chondrite normalized REE patterns for zircon grains from felsic samples (Fig. 4a-c) are characterized by HREE enrichment ($(\text{Lu}/\text{Gd})_{\text{N}} \sim 40 - 70$), positive Ce anomalies, and mostly negative Eu anomalies ($\text{Eu}/\text{Eu}^* \sim 0.5$).

Zircon grains from the felsic samples record no significant differences in concentrations of major constituents, such as Hf (Fig. 5a), or Zr, which translates to rather homogenous Zr/Hf ratios $\sim 40 - 60$, typical for calc-alkaline intermediate to felsic rocks (Pupin, 2001). In contrast, trace element ratios such as Y/Hf, $(\text{Lu}/\text{Gd})_{\text{N}}$ and Th/U vary by a factor of two and Nb/Zr varies up to a factor of eight. Based on the observed trace element variations in zircon, the individual

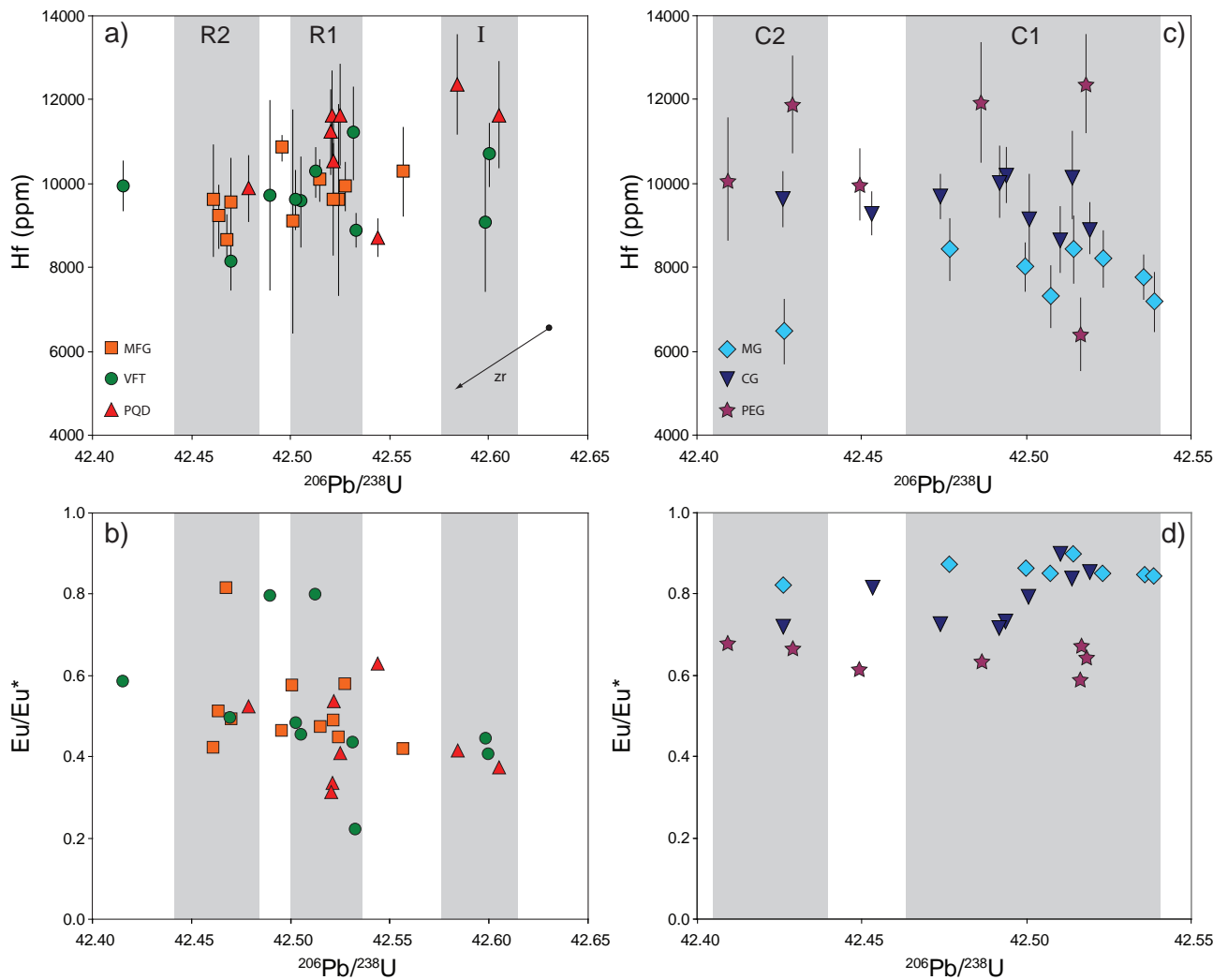


Figure 5: Variations of trace element concentrations and ratios of zircon through time, analyzed by TIMS-TEA. The light grey bands correspond to the periods of enhanced zircon crystallization (identified by the peaks in Figure 3). I = initial felsic intrusions; R1, R2 = periods of rejuvenation of felsic crystal mushes; C1, C2 = periods of zircon crystallization associated with cooling. (See text for discussion)

felsic units cannot be clearly distinguished nor do they record coherent fractional crystallization trends through time (Fig. 5), as observed in the northerly Lago della Vacca complex (Schoene et al., 2012). Thus, the non-systematic trace element correlations with time point to the chemical variability within the felsic magmas during zircon crystallization.

The zircon grains from the gabbro samples (MG, CG) have chondrite normalized REE patterns typical for zircon (Fig. 4d-e), with

generally enriched HREE ($(\text{Lu/Gd})_N \sim 20 - 80$), a positive Ce anomaly, but lacking a negative Eu anomaly ($\text{Eu/Eu}^* \sim 0.9 - 0.8$), whereas zircon from the pegmatite sample (Fig. 4f) exhibit a weak negative Eu anomaly ($\text{Eu/Eu}^* \sim 0.7$). Zircon grains from the mafic samples record rather homogenous concentrations of Hf (Fig. 5c) and Zr that are distinct for each unit, which translates to Zr/Hf ratios of MG $\sim 60 - 75$; CG $\sim 50 - 55$; Peg $\sim 30 - 50$, typical for mantle derived rocks (MG) and calc-alkaline intermediate rocks

Table 4:
LA-ICP-MS zircon trace element results for samples from the Val Fredda Complex

		Zr wt%	T°C	Ti	Y	Nb	La	Ce	Pr	Nd	Sm	Eu	Gd	Tb	Dy	Ho	Er	Tm	Yb	Lu	Hf	Ta	Th	U	
Marginal Facies granodiorite																									
CB03 z15_1	core	61.0	804.7	12.5	1361	6.8	0.20	51.9	0.37	5.5	9.6	2.0	40.3	11.4	130	46.4	210	47.9	437	82.8	10372	2.1	358	290	
CB03 z14_1	core	60.7	770.8	9.0	1464	8.3	0.25	20.4	0.14	1.7	3.8	0.8	24.9	8.9	128	51.9	255	58.5	542	97.2	10718	3.4	355	833	
CB03 z13_1	core	63.1	711.4	4.7	797	2.0	0.03	26.5	0.21	2.3	3.7	1.4	16.3	5.1	68	25.9	135	34.6	380	92.5	9846	1.2	857	937	
CB03 z12_1	core	60.7	695.7	3.9	1571	5.7	0.01	24.5	0.04	0.9	2.4	0.9	20.1	7.8	120	52.2	286	71.1	744	159.4	10332	2.1	429	914	
CB03 z11_1	core	64.7	705.1	4.4	1427	7.2	0.02	24.1	0.06	0.5	2.2	0.9	19.0	7.4	113	48.1	256	62.2	660	133.1	13218	4.1	343	818	
CB03 z10_1	core	61.5	784.0	10.3	3450	31.8	0.12	73.9	0.26	3.5	8.0	2.6	55.0	19.6	271	107.5	523	120.1	1153	228.9	10527	7.5	2241	2333	
CB03 z07_1	core	64.0	907.5	30.7	2210	13.1	0.56	22.0	0.21	2.1	3.6	1.1	27.1	13.1	195	79.1	414	98.2	957	186.3	12489	7.8	448	1772	
CB03 z06_1	core	63.1	729.9	5.8	3797	23.7	0.03	40.2	0.08	1.2	4.8	2.1	44.0	20.6	318	131.5	681	156.5	1561	298.2	11971	7.1	622	1692	
CB03 z05_1	core	63.3	-	-	1598	4.7	0.06	23.1	0.11	1.4	3.8	1.0	23.9	9.4	132	54.8	282	64.4	652	136.3	11398	1.8	457	866	
CB03 z04_1	core	64.1	-	-	1968	8.6	0.08	42.4	0.11	1.8	4.3	1.6	30.9	10.9	150	60.8	321	75.8	803	173.5	10826	2.6	691	1008	
CB03 z03_1	core	56.7	-	-	2647	15.7	0.02	38.4	0.06	1.4	4.6	1.8	35.3	15.0	220	87.8	461	105.5	1047	213.2	9773	4.9	947	1710	
CB03 z20_1	core	56.1	718.5	5.1	1770	6.1	0.03	15.4	0.07	1.5	3.6	1.2	26.0	9.6	152	60.4	314	73.4	739	157.0	9348	5.1	206	521	
CB03 z18_1	core	62.0	672.3	3.0	701	3.3	0.00	16.5	0.03	0.7	1.4	0.6	9.4	3.5	54	24.0	120	33.7	368	91.0	10925	1.4	319	800	
CB03 z17_1	core	42.7	1005.5	63	2548	4.9	0.05	40.9	0.34	6.0	8.5	4.5	43.9	16.5	206	81.9	447	92.0	1125	227.4	6767	1.4	745	727	
CB03 z15_2	rim	59.7	714.1	4.9	1149	8.0	0.02	38.2	0.06	1.1	2.9	0.9	17.2	6.3	86	34.6	183	43.6	452	96.1	10138	3.2	740	1025	
CB03 z14_2	rim	59.4	732.6	6.0	3351	34.0	0.11	55.6	0.11	1.9	5.9	2.5	53.1	20.9	302	121.1	574	128.8	1216	238.1	11115	11.0	1681	2761	
CB03 z13_2	rim	59.9	726.0	5.6	1030	8.4	0.01	46.1	0.06	1.1	2.3	0.9	14.8	5.3	77	31.1	162	39.1	416	94.5	10341	3.5	986	1475	
CB03 z12_2	rim	61.1	850.9	19.1	1497	12.0	0.08	47.5	0.09	1.3	3.1	1.1	23.3	8.5	118	48.8	251	61.6	646	136.7	11049	4.6	836	1274	
CB03 z11_2	rim	60.4	724.0	5.5	2921	48.5	-	64.8	0.04	0.9	3.1	1.1	30.2	13.3	207	89.9	483	114.1	1165	246.4	11051	13.2	955	2234	
CB03 z10_2	rim	58.7	662.7	2.6	1399	10.1	0.04	39.4	0.08	1.2	2.6	0.9	20.3	7.6	107	43.1	225	54.8	559	119.4	10123	4.4	766	1120	
CB03 z09_1	rim	62.7	792.0	11.1	1725	12.4	0.04	52.2	0.08	1.5	3.4	1.2	23.8	9.2	132	57.2	306	76.5	835	179.8	10395	4.2	748	1138	
CB03 z08_2	rim	59.6	917.4	33	1450	7.7	0.01	30.5	0.05	1.0	2.9	1.1	19.1	7.2	106	43.4	233	55.7	587	125.7	9897	2.5	466	814	
CB03 z08_1	rim	62.6	731.8	6.0	2112	8.7	0.02	64.1	0.20	3.2	5.8	2.8	36.5	11.6	162	65.1	344	83.9	892	192.3	8820	2.4	1611	1349	
CB03 z08_2	rim	61.0	698.7	4.1	2035	18.8	0.01	63.8	0.07	1.5	3.5	1.3	23.5	9.9	143	61.8	335	83.1	891	190.4	9626	5.3	758	1190	
CB03 z07_2	rim	63.3	732.1	6.0	1444	8.6	0.08	32.6	0.07	0.9	2.2	1.0	17.9	7.0	105	43.9	247	60.7	664	149.5	11421	3.5	363	812	
CB03 z06_2	rim	58.7	713.4	4.8	992	6.2	0.02	30.4	0.07	0.8	2.2	0.9	15.6	5.8	76	31.1	155	36.1	380	80.8	9750	2.3	612	827	
CB03 z05_2	rim	59.2	693.5	3.8	1383	9.4	-	38.6	0.06	1.4	3.4	1.3	22.1	7.4	106	42.1	225	54.5	572	125.0	10082	3.3	881	1201	
CB03 z04_2	rim	60.1	714.4	4.9	1576	11.1	0.04	51.9	0.09	1.6	3.2	1.2	21.9	8.0	115	47.4	259	64.7	685	153.9	10084	4.0	824	1155	
CB03 z03_2	rim	59.7	-	-	1088	7.2	0.01	37.7	0.07	1.2	2.8	0.9	15.9	5.5	76	31.9	168	41.0	437	94.1	9816	2.7	723	935	
CB03 z02_1	rim	59.3	774.6	9.3	2018	12.6	0.14	34.5	0.15	1.7	4.2	1.6	28.1	11.0	155	60.4	308	72.6	753	153.0	10282	4.5	867	1346	
CB03 z01_1	rim	60.9	701.4	4.2	1634	8.2	0.05	25.5	0.06	0.9	2.5	0.8	19.1	8.5	122	48.7	261	61.0	670	132.0	12156	3.6	341	1077	
CB03 z20_2	rim	60.1	694.0	3.9	1945	15.5	0.11	48.6	0.07	1.1	3.0	1.0	22.8	9.3	140	59.6	330	80.5	859	190.8	8890	5.3	466	1054	
CB03 z18_2	rim	52.9	729.8	5.8	998	6.5	0.00	28.3	0.05	1.0	1.9	1.0	12.2	5.1	73	29.3	165	37.1	419	96.6	9490	2.5	579	1017	
CB03 z17_2	rim	64.6	735.9	6.2	1126	10.0	0.07	41.7	0.08	0.9	2.7	1.0	19.5	7.4	108	49.0	201	56.4	530	117.8	11060	3.4	603	915	
Mattioni gabbro																									
CB04 z01_2	core	66.1	866.9	22.0	3658	15.7	0.05	124.3	0.23	3.5	6.1	4.5	40.4	16.7	250	118.8	615	153.5	1752	382.1	7111	3.2	3525	2433	
CB04 z02_2	core	60.4	841.6	17.6	2732	10.0	0.10	73.0	0.56	6.7	8.4	4.8	41.5	13.7	196	86.5	482	122.2	1313	307.3	5861	2.5	1418	1336	
CB04 z03_1	core	62.4	-	-	1721	6.1	0.04	45.4	0.22	2.8	4.1	2.4	22.6	8.1	120	52.1	276	70.5	803	193.7	6422	1.8	815	724	
CB04 z04_1	core	58.9	867*	43.8	2790	49.8	0.30	335.4	2.09	22.0	20.2	10.3	78.4	22.1	260	89.7	402	85.9	859	176.7	6917	8.5	13854	3669	
CB04 z06_1	core	60.5	851.3	19.2	3930	13.1	0.67	143.5	3.55	40.0	34.1	17.5	120.3	33.1	393	130.8	591	130.8	1297	272.6	6713	1.8	2292	932	
CB04 z07_1	core	62.3	813.3	13.6	2898	10.4	0.11	87.8	0.45	5.6	6.5	4.4	39.0	14.3	209	89.0	500	127.4	1364	332.1	6581	3.1	2144	1792	
CB04 z08_1	core	61.9	-	-	1920	5.7	0.14	56.0	0.58	6.4	7.5	4.4	35.2	11.2	155	60.7	302	73.4	801	182.0	7484	1.5	1189	897	
CB04 z09_2	core	61.3	749.4	7.2	2430	7.7	0.16	78.8	0.80	8.3	9.7	5.4	45.4	14.4	191	72.9	366	87.0	936	216.3	7274	1.5	1676	1076	
CB04 z10_1	core	67.3	-	-	2741	8.7	0.15	77.4	1.10	13.9	15.1	7.8	63.1	19.1	230	88.4	434	99.7	1050	228.7	6985	1.6	1247	853	
CB04 z12_1	core	60.9	832.1	16.2	3386	11.8	0.45	107.7	1.91	20.4	20.2	11.3	80.9	24.5	302	107.3	509	116.4	1159	248.8	6817	1.8	2105	1070	
CB04 z13_1	core	65.0	793.1	11.2	2838	8.9	0.50	96.5	1.70	14.4	14.5	8.1	66.3	19.8	246	88.9	440	105.7	1076	233.2	7696	1.4	2112	1165	
CB04 z14_1	core	61.9	801.7	12.2	3191	10.2	0.26	103.5	1.71	18.1	19.4	9.8	77.7	23.2	283	103.7	486	112.7	1138	246.0	6926	1.8	1742	856	
CB04 z15_1	core	64.5	802.7	12.3	2714	8.1	0.28	91.7	1.15	11.5	11.0	7.1	53.8	16.2	223	83.2	418	101.6	1038	247.0	7462	1.4	2047	1213	
CB04 z19_1	core	54.9	873*	46.2	2655	46.2	0.30	322.3	1.98	19.															

Table 4:
continued

		Zr wt%	T°C	Ti	Y	Nb	La	Ce	Pr	Nd	Sm	Eu	Gd	Tb	Dy	Ho	Er	Tm	Yb	Lu	Hf	Ta	Th	U
Val Fredda tonalite (continued)																								
CB09 z13_1	rim	63.7	-	-	870	4.8	-	31.5	0.05	1.0	2.1	0.7	12.6	4.5	64	25.7	140	35.4	393	88.3	11134	2.1	510	759
CB09 z13_2	rim	66.1	-	-	1688	10.3	-	48.6	0.06	1.4	2.8	1.1	20.8	7.3	115	49.0	267	67.8	737	170.5	10047	3.6	583	976
CB09 z12_2	rim	62.4	756.5	7.8	1229	7.2	0.02	32.8	0.04	0.9	2.2	0.9	14.5	5.3	82	35.9	206	51.3	561	132.0	9695	2.8	397	708
CB09 z11_1	rim	66.8	770.1	8.9	1734	9.0	-	50.0	0.08	1.5	3.2	1.2	22.1	8.5	123	53.7	292	70.5	775	179.8	9832	2.9	696	918
CB09 z11_2	rim	73.8	805.0	12.6	1837	10.7	-	45.4	0.11	1.6	3.7	2.1	24.1	8.9	138	59.6	309	81.8	860	199.1	12027	3.6	656	1026
CB09 z10_2	rim	65.0	755.5	7.7	1531	11.7	0.02	41.6	0.09	1.0	3.4	0.9	21.3	8.1	113	48.0	258	61.9	655	142.3	11165	4.4	638	1084
CB09 z09_2	rim	63.1	777.4	9.6	985	6.0	-	36.4	0.07	0.7	2.6	0.8	14.3	5.3	71	29.7	158	38.2	410	92.4	10177	2.5	723	935
CB09 z08_1	rim	64.7	-	-	1878	12.7	0.03	48.4	0.09	1.6	3.4	1.1	26.7	9.5	139	56.5	306	71.9	777	171.4	10844	4.2	1036	1361
CB09 z07_2	rim	64.3	755.3	7.7	1622	10.9	-	49.0	0.11	1.5	3.4	1.0	20.6	7.9	115	49.3	265	65.7	713	163.6	10572	3.6	817	1136
CB09 z06_1	rim	62.3	754.0	7.6	952	5.6	0.02	35.2	0.06	1.1	2.5	0.7	13.7	5.2	70	27.8	154	36.3	407	90.8	10622	2.4	674	906
CB09 z4_1	rim	64.2	776.8	9.6	1381	9.3	0.06	41.6	0.08	1.0	2.2	0.9	17.5	6.6	98	37.8	214	53.2	593	136.8	10879	3.2	629	976
CB09 z3_2	rim	60.9	739.6	6.5	1484	9.6	0.06	36.7	0.07	1.4	2.7	1.0	17.7	6.5	98	42.4	240	59.9	678	154.5	9387	3.5	453	840
CB09 z2_2	rim	64.7	719.3	5.2	1398	9.4	0.01	38.3	0.06	1.0	2.9	1.0	18.0	6.7	102	41.9	225	55.2	584	134.2	11102	3.9	530	937
CB09 z16_2	rim	46.6	980.8	53	1699	11.8	0.01	39.2	0.06	1.0	2.7	1.2	21.2	8.4	124	53.6	291	71.6	764	172.3	10733	3.8	452	879
CB09 z17_1	rim	47.3	808.3	13.0	1504	11.1	0.02	41.2	0.06	1.1	3.0	1.1	21.6	8.0	118	48.9	257	61.3	636	140.5	11439	4.6	801	1242
CB09 z18_2	rim	49.9	795.9	11.5	1023	6.4	0.04	34.4	0.08	1.0	2.6	0.8	16.2	5.7	80	32.7	173	41.4	447	99.0	12144	2.9	674	986
CB09 z19_1	rim	45.3	732.7	6.0	1899	12.8	0.03	42.8	0.06	1.1	3.1	1.2	23.1	9.3	142	60.5	328	79.7	828	183.7	10027	3.8	479	955
Plagioclase quartz diorite																								
CB13 z15_1	core	62.6	707.6	4.5	1451	6.8	-	24.0	0.03	0.7	2.2	0.8	17.5	6.8	102	46.3	243	61.7	658	146.9	10966	2.4	332	765
CB13 z14_1	core	68.5	-	-	1174	7.0	0.02	26.9	0.03	0.9	2.2	0.8	16.6	6.4	93	42.4	221	57.0	587	127.1	13846	3.4	528	936
CB13 z11_1	core	59.3	724.2	5.5	1736	7.8	0.02	24.2	0.06	0.9	2.9	1.0	21.1	8.6	131	54.8	292	67.3	708	151.0	10852	2.7	366	862
CB13 z10_1	core	63.4	758.9	8.0	1846	11.2	0.50	62.3	0.34	3.2	5.3	2.2	30.1	10.7	145	59.0	294	69.8	736	157.8	10196	3.9	2066	2326
CB13 z09_1	core	58.0	713.3	4.8	1578	7.7	0.05	33.7	0.07	1.2	3.4	1.2	21.9	8.3	119	50.0	262	63.2	675	148.4	10029	2.6	624	927
CB13 z07_1	core	54.6	759.6	8.0	2183	7.1	0.09	24.1	0.11	1.4	5.1	1.7	33.4	13.1	190	75.2	378	87.1	852	169.2	10267	2.7	454	931
CB13 z03_1	core	57.5	720.3	5.2	1794	8.4	0.31	30.9	0.15	1.7	3.4	1.0	22.9	9.1	132	55.2	299	71.5	734	159.3	9978	2.7	533	943
CB13 z02_1	core	55.9	714.6	4.9	1877	13.9	0.06	38.7	0.07	1.3	3.8	1.4	25.6	10.1	145	60.4	304	71.6	718	153.4	9549	4.6	789	1315
CB13 z19_1	core	47.7	693.2	3.8	3466	8.6	0.03	22.1	0.06	1.5	4.6	1.9	41.9	18.2	283	122.4	619	139.3	1327	264.4	10767	2.8	366	1111
CB13 z18_1	core	51.0	745.0	6.9	1250	3.4	0.02	18.5	0.03	0.8	2.4	0.7	16.7	6.7	98	39.4	198	45.8	450	94.3	12125	1.4	278	555
CB13 z17_1	core	51.9	702.9	4.3	2516	16.6	0.03	45.8	0.07	1.4	4.9	1.9	37.5	14.7	210	87.4	450	104.0	1036	228.0	11031	5.3	1043	1731
CB13 z15_2	rim	55.8	705.9	4.4	967	6.0	0.03	32.9	0.05	1.1	2.3	0.7	13.4	5.0	70	28.4	148	37.4	414	91.0	9361	2.3	464	721
CB13 z14_2	rim	58.9	708.5	4.6	1317	8.8	0.01	38.6	0.06	1.1	2.7	1.0	15.9	6.6	95	41.1	227	56.0	623	140.9	10906	3.7	572	934
CB13 z13_1	rim	61.4	742.1	6.7	1319	6.6	0.04	35.9	0.07	1.2	2.5	1.4	17.7	6.6	95	38.6	200	47.3	507	117.8	10025	2.4	855	1276
CB13 z11_2	rim	64.1	675.0	3.1	1162	7.1	-	43.6	0.08	1.3	2.5	1.0	16.3	6.1	81	33.1	168	41.5	438	98.0	10083	2.9	892	1045
CB13 z10_2	rim	61.1	701.2	4.2	1199	7.4	0.04	36.4	0.07	1.2	2.3	0.9	15.7	5.8	83	35.1	190	47.0	516	114.2	10383	3.4	633	1041
CB13 z09_2	rim	67.9	805.3	12.6	1504	9.7	4.17	54.8	0.98	3.3	3.1	1.1	17.4	7.2	115	51.5	263	70.5	755	168.1	12234	3.6	683	1118
CB13 z07_2	rim	57.1	726.1	5.6	1641	11.7	0.01	35.4	0.05	1.1	2.8	1.3	21.6	8.5	124	52.0	267	63.5	672	144.5	9892	4.2	528	1001
CB13 z03_2	rim	59.4	743.0	6.7	1548	10.2	0.04	42.2	0.06	1.2	2.4	0.9	19.8	6.9	105	46.0	256	63.6	707	158.9	10003	3.6	517	889
CB13 z02_2	rim	58.8	693.3	3.8	1099	7.4	0.05	37.9	0.08	1.3	2.6	0.9	16.2	6.0	80	32.7	170	41.4	429	92.4	9731	2.8	787	977
CB13 z20_1	rim	49.5	713.1	4.8	1193	8.3	0.01	30.2	0.04	0.9	2.6	0.8	17.4	6.6	95	40.4	209	49.9	526	116.8	11885	3.4	495	914
CB13 z19_2	rim	50.4	703.6	4.3	1014	6.3	0.00	36.0	0.05	0.9	2.2	1.0	15.3	5.5	78	31.0	162	39.5	415	93.3	10458	2.6	701	944
CB13 z18_2	rim	49.4	721.3	5.3	1625	12.9	0.11	32.6	0.07	1.0	2.8	0.9	19.4	7.7	119	51.1	279	68.8	732	167.5	10480	4.5	357	837
CB13 z17_2	rim	51.2	715.6	5.0	1415	10.7	0.04	32.9	0.06	0.9	2.6	1.0	19.2	7.1	107	45.6	245	61.0	638	142.7	10531	4.1	419	873
CB13 z16_1	rim	54.3	696.0	4.0	426	3.0	0.00	18.6	0.04	0.6	1.3	0.6	6.8	2.4	32	12.6	67	16.4	177	42.9	10416	1.4	511	798
CB13 z16_2	rim	56.4	727.8	5.7	715	5.5	0.02	28.0	0.06	0.9	1.5	0.8	11.2	3.8	54	22.0	117	28.9	316	78.5	10820	2.3	785	1166

Zirconium is reported in wt.% and elements are reported in ppm

Ti-in-zircon temperatures are calculated using the equation of Ferry and Watson (2007) using $a_{\text{SiO}_2} = 1$ and $a_{\text{TiO}_2} = 0.7$

* Ti-in-zircon temperatures calculated using $a_{\text{SiO}_2} = 0.5$

“ - “ analysis below detection limit

(CG, Peg; Pupin, 2001). In contrast, zircon trace element ratios such as Th/U, Y/Hf and (Lu/Gd)_N vary over a factor of two to three among the mafic samples. Based on trace elements in zircon, the individual mafic units can be distinguished from each other; however no coherent fractional crystallization trends are observed through time (Fig. 5c-d).

The major advantage of analyzing trace elements by TIMS-TEA is obtaining trace element information from the exact same volume of zircon we have high-precision temporal information from. We were, however, not able to obtain

significant Ti concentrations, to be employed for the Ti-in-zircon thermometry (Watson et al., 2006; Ferry and Watson, 2007). Therefore, in order to build a robust trace element data set that includes Ti, we analyzed trace element concentrations of 10 – 20 zircons per sample by laser ablation ICP-MS, in addition to the TIMS-TEA data. Both cores and rims were analyzed whenever possible separately, and the data are reported in Table 4.

For each of the VFC units we obtained REE patterns that are in good agreement between TIMS-TEA and LA-ICP-MS (Fig. 4). The

chondrite normalized REE patterns for the zircons from the felsic units, analyzed by LA-ICP-MS, do not show any significant difference to the TIMS-TEA data. The zircon grains from the gabbro units (MG, CG) have identical chondrite normalized REE patterns as from TIMS-TEA, which equally show the lack of a negative Eu anomaly ($\text{Eu}/\text{Eu}^* \sim 0.9 - 0.7$).

The MFG zircon grains show little variation in REE patterns between core and rim analyses. The chondrite normalized REE patterns for MFG zircons, obtained by TIMS-TEA, corresponds to the average concentration between the core and rim concentrations (Fig. 4a). Both the PQD and the VFT zircon grains exhibit an overall decrease in trace element concentrations from cores to rims. The chondrite normalized REE patterns for both PQD and VFT zircons, obtained by TIMS-TEA, mainly correspond with their respective rim concentrations. The distinguishing feature of the mafic zircons is their lack of an Eu anomaly in both cores and rims (Fig. 4d-e). The MG zircons show an overall decrease in trace element concentrations from cores to rims, whereas the REE pattern for CG zircons show an opposite trend. REE concentrations of the whole zircon volume by the TIMS-TEA method mainly correlate with the REE concentrations corresponding to the rim analyses. This reflects that the trace element concentrations measured by TIMS-TEA, although representing the

average concentrations in the zircon grain during crystallization, are weighted towards the larger volume of the rim portion of the zircon grains (Samperton et al., 2012). Even though TIMS-TEA records the average trace element concentrations, they still record trace element variability (e.g. Hf, $(\text{Lu}/\text{Gd})_N$, and Th/U) which strongly overlaps with our core-rim data obtained by LA-ICP-MS (Fig. 6).

Trace element variations during zircon growth: LA-ICP-MS results from cores and rims

Cathodoluminescence (CL) images of individual zircon grains were used to reveal older cores, magmatic zoning and any disturbances during zircon growth. A laser ablation spot size of 25 μm was used for trace element analysis, in order to target specific zones of zircon growth, concentrating when possible on separate core and rim analyses. The core-rim dataset may be explored in terms of reconstructing changes in the trace element budget during the initial magma conditions (cores) through the final stages of zircon crystallization (rims). Zircon trace element data are reported in Table 4.

CL images of MFG zircons (Fig. 7a-b and A3) reveal two different zoning patterns; (1) continuous oscillatory zoning with no distinct cores (e.g., Fig. 7a), and (2) cores associated with a surrounding dark zone followed by typical magmatic oscillatory zoning (e.g. Fig 7b). Of

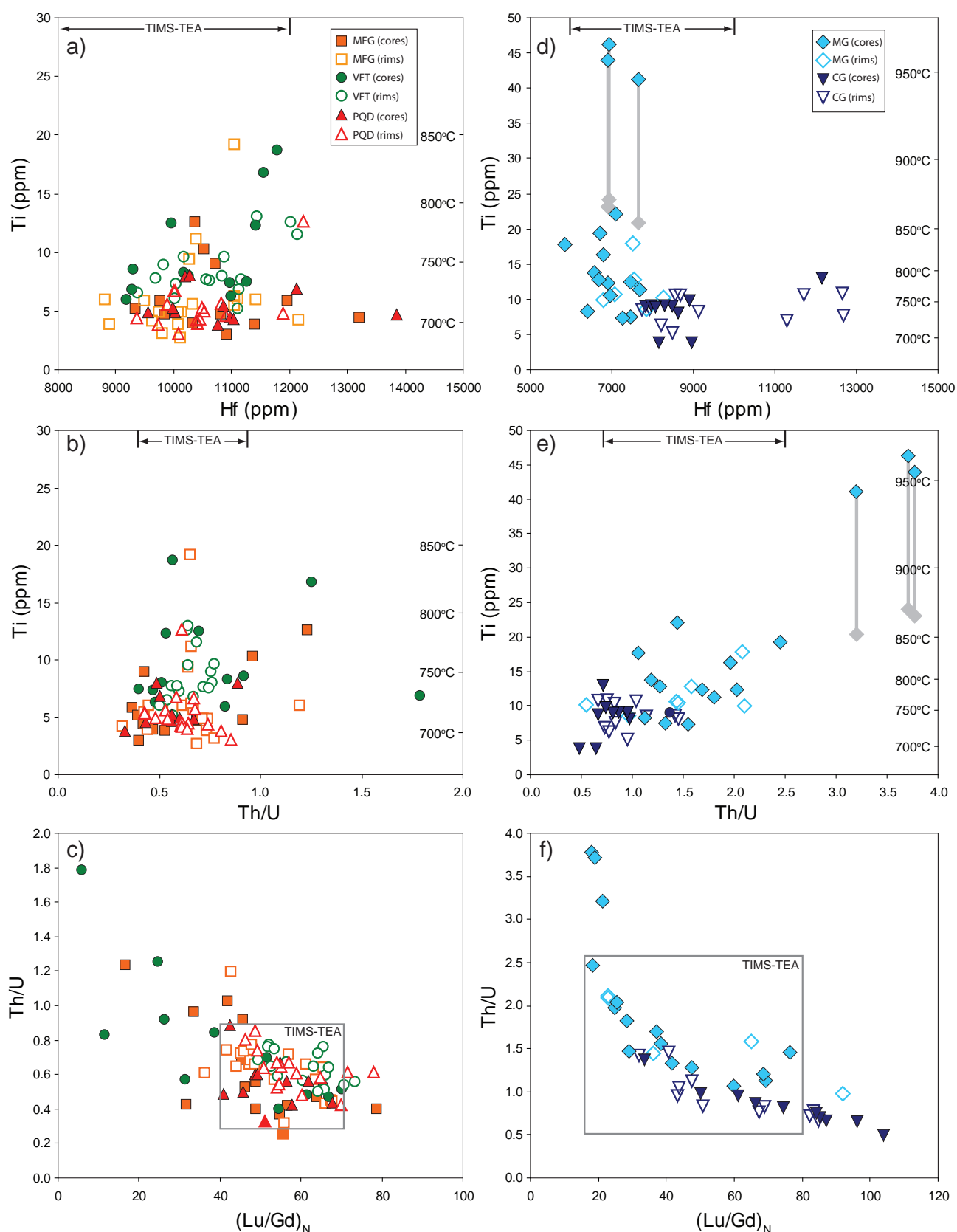


Figure 6: LA-ICP-MS trace element data for cores and rims of zircon crystals from the same population of zircon as used for CA-ID-TIMS dating. The corresponding range of TIMS-TEA results are indicated for comparison. The effect of applying a silica activity of 0.5 to three of the MG cores, shown in gray in Fig. 6d-e, in comparison to using a silica activity of 1, reduces the calculated Ti-in-zircon temperatures by ~85°C. (See text for discussion)

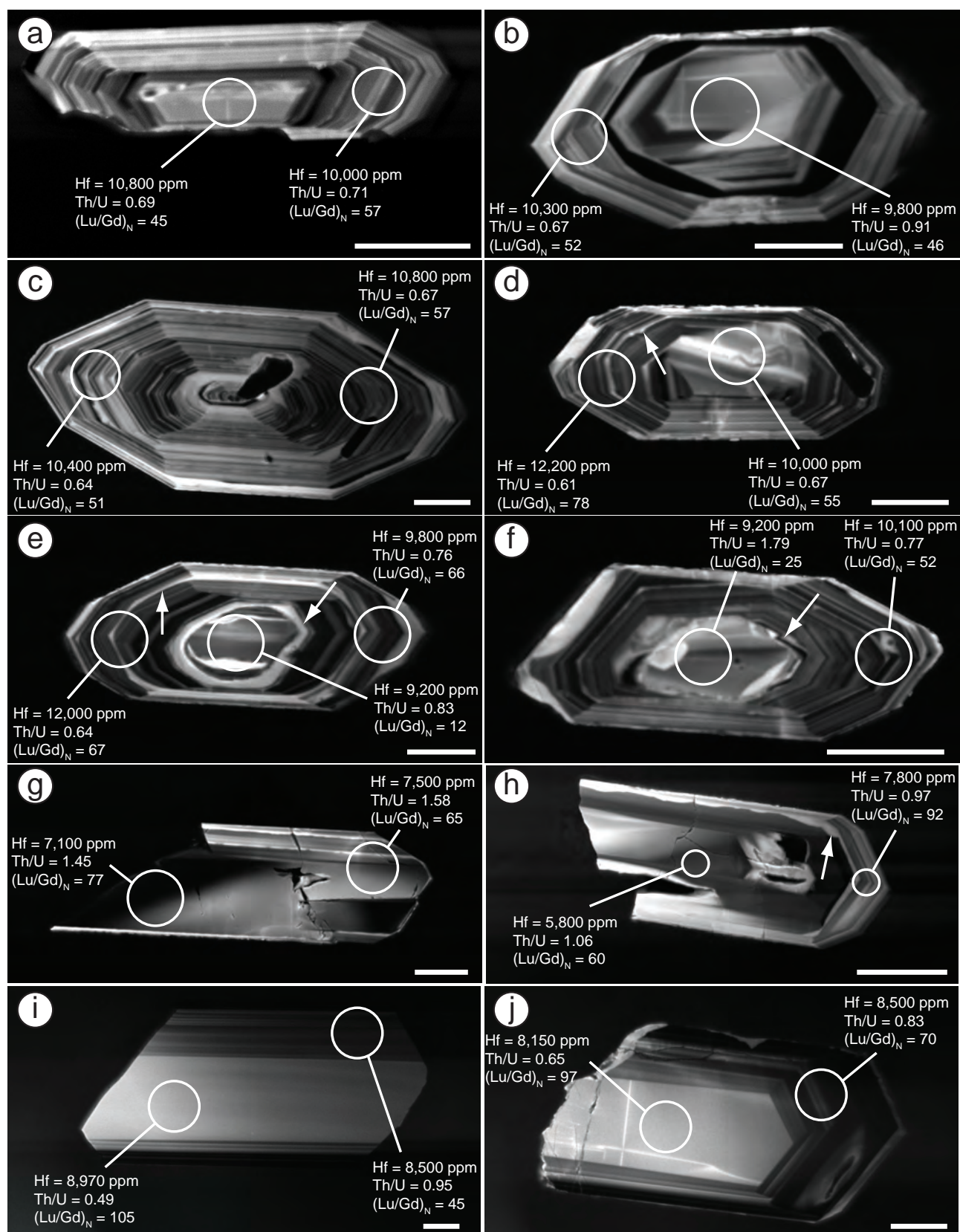


Figure 7: Cathodoluminescence images of zircon showing locations of trace element analysis spots and corresponding trace element data. a) MFG type 1 zircon; b) MFG type 2 zircon; c) PQD type 1 zircon; d) PQD type 2 zircon; e) VFT type 1 zircon; f) VFT type 2 zircon; g) MG type 1 zircon; h) MG type 2 zircon; i) CG type 1 zircon; j) CG type 2 zircon. Arrows point to periods of resorption. (See text for discussion)

the MFG zircons, type 2 is the most abundant. The dark zone that occurs around the sometimes resorbed cores is variable in thickness between zircons (~1 - 20 μ m) and could not be analyzed specifically. As demonstrated above, the MFG zircons have chondrite normalized REE patterns are variable between zircons and within individual grains. MFG zircons show trends that record both increasing and decreasing REEs from core to rim and equivalent REEs between cores and rims. There is no correlation between zoning patterns and observed REE concentration differences.

CL images of PQD zircons (Figs. 7c-d and A4) reveal two zoning patterns; (1) continuous oscillatory zoning with no distinct cores (e.g. Fig. 7c), (2) resorbed cores, occasionally multiple cores are observed, followed by typical magmatic oscillatory zoning (e.g. Fig. 7d). Type 2 is the most common in the PQD sample, with the oscillatory zoning being mostly continuous, but occasionally truncated oscillatory zoning is observed. PQD chondrite normalized zircon REE patterns show both stable and decreasing REEs from core to rim, uncorrelated to zoning types.

CL images of VFT zircons (Figs. 7e-f and A5) reveal that all zircons contain one or more cores and all zircons end with a marginal, light zone. VFT zircons also indicate two distinct zoning patterns; (1) resorbed cores that are associated

with a surrounding dark zone followed by continuous oscillatory zoning (e.g. Fig. 7e) and, (2) resorbed cores with truncated oscillatory zoning (e.g. Fig. 7f), type 1 being the most abundant in the VFT sample. VFT chondrite normalized zircon REE patterns show both trends, a decrease in REEs from core to rim and equivalent REEs between core and rim, unrelated to the type of zoning.

CL images reveal that zircons record complex histories of multiple periods of growth and dissolution (Fig. 7) within individual felsic magmas over similar 100 ka timescales, however among MFG zircons no periods of resorption are observed whereas VFT zircons record multiple periods of resorption (e.g. Fig. 7e). Despite the observed differences in CL textures, based on trace element concentrations and ratios in zircon only minor variations are observed between the felsic units (Fig. 6a-c). While the felsic units can not be discriminated on the basis of zircon chemistry, individual samples zircons record inter-grain variations pointing to changes in both composition (e.g. (Lu/Gd)_N, Th/U) and temperature (e.g. Ti) during zircon crystallization (Fig. 6a-b). However, these fluctuations do not record monotonic trends between cores and rims typical for crystallization within a cooling magma. Rather, the large and non-systematic scatter in the trace element concentrations points to zircon crystallization from contrasting

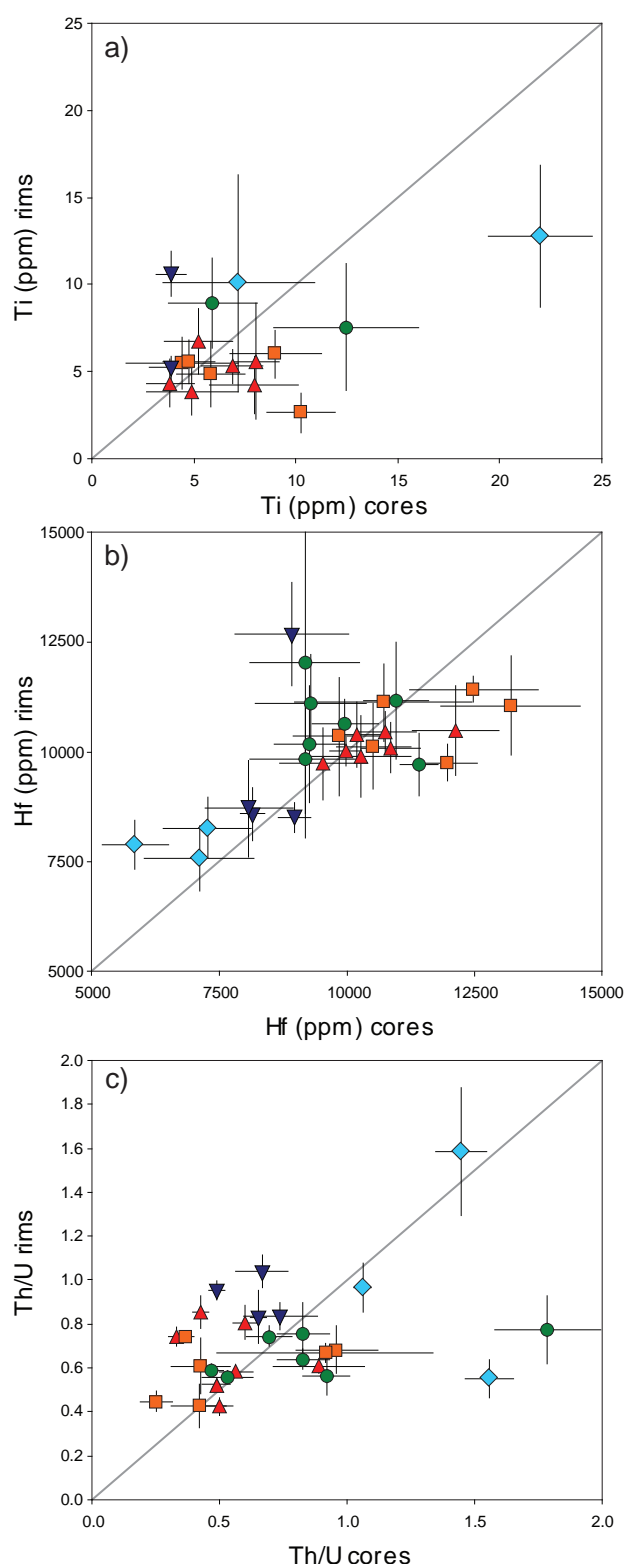


Figure 8: LA-ICP-MS trace element data for core-rim pairs. a) Ti ppm concentrations between core-rim pairs; b) Hf ppm concentrations between core-rim pairs; c) Th/U ratios ppm concentrations between core-rim pairs. Symbols are the same as in Figure 5.

(different?) magmatic environments (batches) within individual felsic units. In zircon grains

where both cores and rims were analyzed, zircons record intra-grain variability in temperature (e.g. Ti; Fig. 8a) and in composition (e.g. Hf, Th/U; Fig. 8b-c). However, the zircon cores, in general, record larger trace element variations whereas the rims appear to be more restricted in their compositions and their Ti temperatures (Fig. 8), suggesting that zircon cores crystallized from more chemically distinct magma batches prior to being “assembled” followed by rim crystallization from more compositionally similar magmas.

Among the mafic samples, CL images of MG zircons (Figs. 7g-h and A6) reveals two distinct zoning patterns; (1) simple, broad zoning (e.g. Fig. 7g) and (2) dark, slightly resorbed cores followed by oscillatory zoned rims which end with a light marginal zone (e.g. Fig. A6). Type 2 is the most abundant in the MG sample. MG chondrite normalized REE patterns for type 1 zircons indicate equivalent REEs between zones. While many oscillatory zoned rims were too small to be analyzed with the laser, type 2 zircons have REE patterns that suggest an overall decrease in REEs from core to rim.

CL images of CG zircons (Figs. 7i-j and A7) reveals two distinct zoning patterns; (1) simple, broad zoning (e.g. Fig. 7i) and (2) light central portion with oscillatory zoned rims (e.g. Fig. 7j). Only one zircon from type 1 was large enough for multiple analyses, which yielded equivalent

REEs between zones. Type 2 zircons are most abundant in the CG sample and indicate an increase in REEs from core to rim.

In conclusion, CL images reveal that the gabbro zircons record less complex growth histories as observed by the simple, board zoning, but contain multiple growth periods (Fig. 7g-j) with little evidence for dissolution. Trace element concentrations in MG zircons record, in general, higher Ti and Th/U contents and lower Hf and $(\text{Lu/Gd})_N$ contents in comparison to the CG zircons, thus making them chemically distinct. Three MG zircon cores record extreme Th/U ratios, $\sim 3.0 - 3.5$, corresponding to lower Hf concentrations (~ 7000 ppm) and low $(\text{Lu/Gd})_N \sim 20$ (Fig.6). Inter-grain variations, within individual gabbros, point to similar trace element evolutions that overall record fractionation (e.g. increasing Hf; Claiborne et al., 2010) within a cooling magma (e.g. Ti-in-zircon temperatures), although overlapping concentrations are recorded between cores and rims (Fig. 6d-f), pointing zircon crystallization experiencing fluctuating conditions within fractionating magmas. In zircon grains where both cores and rims were analyzed, gabbro zircons record non-systematic intra-grain variability (Fig. 8a-c) suggesting that zircons are recording fluctuating conditions during crystallization.

Ti-in-zircon thermometry

The application of the Ti-in-zircon thermometer (Watson and Harrison, 2005; Watson et al., 2006; Ferry and Watson, 2007) has been shown to be a valuable tool in constraining the temperatures at which zircon crystallize in evolving magmas (Fu et al., 2008; Grimes et al., 2009; Claiborne et al., 2010; Reid et al., 2010; Ickert et al., 2010). The thermometer, which is based on the incorporation of Ti into zircon as a function of temperature, requires the knowledge of both SiO_2 and TiO_2 activities in the melt in order to apply the thermometer accurately. Quartz is abundant in the VFC felsic samples, and is occasionally present as inclusions in zircon. In the VFC gabbros, zircons in thin section are mainly included in quartz and plagioclase, and occasionally contain quartz inclusions. The silica activity is therefore considered to be equal to 1 for all VFC samples, with the exception of three cores analyzed from the Mattoni gabbro (CB04 z04_1, CB04 z18_1 and CB04 z19_1). These three cores are considered to have crystallized from more primitive melts (e.g. enriched in Ti, Th/U and depleted in $(\text{Lu/Gd})_N$), prior to silica saturation, therefore an estimated silica activity of 0.5 is applied to these three MG cores (Table 4). Using a silica activity of 0.5 instead of 1 will change the calculated temperatures by -85°C at $\sim 900^\circ\text{C}$ (Fig. 6d-e). Rutile is not present in any of the VFC samples; therefore the titanium

activity is less than unity (< 1). Hayden and Watson (2007) have demonstrated that most magmas have a titanium activity between 0.5 and 0.9. The presence of Ti-rich minerals such as titanite and ilmenite, in all VFC samples, suggests a rather high titanium activity, therefore an estimated titanium activity of 0.7 is applied

to all samples. Using a titanium activity of 0.5 or 0.9, instead of 0.7, will change the calculated temperatures by $+33^{\circ}\text{C}/-25^{\circ}\text{C}$ at 750°C .

All Ti-in-zircon temperatures calculated according to Ferry and Watson (2007) using $a_{\text{TiO}_2} = 0.7$ and $a_{\text{SiO}_2} = 1$ yield variable temperatures (Table 4) with no clear correlations between

Table 5:
Solution MC-ICPMS Lu-Hf isotope data of U-Pb dated zircons from the Val Fredda Complex

	$^{176}\text{Yb}/^{177}\text{Hf}$	$\pm 2\sigma$	$^{176}\text{Lu}/^{177}\text{Hf}$	$\pm 2\sigma$	$^{178}\text{Hf}/^{177}\text{Hf}$	$^{180}\text{Hf}/^{177}\text{Hf}$	$\text{Sig}_{\text{Hf}}(\text{V})$	$^{176}\text{Hf}/^{177}\text{Hf}$	$\pm 2\sigma$	$^{176}\text{Hf}/^{177}\text{Hf}_{(t)}$	$\epsilon_{\text{Hf}}(t)$	$\pm 2\sigma$	$T_{\text{NC}}(\text{Ga})$
Marginal Facies granodiorite													
MFG-z1	0.0677	54	0.00238	14	1.46716	1.88669	33	0.282861	9	0.282859	3.56	0.32	0.75
MFG-z2	0.0618	50	0.00252	15	1.46715	1.88665	26	0.282836	10	0.282834	2.66	0.35	0.80
MFG-z3	0.0651	52	0.00240	14	1.46714	1.88671	14	0.282917	15	0.282915	5.52	0.54	0.64
MFG-z4	0.0727	58	0.00261	16	1.46716	1.88663	21	0.282920	16	0.282918	5.62	0.56	0.64
MFG-z5	0.0695	56	0.00224	13	1.46715	1.88663	75	0.282928	9	0.282926	5.91	0.31	0.62
MFG-z6	0.0664	53	0.00267	16	1.46713	1.88664	55	0.282851	9	0.282849	3.19	0.32	0.77
MFG-z7	0.0476	38	0.00177	11	1.46716	1.88666	21	0.282966	14	0.282965	7.28	0.49	0.54
MFG-z8	0.0647	52	0.00263	16	1.46715	1.88662	11	0.282831	16	0.282829	2.50	0.56	0.81
MFG-z9	0.0502	40	0.00187	11	1.46718	1.88669	6	0.282906	13	0.282906	5.15	0.46	0.45
MFG-z10	0.0528	42	0.00189	11	1.46718	1.88671	11	0.282897	10	0.282896	4.85	0.34	0.46
MFG-z11	0.0599	48	0.00208	12	1.46719	1.88675	9	0.282855	8	0.282854	3.36	0.32	0.55
MFG-z12	0.0676	54	0.00214	13	1.46719	1.88667	14	0.282986	7	0.282984	7.98	0.28	0.29
MFG-z13	0.0643	51	0.00209	13	1.46719	1.88672	19	0.282901	7	0.282899	4.98	0.26	0.46
MFG-z14	0.0392	31	0.00157	9	1.46721	1.88680	8	0.282874	9	0.282873	4.04	0.33	0.51
Mattoni gabbro													
MG-z1	0.0466	37	0.00169	10	1.46715	1.88661	89	0.283090	8	0.283089	11.67	0.28	0.30
MG-z2	0.0514	41	0.00193	12	1.46715	1.88665	40	0.283091	8	0.283090	11.71	0.29	0.30
MG-z3	0.0660	53	0.00229	14	1.46716	1.88662	98	0.283094	8	0.283093	11.81	0.30	0.29
MG-z4	0.0644	52	0.00220	13	1.46715	1.88667	58	0.283090	9	0.283089	11.67	0.31	0.30
MG-z5	0.0703	56	0.00239	14	1.46714	1.88663	81	0.283113	8	0.283111	12.46	0.28	0.26
MG-z6	0.0509	41	0.00193	12	1.46719	1.88672	27	0.283071	7	0.283069	10.99	0.25	0.12
MG-z7	0.0783	63	0.00271	16	1.46720	1.88674	56	0.283113	6	0.283111	12.47	0.21	0.04
MG-z8	0.0640	51	0.00213	13	1.46721	1.88673	30	0.283080	7	0.283079	11.31	0.25	0.10
MG-z9	0.1150	92	0.00341	20	1.46719	1.88669	47	0.283088	6	0.283086	11.57	0.22	0.09
MG-z10	0.0649	52	0.00241	14	1.46718	1.88673	9	0.283092	9	0.283090	11.71	0.33	0.08
Cadino gabbro													
CG-z1	0.0540	43.2	0.00198	12	1.4671326	1.88661	96	0.2830895	8	0.283088	11.65	0.29	0.302
CG-z2	0.0398	31.9	0.00149	9	1.4671404	1.88658	150	0.2830065	9	0.283005	8.72	0.31	0.464
CG-z3	0.0582	46.6	0.00227	14	1.4671326	1.88666	78	0.2830101	9	0.283008	8.83	0.32	0.459
CG-z4	0.0789	63.2	0.00301	18	1.4671461	1.88664	78	0.2830168	8	0.283014	9.05	0.29	0.447
CG-z5	0.0614	49.2	0.00218	13	1.4671381	1.88656	156	0.2830116	8	0.283010	8.88	0.29	0.456
CG-z6	0.0439	35.1	0.00158	9	1.4671372	1.88658	77	0.2830134	9	0.283012	8.97	0.31	0.451
CG-z7	0.0553	44.3	0.00200	12	1.4671371	1.88658	81	0.2830139	8	0.283012	8.97	0.29	0.451
CG-z8	0.0605	48.4	0.00213	13	1.4671321	1.8866	86	0.2830107	8	0.283009	8.85	0.28	0.457
CG-z9	0.0725	58	0.00257	15	1.467124	1.88661	54	0.2830184	9	0.283016	9.12	0.31	0.443
Val Fredda tonalite													
VFT-z1	0.0774	62	0.00295	18	1.4671441	1.88660	6	0.282915	23	0.282913	5.45	0.81	0.645
VFT-z2	0.0538	43	0.00191	11	1.4671407	1.88668	46	0.282941	8	0.282939	6.39	0.3	0.593
VFT-z3	0.0490	39	0.00176	11	1.46712	1.88669	15	0.282822	13	0.282821	2.20	0.47	0.825
VFT-z4	0.0711	57	0.00232	14	1.4671322	1.88665	49	0.282991	9	0.282989	8.15	0.31	0.496
VFT-z5	0.0491	39	0.00187	11	1.4671408	1.88663	25	0.282934	13	0.282933	6.16	0.45	0.606
VFT-z6	0.0548	44	0.00180	11	1.46714	1.88664	34	0.282870	9	0.282869	3.90	0.32	0.73
VFT-z7	0.0570	46	0.00212	13	1.46714	1.88660	25	0.282934	13	0.282933	6.16	0.47	0.61
VFT-z8	0.0406	32	0.00123	7	1.46720	1.88675	136	0.282900	5	0.282899	4.97	0.19	0.46
VFT-z9	0.0335	27	0.00117	7	1.46718	1.88672	42	0.282960	6	0.282960	7.11	0.21	0.34
VFT-z10	0.0553	44	0.00182	11	1.46719	1.88674	38	0.282887	7	0.282886	4.50	0.23	0.48
VFT-z11	0.0402	32	0.00140	8	1.46720	1.88673	60	0.282925	5	0.282924	5.84	0.19	0.41

Table 5:
continued

	$^{176}\text{Yb}/^{177}\text{Hf}$	$\pm 2\sigma$	$^{176}\text{Lu}/^{177}\text{Hf}$	$\pm 2\sigma$	$^{178}\text{Hf}/^{177}\text{Hf}$	$^{180}\text{Hf}/^{177}\text{Hf}$	$\text{Sig}_{\text{Hf}}(\text{V})$	b^{b}	$^{176}\text{Hf}/^{177}\text{Hf}$	$\pm 2\sigma$	$^{176}\text{Hf}/^{177}\text{Hf}_{(t)}$	$\epsilon_{\text{Hf}}(t)$	$\pm 2\sigma^{\text{c}}$	$T_{\text{NC}}(\text{Ga})^{\text{e}}$
Plagioclase quartz-diorite														
PQD-z1	0.0714	57	0.00287	17	1.46713	1.88663	17		0.282930	16	0.282928	5.97	0.6	0.62
PQD-z2	0.0512	41	0.00213	13	1.46715	1.88674	6		0.282951	18	0.282950	6.76	0.6	0.57
PQD-z3	0.0475	38	0.00182	11	1.46724	1.88679	3		0.282933	15	0.282932	6.12	0.53	0.39
PQD-z4	0.0559	45	0.00203	12	1.46719	1.88672	35		0.282918	7	0.282917	5.59	0.23	0.42
PQD-z5	0.0470	38	0.00181	11	1.46722	1.88671	5		0.282923	14	0.282921	5.76	0.51	0.41
PQD-z6	0.0610	49	0.00205	12	1.46720	1.88674	30		0.282867	6	0.282866	3.78	0.22	0.52
PQD-z7	0.0490	39	0.00192	12	1.46721	1.88668	4		0.282923	16	0.282921	5.75	0.55	0.41
PQD-z8	0.0556	44	0.00179	11	1.46719	1.88674	54		0.282954	6	0.282953	6.88	0.20	0.35
Pegamite														
Peg-z1	0.0799	64	0.00317	19	1.46717	1.88664	26		0.283031	6	0.283028	9.53	0.23	0.20
Peg-z2	0.0563	45	0.00204	12	1.46718	1.88674	35		0.283018	7	0.283017	9.12	0.24	0.23
Peg-z3	0.0767	61	0.00244	15	1.46719	1.88692	120		0.283008	6	0.283006	8.76	0.20	0.25
Peg-z4	0.0770	62	0.00250	15	1.46718	1.88683	85		0.283027	5	0.283025	9.43	0.19	0.21
Peg-z5	0.0622	50	0.00268	16	1.46715	1.88671	12		0.283040	9	0.283038	9.87	0.33	0.18
Peg-z6	0.0492	39	0.00183	11	1.46716	1.88681	18		0.283031	7	0.283030	9.59	0.24	0.20
Peg-z7	0.0600	48	0.00205	12	1.46719	1.88680	44		0.283032	6	0.283031	9.63	0.20	0.20
Peg-z8	0.0556	44	0.00215	13	1.46719	1.88671	12		0.283039	8	0.283038	9.87	0.29	0.18

Quoted uncertainties (absolute) relate to the last quoted figure. Accuracy and reproducibility was checked by repeated analyses ($n = 21$) of 10 ppb solutions of JMC475.

(a) $^{176}\text{Yb}/^{177}\text{Hf} = (^{176}\text{Yb}/^{173}\text{Yb})_{\text{true}} \times (^{173}\text{Yb}/^{177}\text{Hf})_{\text{meas}} \times (M^{173}(\text{Yb})/M^{177}(\text{Hf}))b(\text{Hf})$, $b(\text{Hf}) = \ln(^{179}\text{Hf}/^{177}\text{Hf}_{\text{true}} / ^{179}\text{Hf}/^{177}\text{Hf}_{\text{measured}}) / \ln(M^{179}(\text{Hf})/M^{177}(\text{Hf}))$, M = mass of respective isotope. The $^{176}\text{Lu}/^{177}\text{Hf}$ were calculated in a similar way by using the $^{175}\text{Lu}/^{177}\text{Hf}$ and $b(\text{Yb})$.

(b) Mean Hf signal in volt.

(c) Uncertainties are quadratic additions of the within-run precision and the daily reproducibility of the 10ppb-JMC475 solution. Uncertainties for the JMC475 quoted at 2SD (2 standard deviation).

(d) Initial $^{176}\text{Hf}/^{177}\text{Hf}$ and ϵ_{Hf} calculated using the apparent U-Pb age determined by ID-TIMS, and the CHUR parameters: $^{176}\text{Lu}/^{177}\text{Hf} = 0.0336$, and $^{176}\text{Hf}/^{177}\text{Hf} = 0.282785$ (Bouvier et al., 2008).

(e) two stage model age in billion years using the measured $^{176}\text{Lu}/^{177}\text{Lu}$ of each spot (first stage = age of zircon), a value of 0.0113 for the average continental crust (second stage), and a juvenile crust (NC) $^{176}\text{Lu}/^{177}\text{Lu}$ and $^{176}\text{Hf}/^{177}\text{Hf}$ of 0.0384 and 0.2

cores and rims (Fig. 6 b, e). Measured Ti concentrations in zircon are higher in zircons from the gabbro samples (~7 – 45 ppm) in comparison with zircons from the felsic samples (~4 – 12 ppm), translating to higher Ti-in-zircon temperatures for the zircons from the gabbros (750°C - 900°C and 700°C - 800°C, respectively). The Ti concentrations and calculated temperatures, for the zircons from the gabbro samples, decrease with increasing Hf concentrations and decreasing Th/U ratios (Fig. 6 d, e). The MG cores show larger variations in Ti

concentrations compared to the rims (7 – 45 ppm and 8 – 18 ppm, respectively), whereas no clear distinctions in Ti concentrations can be made between CG cores and rims (8 – 13 ppm and 6 – 11 ppm, respectively). The Ti concentrations and calculated temperatures, for the zircons from the felsic samples, show no correlations with other trace elements (Fig. 6 a, b). The MFG and PQD zircons, both cores and rims, show little variability in their Ti concentrations, 3 -12 ppm in the cores and 3 -19 ppm in the rims, which translates to average temperatures of $730 \pm$

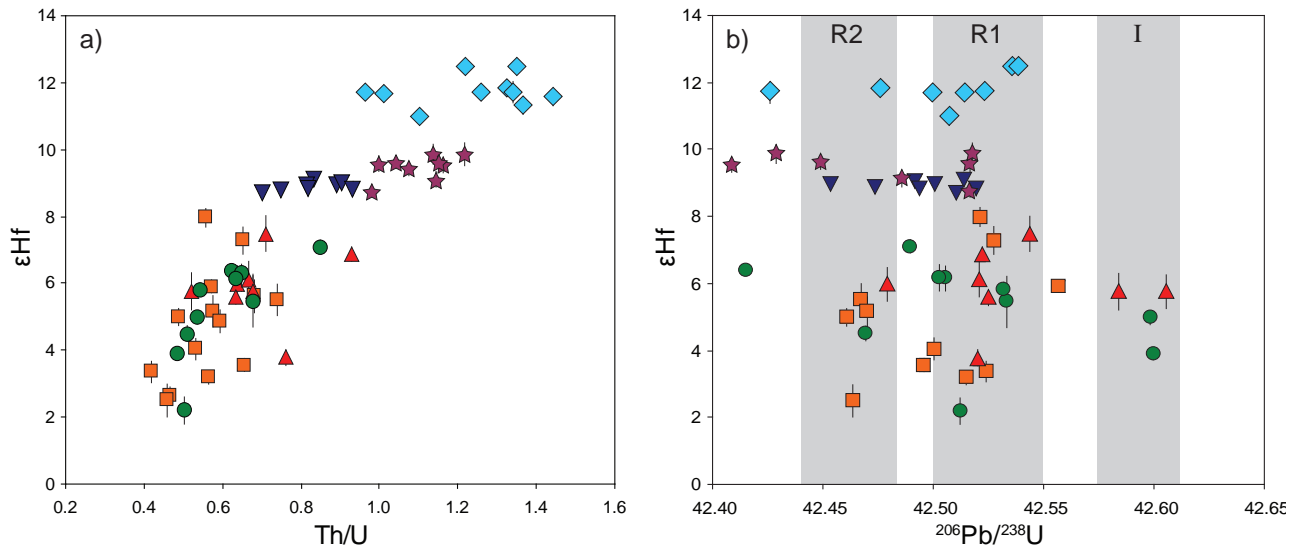


Figure 9: a) Hf isotopic compositions and Th/U ratios from the same volume of zircon; b) zircon Hf isotopic compositions indicating increased mixing between felsic magmas with the Cadino gabbro through time. I = initial felsic intrusions; R1, R2 = periods of rejuvenation of felsic crystal mushes. Symbols are the same as in Figure 5.

50°C (cores) and $745 \pm 55^\circ\text{C}$ (rims), suggesting that they mainly crystallized at or below 750°C . The VFT zircon cores are slightly more variable in Ti concentrations, and both cores and rims record slightly higher average temperatures, $775 \pm 40^\circ\text{C}$ (cores) and $760 \pm 30^\circ\text{C}$ (rims), in comparison to the other felsic units.

A zircon saturation temperature of $\sim 730^\circ\text{C}$ was estimated for the MFG sample using the experimental calibration of Watson and Harrison (1983) ($M = (2\text{Ca} + \text{K} + \text{Na})/(\text{Al} * \text{Si}) = 1.72$). This temperature is consistent with the majority of our Ti-in-zircon temperatures for the MFG sample, indicating that zircon saturation and crystallization occurred at low temperatures close to the solidus ($\sim 680^\circ\text{C} - 700^\circ\text{C}$; Piwinski, 1968). The other VFC units (PQD, VFT, MG, CG) have whole rock compositions that fall outside of the calibration range ($M > 1.9$),

therefore zircon saturation temperatures for these units could not be estimated from whole rock compositions. However, using the methods described by Verberne (2013), which calculates zircon saturation temperatures from modeled residual melt compositions rather than whole rock compositions, yields zircon saturation temperatures of $\sim 830^\circ\text{C}$ to 850°C for the MFG, compared to the $\sim 730^\circ\text{C}$ calculated on the basis of whole rock compositions; $\sim 850^\circ\text{C}$ to 870°C for the VFT; and $\sim 850^\circ\text{C}$ to 900°C for the PQD. This indicates that zircon has the potential to saturate early in the felsic magmas and explains the higher temperatures ($>800^\circ\text{C}$) obtained from Ti-in-zircon geothermometry (Fig. 6a-b). While we acknowledge that our Ti-in-zircon temperatures indicate low temperature crystallization, the calculated temperatures are consistent with independent temperature

estimates from amphibole-plagioclase pairs for the VFC felsic units (MFG: 695°C - 800°C; PQD: 670°C - 800°C; VFT: 730°C - 865°C; Stauffacher, 2012).

2.4.4 Hf isotopes of zircon

Hf isotope compositions in zircon were obtained from the same volume of zircon used for trace element analysis and U-Pb age determinations. The isotopic data, including ϵ_{Hf} values and Lu-Hf depleted mantle model ages (T_{DM}) are presented in Table 5. Zircon grains from the VFC show considerable variation in Hf isotopic composition, ϵ_{Hf} varies from +2.2 to +12.5, indicating the existence of at least two source components involved in the generation of the VFC magmas. Zircons from the felsic units (MFG, PQD, VFT) have initial Hf isotopic composition that range between ϵ_{Hf} values of +2.2 to +8 (Fig. 9a). The mafic zircons from the VFC show less variation in their initial Hf isotopic compositions in comparison with the felsic units: The ϵ_{Hf} values of MG zircons scatter between +11 to +12.5, distinct from the values obtained for CG zircons between +8.7 to +9. The ϵ_{Hf} values of Peg zircons are intermediate between +9 to +10, which is not in line with an explanation as a residual liquid from either of the gabbros. Zircons from the mafic units indicate more juvenile sources making them clearly distinguishable from the felsic zircons.

2.5 Discussion

2.5.1 Interpretation of zircon ages

The U-Pb data presented above indicate that zircons crystallized over 100 – 180 ka in felsic magmas and over 90 – 110 ka in mafic magmas. The scatter in our U-Pb zircon dates may reflect one or several of the following processes: 1) youngest zircons may have been affected by post crystallization lead loss, 2) zircon dates may be biased by the incorporation of xenocrystic cores or 3) the scatter in U-Pb dates reflects protracted zircon growth or mixing of episodic growth zones within zircons of the VFC magmas. We are confident that we have removed the zircon domains affected by post crystallization loss of radiogenic lead by applying the chemical abrasion techniques of Mattinson (2005). Inter-calibration of CA-ID-TIMS data of the Geneva laboratory with independent age constraints such as Ar-Ar dates and astronomical age solutions provides evidence that very likely no residual lead loss is left after chemical abrasion (Wotzlaw et al., 2013 and in prep.) which yield equivalent clusters. Additional evidence comes from inter-laboratory reproducibility using same analytical approaches at two different sites (Kennedy et al. in prep.) and overlapping U-Pb dates of titanite and the youngest zircons are an argument in favor of excluding Pb loss as the source of scatter in our zircon dates.

CL images confirm the presence of resorbed and

truncated cores overgrown by euhedral rims (Figs. 7 and A3-A7). Overlapping trace element concentrations from our core-rim analyses (Fig. 6) argues against xenocrystic cores contributing to the scatter in U-Pb dates. Therefore, the observed cores are assumed to represent earlier crystal growth (antecrysts after Miller et al., 2007) that were subsequently resorbed and overgrown within the last batch of magma they resided in. Based on the arguments outlined above, we consider that the scatter in our U-Pb zircon dates is recording prolonged zircon growth during multiple periods of enhanced zircon crystallization, as indicated by multiple peaks in probability density distribution curves (Fig. 3), within single zircon populations on 100 – 200 ka timescales. We consider that the peaks indicate periods of enhanced zircon crystallization associated with crystallization within a cooling magma, whereas the curve minima are the result of new magma injections, which caused thermal fluctuations due to the transfer of heat and volatiles (Bachmann and Bergantz, 2003, 2006; Huber et al., 2011; Pistone et al., 2013), leading to reduced zircon crystallization and possible zircon resorption. Cycles of zircon crystallization indicate that magmas fluctuated between periods of zircon saturation and undersaturation, where periods of enhanced zircon crystallization are strongly correlated among felsic units and among mafic

units (Fig. 3), indicating that zircons from the different VFC units are recording a common thermal evolution. We exclude from the following discussion the zircon dates identified as antecrysts (MFG z3, z9; MG z8, z9; PEG z4, z6; see Table 1, Fig. 2), because they are considered to have no connection to the thermal evolution of the magmas in the growing VFC pluton.

The oldest zircons of the felsic samples, excluding the MFG antecrysts, represent the initial intrusions and emplacement of the felsic magmas, referred to as I (Fig. 3a ,5) followed by subsequent cooling and in situ crystallization corresponding to the peak from 42.62 to 42.58 Ma (Fig. 3). All VFC units exhibit pronounced zircon crystallization from 42.54 Ma to 42.50 Ma for felsic samples, termed R1 in Fig. 3a, and 42.54 Ma to 42.48 Ma for mafic units, termed C1 in Fig. 3b, which accounts for ~60% of the entire volume of zircon crystallized in the VFC. We argue that coinciding prominent crystallization peaks, corresponding to the oldest zircons within the mafic units with the dominant period of enhanced zircon crystallization within the felsic units, provides evidence for the rejuvenation of the felsic crystal mushes as the result of thermal fluctuations due to the repeated mafic sill injections. Following the onset of mafic sill injections, the transfer of heat and volatiles from the cooling mafic sheets, referred to as C1

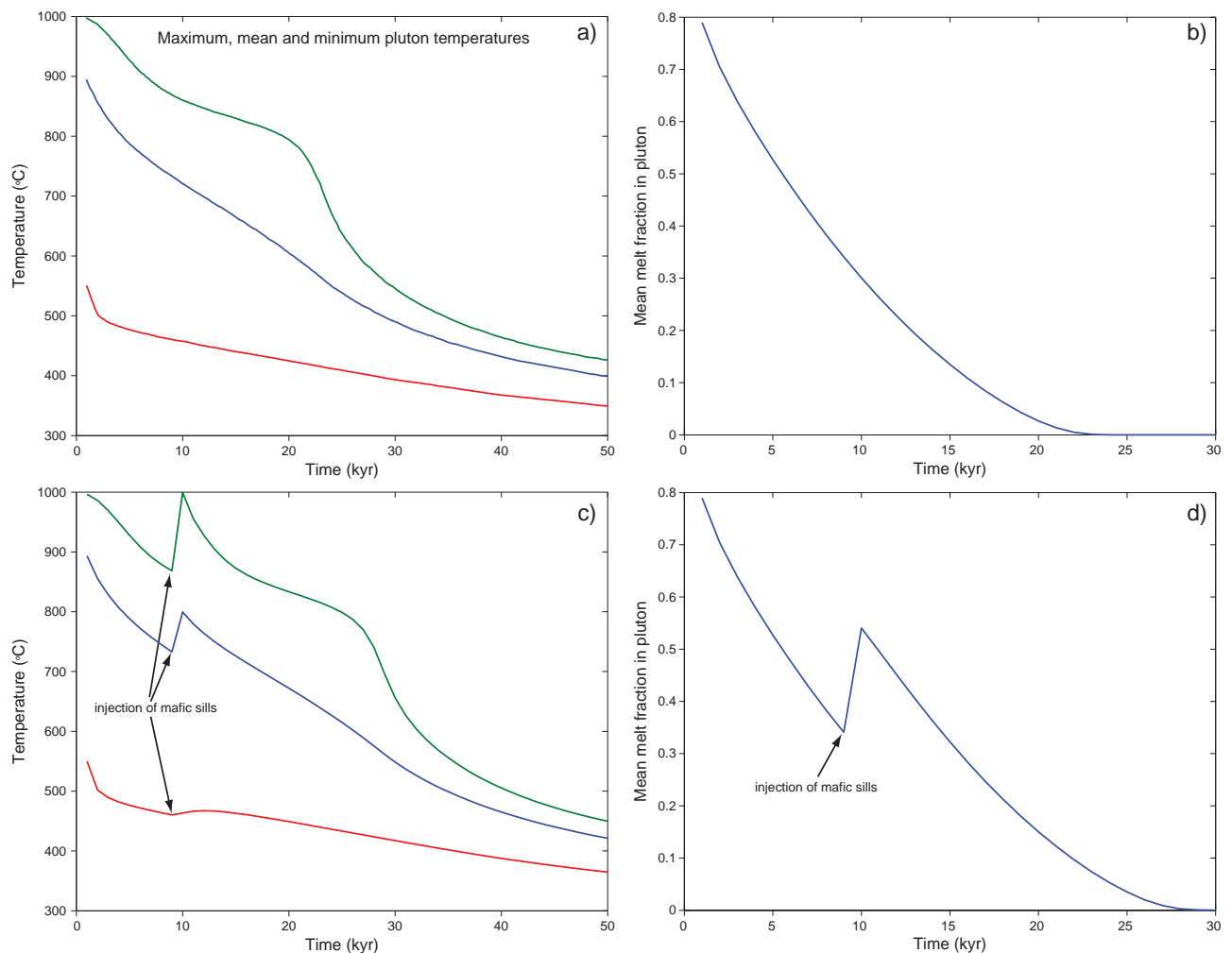


Figure 10: Maximum, mean and minimum pluton temperature results and mean melt fraction as a function of time, obtained from thermal modeling: a) a single pulse of tonalite magma reaches solidus conditions before ~25 ka; b) decrease in melt fraction as a function of time due to cooling and crystallization of the tonalite magma; c) injection of mafic sills into the host tonalite at 10 ka increases the time for the tonalite magma to reach solidus conditions, ~30 ka; d) the injection of the mafic sills melts the host tonalite and thus increases the melt fraction.

(Fig. 3,5) to the host felsic crystal mushes led to reheating and remobilization, consistent with field observations (e.g. hybridization, back-veining, etc.). During this period of thermal rejuvenation, referred to as R1 (Fig. 3,5), the felsic crystal mushes were remelted producing a decrease in crystal content (e.g. zircon dissolution and/or resorption) and then upon subsequent cooling new crystal growth would occur, as observed in CL images (Fig. 7a-f). The occurrence of repeated mafic sill injections

into the crystallizing felsic magmas resulted in repeated cycles of thermal fluctuations, referred to as R2 and C2 (Fig. 3,5), indicated by multiple, separate periods of zircon growth observed in numerous CL images (Fig. 7 and A1-A3). We suggest that these thermal cycles kept the felsic magmas above solidus conditions, in a “crystal mush state” with the proportions of crystals and melt varying throughout most of its history.

2.5.2 VFC thermal modeling

In order to constrain the time required for the VFC to reach its solidus following magma emplacement, and the effect repeated mafic sill injections have on the time required for the VFC to reach its solidus, we used 3-D thermal modeling to calculate the evolution of magma temperatures and melt fraction as a function of time.

The first thermal model, in which a single 1000°C, 2 km thick cylindrical pluton (12 km³) intrudes at 10 km depth into the host rock (geothermal gradient = 30°C/km), shows that the VFC would reach solidus conditions (~680°C; Piwinski, 1968) before ~25 ka after emplacement (Fig. 10a-b). These results indicate that the 100 – 200 ka durations recorded by our zircon U-Pb dates do not reflect crystallization from a single, cooling pulse of magma.

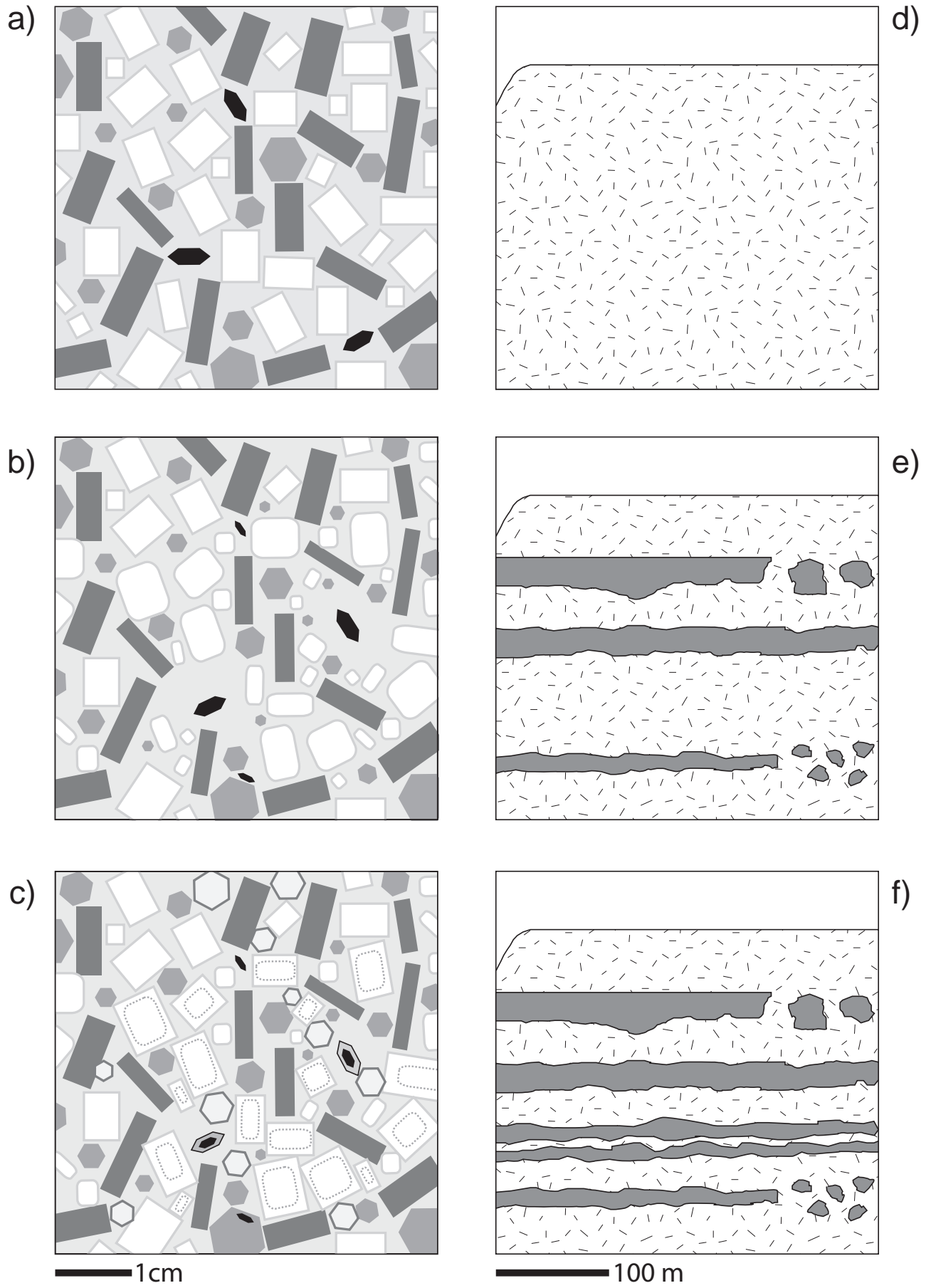
The second thermal model incorporates the injection of three 100 m thick by 1 km long mafic sills into the host tonalite. The mafic sills are vertically separated from each other by 500 m, and are injected at 1100°C into the tonalite, ~10 ka after the initial tonalite emplacement. This model suggests that the VFC would reach solidus conditions ~30 ka after emplacement (Fig. 10c-d). The results from this simple thermal model illustrate the effect of mafic sill injections on the crystallizing tonalite, which include a prolonged time to reach solidus conditions as a

Figure 11: (facing page) A conceptual model for zircon crystallization at the crystal scale and at the outcrop scale for VFC emplacement. a) initial felsic intrusions (I) record subsequent cooling and crystallization (~60 - 70% crystals); b) felsic crystal mushes during R1 become reheated causing melting and a decrease in crystal content (~ 50%) due to resorption and dissolution; c) crystal mushes further crystallized (~ 80 – 90%) upon cooling; d) initial felsic intrusions (I); e) during the onset of mafic sheet injections (C1) the mafic sheets break up into enclave swarms and the felsic units become remobilized (R1); f) continued smaller volume of mafic injections (C2). (Crystal sizes are not drawn to scale; see text for discussion)

result of heating and melting of the host tonalite (Fig. 10d) which is consistent with the resorption features observed in VFC zircons (Fig. 7). While the duration for the VFC to reach its solidus was increased to ~30 ka, we postulate based on the numerous mafic sills observed in the field (Fig. A1), that multiple mafic injections occurring at different times throughout the history of the VFC would not only further increase the time in which it takes the VFC to reach its solidus, but would also result in repeated cycles of thermal fluctuations (Fig. 10d). These results from our thermal modeling support our interpretation of our zircon U-Pb dates reflecting different periods of enhanced zircon crystallization as the result of repeated mafic sill injections (Fig. 3).

2.5.3 A conceptual model part 1: zircon crystallization

Based on its slow trace element diffusivities (Cherniak et al., 1997a; Cherniak et al., 1997b;



Cherniak and Watson, 2001) zircon has the potential to record fractional crystallization trends on the 100 ka timescales (see, e.g., Wotzlaw et al., 2013). Schoene et al. (2012) presented a detailed U-Pb dating study from the northerly adjacent Lago della Vacca complex (LVC) and demonstrated the existence of 1.5 – 5.0 km³ magma batches (John and Blundy, 1993) that cooled and crystallized coherently, evidenced by coherent trace element trends in zircon over 400 ka. In contrast, our results from the VFC reveal no coherent trace element correlations over 100 – 200 ka timescales, suggesting that the durations recorded by U-Pb zircon dates do not record the crystallization of a single cooling magma. As we have shown above, each of the VFC magmas evolved via multiple periods of injection of mafic magmas, rejuvenating the crystal mush and leading to the observed peaks of enhanced zircon crystallization (Fig. 3) and possibly resorption; even multiple resorption events, as shown in Figure 7e. Growth textures visible in CL images confirm complex histories of zircon growth and dissolution (Fig. 7). To link this information to the precisely dated periods of enhanced zircon crystallization, we need to combine the results of CL-controlled in-situ (laser ablation) and whole grain (TIMS-TEA) trace element determinations. In the following we discuss first a model of zircon crystallization in the felsic mushes, afterwards in the mafic

magmas:

Following the initial intrusions (I) the felsic magmas subsequently cooled and reached crystallinities of ~60 - 70% (Fig. 11a) (Piwinski, 1968; Blundy and Sparks, 1992). Since felsic magmas can reach zircon saturation early in their evolution, zircons crystallizing from the initial intrusions have the potential to record fractional crystallization trends. However, VFC zircons from this early period only record homogenous trace element compositions (Fig. 5). We acknowledge that the preservation of zircon from the initial intrusions is most likely fragmentary due to dissolution during periods of higher magma temperatures, thus erasing the previously established trace element trends indicative of fractional crystallization.

During the remobilization of the felsic crystal mushes (R1), existing crystals were resorbed to a variable degree, and the crystal content of the magma was decreased to ~50% in our conceptual model (Fig. 11b). The trace element analyses of whole zircon grains (Fig. 5) as well as the in-situ core-rim data (Fig. 6) do not record simple fractional crystallization trends that could be attributed to monotonic cooling.

We therefore interpret the non-systematic trace element variations in zircon to represent the chemical variability within different isolated magma batches that coexisted among the remobilized felsic crystal mush (Fig. 11b), that

formed from the remelting and rejuvenation of the initial felsic intrusions by the mafic melt injections. Additional evidence comes from ubiquitous resorbed plagioclase in the felsic magmas recording large variations in Sr isotopes ($^{87}\text{Sr}/^{86}\text{Sr}$)_i ranging from 0.704342 to 0.708856, and in Sr and Ba concentrations, which requires crystallization from different magma batches (Blundy and Shimizu, 1991; Stauffacher, 2012). Another argument in favor of the existence of multiple magma batches comes from our zircon Hf isotopic compositions that record large variations in ϵHf ranging from +2 to +8, during R1, and point to increased mixing with the Cadino gabbro through time (Fig. 9b). The variability of ϵHf in zircon crystallizing during R1 is consistent with field evidence where we observe that different magma batches have experienced different degrees of mingling and hybridization (Fig. A1).

The peaks in the probability density curves deduced from the U-Pb data indicate that thermal fluctuations continued during the period R2, postdating the major crystallization peak after initial rejuvenation of the felsic crystal mushes (R1; Fig. 3a). Evidence for continued thermal fluctuations is supported by increased Ti temperatures recorded in a small percentage (< 10%) of zircon rims (Fig. 6a-b) demonstrating that individual zircons record distinct thermal histories. We may correlate the

thermal fluctuations recorded by R2 with the waning stages of mafic injections (C2) into the felsic crystal mushes. This is supported by the Hf isotopic compositions in zircon crystallized during this stage, which drop down to ϵHf values of +4.5 to +6, indicating a decreased interaction between the mafic melts and the felsic crystal mushes (Fig. 9b). However, zircons crystallizing during R2 have trace element compositions that document similar fluctuations in compositions and temperatures as observed in R1 (Fig. 5), which is consistent with broadly overlapping core-rim trace element compositions (Fig. 6, 8). Together, this suggests that zircon crystallization during R2 occurred as a result of temperature fluctuations around zircon saturation temperatures within magma batches of variable composition that did not undergo mixing with the mafic melts. Therefore, we propose that felsic crystal mushes during R2 were less remobilized and rejuvenated by mafic magmas, due to the decreasing mafic magma flux into the felsic mushes and the resulting temperature decrease of the magmatic system (Fig. 11c).

Following the onset of repeated mafic injections, zircons crystallizing from the cooling mafic sheets during periods C1 and C2 record variable trace element compositions (Fig. 5d) but the observed scatter from whole grain zircons does not reflect fractional crystallization trends within C1 and

C2. However, our in situ core-rim data record systematic trace element variations that are consistent with fractional crystallization during cooling (Fig. 6d-f), although in situ core-rim Ti concentrations and calculated temperatures between cores and rims (Fig. 6d,e) do not correspond to monotonic cooling. Therefore, zircon crystallization in the mafic sheets occurred as a result of temperature fluctuations around zircon saturation temperatures, as evidenced by thermal fluctuations recorded in our U-Pb data (Fig. 3b). During the repeated mafic sill injections (C1 and C2) zircons record rather homogenous Hf concentrations (Fig. 5c), and homogenous Hf isotopic compositions (Fig. 9a) within individual magmas (MG, CG), indicating that during the remobilization of the felsic crystal mushes (R1) the mafic magmas evolved in a more closed system and do not record the mingling and hybridization as observed in the felsic crystal mushes.

2.5.4 A conceptual model part 2: emplacement of the VFC

On the basis of the crystallization history discussed above we postulate that the VFC was assembled incrementally by repetitive mafic sill emplacement that resulted in the repeated reheating and rejuvenation of felsic crystal mushes. Zircon grains record a complex history of dissolution and growth, as observed in CL

images (Fig. 7), from variable magma batch compositions, resulting in the poor preservation of early zircons, so-called “antecrysts”. The presence of zircon, from single hand-size samples, which record multiple age distributions, chemical and isotopic variability demonstrate that variable magma batch compositions assembled prior to solidification. Our zircon data, collected from representative samples distributed throughout the VFC (Fig. 1b), reveal that all units share a common thermal evolution (Fig. 3) and is representative for the VFC. Therefore we propose the following emplacement model for the VFC based on field relations, thermal modelling and zircon geochronology.

1) ~42.62 – 42.58 Ma (I): Initial felsic intrusions are emplaced followed by subsequent cooling and crystallization (Fig. 11d). Zircon grains associated with the initial felsic intrusions are poorly preserved during subsequent phases of heat advection by injection of mafic sills, leading to temperatures in excess of the zircon saturation temperature and resorption/dissolution of zircon grains. Based on the 2 kbar tonalite experimental data of Piwinski (1968) and rheology constraints, Blundy and Sparks (1992) estimated that the felsic crystal mushes were ~ 60 – 70% crystalline, corresponding to temperatures of 850°C to 800°C, prior to the emplacement of the mafic sheets.

2) ~42.54 – 42.48 Ma (C1): The Mattoni and

Cadino gabbros were emplaced as a series of horizontal sheets into cooling and crystallizing felsic crystal mushes (Fig. 11e). Upon emplacement, the mafic sheets were quenched to temperatures of $\sim 950^{\circ}\text{C}$ corresponding to $\sim 40\%$ crystals (Blundy and Sparks, 1992), resulting in volume contraction and the formation of crenulate and lobate sheet margins (Fig. A1). Additional evidence for quenching comes from the presence of chilled margins of some enclaves and mafic sheets. Upon cooling, the transfer of heat and hydrous volatiles was efficient enough to remelt and remobilize the felsic crystal mushes (Bachmann and Bergantz, 2003, 2006; Huber et al., 2011; Pistone et al., 2013), causing the mafic sheets to break up laterally leading to the formation of enclave swarms (Fig. 10e; A1).

3) $\sim 42.54 - 42.50$ Ma (R1): During this period of remelting and remobilization of the felsic crystal mushes (R1), the crystal content was decreased to $\sim 50\%$, corresponding to temperatures $\sim 850^{\circ}\text{C} - 900^{\circ}\text{C}$ (Piwinskii, 1968). Felsic crystal mushes containing 50% crystals are rheologically “locked-up” and prevent the existence of a convecting magma chamber and as a consequence the felsic crystal-rich mushes were never eruptible (Bachmann and Bergantz, 2006; Huber et al., 2010, 2011). Therefore we conclude that resulting felsic melts formed isolated magma batches which mingled with

the interstitial melt from the mafic sheets and enclaves (Fig. A1). Zircon grains associated with initial rejuvenation of the felsic mushes (R1) document crystallization from isolated magma batches consistent with different degrees of mingling and hybridization (Fig. 9b).

4) $\sim 42.48 - 42.40$ Ma (C2 and R2): Mafic magmas continued to be injected into the felsic crystal mushes (Fig. 11f). During this period the non-steady state decrease of smaller volumes of mafic melt no longer provide the sufficient heat required to remelt and remobilize the felsic crystal mushes resulting in a temperature decrease within the mush $\sim 750^{\circ}\text{C} - 760^{\circ}\text{C}$ ($\sim 80\% - 90\%$ crystals). However, zircon grains associated with R2 record dissolution and growth textures (Fig. 7) suggesting that the waning stages of mafic injections provided enough heat to felsic crystal mushes, resulting in temperature fluctuations around zircon saturation temperatures. Following the termination of mafic injections, the VFC felsic crystal mushes further crystallized upon cooling through solidus temperatures ($\sim 680^{\circ}\text{C} - 700^{\circ}\text{C}$; Piwinskii, 1968) between 42.48 Ma and 42.42 Ma, recorded by the youngest zircon dates and coeval titanite dates (Fig. 2). Whereas, the VFC mafic sheets cooled and crystallized more slowly through solidus temperatures ($\sim 800^{\circ}\text{C}$; Blundy and Sparks, 1992) recorded by the youngest zircon ages of 42.43 Ma and 42.41 Ma and corresponding coeval titanite ages.

2.6 Conclusions and Outlook

The high-precision dates of the VFC demonstrate the difficulty to relate zircon dates to physical processes such as the emplacement of magma, but represent repeated periods of enhanced zircon crystallization in the “crystal mush state” at temperatures closely above the solidus. Furthermore, the initial classification of zircons (e.g. autocrysts vs. antecrysts), described by Miller et al., 2007, cannot be applied to the majority of VFC zircons, indicating that the application of these terms relative to the process of physical emplacement of the magma has to be done with caution and requires additional constraints (e.g. chemical and isotopic data) to provide insights into magma evolution such as changes in crystallinity, temperature and melt composition.

The initial stages of magma emplacement in the southern tip of the Adamello batholith resulted in the VFC emplacement into the “cold” crust, based on peak metamorphic temperatures of $\sim 500^{\circ}\text{C}$ in the contact aureole (Frisch and Helgeson, 1894; Blundy, 1989), persevering compositionally distinct magma batches. The chemical composition of crystallizing zircon reflects changes of ambient conditions, such as temperature and crystallinity, from chemically distinct magma batches. Fluctuating temperatures are consistent with the rejuvenation and remobilization of felsic crystal mushes by

the repeated injection of mafic melts, preserved as the Mattoni and Cadino gabbro sills. The lack of chemical homogenization is the result of the VFC never reaching the thermally mature stage of an eruptible convecting magma chamber, thus leading to stalling of the felsic crystal mushes in the upper crust and subsequent solidification.

Detailed petrographic studies combined with texturally controlled high precision ages may help in order to better understand ID-TIMS U-Pb zircon dates. This will potentially allow us to link periods of enhanced zircon crystallization to the petrology of major mineral phases and allow for more precise interpretations of high precision U-Pb zircon data.

Acknowledgements

This study was carried out as a part of the ProDoctoral school “Adamello 4-D”, funded by the Swiss National Research Fonds and the Swiss University Conference. M. Senn, M. Ovtcharova and J. Wotzlaw contributed with technical help during this research.

References

- Annen, C., 2011, Implications of incremental emplacement of magma bodies for magma differentiation, thermal aureole dimensions and plutonism-volcanism relationships: *Tectonophysics*, v. 500, p. 3-10.
- Annen, C., Blundy, J.D., and Sparks, R.S.J., 2006, The genesis of intermediate and silicic magmas in deep crustal hot zones: *Journal of Petrology*, v. 47, p. 505-539.
- Bachmann, O., and Bergantz, G.W., 2003, Rejuvenation of the Fish Canyon magma body: A window into the evolution of large-volume silicic magma systems:

- Geology, v. 31, p. 789-792.
- Bachmann, O., and Bergantz, G.W., 2006, Gas percolation in upper-crustal silicic crystal mushes as a mechanism for upward heat advection and rejuvenation of near-solidus magma bodies: *Journal of Volcanology and Geothermal Research*, v. 149, p. 85-102.
- Bindeman, I.N., Schmitt, A.K., Valley, J.W., 2006, U-Pb zircon geochronology of silicic tuffs from the Timber Mountain/Oasis Valley caldera complex, Nevada: rapid generation of large volume magmas by shallow-level remelting: *Contributions to Mineralogy and Petrology*, v. 152, p. 649-665.
- Blackburn, T.J., Olsen, P.E., Bowring, S.A., McLean, N.M., Kent, D.V., Puffer, J., McHone, G., Rasbury, E.T., and Et-Touhami, M., 2013, Zircon U-Pb Geochronology Links the End-Triassic Extinction with the Central Atlantic Magmatic Province: *Science*, v. 340, p. 941-945.
- Blundy, J.D., and Shimizu, N., 1991, Trace element evidence for plagioclase recycling in calc-alkaline magmas: *Earth and Planetary Science Letters*, v. 102, p. 178-197.
- Blundy, J.D., and Sparks, R.S.J., 1992, Petrogenesis of mafic inclusions in granitoids of the Adamello Massif, Italy: *Journal of Petrology*, v. 33, p. 1039-1104.
- Bowring, J.F., McLean, N.M., and Bowring, S.A., 2011, Engineering cyber infrastructure for U-Pb geochronology: Tripoli and U-Pb_Redux: *Geochemistry Geophysics Geosystems*, v. 12, p. Q0AA19.
- Brack, P., 1983, Multiple intrusions-examples from the Adamello batholith (Italy) and their significance on the mechanism of intrusion: *Mem. Soc. Geol. Ital*, v. 26, p. 145-157.
- Callegari, E., and Brack, P., 2002, Geological map of the Tertiary Adamello Batholith (Northern Italy) Explanatory notes and legend: *Mem. Sci. Geol*, v. 54, p. 19-49.
- Cherniak, D.J., 1993, Lead diffusion in titanite and preliminary results on the effects of radiation damage on Pb transport: *Chemical Geology*, v. 110, p. 177-194.
- Cherniak, D.J., Hanchar, J.M., and Watson, E.B., 1997, Diffusion of tetravalent cations in zircon: *Contributions to Mineralogy and Petrology*, v. 127, p. 383-390.
- Cherniak, D.J., Hanchar, J.M., and Watson, E.B., 1997, Rare-earth diffusion in zircon: *Chemical Geology*, v. 134, p. 289-301.
- Cherniak, D.J., and Watson, E.B., 2001, Pb diffusion in zircon: *Chemical Geology*, v. 172, p. 5-24.
- Claiborne, L.L., Miller, C.F., and Wooden, J.L., 2010, Trace element composition of igneous zircon: a thermal and compositional record of the accumulation and evolution of a large silicic batholith, Spirit Mountain, Nevada: *Contributions to Mineralogy and Petrology*, v. 160, p. 511-531.
- Coleman, D.S., Gray, W., and Glazner, A.F., 2004, Rethinking the emplacement and evolution of zoned plutons: Geochronologic evidence for incremental assembly of the Tuolumne Intrusive Suite, California: *Geology*, v. 32, p. 433-436.
- Cortecci, G., Del Moro, A., Leone, G., and Pardini, G.C., 1979, Correlation between strontium and oxygen isotopic compositions of rocks from the Adamello Massif (Northern Italy): *Contributions to Mineralogy and Petrology*, v. 68, p. 421-427.
- de Saint Blanquat, M., Horsman, E., Habert, G., Morgan, S., Vanderhaeghe, O., Law, R., and Tikoff, B., 2011, Multiscale magmatic cyclicity, duration of pluton construction, and the paradoxical relationship between tectonism and plutonism in continental arcs: *Tectonophysics*, v. 500, p. 20-33.
- Del Moro, A., Pardini, G.C., Quercioli, C., Villa, I.M., and Callegari, E., 1983, Rb/Sr and K/Ar chronology of Adamello granitoids, southern Alps: *Mem. Soc. Geol. Ital*, v. 26, p. 285-299.
- Ferry, J.M., and Watson, E.B., 2007, New thermodynamic models and revised calibrations for the Ti-in-zircon and Zr-in-rutile thermometers: *Contributions to Mineralogy and Petrology*, v. 154, p. 429-437.

- Frost, B.R., Chamberlain, K.R., and Schumacher, J.C., 2001, Sphene (titanite): phase relations and role as a geochronometer: *Chemical Geology*, v. 172, p. 131-148.
- Fu, B., Page, F.Z., Cavosie, A.J., Fournelle, J., Kita, N.T., Lackey, J.S., Wilde, S.A., and Valley, J.W., 2008, Ti-in-zircon thermometry: applications and limitations: *Contributions to Mineralogy and Petrology*, v. 156, p. 197-215.
- Glazner, A.F., Bartley, J.M., Coleman, D.S., Gray, W., and Taylor, R.Z., 2004, Are plutons assembled over millions of years by amalgamation from small magma chambers?: *GSA today*, v. 14, p. 4-12.
- Grimes, C.B., John, B.E., Cheadle, M.J., Mazdab, F.K., Wooden, J.L., Swapp, S., and Schwartz, J.J., 2009, On the occurrence, trace element geochemistry, and crystallization history of zircon from in situ ocean lithosphere: *Contributions to Mineralogy and Petrology*, v. 158, p. 757-783.
- Hanchar, J.M., and Watson, E.B., 2003, Zircon saturation thermometry: Reviews in mineralogy and geochemistry, v. 53, p. 89-112.
- Hansmann, W., and Oberli, F., 1991, Zircon inheritance in an igneous rock suite from the southern Adamello batholith (Italian Alps): *Contributions to Mineralogy and Petrology*, v. 107, p. 501-518.
- Hayden, L.A., and Watson, E.B., 2007, Rutile saturation in hydrous siliceous melts and its bearing on Ti-thermometry of quartz and zircon: *Earth and Planetary Science Letters*, v. 258, p. 561-568.
- Huber, C., Bachmann, O., and Dufek, J., 2010, The limitations of melting on the reactivation of silicic mushes: *Journal of Volcanology and Geothermal Research*, v. 195, p. 97-105.
- Huber, C., Bachmann, O., and Dufek, J., 2011, Thermo-mechanical reactivation of locked crystal mushes: Melting-induced internal fracturing and assimilation processes in magmas: *Earth and Planetary Science Letters*, v. 304, p. 443-454.
- Ickert, R.B., Williams, I.S., and Wyborn, D., 2010, Ti in zircon from the Boggy Plain zoned pluton: implications for zircon petrology and Hadean tectonics: *Contributions to Mineralogy and Petrology*, v. 162, p. 447-461.
- John, B.E., and Blundy, J.D., 1993, Emplacement-related deformation of granitoid magmas, southern Adamello Massif, Italy: *Geological Society of America Bulletin*, v. 105, p. 1517-1541.
- Krogh, T.E., 1973, A low contamination method for hydrothermal decomposition of zircon and extraction of U and Pb for isotope age determination: *Geochem. Cosmochim. Acta*, v. 37, p. 485-494.
- Leuthold, J., Müntener, O., Baumgartner, L.P., Putlitz, B., Ovtcharova, M., and Schaltegger, U., 2012, Time resolved construction of a bimodal laccolith (Torres del Paine, Patagonia): *Earth and Planetary Science Letters*, v. 325, p. 85-92.
- Ludwig, K.R., 2005, Isoplot/Ex Version 3.00: a geological toolkit for Microsoft Excel: Berkeley Geochronology Center Special Publication, 70pp, v. 4.
- Mattinson, J.M., 2005, Zircon U-Pb chemical abrasion ("CA-TIMS") method: combined annealing and multi-step partial dissolution analysis for improved precision and accuracy of zircon ages: *Chemical Geology*, v. 220, p. 47-66.
- Matzel, J.E.P., Bowring, S.A., and Miller, R.B., 2006, Time scales of pluton construction at differing crustal levels: Examples from the Mount Stuart and Tenpeak intrusions, North Cascades, Washington: *Geological Society of America Bulletin*, v. 118, p. 1412-1430.
- McLean, N.M., Bowring, J.F., and Bowring, S.A., 2011, An algorithm for U-Pb isotope dilution data reduction and uncertainty propagation: *Geochemistry, Geophysics, Geosystems*, v. 12.
- Memeti, V., Paterson, S., Matzel, J., Mundil, R., and Okaya, D., 2010, Magmatic lobes as "snapshots" of magma chamber growth and evolution in large, composite batholiths: An example from the Tuolumne intrusion, Sierra Nevada, California: *Geological Society of America Bulletin*, v. 122, p. 1912-1931.
- Michel, J., Baumgartner, L., Putlitz, B.,

- Schaltegger, U., and Ovtcharova, M., 2008, Incremental growth of the Patagonian Torres del Paine laccolith over 90 ky: *Geology*, v. 36, p. 459-462.
- Miller, C.F., Furbish, D.J., Walker, B.A., Claiborne, L.L., Koteas, G.C., Bleick, H.A., and Miller, J.S., 2011, Growth of plutons by incremental emplacement of sheets in crystal-rich host: Evidence from Miocene intrusions of the Colorado River region, Nevada, USA: *Tectonophysics*, v. 500, p. 65-77.
- Miller, J.S., Matzel, J.E.P., Miller, C.F., Burgess, S.D., and Miller, R.B., 2007, Zircon growth and recycling during the assembly of large, composite arc plutons: *Journal of Volcanology and Geothermal Research*, v. 167, p. 282-299.
- Nimis, P., and Ulmer, P., 1998, Clinopyroxene geobarometry of magmatic rocks Part 1: An expanded structural geobarometer for anhydrous and hydrous, basic and ultrabasic systems: *Contributions to Mineralogy and Petrology*, v. 133, p. 122-135.
- Pistone, M., Caricchi, L., Ulmer, P., Reusser, E., and Ardia, P., 2013, Rheology of volatile-bearing crystal mushes: Mobilization vs. viscous death: *Chemical Geology*.
- Piwinskii, A.J., 1968, Experimental studies of igneous rock series central Sierra Nevada batholith, California: *The Journal of Geology*, p. 548-570.
- Prowatke, S., and Klemme, S., 2005, Effect of melt composition on the partitioning of trace elements between titanite and silicate melt: *Geochimica et Cosmochimica Acta*, v. 69, p. 695-709.
- Reid, M.R., Vazquez, J.A., and Schmitt, A.K., 2010, Zircon-scale insights into the history of a Supervolcano, Bishop Tuff, Long Valley, California, with implications for the Ti-in-zircon geothermometer: *Contributions to Mineralogy and Petrology*, v. 161, p. 293-311.
- Rioux, M., Lissenberg, C.J., McLean, N.M., Bowring, S.A., MacLeod, C.J., Hellebrand, E., and Shimizu, N., 2012, Protracted timescales of lower crustal growth at the fast-spreading East Pacific Rise: *Nature Geoscience*, v. 5, p. 275-278.
- Rubatto, D., and Hermann, J.r., 2007, Experimental zircon/melt and zircon/garnet trace element partitioning and implications for the geochronology of crustal rocks: *Chemical Geology*, v. 241, p. 38-61.
- Samperton K, Schoene B, Cottle J, Crowley JL, 2012, Integrated TIMS-TEA/LA-ICPMS constraints on pluton emplacement, Goldschmidt Conference Abstracts 2012
- Schaltegger, U., Brack, P., Ovtcharova, M., Peytcheva, I., Schoene, B., Stracke, A., Marocchi, M., and Bargossi, G.M., 2009, Zircon and titanite recording 1.5 million years of magma accretion, crystallization and initial cooling in a composite pluton (southern Adamello batholith, northern Italy): *Earth and Planetary Science Letters*, v. 286, p. 208-218.
- Schärer, U., 1984, The effect of initial ^{230}Th disequilibrium on young U-Pb ages: the Makalu case, Himalaya: *Earth and Planetary Science Letters*, v. 67, p. 191-204.
- Schmitz, M.D., and Bowring, S.A., 2001, U-Pb zircon and titanite systematics of the Fish Canyon Tuff: an assessment of high-precision U-Pb geochronology and its application to young volcanic rocks: *Geochimica et Cosmochimica Acta*, v. 65, p. 2571-2587.
- Schoene, B., Latkoczy, C., Schaltegger, U., and Günther, D., 2010, A new method integrating high-precision U-Pb geochronology with zircon trace element analysis (U-Pb TIMS-TEA): *Geochimica et Cosmochimica Acta*, v. 74, p. 7144-7159.
- Schoene, B., Schaltegger, U., Brack, P., Latkoczy, C., Stracke, A., and Günther, D., 2012, Rates of magma differentiation and emplacement in a ballooning pluton recorded by U-Pb TIMS-TEA, Adamello batholith, Italy: *Earth and Planetary Science Letters*, v. 355, p. 162-173.
- Stacey, J.S., and Kramers, J.D., 1975, Approximation of terrestrial lead isotope evolution by a two-stage model: *Earth and Planetary Science Letters*, v. 26, p.

- 207-221.
- Stauffer, A.K., 2012, Petrology and mineral chemistry of the Val Fredda Complex leucocratic units, Adamello, Italy, MSc thesis, ETH Zürich.
- Storey, C.D., Jeffries, T.E., and Smith, M., 2006, Common lead-corrected laser ablation ICP-MS U-Pb systematics and geochronology of titanite: *Chemical geology*, v. 227, p. 37-52.
- Tera, F., and Wasserburg, G.J., 1972, U-Th-Pb systematics in three Apollo 14 basalts and the problem of initial Pb in lunar rocks: *Earth and Planetary Science Letters*, v. 14, p. 281-304.
- Thomas, J.B., Bodnar, R.J., Shimizu, N., and Chesner, C.A., 2003, Melt inclusions in zircon: *Reviews in mineralogy and geochemistry*, v. 53, p. 63-87.
- Tiepolo, M., and Tribuzio, R., 2005, Slab-melting during Alpine orogeny: evidence from mafic cumulates of the Adamello batholith (Central Alps, Italy): *Chemical geology*, v. 216, p. 271-288.
- Tiepolo, M., Tribuzio, R., and Langone, A., 2011, High-Mg andesite petrogenesis by amphibole crystallization and ultramafic crust assimilation: Evidence from Adamello hornblendites (Central Alps, Italy): *Journal of Petrology*, v. 52, p. 1011-1045.
- Tiepolo, M., Tribuzio, R., and Vannucci, R., 2002, The compositions of mantle-derived melts developed during the Alpine continental collision: *Contributions to Mineralogy and Petrology*, v. 144, p. 1-15.
- Ulmer, P., Callegari, E., and Soderegger, U.C., 1983, Genesis of the mafic and ultramafic rocks and their genetical relations to the tonalitic-trondhjemitic granitoids of the southern part of the Adamello batholith (Northern Italy): *Mem. Soc. Geol. Ital.*, v. 26, p. 171-222.
- Verbene, R., 2013, The role of magma rheology during the emplacement of the Listino Suite, Adamello Massif, Italy, PhD thesis, UNIL
- Watson, E.B., and Harrison, T.M., 1983, Zircon saturation revisited: temperature and composition effects in a variety of crustal magma types: *Earth and Planetary Science Letters*, v. 64, p. 295-304.
- Watson, E.B., and Harrison, T.M., 2005, Zircon thermometer reveals minimum melting conditions on earliest Earth: *Science*, v. 308, p. 841-844.
- Watson, E.B., Wark, D.A., and Thomas, J.B., 2006, Crystallization thermometers for zircon and rutile: *Contributions to Mineralogy and Petrology*, v. 151, p. 413-433.
- Wotzlaw, J.-F., Schaltegger, U., Frick, D. A., Dungan, M. A., Gerdes, A., and Günther, D., 2013, Tracking the evolution of large-volume silicic magma reservoirs from assembly to supereruption: *Geology*.

Chapter 3

TEXTURALLY CONTROLLED ID-TIMS U-PB DATING OF ZIRCON FROM THIN SECTIONS: AN EXAMPLE FROM THE VAL FREDDA COMPLEX, N. ITALY*

Abstract

We present ID-TIMS U-Pb dates for zircons that were extracted from thin sections of the Val Fredda Complex (VFC), N. Italy, in order to evaluate whether protracted periods of zircon growth are related to distinct stages in the paragenetic sequence of a magma. Back scatter electron (BSE) images reveal abundant zircons in thin sections, and based on textural relationships, zircon saturated early in the VFC felsic magmas and crystallized throughout the paragenetic sequence. Despite the abundance of zircons exposed at the surface of our thin sections from the felsic samples, cathodoluminescence images reveal the presence of older and/or inherited cores in many of the located zircons. Therefore zircons containing cores were excluded in order to avoid bias towards older ages, thus severely limiting our selection of grains for ID-TIMS analysis. The remaining “core-free” grains are typically less than 100 μm in length and contain low amounts of radiogenic lead (0.62 – 0.86 picograms) resulting in low analytical precision, up to 1% on single $^{206}\text{Pb}/^{238}\text{U}$ dates. Our investigation of the VFC felsic samples highlights the limitations of our texturally controlled ID-TIMS dating method, which requires “core-free” zircons with sufficient amounts of radiogenic lead to achieve the necessary precision of 0.1% on single $^{206}\text{Pb}/^{238}\text{U}$ dates. Based upon this, we were unable to link periods of zircon crystallization within the VFC felsic magmas to the stage at which they crystallized in the paragenetic sequence.

The identification of zircon grains in the Mattoni gabbro (MG) was limited to 10 grains and zircon crystallization is constrained to the matrix. High precision (0.08 – 0.18 %) single, texturally controlled $^{206}\text{Pb}/^{238}\text{U}$ dates were obtained as a result of large zircon grains (< 100 μm) and high Pb*. However due to the late saturation of zircon in the MG and its association with late crystallizing phases (e.g. plagioclase and quartz), and due to the lack of significant differences in our U/Pb dates, we were unable to resolve the absolute timing the paragenetic sequence of the MG. However, the age dispersion recorded by our high precision, texturally controlled zircon dates (42.451 ± 0.077 Ma to 42.546 ± 0.061 Ma) is consistent with the previous age dispersion recorded by conventional separation techniques

* Manuscript (Broderick, Ovtcharova, Wotzlaw, Schaltegger) in preparation

(42.426 ± 0.039 Ma to 42.539 ± 0.033 Ma, thus providing evidence that our dates are representative of MG zircon crystallization.

3.1 Introduction

Detailed high precision U-Pb zircon geochronology studies have highlighted the complexities within zircon populations, indicating protracted zircon growth over 10 ka to Ma timescales (Michel et al., 2008; Schaltegger et al., 2009; Memeti et al., 2010; Schoene et al., 2012; Leuthold et al., 2012; Broderick, Chapter 2). In addition, high precision U-Pb dates point to multiple periods of enhanced zircon crystallization within single zircon populations (Wotzlav et al., 2013; Broderick, Chapter 2), consistent with Cathodoluminescence (CL) images which reveal that individual zircons have distinct histories and record periods of growth and dissolution (Miller et al., 2007; Broderick, Chapter 2). Therefore, does the protracted growth recorded by zircon reflect sub-populations of zircons that are associated with specific crystallizing phases? For example, during periods of protracted zircon growth over 100 ka timescales, can the zircons that are included in amphibole be distinguished from the zircons that are included in quartz? In order to make these distinctions within complex zircon populations the petrographic context of zircon

needs be established prior to dating.

While previous studies (Rubatto, 2002; Möller et al., 2003; Zong et al., 2010) have used in situ zircon U-Pb geochronology (e.g. ion probe and LA-ICP-MS), which provides high spatial resolution to target specific growth textures observed in CL images, they do not provide the necessary 10 to 100 ka precision for resolving the timing of magmatic processes. Whereas, ID-TIMS zircon U-Pb geochronology provides the necessary precision to resolve timescales of magmatic processes, textural relationships are lost during conventional separation techniques. In this study we combine high precision ID-TIMS zircon geochronology with the petrographic context of zircon by extracting zircons by micro-drilling directly from thin sections. We utilize high precision CA-ID-TIMS (chemical abrasion, isotope-dilution, thermal ionization mass spectrometry) zircon geochronology, and trace element compositions of zircons that have been micro-drilled from thin sections based on textural relationships. Combining high precision U-Pb dates with textural relationships from back-scatter electron (BSE) images and internal growth textures observed in CL images,

we attempt to link periods of enhanced zircon growth to the crystallization of major mineral phases, within the paragenetic sequence of a magma. In addition, given the limitation of zircon grains that are exposed at the surface of the thin sections, we test if the extracted zircon grains are representative of zircon crystallization with a magma and how they compare to the age dispersion obtained on zircon grains selected from conventional separation techniques from Chapter 2.

The Val Fredda Complex in the southern tip of the Adamello Batholith, N. Italy, has been constructed by multiple injections of compositionally diverse magmas, ranging from gabbro to granodiorite. Field observations reveal complex relationships among mafic magmas injected into solidifying felsic magmas, where both magma mingling and hybridization can be observed. Previous high precision U-Pb zircon results (see Chapter 2) document 100 – 200 ka periods of protracted zircon growth, recording multiple periods of enhanced zircon crystallization associated with cooling after episodes of rejuvenation of the felsic crystal mush by repeated mafic injections. The zircon results presented here highlights the reproducibility of the age dispersion between studies indicates that the U-Pb dates are representative of zircon crystallization and that our high precision U-Pb dates are not biased by grain selection.

3.2 Geologic setting

The Tertiary Adamello Batholith is exposed over an area of ~670 km² with ~2 km of vertical relief, in the Southern Alps, Northern Italy (Brack, 1983; Callegari and Brack, 2002). The Adamello batholith is mainly composed of tonalites, thondjemites and granodiorites with minor mafic units in the southern most part of the batholith (Brack, 1983; Callegari and Brack, 2002). The mafic rocks occur mainly in the periphery and are best exposed in the Val Fredda Complex and the Blumone Complex (Ulmer et al., 1983; Blundy and Sparks, 1992; Tiepolo et al., 2005, 2011).

This study focuses on the Val Fredda Complex (VFC), a small marginal intrusion exposed over ~6 km² in the southern most part of the batholith (Fig.1), that consists of five distinct, lithological units: (1) the Val Fredda tonalite (VFT) outcrops mainly in the north of the complex; (2) the plagioclase quartz diorite (PQD) outcrops mainly in the central and northern parts; (3) the marginal facies granodiorite (MFG) outcrops mainly along the southern and eastern margins; (4) the Mattoni gabbro (MG) occurs mainly in the southern most part of the pluton near Monte Mattoni; (5) the Cadino gabbro (CG) occurs through out the pluton as a series of horizontal sheets separated by felsic units (PQD, VFT) of variable thickness (mm to m scale) depending

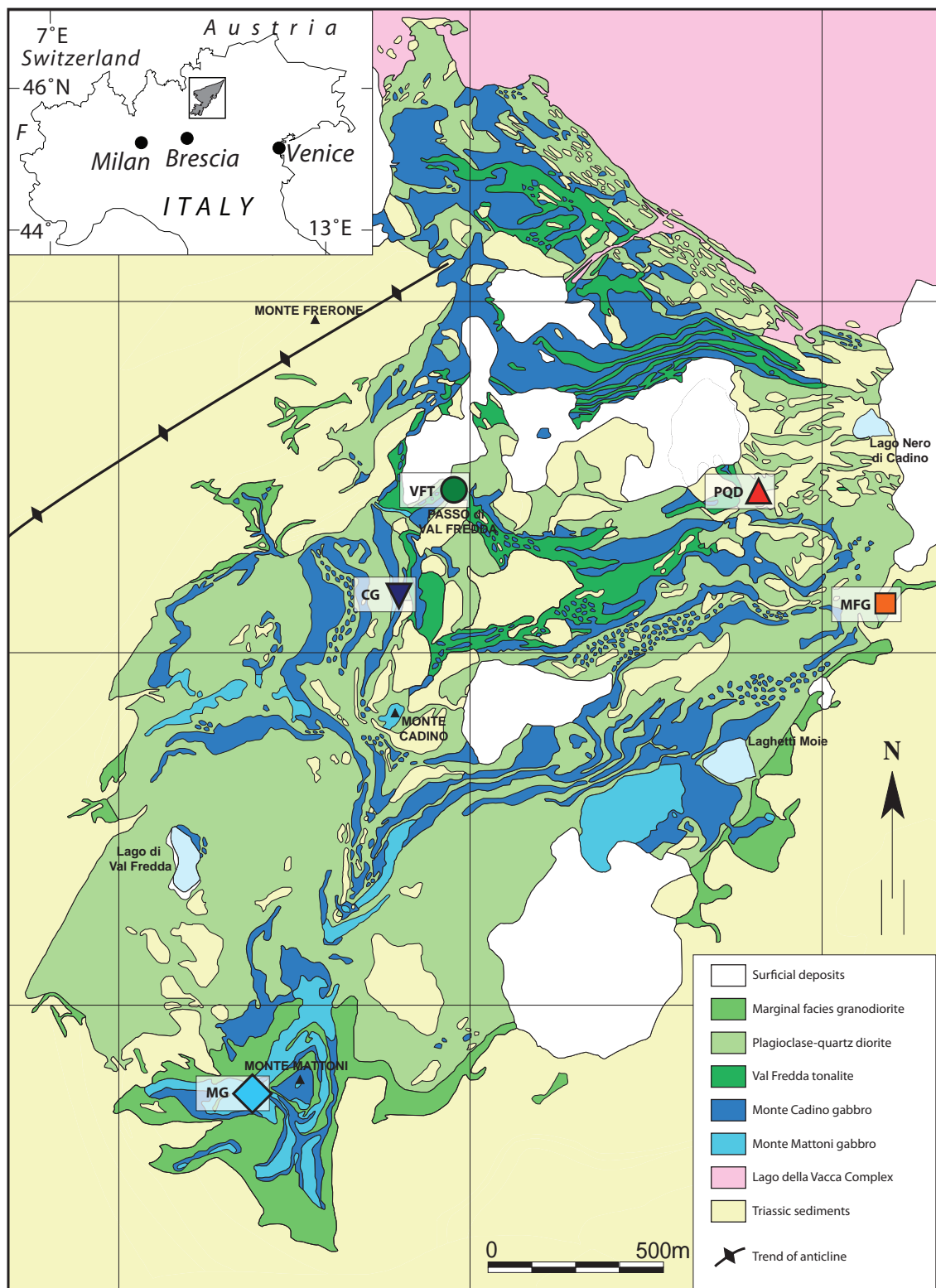


Figure 1: Simplified geologic map of the Val Fredda Complex, modified after Blundy and Sparks (1992), located in the southern most part of the Adamello batholith (see inset map for location). Sample locations for zircon in situ analysis and ID-TIMS dating are labeled: MFG = Marginal facies granodiorite; PQD = Plagioclase quartz diorite; VFT = Val Fredda tonalite; CG = Cadino gabbro; MG = Mattoni gabbro.

on the locality but outcrops most abundantly at Monte Cadino.

Based on detailed fieldwork (Brack, 1983;

Ulmer et al., 1983; Blundy and Sparks, 1992)

the VFC intrusion was described as a complex

system that was constructed by a series of

felsic magmas that show vertical accretion by horizontal injections of mafic sills, of variable thickness (~0.5 – 100 m), into the crystallizing roof of a larger magmatic system. High precision U-Pb zircon dates, from the VFC felsic and mafic units, presented in Broderick Chapter 2, record protracted zircon growth over 100 – 200 ka within individual units. U-Pb probability density distribution curves, for individual units, record multiple periods of enhanced zircon crystallization. Coinciding periods of enhanced

crystallization indicate that the VFC units share a common thermal history associated with cooling after episodes of rejuvenation the felsic crystal mushes by repeated mafic injections (Broderick, Chapter 2).

3.3 Petrography

Sample locations are shown in Fig. 1 and average modal abundances from the studied thin sections are given in Table 1.

Table 1:
Modal abundances of samples from the Val Fredda Complex

Sample	MFG	PQD	VFT	MG	CG
Plagioclase	40	55	57	27	52
Quartz	33	11	24	6	10
K-feldspar	15	-	0.5	-	-
Amphibole	0.9	13	8	35c - 20r*	30
Biotite	10	7	10	-	7
Clinopyroxene	-	-	-	10	-
Titanite	0.03	0.01	0.01	0.24	0.01
Zircon	0.1	0.02	0.02	0.01	0.01
accessories	ap, al, mag	ap, al, mag	ap, mag	ap, mag, cc	ap, mag

Representative modal data collected from point counting.

“-” not identified

* amphibole was distinguished between cores (c) and rims (r).

ap = apatite; al = allanite; mag = magnetite; cc = calcite

The Val Fredda tonalite (VFT; Fig. B1) has a weakly porphyritic texture and is characterized by euhedral plagioclase (≤ 7 mm) and rounded quartz (≤ 3 mm) phenocrysts and minor K-feldspar (< 1 mm). Plagioclase grains record variable compositions (An_{85-15} ; Blundy and Shimizu, 1991) and typically contain resorbed calcic cores with oscillatory zoned sodic

rims. Mafic minerals are euhedral biotite (≤ 4 mm), amphibole (≤ 7 mm; Mg-hornblende; Stauffacher, 2012) and anhedral magnetite (< 1 mm) and accessory minerals include titanite, zircon, apatite and interstitial ilmenite. Titanite is euhedral to subhedral, but mainly occurs as overgrowths around magnetite. The VFT contains mafic microgranular enclaves (Fig.

B1) that are attributed to the mingling and hybridization between mafic magmas and the VFT (Blundy and Sparks, 1992).

The Plagioclase quartz diorite (PQD; Fig. B2) has an equigranular texture, composed of plagioclase (≤ 4 mm), quartz (≤ 4 mm) and lacks K-feldspar. Plagioclase grains typically contain resorbed cores and exhibit oscillatory zoning, but show weak compositional variations (e.g. An_{43-40} ; Blundy and Shimizu, 1991). Mafic minerals are euhedral biotite (≤ 4 mm), amphibole (≤ 6 mm; Mg-hornblende; Stauffacher, 2012) and anhedral magnetite (< 1 mm). Accessory minerals are subhedral to euhedral grains of titanite, zircon and apatite.

The Marginal Facies granodiorite (MFG; Fig. B3) has a porphyritic texture and is characterized by ~ 30 % phenocrysts of euhedral plagioclase (≤ 5 mm), biotite (≤ 4 mm) and rounded quartz (≤ 4 mm) in a fine grained aplitic matrix of K-feldspar and quartz, and the lacks significant amounts of amphibole (~ 1 %). Plagioclase grains are oscillatory zoned and record zoned compositions from An_{72-41} in the cores to An_{24-19} in the rims (Blundy and Shimizu, 1991). Accessory minerals include titanite, zircon and apatite forming subhedral to euhedral grains and anhedral magnetite.

The Mattoni gabbro (MG; Fig. B4) has a porphyritic texture and is characterized by large prismatic brown-green amphiboles (up to 8 mm)

in a matrix mainly composed of plagioclase (≤ 4 mm), euhedral clinopyroxene (< 1 mm), green amphibole (≤ 3 mm) and minor plagioclase and quartz. Larger amphiboles are compositionally zoned and contain brown cores (Ti-pargasite; Tiepolo et al., 2002), which contain inclusions of clinopyroxene and olivine. Green amphibole rims (Mg-hornblende; Tiepolo et al., 2005) are compositionally similar to the matrix amphiboles. Clinopyroxene occurs as corroded, Al and Cr-rich grains in amphibole cores and as euhedral Al-poor grains in the matrix (Ulmer et al., 1983; Tiepolo et al., 2002, 2005). Plagioclase grains are poikilitic and record continuous compositional zoning, with decreasing An content towards the rim (An_{98-22} ; Blundy and Shimizu, 1991). Accessory minerals are titanite, zircon, apatite and calcite. Titanite grains are large, up to 2 mm, and are subhedral to euhedral. Calcite occurs as interstitial grains and as single rounded grains rimmed by small clinopyroxene grains referred to as “ocelli” (Ulmer et al., 1983; Blundy and Sparks, 1992). The presence of these ocelli in the MG, are the result of when the residual melt became fluid over saturated and gas bubbles formed which were subsequently filled with calcite as the result of the liquid immiscibility produced between the late stage melts and melts rich in H_2O and CO_2 (Ulmer et al., 1983). In addition to calcite, plagioclase and quartz grains also form ocelli within the MG (Fig. B4).

Experimental work by Ulmer et al., (1983) show that the crystallization sequence for the MG is olivine + spinel \rightarrow clinopyroxene (1) \rightarrow hornblende + orthopyroxene \rightarrow plagioclase + clinopyroxene (2). These results indicate early hornblende crystallization and delayed plagioclase crystallization, and combined with geothermometry and geobarometry indicate that the MG formed from a deep, hot magma 1000-1100°C at 0.8 -1 GPa, which was subsequently emplaced in the shallow crust (0.2-0.3 GPa) at \sim 900°C (Ulmer et al., 1983; Blundy and Sparks, 1992; Nimis and Ulmer, 1998; Tiepolo et al., 2011). The shallow emplacement is consistent with Al-in-hornblende geobarometry of 0.2-0.3 GPa obtained for the felsic units (Stauffer, 2012).

The Cadino gabbro (CG; Fig. B5) is characterized by acicular amphiboles (≤ 5 mm) in a matrix of anhedral plagioclase (≤ 4 mm), quartz (≤ 3 mm) and biotite (< 1 mm). Plagioclase grains record zoned compositions of An_{94-71} in the cores to An_{44-35} in the rims (Blundy and Shimizu, 1991). Accessory minerals are titanite, zircon, apatite and ilmenite. No zircons were exposed at the surface of our thin sections of the CG, even though abundant euhedral zircons were recovered using conventional separation techniques.

Experimental work by Blundy and Sparks (1992) show that the crystallization sequence for

the CG is hornblende + plagioclase + magnetite and the lack of olivine and clinopyroxene is the result of rapid cooling of a magma from super-liquidus conditions at 1000-1050°C down to \sim 950°C. These results are consistent with chilled margins observed along CG sheet edges and that the acicular hornblendes are the result of rapid cooling and crystallization.

3.4 Analytical techniques

3.4.1 Locating zircons in thin sections

Zircon grains were located in polished 100 μ m thick sections (5 cm x 3.5 cm) through back scattered electron (BSE) imaging, using a Jeol JSM- 7001F scanning electron microscope (SEM) at the University of Geneva. The sections were manually scanned for BSE brightness close to that of zircon and for each potential zircon grain, energy dispersive X-ray spectra (EDS) were collected. Zircons were identified based on the pronounced Zr peak in the EDS spectra. Locations of zircon grains were recorded on thin section maps for subsequent analyses. Cathodoluminescence (CL) images of individual zircon grains were acquired using a CamScan SEM working at 10 kV at the University of Lausanne. Based on CL images, zircon grains free of visible cores were selected for in situ analyses.

3.4.2 LA-ICP-MS zircon trace element analysis

In situ trace element analyses of zircon were carried out on the 100 μm thick, polished sections by LA-ICP-MS using a Thermo Scientific Element XR mass spectrometer coupled to a New Wave Research ArF 193 nm laser ablation system at the University of Lausanne. Operating conditions of the laser include using a 20 μm ablation pit, a 10 Hz frequency and an on-sample energy density of $\sim 6 \text{ J/cm}^2$. Helium was used as a cell gas. The acquisition times for the background and the ablation interval corresponded to 60 and 30 seconds, respectively. Dwell times per isotope ranged from 10 to 20 ms and peak hopping mode was employed. The ThO^+/Th^+ and $\text{Ba}^{2+}/\text{Ba}^+$ ratios were optimized to 0.035 – 0.05% and 2.9%, respectively. Measurements of unknowns within each thin section were bracketed by NIST SRM-612 glass measurements which were employed for the external standardization. Silicon was chosen as the internal standard element ($\text{SiO}_2 = 32.8 \text{ wt. \%}$). Intensity versus time data was reduced in LAMTRACE. All spectra were checked for the presence of surface contamination and intensity spikes and corrected when necessary. Data are presented in Table 2.

3.4.3 Texturally controlled ID-TIMS zircon dating

Based on BSE and CL images, individual zircon grains were extracted from thin sections using a Medenbach micro-drill mounted on a petrographic microscope. Zircons ($\leq 200 \mu\text{m}$) were removed from the polished thin sections in 350 μm diameter disks in order to preserve intact zircon grains. Extracted zircons were then individually thermally annealed and chemically abraded (Mattinson 2005), in order to minimize lead loss, due to the effects of radioactive decay damage, which is essential for the interpretation of our zircon ages. A total of 18 zircon grains were analyzed for their U-Pb isotopic composition using high precision ID-TIMS techniques (See Appendix B for full analytical details). Zircon grains were spiked using the EARTHTIME (<http://www.earth-time.org>) ^{202}Pb - ^{205}Pb - ^{233}U - ^{235}U -tracer solution and dissolved in Teflon microcapsules inside a PARR dissolution vessel. All measurements were performed at the University of Geneva on a Thermo-Scientific TRITON thermal ionization mass spectrometer equipped with a MasCom discrete dynode electron multiplier operated in ion counting mode. The initial statistical analysis was done using the TRIPOLI program followed by data reduction and age calculation using the U-Pb Redux software (Bowring et al., 2011), using the algorithms of McLean et al. (2011). The data

were corrected for mass fractionation with the ET2535 tracer composition using a $^{202}\text{Pb}/^{205}\text{Pb}$ ratio of 0.99924 and a U-Pb ratios and dates were calculated relative to $^{235}\text{U}/^{205}\text{Pb}$ ratio of 100.23. Initial ^{230}Th disequilibrium correction was applied to all data using the methods described in Broderick Chapter 2 (See Appendix B for details). $^{206}\text{Pb}/^{238}\text{U}$ age ranked data are plotted using the ISOPLOT/Ex v.3 program of Ludwig (2005). All uncertainties are reported at the two-sigma level. Data are presented in Table 3.

3.5 Results

3.5.1 Zircon occurrence and textural relationships

Val Fredda tonalite (VFT)

Back scatter electron (BSE) imaging of polished sections from the VFT sample revealed abundant zircon grains, ~30 per thin section (Fig. B1), ranging from ~10 μm to ~100 μm . Based on their textural relationships, VFT zircons (Fig. 2) are classified into two types: 1) zircons which crystallize at grain boundaries (33%; Fig. 2a-d) and; 2) zircons which occur as inclusions in the main VFT forming minerals; quartz (8%; Fig. 2e), plagioclase (21%; Fig. 2f), biotite (25%; Fig. 2g-h) and amphibole (13%; Fig. 2i). Type 1 zircons are composed of subhedral and euhedral crystals, but they occur predominately as subhedral grains (~75%). Type 2 zircons which are included in quartz are all euhedral, whereas

type 2 zircons included in plagioclase and biotite are mostly euhedral (70% and 75%, respectively). In contrast zircons included in amphibole form both euhedral and subhedral grains in equal amounts. Two type 1 zircons contained mineral inclusions; a euhedral zircon with a biotite inclusion and a subhedral grain with a rounded K-feldspar inclusion. A biotite inclusion was also observed in a subhedral zircon included in amphibole. Ilmenite inclusions were observed in two euhedral zircon grains, one included in biotite and one included in plagioclase. A subhedral zircon, included in plagioclase, with an apatite inclusion was also observed (Fig. 2f). Cathodoluminescence (CL) imaging of VFT zircons reveals typical magmatic oscillatory zoning and that > 50% of VFT zircons contain truncated or resorbed cores (Fig. 3). Based on observed petrographic textural relationships, the VFT reached zircon saturation early, as evidenced by zircon inclusions in amphibole (Fig. 2i), and crystallized throughout the history of the magma recording periods of growth and dissolution, based on growth textures observed in CL images (e.g. Fig. 3f-h).

Plagioclase quartz-diorite (PQD)

BSE imaging of polished sections from the PQD sample (Fig. B2) revealed 51 zircon grains which range in size from ~10 μm to ~100 μm . Based on their textural relationships, PQD zircons (Fig. 4)

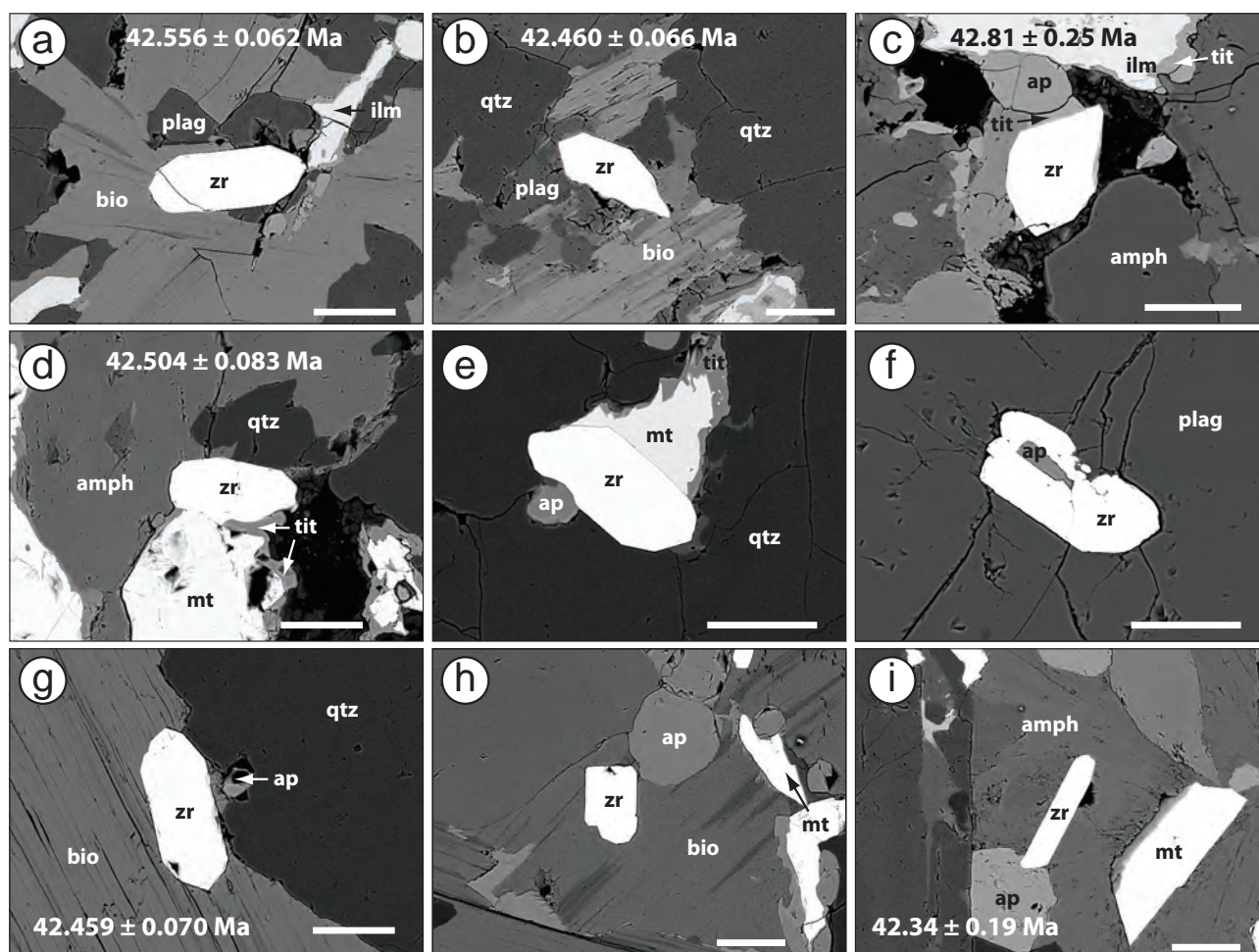


Figure 2: BSE images of representative zircon grains in thin sections from the VFT. $^{206}\text{Pb}/^{238}\text{U}$ dates are given for zircons which were extracted for ID-TIMS dating (a-d,g,i). amph = amphibole; ap = apatite; bio = biotite; ilm = ilmenite; mt = magnetite; plag = plagioclase; qtz = quartz; tit = titanite; zr = zircon. Scale bars = 50 μm

are classified into two types: 1) zircons which crystallize at grain boundaries (33%; Fig. 4a) and; 2) zircons which occur as inclusions in the main PQD forming minerals; quartz (14%; Fig. 4b-c), plagioclase (18%), biotite (25%; Fig. 4d-e) and amphibole (10%; Fig. 4c,f). Type 1 zircons form both subhedral and euhedral crystals. Type 2 zircons that are included in quartz are all euhedral, whereas type 2 zircons included in biotite and amphibole are mostly euhedral (70% and 60%, respectively). In contrast, type 2 zircons included in plagioclase are mostly

subhedral (~75%). No mineral inclusions were observed in any of the 51 zircon grains identified. CL images of PQD zircons reveal that ~50% of zircon grains contain resorbed or truncated cores and all zircons have typical magmatic oscillatory zoning (Fig. 5). Based on observed petrographic textural relationships, the PQD reached zircon saturation early, as evidenced by zircon inclusions in amphibole (Fig. 4c,f), and crystallized throughout the history of the magma recording periods of growth and dissolution, based on growth textures observed

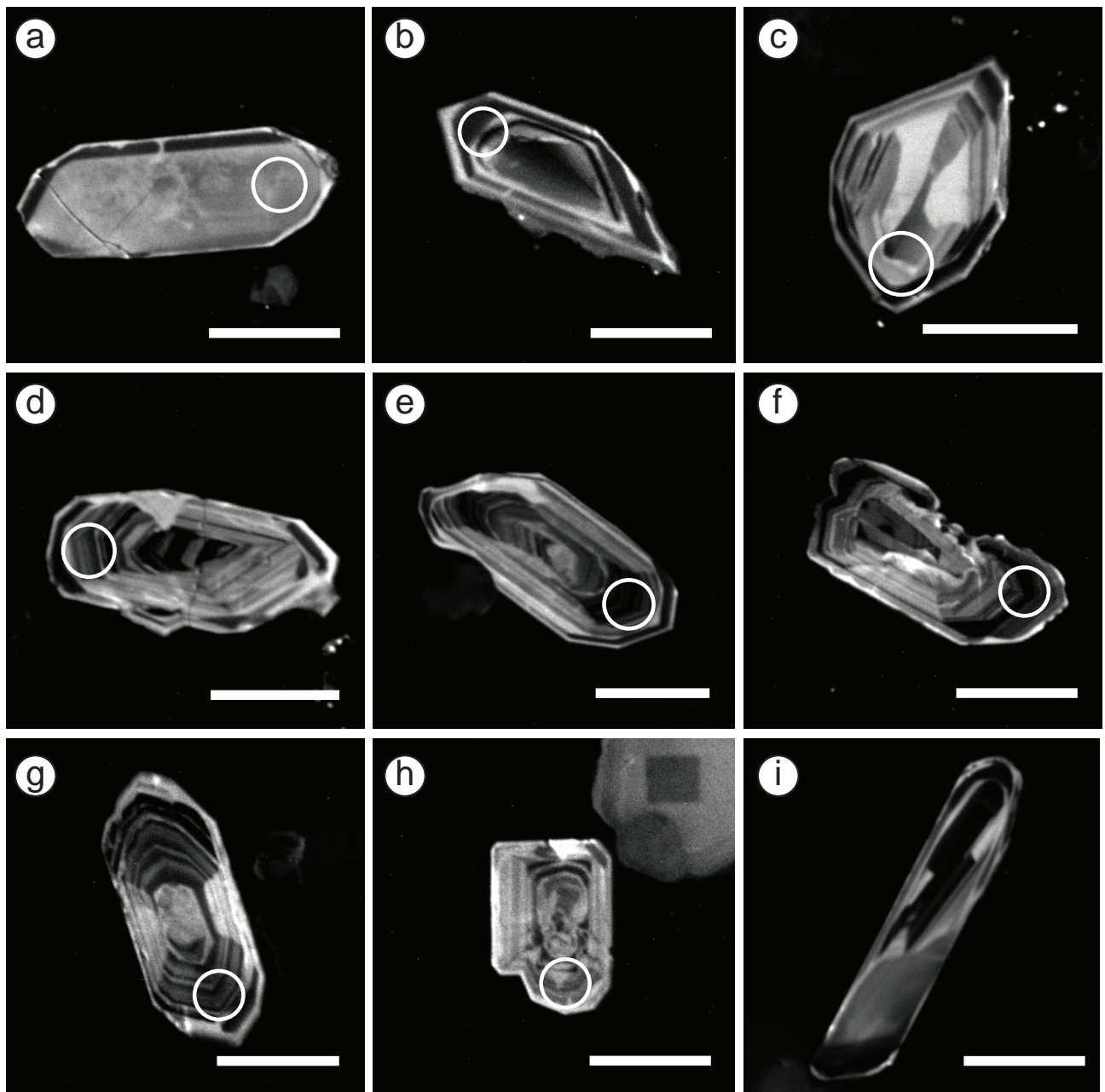


Figure 3: CL images of the zircons grains in thin section, from Fig. 2, from the VFT. White circles show the approximate location of 20 μm spots for trace element analysis by LA-ICP-MS. Scale bars = 50 μm

in CL images (Fig. 5).

Marginal facies granodiorite (MFG)

BSE imaging of polished sections from the MFG sample revealed abundant zircon grains, ~30 per thin section (Fig. B3), ranging from ~10 μm to ~100 μm . Based on their textural relationships, MFG zircons (Fig. 4) are classified into two types:

1) zircons which crystallize at grain boundaries (42%; Fig. 4g-i) and; 2) zircons which occur as inclusions in the main MFG forming minerals; quartz (10%), plagioclase (16%; Fig. 4k), biotite (30%; Fig. 4l) along with two subhedral zircon grains, ~5 μm each, included in apatite. Type 1 zircons form both subhedral and euhedral crystals. Type 2 zircons included in quartz are all

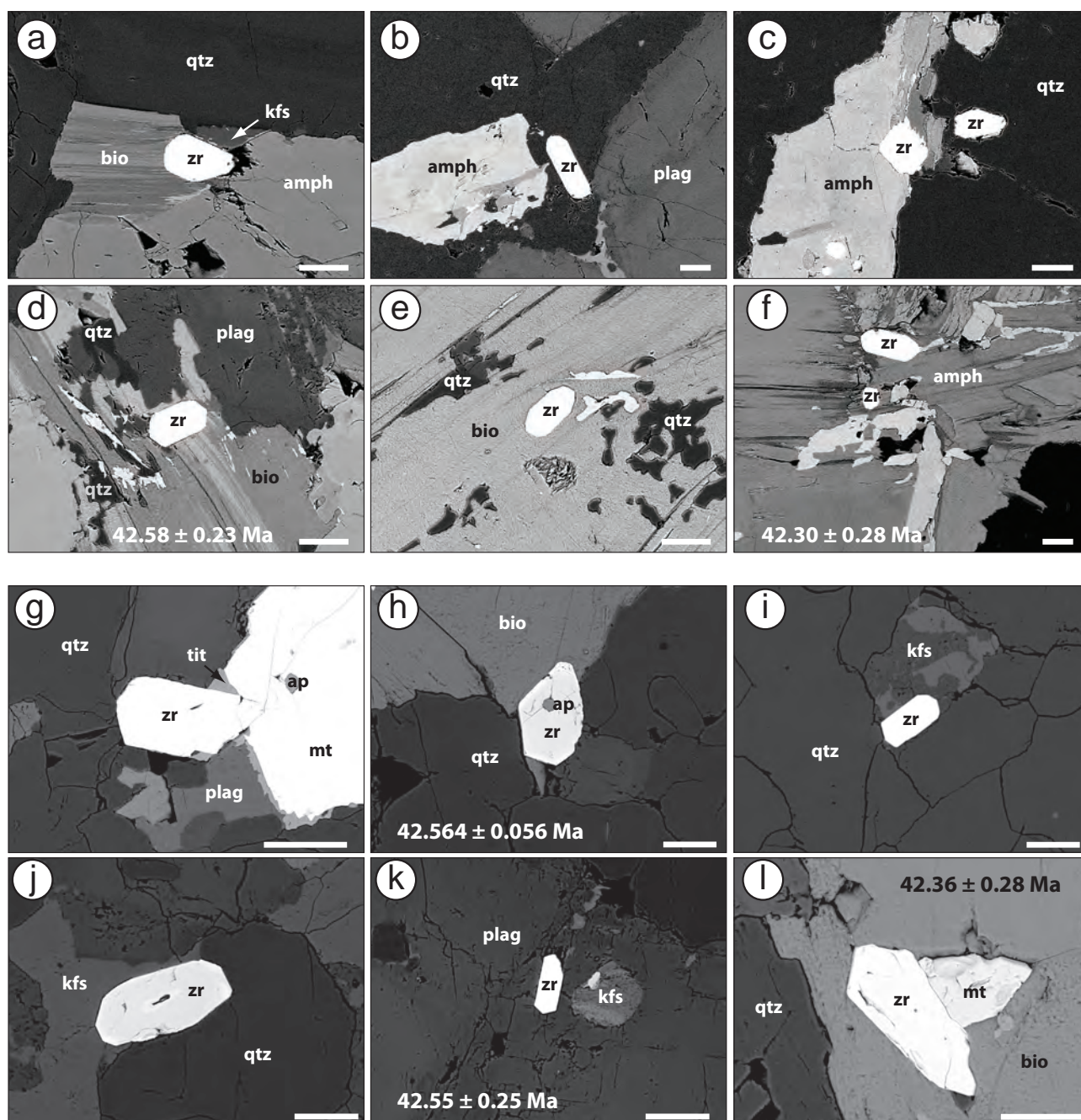


Figure 4: BSE images of representative zircon grains in thin sections from: (a-f) PQR and; (g-l) MFG. $^{206}\text{Pb}/^{238}\text{U}$ dates are given for zircons which were extracted for ID-TIMS dating (d,f,h,k,l). amph = amphibole; ap = apatite; bio = biotite; kfs = K-feldspar; mt = magnetite; plag = plagioclase; qtz = quartz; tit = titanite; zr = zircon. Scale bars = 50 μm

euhedral and the zircons included in plagioclase are mostly euhedral (60%), whereas zircons included in biotite are mostly subhedral (65%). Four type 1 zircons have apatite inclusions, where one zircon grain contains apatite and quartz. Only one type 2 zircon, included in biotite, contains an apatite inclusion. CL images

of PQR zircons reveal that ~50% of zircon grains contain resorbed cores, occurring in both type 1 and type 2 zircons, and all zircons have typical magmatic oscillatory zoning (Fig. 5). Based on observed petrographic textural relationships combined with growth textures observed in CL, the MFG zircons crystallized throughout

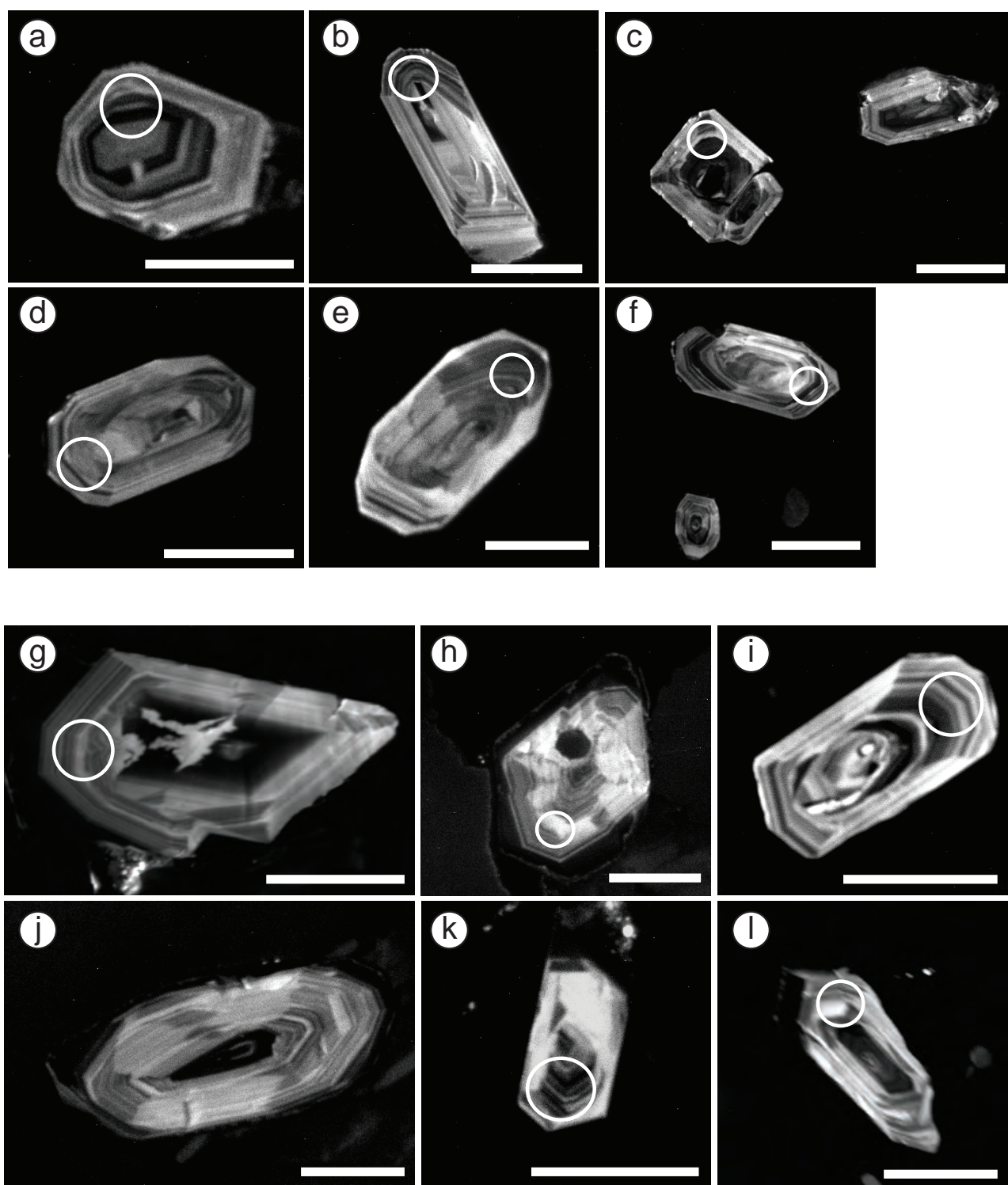


Figure 5: CL images of the zircons grains in thin section, from Fig. 4, from: (a-f) PQD and; (g-l) MFG. White circles show the approximate location of 20 μm spots for trace element analysis by LA-ICP-MS. Scale bars = 50 μm

the history of the magma recording periods of growth and dissolution (Fig. 5).

Mattoni gabbro (MG)

BSE imaging of polished sections from the Mattoni gabbro sample revealed only ten zircons (Fig. B4), ranging in size from $\sim 80 \mu\text{m}$ to 200

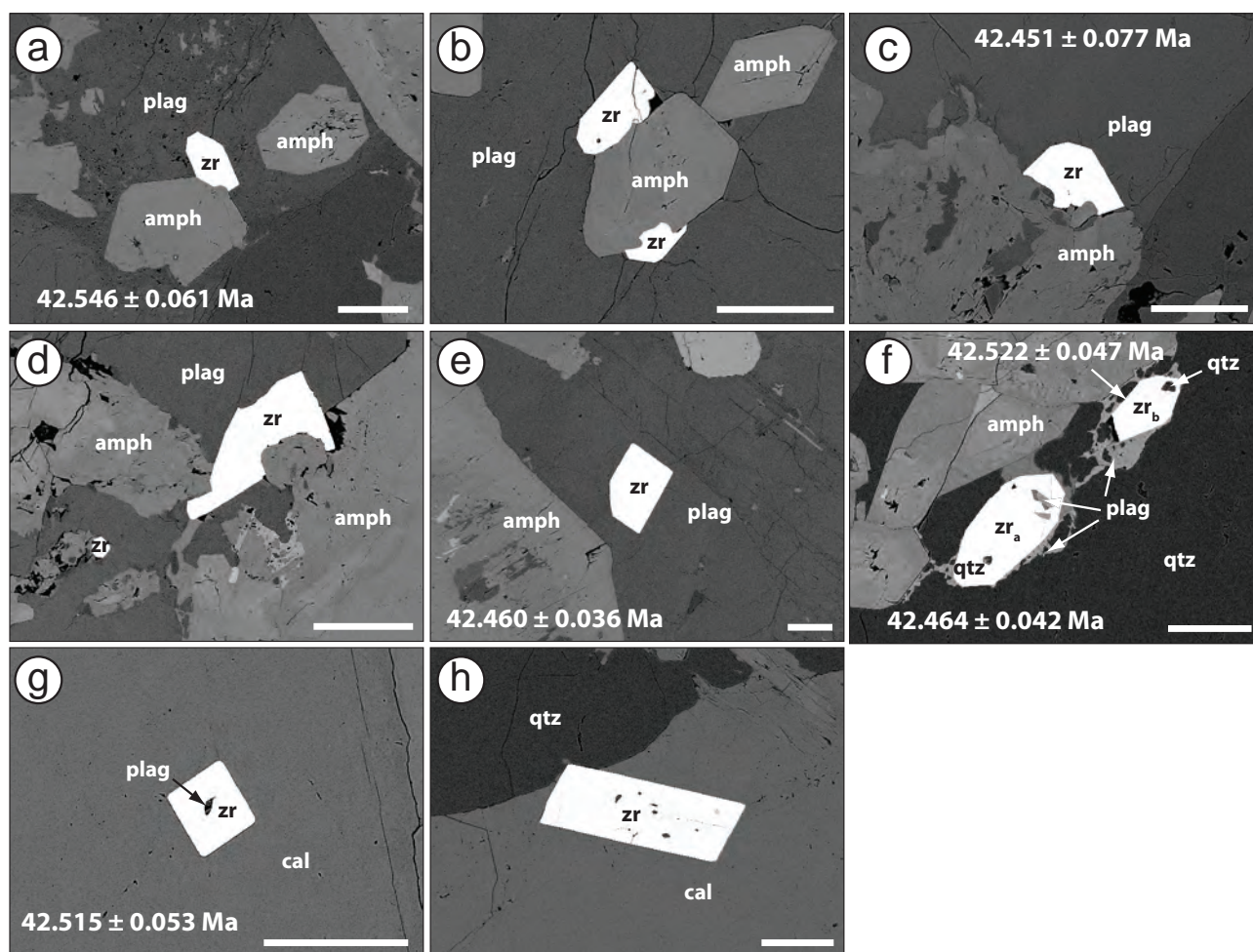


Figure 6: BSE images of representative zircon grains in thin sections from the MG. $^{206}\text{Pb}/^{238}\text{U}$ dates are given for zircons which were extracted for ID-TIMS dating (a,c,e-g). amph = amphibole; cal = calcite; plag = plagioclase; qtz = quartz; zr = zircon. Scale bars = 100 μm

μm . Based on their textural relationships, MG zircons (Fig. 6) are classified into two types: 1) zircons which crystallize at grain boundaries (50%; Fig. 6a-d) and; 2) zircons which are included in the late matrix forming minerals plagioclase (10%; Fig. 6e), quartz (20%; Fig. 6f) and calcite (20%; Fig. 6g-h). Type 1 zircons exhibit both anhedral forms and euhedral crystal faces within single grains. The anhedral zircon forms are always spatially associated with the matrix amphiboles, whereas the corresponding euhedral crystal face is always adjacent to plagioclase (Fig. 6a-d). Type 2 zircons are mainly

euhedral and commonly contain inclusions of the matrix forming minerals plagioclase, and quartz (Fig. 6f-h). Two zircons included in calcite have plagioclase inclusions in their cores (Fig. 6g-h), whereas the two zircons included in quartz contain plagioclase and quartz inclusions in their rims (Fig. 6f). The occurrence of zircons limited to the matrix indicates that the MG reached zircon saturation after emplacement at 0.2 – 0.3 GPa (Ulmer et al., 1983) and based on textural relationships the MG reached zircon saturation late, following the crystallization of the matrix amphibole.

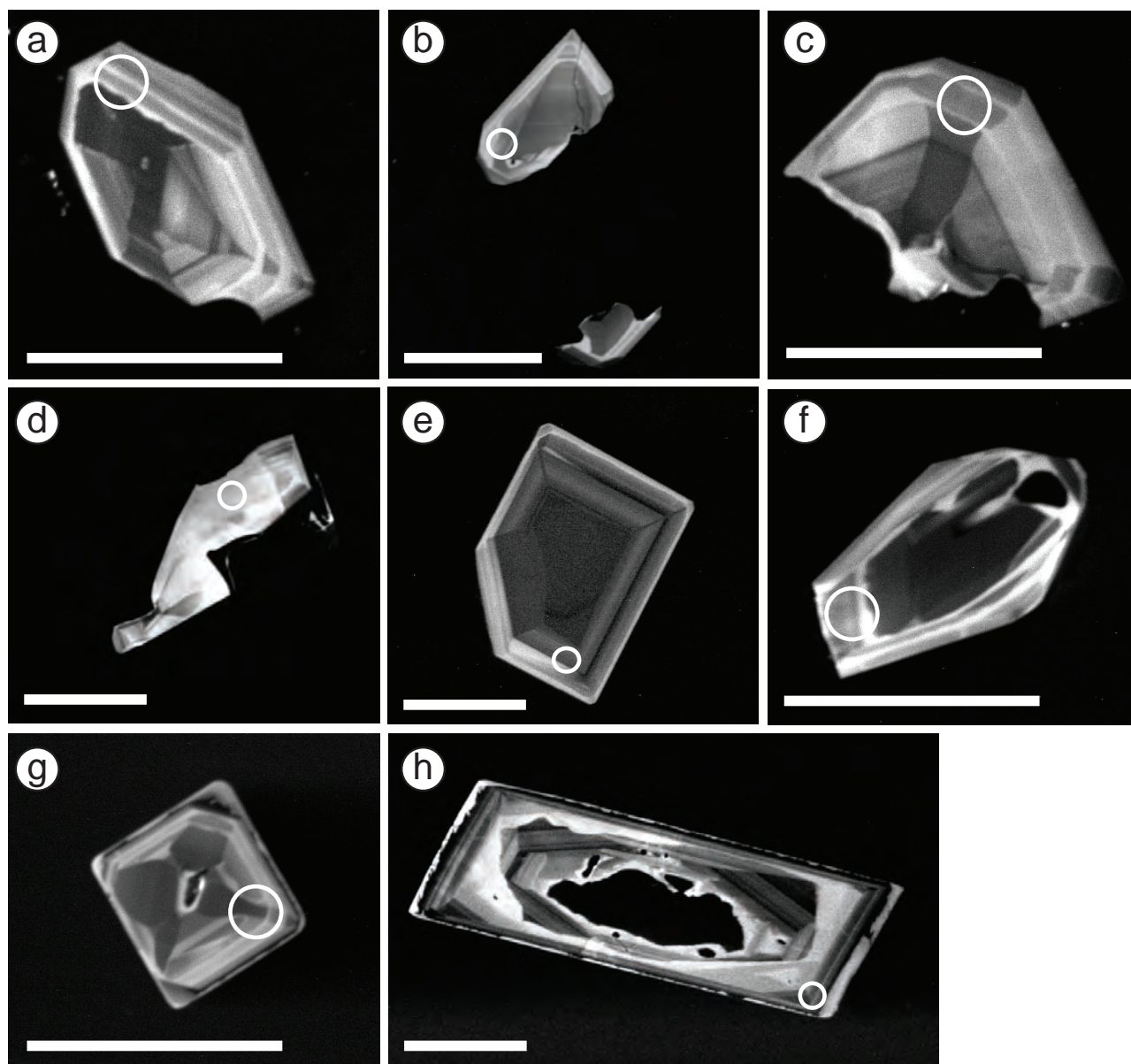


Figure 7: CL images of the zircons grains in thin section, from Fig. 6, from the MG. White circles show the approximate location of 20 μm spots for trace element analysis by LA-ICP-MS. Scale bars = 100 μm

CL imaging of MG zircons reveals complex internal structures exhibiting sector zoning and magmatic oscillatory zoning (Fig. 7). Type 1 zircon grains are characterized by sector zoning and commonly exhibit bright oscillatory zoned rims (Fig. 7a-d). Type 2 zircon grains mostly exhibit dark centers with light oscillatory zoned rims (Fig. 7e-g). One Type 2 zircon grain contains a resorbed oscillatory zoned core, an

intermediate high-luminescence zone, which is overgrown by an oscillatory zoned rim (Fig. 7h). The presence of sector zoning in the MG zircons may be attributed to initial rapid zircon growth (Corfu et al., 2003) before recording typical magmatic oscillatory zoning.

Table 2:
LA-ICP-MS in-situ zircon trace element results for samples from the Val Fredda Complex

	Zr wt%	Ti ppm	Sr	Y	Nb	La	Ce	Pr	Nd	Sm	Eu	Gd	Tb	Dy	Ho	Er	Tm	Yb	Lu	Hf	Ta	Pb	Th	U
Marginal Facies granodiorite (VFC03)																								
included in plagioclase																								
03-b1-z30	63.3	-	6.1	2922	16.9	0.06	52.9	0.17	2.8	5.6	2.6	37.3	15.8	224.1	97.3	460.5	101.2	997.6	226.0	11613.9	5.2	51.9	961.5	1686.0
03-a2-z32	54.8	13.0	1.8	1796	13.2	0.04	45.9	0.09	1.4	2.7	1.1	23.2	8.7	127.1	55.5	315.7	71.1	791.7	180.3	9865.7	3.7	41.6	833.0	1422.9
included in biotite																								
03-a1-z22	60.0	10.2	1.0	3747	24.1	1.94	65.8	0.42	3.8	8.9	2.8	60.5	23.4	322.6	121.4	620.2	128.7	1209.1	243.7	10888.5	6.8	61.6	1819.5	2058.9
03-a1-z23	49.9	-	2.9	1109	31.6	0.90	20.1	0.24	1.2	3.1	1.4	16.9	5.5	82.1	35.8	188.2	46.3	455.1	107.0	8812.8	3.4	17.6	323.6	542.4
03-a2-z6	58.4	-	1.0	1590	12.5	0.03	46.6	0.07	1.4	3.3	1.3	21.3	8.5	131.4	51.8	252.4	57.9	615.4	140.8	10663.7	4.5	37.8	1133.4	1488.5
03-a2-z31	67.7	7.1	1.9	2584	17.1	0.10	80.7	0.18	3.0	7.3	2.3	37.5	14.0	205.1	84.7	397.8	93.0	997.5	241.8	11911.7	5.5	44.0	1502.7	2018.2
at grain boundaries																								
03-a1-z5	62.6	6.9	0.9	1718	11.7	0.07	50.7	0.11	1.4	3.2	1.2	19.5	8.1	114.3	49.0	272.0	64.6	663.7	159.1	10351.2	3.7	24.8	734.6	1001.8
03-a1-z21	66.1	-	1.0	1278	8.3	0.02	46.4	0.05	1.2	2.9	1.0	17.9	6.3	93.8	39.7	204.2	49.3	526.3	122.2	11308.1	3.5	29.6	917.3	1145.2
03-a1-z38	64.4	10.2	1.6	2048	12.8	0.03	67.4	0.14	1.8	4.5	1.8	27.2	9.8	147.7	62.7	323.7	74.7	775.9	183.0	10252.1	4.6	43.3	1586.7	1594.1
03-a2-z17	62.1	5.6	1.5	2080	19.7	0.04	67.8	0.06	1.4	3.4	1.0	24.8	9.4	152.6	66.3	345.3	81.1	909.9	196.6	9892.0	5.7	34.5	876.7	1380.3
03-b1-z6	60.2	5.0	0.8	1970	14.0	0.23	44.0	0.13	1.3	3.4	1.3	23.4	9.0	139.9	60.7	298.1	70.1	724.7	165.9	10852.8	4.1	28.9	608.6	1106.0
03-b1-z26	59.0	4.9	1.1	1558	9.8	0.02	46.5	0.07	1.6	2.8	1.2	20.6	7.5	110.5	50.0	261.1	66.1	692.3	167.0	10091.1	3.2	28.4	651.7	982.8
03-b2-z7	64.3	3.6	1.4	1184	8.0	2.56	47.1	0.65	3.7	2.5	1.1	15.5	6.1	79.2	30.6	202.7	46.9	448.6	95.7	9138.5	3.0	20.2	629.0	812.6
03-b2-z8	54.1	6.0	1.4	928	6.9	0.24	33.2	0.10	1.5	2.6	0.6	13.7	5.3	72.4	30.1	158.3	36.4	380.7	90.1	10275.2	2.7	23.6	606.8	870.7
03-b2-z9	65.7	6.6	2.5	1421	10.0	6.23	53.5	2.65	12.9	7.4	1.2	24.4	8.4	109.9	44.0	218.9	51.7	606.1	132.3	11528.8	3.8	33.3	749.3	1150.9
Mattoni gabbro (VFC04)																								
included in plagioclase																								
04-b2-z7	55.4	5.3	0.8	1650	5.1	0.14	48.8	0.64	7.3	8.1	4.1	33.1	10.6	143.1	50.7	237.1	59.7	657.6	143.9	7359.5	1.0	18.7	1132.4	670.7
included in quartz																								
04-b1-z5a	67.8	6.0	0.4	682	1.2	0.04	8.9	0.04	0.1	0.9	0.4	7.6	2.2	42.8	19.7	136.5	34.9	348.7	103.3	9524.6	0.2	15.1	462.5	681.2
04-b1-z5b	62.8	4.8	0.8	1015	1.4	0.04	10.5	0.08	0.6	1.8	1.5	13.8	4.5	68.5	29.4	152.7	34.8	390.8	100.1	8360.9	0.2	16.4	569.1	652.3
included in calcite																								
04-b1-z1	66.2	9.9	0.9	381	0.6	0.04	2.2	0.04	0.4	0.5	0.5	5.1	1.8	25.3	11.8	69.8	17.3	196.5	55.5	9594.4	0.1	10.1	210.4	376.6
04-b1-z2	59.2	6.6	0.7	1549	4.4	0.08	40.7	0.39	4.1	4.8	3.1	29.2	8.3	113.1	49.2	236.7	55.2	629.5	161.7	7389.5	1.0	22.9	817.1	728.3
at grain boundaries																								
04-a2-z2	57.3	-	0.8	1237	3.5	0.06	29.2	0.27	2.8	3.7	2.4	18.4	6.0	85.2	34.6	186.7	43.4	497.7	127.1	7457.0	0.9	14.2	564.1	531.4
04-a2-z3	64.4	10.1	0.9	1840	5.6	0.07	50.8	0.44	5.3	5.9	3.5	35.2	10.3	147.3	54.1	262.3	62.7	700.6	156.6	7829.5	1.0	19.1	1042.2	715.9
04-b1-z6	55.7	-	0.5	136	0.6	0.02	0.9	0.02	0.0	0.4	0.2	1.4	0.7	8.3	4.3	25.6	6.9	88.7	22.2	8744.2	0.1	4.0	68.4	140.7
04-b1-z3	55.5	7.0	0.9	1802	6.4	0.10	57.2	0.48	5.1	6.0	3.9	31.1	10.5	142.5	58.8	321.9	74.4	877.1	201.3	7884.3	1.4	25.9	1344.2	988.4
Val Fredda Tonalite (VFC09)																								
included in plagioclase																								
09-a2-z22	76.0	6.2	0.9	3606	26.5	0.03	86.0	0.07	2.2	5.0	2.4	49.8	18.6	240.9	115.6	596.1	118.3	1127.6	253.6	14158.3	8.3	55.2	1452.3	2559.7
09-b2-z26	66.9	8.9	1.9	3175	29.9	0.48	74.0	0.19	2.6	6.5	1.8	47.0	22.9	329.2	119.6	554.0	136.0	1417.7	282.6	13842.4	9.6	57.7	1802.3	2278.7
included in quartz																								
09-b1-z5	61.1	4.7	1.2	1440	8.6	0.03	40.1	0.07	1.5	3.0	0.9	19.0	7.2	105.6	43.0	229.7	58.7	622.6	147.1	9845.0	2.7	24.1	580.0	871.4
09-b1-z7	66.0	6.1	0.9	1882	14.8	0.07	61.8	0.12	1.5	5.0	0.9	23.2	10.5	144.1	56.8	319.0	72.8	868.3	211.9	10135.9	4.7	33.6	1094.8	1421.6
included in biotite																								
09-a1-z6	64.0	8.3	1.4	1708	11.8	0.76	51.3	0.34	2.2	3.4	1.4	26.3	10.6	134.1	54.4	302.0	62.1	672.7	143.7	10126.5	3.3	25.7	824.2	927.7
09-a1-z11	65.8	5.7	0.9	1854	12.9	0.02	43.4	0.08	1.1	2.8	1.1	22.5	8.3	127.9	53.9	285.6	69.7	739.6	168.6	10131.5	3.9	25.9	608.7	974.8
09-a2-z27	56.3	6.0	0.8	1457	11.0	0.02	46.1	0.09	1.5	3.1	0.9	18.9	7.4	100.8	41.0	213.9	60.5	624.3	128.0	8771.4	3.2	24.2	706.5	926.1
09-a2-z21	66.2	-	1.3	1764	6.4	0.03	53.2	0.17	2.4	5.5	1.8	26.6	7.6	121.1	56.9	300.4	70.3	979.6	251.2	8975.7	2.1	28.3	899.2	1374.3
09-b1-z13	64.0	3.0	0.8	1447	9.5	0.01	30.1	0.06	0.6	2.8	0.9	19.3	8.1	109.0	44.9	256.0	65.1	656.5	144.9	10580.1	3.0	19.7	405.5	846.5

Table 2:
continued

	Zr wt%	Ti ppm	Sr	Y	Nb	La	Ce	Pr	Nd	Sm	Eu	Gd	Tb	Dy	Ho	Er	Tm	Yb	Lu	Hf	Ta	Pb	Th	U
Val Fredda Tonalite (VFC09)																								
included in biotite																								
09-b1-z3	68.5	-	1.2	1513	13.8	0.11	57.4	0.08	1.1	4.3	0.8	22.8	7.9	104.5	42.0	222.6	54.6	589.3	142.3	11874.8	4.2	28.9	1049.0	1208.9
09-b2-z20	56.8	5.4	0.8	1478	8.6	0.02	39.4	0.06	1.3	3.0	1.0	16.7	6.8	103.8	45.1	239.9	60.5	639.8	148.6	8950.6	2.5	21.9	494.0	786.3
09-b2-z30	65.4	6.8	0.7	1306	8.3	0.02	37.6	0.06	1.3	2.7	1.1	17.1	6.2	96.6	41.5	220.7	56.1	566.6	137.3	11672.3	2.8	19.0	494.1	786.4
09-b2-z29	54.9	10.3	1.4	1645	11.2	2.40	46.9	0.40	2.5	4.0	1.6	22.6	8.1	119.1	48.8	252.5	63.3	651.3	142.7	9524.8	3.9	26.2	662.7	913.2
included in amphibole																								
09-a1-z19	63.6	16.7	0.9	1398	7.4	0.31	32.4	0.19	2.2	3.2	1.2	20.0	7.4	103.8	42.9	241.5	56.9	596.1	141.2	10491.2	2.5	22.5	486.2	767.3
at grain boundaries																								
09-a1-z14	65.6	8.4	1.0	1834	14.9	0.01	48.9	0.06	1.1	3.6	1.1	21.5	8.7	133.0	57.6	307.4	73.8	847.1	181.2	10636.3	4.5	27.6	572.2	1022.6
09-a2-z24	60.7	7.1	0.8	1728	16.6	0.06	66.4	0.13	2.3	4.7	1.4	33.1	10.7	143.6	56.5	283.2	69.5	736.6	165.1	10365.5	5.0	43.5	1455.6	1598.6
09-a2-z23	64.4	8.0	0.9	1702	10.1	0.04	54.4	0.10	1.7	3.5	1.8	25.4	8.9	125.3	54.4	270.8	68.8	712.3	162.4	9837.9	3.5	30.4	1045.8	1196.1
09-b1-z16	61.0	6.0	0.9	2365	8.7	0.99	34.5	0.30	2.2	4.5	1.3	30.6	12.2	174.5	77.1	381.7	90.7	964.9	206.2	10172.4	2.5	36.1	592.7	1048.9
09-b2-z18	64.0	36.9	0.7	1066	3.0	0.11	19.9	0.24	2.3	4.9	2.0	17.7	6.5	93.7	35.9	189.3	41.4	454.7	109.9	7709.7	1.1	7.4	421.8	308.7
09-b2-z28	56.3	5.8	0.9	2452	12.6	0.19	49.6	0.16	2.1	4.7	1.7	34.6	12.7	181.8	74.5	384.4	90.9	921.7	191.3	8943.1	3.4	37.9	1126.6	1348.6
Plagioclase quartz diorite (VFC13)																								
included in quartz																								
13-c1-z10	61.0	6.5	0.6	1365	11.6	0.05	53.8	0.13	1.9	3.6	1.2	28.0	10.3	109.2	40.1	229.4	72.5	722.7	120.3	11354.9	3.9	21.5	949.8	803.7
13-c2-z26	52.7	-	1.5	1726	10.8	0.05	68.3	0.17	2.5	4.9	2.3	28.0	8.8	120.7	52.2	267.0	58.9	575.7	155.8	8558.2	3.1	29.7	1522.4	1399.8
included in biotite																								
13-c1-z26	59.5	-	1.5	2418	21.1	0.02	71.7	0.11	1.5	6.0	1.6	32.8	14.4	219.8	90.4	398.2	87.9	1108.5	272.7	10979.6	6.1	48.2	1346.4	1802.1
13-c1-z15	60.2	4.1	0.7	1384	6.9	0.36	28.3	0.13	1.5	3.2	1.3	20.6	7.5	119.3	46.0	270.2	67.9	664.4	138.7	10697.3	2.8	23.1	443.7	778.4
13-c2-z23	67.2	-	1.2	1620	9.5	0.43	39.3	0.44	2.0	3.1	1.0	20.6	6.6	119.6	46.6	239.6	62.4	708.6	161.0	10522.1	2.9	21.9	572.5	895.1
included in amphibole																								
13-c1-z11	59.7	5.5	0.4	1390	8.1	0.02	41.0	0.12	1.8	3.2	0.9	18.9	7.4	103.8	43.2	229.5	60.3	694.8	154.0	10643.0	2.4	21.9	638.9	780.3
13-c2-z28	64.7	7.4	1.6	3076	21.8	0.15	35.9	0.08	1.1	3.4	1.6	32.8	13.4	222.8	92.6	511.7	109.6	1081.3	238.7	12573.0	7.2	36.6	504.4	1426.5
at grain boundaries																								
13-c2-z21	62.7	8.9	0.7	1447	7.3	0.06	33.8	0.08	1.2	3.4	1.0	22.3	7.8	114.9	46.2	244.1	61.3	634.2	155.0	10102.0	2.8	22.3	692.0	885.2
13-d1-z6	63.7	-	0.9	2473	19.2	0.03	69.2	0.11	1.7	5.0	1.7	40.1	12.8	189.8	78.4	421.4	100.0	964.8	211.1	10589.4	5.8	43.4	1195.4	1711.0

Zirconium is reported in wt.% and elements are reported in ppm

“- “ analysis below detection limit

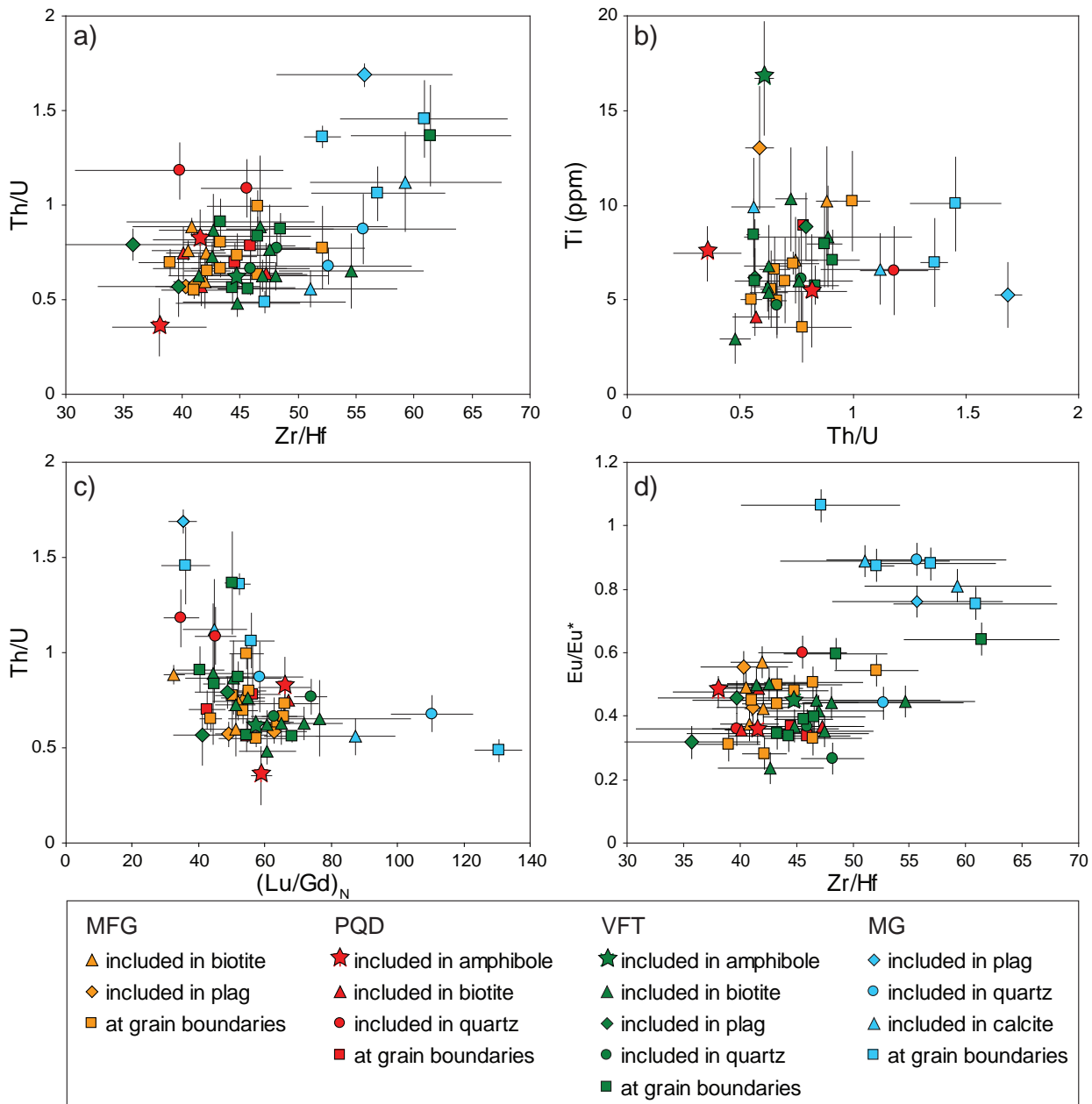


Figure 8: LA-ICP-MS trace element data of zircon crystals in thin sections, and plotted based on zircon textural relationships. Uncertainties are plotted at 2σ .

3.5.2 In situ zircon trace element composition

Zircon grains were analyzed by LA-ICP-MS for trace elements prior to extraction by micro-drill for individual dating. A laser ablation spot size of $20\ \mu\text{m}$ was used to target zircon rims, which record the final stages of zircon growth within the individual magmas. The results are summarized in Table 2 and Figure 8.

Felsic samples: VFT, PQD and MFG

The chondrite normalized REE patterns for zircon grains from felsic samples are characterized by HREE enrichment ($(\text{Lu/Gd})_N \sim 32 - 76$), positive Ce anomalies, and negative Eu anomalies ($\text{Eu/Eu}^* \sim 0.3 - 0.6$; Fig. 8) and are in good agreement with the rim analyses obtained from the conventionally separated zircons (Fig. 9). Zircon grains from the felsic

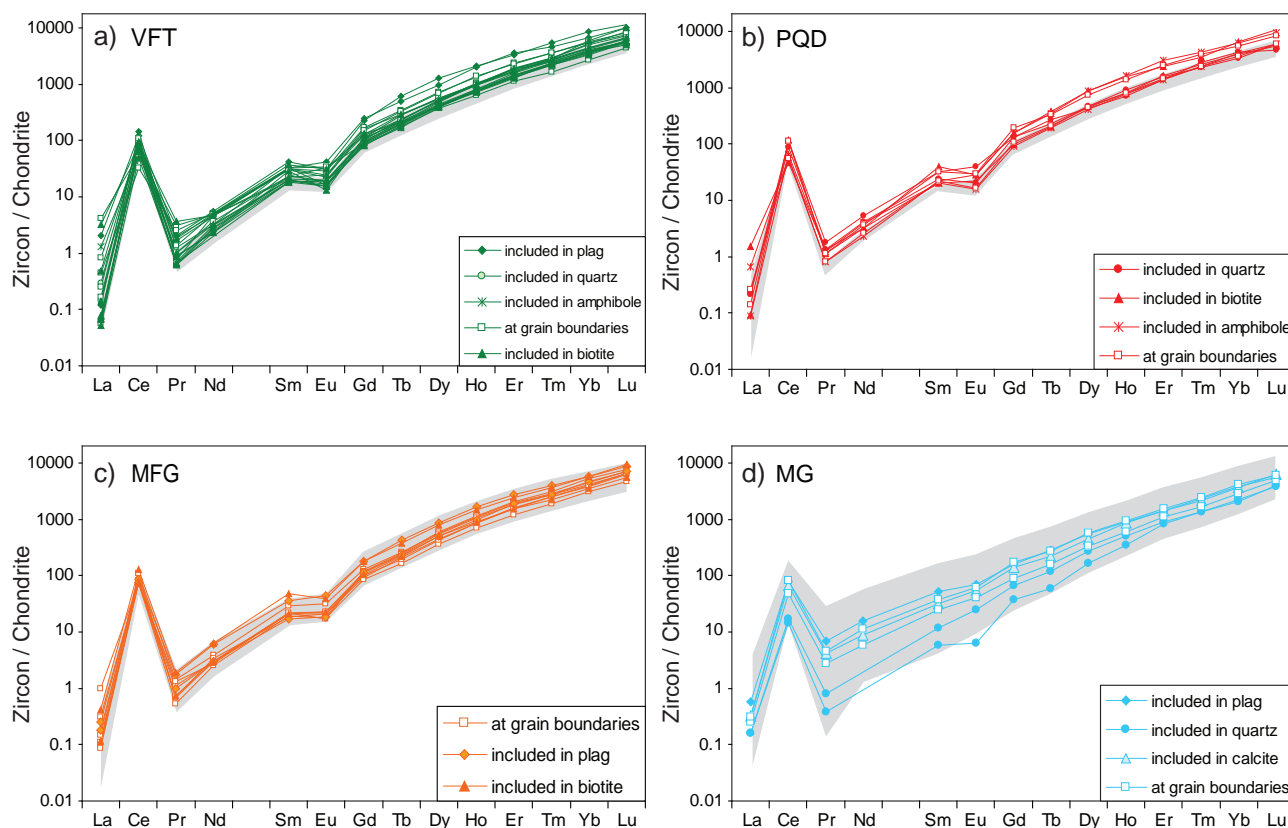


Figure 9: Chondrite normalized REE patterns for zircon, comparison between *in situ* analyses from this study and rim analyses from zircon obtained by conventional separation methods, shown in light gray for comparison.

samples are characterized by large variations in trace element ratios (e.g. Zr/Hf, Eu/Eu*, (Lu/Gd)_N and Th/U) from which individual felsic units cannot be clearly distinguished (Fig. 8).

There is no correlation between observed trace element variations and textural relationships.

Zircons from the felsic samples have Zr/Hf ratios that vary from 35 – 60 (Fig. 8a), with zircons from the PQD sample recording the most limited range (e.g. Zr/Hf = 39 – 45). Ti concentrations in zircons from the felsic samples range from ~ 3 ppm to 17 ppm, which translates into Ti-in-zircon temperatures (Ferry and Watson, 2007; using $a_{\text{TiO}_2} = 0.7$ and $a_{\text{SiO}_2} = 1$) ranging from 670°C to 835°C, consistent with the calculated

temperatures obtained from conventionally separated zircons (~700°C - 850°C; Broderick, Chapter 2). The Ti concentrations and calculated temperatures for zircons from the felsic samples record an overall increase in temperature with increasing Th/U ratios (Fig. 8b), with the exception of zircons from the PQD sample, which record large variations in Th/U ratios (0.35 – 1.2) but have rather homogenous Ti concentrations (4 – 7.5 ppm). The Th/U ratios in zircon vary from ~0.4 to 1.4, with the highest ratios recorded in quartz (PQD) and at grain boundaries (VFT, MFG). Zircons from the felsic samples record large non-systematic variations in their Th/U and Zr/Hf ratios (Fig.

8a), whereas Th/U is inversely correlated with $(\text{Lu/Gd})_N$ (Fig. 8c). Zircons have Zr/Hf ratios that are weakly correlated with Eu/Eu* (Fig. 8d), where the magnitude of the Eu anomaly is increasing with increasing fractionation, as indicated by decreasing Eu/Eu* and Zr/Hf, respectively.

Mattoni gabbro

The chondrite-normalized REE patterns for zircons from the MG sample are characterized by HREE enrichment ($(\text{Lu/Gd})_N \sim 35 - 130$), positive Ce anomalies and the lack of a negative Eu anomaly ($\text{Eu/Eu}^* \sim 0.8 - 0.9$), with the exception of zircon 04b1-z5a, included in quartz, which has a pronounced Eu/Eu* ~ 0.4 (Fig. 9d). These results are in good agreement with the rim analyses obtained from the conventionally separated zircons, although the in situ zircons record more restricted HREE concentrations (Fig. 9d).

Titanium concentrations in the MG zircons range from ~ 5 ppm to 10 ppm, which translates to Ti-in-zircon temperatures (Ferry and Watson, 2007; using $a_{\text{TiO}_2} = 0.7$ and $a_{\text{SiO}_2} = 1$) of 710°C to 780°C (Fig. 8a,c). The Ti concentrations measured in situ MG zircons record a more limited range in comparison to the Ti concentrations obtained from the rim analyses obtained from the conventionally separated zircons (~ 8 ppm to ~ 18 ppm) (see Broderick Chapter 2; Fig. 6). The MG zircons can be easily distinguished from

zircons of the felsic samples based on higher Zr/Hf and Eu/Eu* and by larger variations in Th/U and $(\text{Lu/Gd})_N$ (Fig. 8). MG zircons have Zr/Hf ratios that vary from ~ 47 to 60 and increase systematically with Th/U (Fig. 8a). The Th/U ratios in the MG zircons vary from ~ 0.5 to 1.7, with the highest ratio recorded in the zircon included in plagioclase (Fig. 8b). The large variations recorded in Th/U are inversely correlated with $(\text{Lu/Gd})_N$ indicating that zircon crystallized during the crystallization of titanite, which exerts a strong control on the MREE budget and due to its preferential incorporation of Th over U (Glazner et al., 2004; Claiborne et al., 2010).

3.5.3 Texturally controlled ID-TIMS U-Pb zircon dating

Individual zircon grains were extracted from thin sections, using a Medenbach micro-drill, for ID-TIMS analysis. Zircon U-Pb results are reported based on their textural positions and are summarized in Tables 3, 4 and Figure 10.

Six VFT zircon grains were selected and extracted from the thin sections, based on textural relationships. $^{206}\text{Pb}/^{238}\text{U}$ dates of six zircon grains from the VFT sample range from 42.34 ± 0.19 Ma to 42.81 ± 0.25 Ma (Table 4; Fig. 10a). The VFT zircons scatter over 97 ka, excluding the oldest (09b2-z18) and the youngest (09a1-z10) based on low analytical precision, and yield a

Table 3:
Texturally controlled zircon U-Pb results for samples from the Val Fredda Complex

Fraction	Composition			Isotopic Ratios					Dates (Ma)										
	Th/U ^a	Pb* (pg) ^b	Pbc (pg) ^c	Pb*/Pbc ^d	Th/U (magma) ^e	²⁰⁶ Pb/ ²⁰⁴ Pb ^f	²⁰⁶ Pb/ ²³⁸ U ^g	±2σ %	²⁰⁷ Pb/ ²³⁵ U ^g	±2σ %	²⁰⁷ Pb/ ²⁰⁶ Pb ^g	±2σ %	Corr. coef.	²⁰⁶ Pb/ ²³⁸ U ^h	±2σ abs	²⁰⁷ Pb/ ²³⁵ U ⁱ	±2σ abs	²⁰⁷ Pb/ ²⁰⁶ Pb ^h	±2σ abs
Marginal Facies granodiorite (VFC03)																			
03a2-z6	0.60	0.86	0.62	1.4	2.36	99	0.00658	0.66	0.04120	9.3	0.04540	8.8	0.77	42.36	0.28	41.00	3.7	-39	210
03b1-z30	0.66	0.71	0.67	1.1	2.40	78	0.00661	0.60	0.03770	15	0.04140	15	0.48	42.55	0.25	37.60	5.5	-271	370
03b2-z8	0.60	2.76	0.59	4.7	2.36	293	0.00661	0.13	0.04277	1.9	0.04693	1.9	0.13	42.564	0.056	42.52	0.80	40	46
Mattoni gabbro (VFC04)																			
04a2-z2	0.82	2.69	0.70	3.9	3.28	235	0.00659	0.18	0.04220	2.6	0.04650	2.6	0.22	42.451	0.077	42.00	1.1	16	62
04a2-z3	1.24	5.35	0.80	6.7	4.96	359	0.00661	0.14	0.04295	1.6	0.04716	1.6	0.27	42.546	0.061	42.70	0.66	52	37
04b1-z2	1.20	5.70	0.55	10.3	4.80	547	0.00660	0.12	0.04311	1.2	0.04737	1.1	0.54	42.515	0.053	42.86	0.49	62	26
04b1-z5a	1.03	9.41	0.77	12.2	4.12	667	0.00660	0.098	0.04268	0.95	0.04695	0.91	0.46	42.464	0.042	42.44	0.39	41	22
04b1-z5b	1.02	3.65	0.52	7.1	4.08	396	0.00661	0.11	0.04301	1.5	0.04724	1.5	0.21	42.522	0.047	42.75	0.63	56	36
04b2-z7	1.55	87.4	0.82	107	6.20	5093	0.00660	0.084	0.04273	0.23	0.04701	0.18	0.68	42.460	0.036	42.49	0.094	44.0	4.3
Val Fredda Tonalite (VFC09)																			
09a1-z10	0.54	1.04	0.73	1.4	2.16	102	0.00658	0.44	0.04300	6.2	0.04750	6.2	0.21	42.34	0.19	42.80	2.6	67	150
09a2-z21	1.06	2.81	0.61	4.6	4.24	263	0.00661	0.15	0.04290	2.4	0.04710	2.4	0.18	42.556	0.062	42.60	1.0	47	58
09a2-z23	1.05	13.0	0.57	22.6	4.20	1216	0.00660	0.16	0.04268	0.58	0.04695	0.55	0.32	42.460	0.066	42.44	0.24	41	13
09a2-z24	0.78	2.51	0.54	4.6	3.12	280	0.00660	0.20	0.04240	2.7	0.04660	2.6	0.46	42.504	0.083	42.10	1.1	21	62
09b1-z3	0.78	2.23	0.60	3.8	3.12	231	0.00660	0.16	0.04210	2.6	0.04630	2.6	0.07	42.459	0.070	41.90	1.1	8	64
09b2-z18	0.82	0.83	0.77	1.1	3.28	79	0.00665	0.59	0.04120	8.9	0.04500	8.9	0.17	42.81	0.25	41.00	3.6	-61	220
Plagioclase quartz diorite (VFC13)																			
13c1-z8	0.37	0.62	0.73	0.8	1.08	70	0.00659	1.2	0.03490	19	0.03840	19	0.70	42.46	0.49	34.80	6.7	-467	490
13c1-z11	0.71	0.83	0.74	1.1	2.84	81	0.00657	0.66	0.03420	14	0.03780	14	0.43	42.30	0.28	34.20	4.7	-506	360
13c1-z15	0.45	0.72	0.65	1.1	1.80	85	0.00661	0.55	0.03740	10	0.04100	10	0.32	42.58	0.23	37.30	3.8	-294	260

^a Th contents calculated from radiogenic ²⁰⁸Pb and the ²⁰⁷Pb/²⁰⁶Pb date of the sample, assuming concordance between U-Th and Pb systems.

^b Total mass of radiogenic Pb.

^c Total mass of common Pb.

^d Ratio of radiogenic Pb (including ²⁰⁸Pb) to common Pb.

^e Th/U ratio of magma from which mineral crystallized calculated from $D_{Th/U} = 0.25$ (from Rubatto and Hermann, 2007).

^f Measured ratio corrected for fractionation and spike contribution only.

^g Measured ratios corrected for fractionation, tracer and blank.

^h Corrected for initial Th/U disequilibrium using radiogenic ²⁰⁸Pb and Th/U[magma] specified by ^e.

ⁱ Isotopic dates calculated using the decay constants $\lambda_{238} = 1.55125E-10$ and $\lambda_{235} = 9.8485E-10$ (Jaffey et al. 1971).

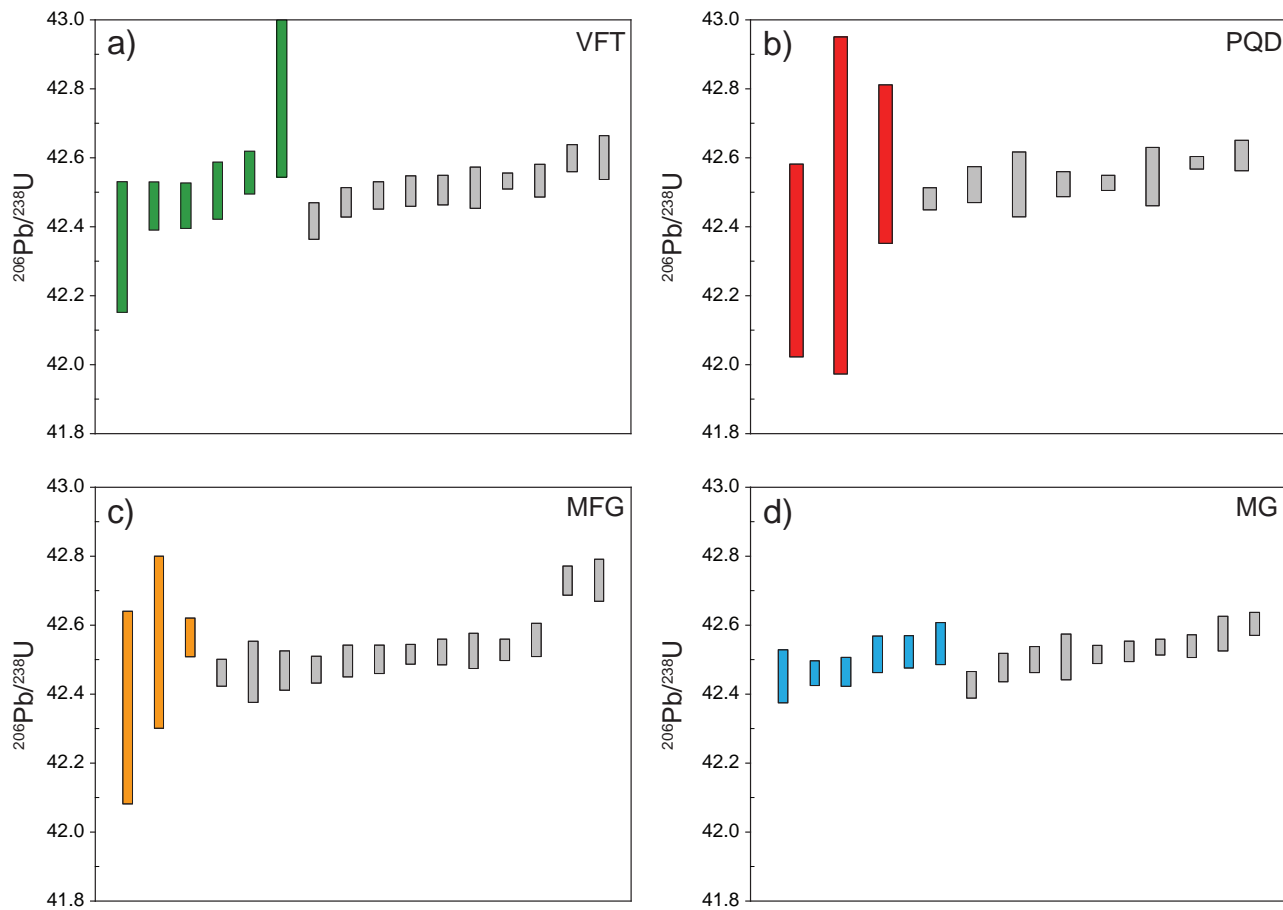


Figure 10: Age ranked plot showing $^{206}\text{Pb}/^{238}\text{U}$ dates for individual zircons extracted from thin sections. Zircon results obtained by conventional separation methods are shown in light gray for comparison.

MSWD of 2.0 ($n = 4$), which overlaps with the expected MSWD uncertainty range (Wendt and Carl, 1991) indicating that the zircon dates are equivalent. These results are in agreement with the ID-TIMS dates obtained from conventional separation methods (Fig. 10a) and the calculated weighted mean age of 42.50 ± 0.03 Ma is consistent with the previously determined period of enhanced zircon crystallization (42.55 to 42.50 Ma) associated with the thermal rejuvenation of the felsic crystal mushes, referred to as R1 (see Chapter 2).

Three PQD zircon grains were selected and extracted from the thin sections, and range from

42.30 ± 0.28 Ma to 42.58 ± 0.23 Ma (Table 4; Fig. 10b). The PQD zircons scatter of 280 ka and yield a calculated weighted mean age of 42.46 ± 0.17 Ma (MSWD = 1.2; $n = 3$). Due to the low analytical precision of PQD zircons (see discussion below) the extracted PQD zircons overlap with the entire set of zircons obtained from conventional separation methods (Fig. 10b) and are insignificant for resolving timescales of zircon crystallization.

Three MFG zircon grains were selected and extracted from the thin sections, and range from 42.36 ± 0.28 Ma to 42.564 ± 0.056 Ma (Table 4; Fig. 10c). Excluding the two low precision

Table 4:
Zircon U-Pb results based on textural relationships

Sample	Dates (Ma) $^{206}\text{Pb}/^{238}\text{U} \pm 2\sigma$	Zircon description
Marginal Facies granodiorite (VFC03)		
03a2-z6	42.36 \pm 0.28 Ma	Included in biotite (Fig. 4l)
03b1-z30	42.55 \pm 0.25 Ma	Included in plagioclase (Fig. 4k)
03b2-z8	42.564 \pm 0.056 Ma	Adjacent to quartz and biotite (Fig. 4h)
Mattoni gabbro (VFC04)		
04a2-z2	42.451 \pm 0.077 Ma	Adjacent to amphibole and plagioclase (Fig. 6c)
04a2-z3	42.546 \pm 0.061 Ma	Adjacent to amphibole and plagioclase (Fig. 6a)
04b1-z2	42.515 \pm 0.053 Ma	Included in calcite (Fig. 6g)
04b1-z5a	42.464 \pm 0.042 Ma	Included in quartz (Fig. 6f)
04b1-z5b	42.522 \pm 0.047 Ma	Included in quartz (Fig. 6f)
04b2-z7	42.46 \pm 0.036 Ma	Included in plagioclase (Fig. 6e)
Val Fredda Tonalite (VFC09)		
09a1-z10	42.34 \pm 0.19 Ma	Included in amphibole (Fig. 2i)
09a2-z21	42.556 \pm 0.062 Ma	Adjacent to biotite, plagioclase and ilmenite (Fig. 2a)
09a2-z23	42.46 \pm 0.066 Ma	Adjacent to biotite, plagioclase and quartz (Fig. 2b)
09a2-z24	42.504 \pm 0.083 Ma	Adjacent to amphibole, quartz and magnetite (Fig. 2d)
09b1-z3	42.459 \pm 0.070 Ma	Included in biotite (Fig. 2g)
09b2-z18	42.81 \pm 0.25 Ma	Adjacent to quartz, titanite and amphibole (Fig. 2c)
Plagioclase quartz diorite (VFC13)		
13c1-z8	42.46 \pm 0.49 Ma	Adjacent to quartz, apatite and biotite
13c1-z11	42.3 \pm 0.28 Ma	Included in amphibole (Fig. 4f)
13c1-z15	42.58 \pm 0.23 Ma	Included in biotite (Fig. 4d)

analyses that overlap with the entire set of zircons obtained from conventional separation methods (Fig. 10c), zircon 03b1-z30 is consistent with the previously determined period of enhanced zircon crystallization (42.60 to 42.56 Ma) associated with the initial felsic intrusions, referred to as I (see Chapter 2).

Six MG zircon grains were selected, based on textural relationships, and extracted from the thin sections for individual ID-TIMS dating. $^{206}\text{Pb}/^{238}\text{U}$ dates of six zircon grains from the MG sample range from 42.451 \pm 0.077 Ma to 42.546 \pm 0.061 Ma (Table 4; Fig. 10d). The MG zircons record scatter over 95 ka and do not overlap at the two sigma level (MSWD = 2.3) indicating that the zircon ages are not equivalent. These

results are in agreement with the ID-TIMS dates obtained from conventional separation methods (Fig. 10d).

3.6 Discussion

3.6.1 Dating small zircons from thin sections

The U-Pb data presented above indicate that our texturally controlled ID-TIMS approach can produce accurate dates, but with decreased precision on single $^{206}\text{Pb}/^{238}\text{U}$ zircon dates (Fig. 10a-c). Our low precision analyses have low radiogenic Pb to common Pb ratios ($\text{Pb}^*/\text{Pbc} < 1.5$; Table 3) relative to the higher precision data ($\text{Pb}^*/\text{Pbc} > 5$) from this study and in comparison to the zircon data obtained by conventional separation techniques (Fig. 11).

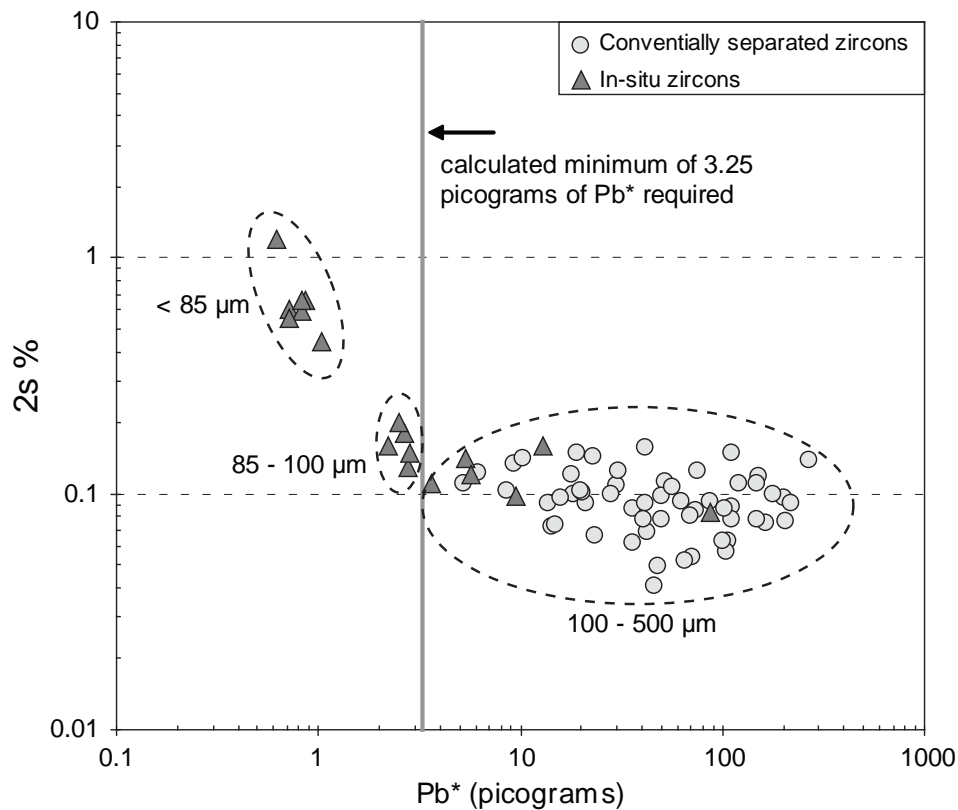


Figure 11: The 2σ % uncertainty from single $^{206}\text{Pb}/^{238}\text{U}$ zircon dates, decreases with increasing amounts of radiogenic lead (Pb^*) and corresponds to grain size. Based on the analytical blank of this study, a minimum of 3.25 picograms of Pb^* is required to obtain 0.1% precision on single $^{206}\text{Pb}/^{238}\text{U}$ dates. (See text for discussion).

Due to the low amounts of radiogenic lead (0.62 – 0.86 picograms) in the analyzed zircons, it becomes increasingly important to minimize and accurately correct for the laboratory Pb blanks (see Appendix B for details).

Schmitz and Schoene (2007) have demonstrated that the analytical blank can contribute significantly to uncertainty on the $^{206}\text{Pb}/^{238}\text{U}$ ratio. However, in this in situ study the use of Teflon microcapsules (Pbc : 0.65 ± 0.09 picograms) reduced our analytical blank by a factor of two from the previous study (Pbc : 1.4 ± 0.6 picograms) which employed the use

of individual Teflon capsules in metal jackets, scaled down 1:10, according to Krogh (1973). Based on the average analytical blank from this study (Pbc : 0.65 ± 0.09 picograms) a minimum of 3.25 picograms of Pb^* is required for a Pb^*/Pbc ratio > 5 , in order to achieve 0.1% precision on single $^{206}\text{Pb}/^{238}\text{U}$ zircon dates. Figure 11 illustrates the relationship between grain size and the required amount of Pb^* in single zircons needed to obtain high precision dates. Therefore to achieve the needed precision of 0.1%, which is necessary to relate periods of zircon growth to the paragenetic sequence, then a minimum zircon

grain size of 100 μm is required, because the extracted grains do not represent whole grains, as observed in CL images. Based on the required amount of Pb^* combined with growth textures observed in CL images (Figs. 3,5), where zircons containing cores were excluded in order to avoid bias towards older ages, then $< 10\%$ of zircons located in thin sections from the felsic samples are considered to be of suitable quality for ID-TIMS dating. Due to the small number of available zircons from the felsic samples, coupled with the low precision on single $^{206}\text{Pb}/^{238}\text{U}$ zircon dates, we are unable to link zircon U-Pb dates to specific textural relationships within the paragenetic sequence for the VFC felsic units.

3.6.2 Texturally controlled ID-TIMS dating: an example from the Mattoni gabbro

Previous high precision U-Pb geochronology of the Mattoni gabbro indicates two periods of enhanced zircon crystallization associated with emplacement, as a series of mafic sills, referred to as C1 and C2 (see Broderick Chapter 2), occurring between 42.54 ± 0.03 Ma to 42.43 ± 0.04 Ma. However these results differ significantly from previous U-Pb determinations obtained by LA-ICP-MS which indicate the presence of xenocrystic cores that range from 51.0 ± 1.1 Ma to 43.9 ± 1.2 Ma, whereas zircon rims and euhedral grains record ages of 40.3 ± 1.0 Ma

(Tiepolo et al., 2011). The observed differences between the two studies could potentially be the result of the different grain morphologies selected for analyses. Both, our data presented in Broderick Chapter 2, as well as the dates in Tiepolo et al. (2011) were obtained on zircons separated through conventional separation techniques, however the grain morphologies selected for ID-TIMS were typically elongate with euhedral margins, similar to zircon 04b1-z1 (Fig. 6h), whereas zircons selected by Tiepolo et al. (2011) for LA-ICP-MS U-Pb dating were typically anhedral fragments and “pseudo-prismatic” grains. While the application of our texturally controlled sampling approach is limited to the zircons which are exposed in our thin sections, the located zircons typically have similar grain morphologies as those described by Tiepolo et al. (2011), allowing us to evaluate whether the observed age differences between ID-TIMS and LA-ICP-MS is the result of dating different grain morphologies.

Our texturally controlled results indicate that among the grains located and analyzed no xenocrystic cores were observed in CL images (Fig. 7) or detected in our U-Pb dates, furthermore we did not observe any significant age differences between anhedral and euhedral grains. In fact, zircons extracted from MG thin sections are in agreement with the previous ID-TIMS dates obtained by conventional

separation methods (Fig. 10d), despite using different grain morphologies for dating. Therefore we argue that our U-Pb zircon dates for the Mattoni gabbro are accurate based on the reproducibility of our results between the two studies and with additional evidence coming from ID-TIMS inter-laboratory reproducibility using the same analytical approaches (Slama et al., 2008; Chiaradia et al., 2013; Kennedy et al., in prep). While the LA-ICP-MS U-Pb dates of Tiepolo et al. (2011) are less precise ($\sim 2 - 3\%$ on weighted mean $^{206}\text{Pb}/^{238}\text{U}$ ages) in comparison to our ID-TIMS U-Pb dates in which we obtain 0.1% precision on single $^{206}\text{Pb}/^{238}\text{U}$ zircon dates. The precision and accuracy of LA-ICP-MS dates are monitored by routine measurements of standard zircons (Kosler and Sylvester, 2003). However, in the study of Tiepolo et al. (2011) during the analytical session in which the so-called xenocrystic zircons were analyzed, the repeat measurements of the zircon standard 91500 (1065 Ma; Weidenbeck et al., 1995) scatter between 1007 Ma to 1165 Ma resulting in a weighted mean age of 1075 Ma ($n = 10$), as a result the authors only used 5 of the 10 measured zircon standards, yielding a weighted mean age of 1063 Ma, to reduce the unknown zircon measurements. Therefore, we conclude that due to the lack of reproducibility on the standard zircon measurements used for calibration, that the xenocrystic U-Pb

zircon dates presented by Tiepolo et al. (2011) are considered unreliable for the MG. For the zircons extracted from the MG sections, we obtained precision between 0.08% and 0.18% on single $^{206}\text{Pb}/^{238}\text{U}$ zircon dates, therefore in the following we attempt to relate the textural relationships between zircons and the matrix forming minerals (e.g. amphibole, quartz, calcite and plagioclase) to periods of zircon growth during the in situ crystallization of the Mattoni gabbro. Based on anhedral zircon forms adjacent to the matrix amphibole faces (Fig. 6a-d) and the absence of zircon inclusions in amphibole, we conclude that matrix amphibole crystallization occurred prior to zircon crystallization. Therefore, based on our U-Pb data the minimum age estimation for amphibole crystallization is constrained by the oldest zircon date of 42.546 ± 0.061 Ma (Fig. 12). Zircons included in quartz, calcite and plagioclase indicate that zircon growth occurred before or during the crystallization of their respective host minerals. Because both zircons 04b1-5a and 04b1-z5b (Fig. 6f) are included in quartz and each zircon has a quartz inclusion, we suggest that zircon and quartz crystallization is coeval at 42.464 ± 0.042 Ma and 42.522 ± 0.047 Ma (Fig. 12). The calcite, in which 04b1-z1 and 04b1-z2 are included, forms the typically round ocelli rimmed with small cpx grains (Fig. S4). The presence of ocelli in the Mattoni gabbro has

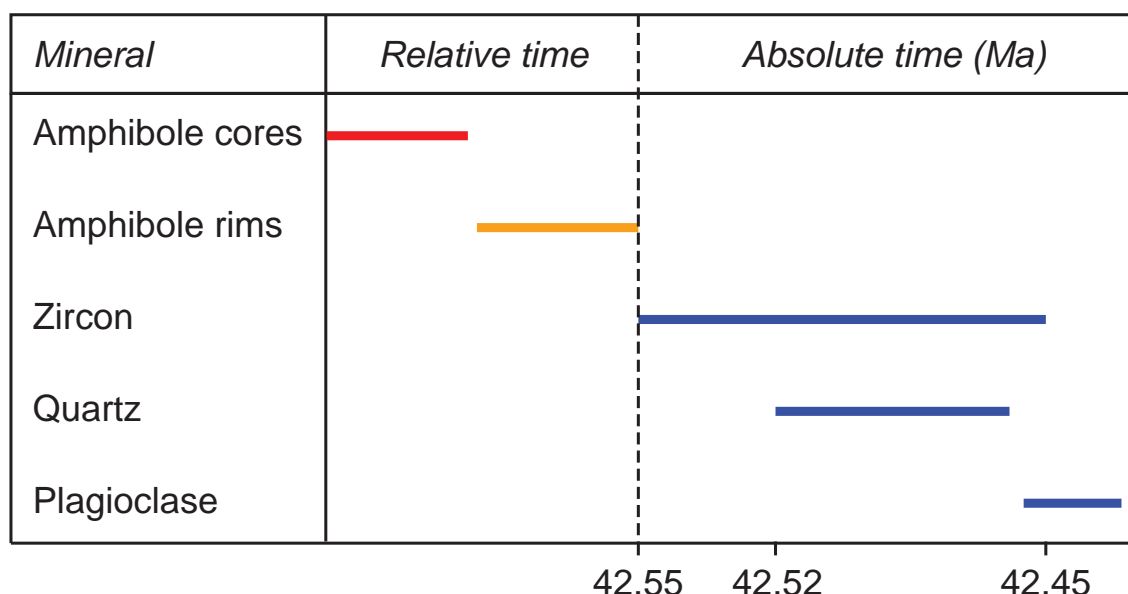


Figure 12: Paragenetic sequence for the Mattoni gabbro. Absolute time is constrained by zircon U-Pb dates and textural relationships. Red line: $T = > 1100^{\circ}\text{C}$; orange line: $T = 950 - 750^{\circ}\text{C}$ (Ulmer et al., 1983; Nimis and Ulmer, 1998); blue lines : $T = < 750^{\circ}\text{C}$ (zircon temperatures based Ti-in zircon from this study, quartz and plagioclase temperatures are estimates based on textural relationships with zircon).

been attributed to the residual melt becoming fluid oversaturated and the formation of gas bubbles that were subsequently filled with calcite, quartz and plagioclase (Ulmer et al., 1983). In contrast, Blundy and Sparks (1992) suggest the presence of ocelli are the result of the reaction between calcite, quartz and plagioclase with the mafic magma and are therefore xenocrystic. Trace element compositions of the two zircons included in the ocelli are consistent with the distinctive zircon trace element ratios (e.g. Zr/Hf, Eu/Eu*) compositions from Mattoni magma (Fig. 8a,d). Therefore we rule out the ocelli containing zircons as xenocrysts. Plagioclase is mainly poikilitic and encloses grains of matrix forming minerals (e.g. amphibole, cpx) and accessory minerals (zircon, titanite), which is consistent with crystallization of plagioclase

late in the paragenetic sequence of the Mattoni gabbro. Zircon 04b1-z5a appears to have a plagioclase inclusion; however upon close inspection of the BSE image of this grain, the plagioclase inclusion is associated with a fracture and is most likely related to the plagioclase overgrowing zircon (Fig. 6f). Zircons included in and adjacent to plagioclase, are euhedral (Fig. 6a-d) and lack Eu anomalies (Fig. 9), thus providing support that zircon crystallized prior to plagioclase crystallization. Therefore, the maximum age estimation for plagioclase crystallization is constrained by the youngest zircon date of 42.451 ± 0.077 Ma (Fig.12). Our previous high precision U-Pb zircon dates from Mattoni gabbro zircons indicates two periods of enhanced zircon crystallization; C1: ~ 42.55 to 42.47 Ma and; C2: ~ 42.45 to 42.41

Ma. The results of this in situ study indicate that zircons, both type 1 and type 2, crystallized during the C1 period of enhanced zircon crystallization, with the exception of the youngest zircon (type 1) which crystallized during the C2 period of enhanced zircon crystallization. Even though we obtained precision between 0.08% and 0.18% on single $^{206}\text{Pb}/^{238}\text{U}$ zircon dates on extracted MG zircons, we are unable to link periods of zircon growth to the paragenetic sequence. This may be the result of the limited number of analyses ($n = 6$), however based on the reproducibility in the spread of $^{206}\text{Pb}/^{238}\text{U}$ zircon dates between this study (42.451 ± 0.077 Ma to 42.546 ± 0.061 Ma) and our previous results from Broderick Chapter 2 (42.426 ± 0.039 Ma to 42.539 ± 0.033 Ma), we conclude that this data set is representative of the zircon crystallization of the MG. While we can identify early amphibole crystallization versus late plagioclase crystallization, our ability to link U-Pb zircon dates to the paragenetic sequence is precluded by the lack of significant differences in our zircon U-Pb dates.

3.7 Conclusions

Our texturally controlled ID-TIMS U-Pb dating of zircon in thin sections combines petrographic information related to zircon growth with high precision dates of zircons extracted from thin

sections in attempt to relate periods of enhanced zircon growth to specific crystallizing phases within individual paragenetic sequences. The results presented here indicated that zircon saturated early and crystallized through the history of the VFC felsic samples, based on observed zircon inclusions in all crystallizing phases. However the low amounts of Pb* in zircons from the felsic samples resulted in low analytical precision, and therefore it was not possible to link zircon U-Pb dates to the crystallization of specific mineral phases.

In contrast, zircon grains extracted from the MG sections contained sufficient amounts of Pb* (> 3.25 picograms of Pb*), resulting in high precision (0.08% - 0.18%) on single $^{206}\text{Pb}/^{238}\text{U}$ zircon dates, thus providing the potential to link zircon U-Pb dates with the crystallization of mineral phases within the MG. However, the results presented here indicate that zircon crystallization is limited to the late crystallizing phases of plagioclase in quartz, within the matrix, therefore due to the late saturation of zircon and the lack of significant differences in our U-Pb zircon dates, we are unable to resolve the absolute timing of the paragenetic sequence of the MG.

However, based on textural relationships with dated zircons, we were able to constrain the timing of early amphibole crystallization and late plagioclase crystallization. In addition we

were able to reproduce the spread in zircon dates previously obtained by conventional separation techniques. This confirms that the zircons dates obtained by conventional separation techniques are representative of zircon crystallization and that our results are not biased by grain selection.

References

- Blundy, J. D., and Shimizu, N., 1991, Trace element evidence for plagioclase recycling in calc-alkaline magmas: *Earth and Planetary Science Letters*, v. 102, no. 2, p. 178-197.
- Bowring, J. F., McLean, N. M., and Bowring, S. A., 2011, Engineering cyber infrastructure for U-Pb geochronology: Tripoli and U-Pb_Redux: *Geochemistry Geophysics Geosystems*, v. 12, p. Q0AA19.
- Brack, P., 1983, Multiple intrusions-examples from the Adamello batholith (Italy) and their significance on the mechanism of intrusion: *Mem. Soc. Geol. Ital*, v. 26, p. 145-157.
- Callegari, E., and Brack, P., 2002, Geological map of the Tertiary Adamello Batholith (Northern Italy Explanatory notes and legend: *Mem. Sci. Geol*, v. 54, p. 19-49.
- Chiaradia, M., Schaltegger, U., Spikings, R., Wotzlaw, J.-F., and Ovtcharova, M., 2013, How Accurately Can We Date the Duration of Magmatic-Hydrothermal Events in Porphyry Systems? -An Invited Paper: *Economic Geology*, v. 108, no. 4, p. 565-584.
- Claiborne, L. L., Miller, C. F., and Wooden, J. L., 2010, Trace element composition of igneous zircon: a thermal and compositional record of the accumulation and evolution of a large silicic batholith, Spirit Mountain, Nevada: *Contributions to Mineralogy and Petrology*, v. 160, no. 4, p. 511-531.
- Coleman, D. S., Gray, W., and Glazner, A. F., 2004, Rethinking the emplacement and evolution of zoned plutons: Geochronologic evidence for incremental assembly of the Tuolumne Intrusive Suite, California: *Geology*, v. 32, no. 5, p. 433-436.
- Corfu, F., Hanchar, J. M., Hoskin, P. W. O., and Kinny, P., 2003, Atlas of zircon textures: *Reviews in mineralogy and geochemistry*, v. 53, no. 1, p. 469-500.
- Ferry, J. M., and Watson, E. B., 2007, New thermodynamic models and revised calibrations for the Ti-in-zircon and Zr-in-rutile thermometers: *Contributions to Mineralogy and Petrology*, v. 154, no. 4, p. 429-437.
- Glazner, A. F., Bartley, J. M., Coleman, D. S., Gray, W., and Taylor, R. Z., 2004, Are plutons assembled over millions of years by amalgamation from small magma chambers?: *GSA today*, v. 14, no. 4/5, p. 4-12.
- Kosler, J. and Sylvester, P. J., 2003, Present trends and the future of zircon in geochronology; laser ablation ICPMS (in Zircon) *Reviews in Mineralogy and Geochemistry*, 53: 243-275
- Krough, T. E., 1973, A low contamination method for hydrothermal decomposition of zircon and extraction of U and Pb for isotope age determination: *Geochem. Cosmochim. Acta*, v. 37, p. 485-494.
- Leuthold, J., Müntener, O., Baumgartner, L. P., Putlitz, B., Ovtcharova, M., and Schaltegger, U., 2012, Time resolved construction of a bimodal laccolith (Torres del Paine, Patagonia): *Earth and Planetary Science Letters*, v. 325, p. 85-92.
- Ludwig, K. R., 2005, Isoplot/Ex Version 5.00: a geological toolkit for Microsoft Excel: *Berkeley Geochronology Center Special Publication*, 70pp, v. 4.
- Mattinson, J. M., 2005, Zircon U-Pb chemical abrasion ("CA-TIMS") method: combined annealing and multi-step partial dissolution analysis for improved precision and accuracy of zircon ages:

- Chemical Geology, v. 220, no. 1, p. 47-66.
- McLean, N. M., Bowring, J. F., and Bowring, S. A., 2011, An algorithm for U-Pb isotope dilution data reduction and uncertainty propagation: *Geochemistry, Geophysics, Geosystems*, v. 12, no. 6.
- Memeti, V., Paterson, S., Matzel, J., Mundil, R., and Okaya, D., 2010, Magmatic lobes as “snapshots” of magma chamber growth and evolution in large, composite batholiths: An example from the Tuolumne intrusion, Sierra Nevada, California: *Geological Society of America Bulletin*, v. 122, no. 11-12, p. 1912-1931.
- Michel, J., Baumgartner, L., Putlitz, B., Schaltegger, U., and Ovtcharova, M., 2008, Incremental growth of the Patagonian Torres del Paine laccolith over 90 ky: *Geology*, v. 36, no. 6, p. 459-462.
- Miller, J. S., Matzel, J. E. P., Miller, C. F., Burgess, S. D., and Miller, R. B., 2007, Zircon growth and recycling during the assembly of large, composite arc plutons: *Journal of Volcanology and Geothermal Research*, v. 167, no. 1-4, p. 282-299.
- Möller, A., O'Brien, P. J., Kennedy, A., and Kröner, A., 2003, Linking growth episodes of zircon and metamorphic textures to zircon chemistry: an example from the ultrahigh-temperature granulites of Rogaland (SW Norway): *Geological Society, London, Special Publications*, v. 220, no. 1, p. 65-81.
- Nimis, P., and Ulmer, P., 1998, Clinopyroxene geobarometry of magmatic rocks Part 1: An expanded structural geobarometer for anhydrous and hydrous, basic and ultrabasic systems: *Contributions to Mineralogy and Petrology*, v. 133, no. 1, p. 122-135.
- Rubatto, D., 2002, Zircon trace element geochemistry: partitioning with garnet and the link between U-Pb ages and metamorphism: *Chemical Geology*, v. 184, no. 1, p. 123-138.
- Schaltegger, U., Brack, P., Ovtcharova, M., Peytcheva, I., Schoene, B., Stracke, A., Marocchi, M., and Bargossi, G. M., 2009, Zircon and titanite recording 1.5 million years of magma accretion, crystallization and initial cooling in a composite pluton (southern Adamello batholith, northern Italy): *Earth and Planetary Science Letters*, v. 286, no. 1, p. 208-218.
- Schmitz, M. D., and Schoene, B., 2007, Derivation of isotope ratios, errors, and error correlations for U-Pb geochronology using ^{205}Pb - ^{235}U -(^{233}U)-spiked isotope dilution thermal ionization mass spectrometric data: *Geochemistry, Geophysics, Geosystems*, v. 8, no. 8.
- Schoene, B., Schaltegger, U., Brack, P., Latkoczy, C., Stracke, A., and Günther, D., 2012, Rates of magma differentiation and emplacement in a ballooning pluton recorded by U-Pb TIMS-TEA, Adamello batholith, Italy: *Earth and Planetary Science Letters*, v. 355, p. 162-173.
- Slàma, J., Kosler, J., Condon, D. J., Crowley, J. L., Gerdes, A., Hanchar, J. M., Horstwood, M. S. A., Morris, G. A., Nasdala, L., and Norberg, N., 2008, Plesovice zircon - a new natural reference material for U-Pb and Hf isotopic microanalysis: *Chemical Geology*, v. 249, no. 1, p. 1-35.
- Stauffer, A. K., 2012, Petrology and mineral chemistry of the Val Fredda Complex leucocratic units, Adamello, Italy: MSc thesis, ETH Zürich.
- Tiepolo, M., and Tribuzio, R., 2005, Slab-melting during Alpine orogeny: evidence from mafic cumulates of the Adamello batholith (Central Alps, Italy): *Chemical geology*, v. 216, no. 3, p. 271-288.
- Tiepolo, M., Tribuzio, R., and Langone, A., 2011, High-Mg andesite petrogenesis by amphibole crystallization and ultramafic crust assimilation: Evidence from Adamello hornblendites (Central Alps, Italy): *Journal of Petrology*, v. 52, no. 5, p. 1011-1045.
- Tiepolo, M., Tribuzio, R., and Vannucci, R., 2002, The compositions of mantle-derived melts developed during the Alpine continental collision: *Contributions to Mineralogy and Petrology*, v. 144, no. 1, p. 1-15.
- Ulmer, P., Callegari, E., and Sönderegger, U. C.,

- 1983, Genesis of the mafic and ultramafic rocks and their genetical relations to the tonalitic-trondhjemitic granitoids of the southern part of the Adamello batholith (Northern Italy): *Mem. Soc. Geol. Ital.*, v. 26, p. 171-222.
- Wiedenbeck, M., Allé, P., Corfu, F., Griffin, W.L., Meier, M., Oberli, F., von Quadt, A., Roddick, J.C., and Spiegel, W., 1995, Three natural zircon standards for U-Th-Pb, Lu-Hf, trace element and REE analyses: *Geostandards Newsletter*, v. 19, p. 1-23.
- Wotzlaw, J.-F., Schaltegger, U., Frick, D. A., Dungan, M. A., Gerdes, A., and Günther, D., 2013, Tracking the evolution of large-volume silicic magma reservoirs from assembly to supereruption: *Geology*.
- Zong, K., Liu, Y., Gao, C., Hu, Z., Gao, S., and Gong, H., 2010, In situ U-Pb dating and trace element analysis of zircons in thin sections of eclogite: refining constraints on the ultra high-pressure metamorphism of the Sulu terrane, China: *Chemical Geology*, v. 269, no. 3, p. 237-251.

Chapter 4

TRACKING REE VARIATIONS IN MELT COMPOSITIONS DURING THE REJUVENATION OF FELSIC CRYSTAL MUSHES USING TRACE ELEMENT COMPOSITIONS OF TITANITE AND ZIRCON

Abstract

We present equilibrium REE melt compositions calculated from trace element concentrations in crystallizing mineral assemblages from the Val Fredda Complex (VFC), N. Italy, in order to track the magmatic evolution of an incrementally assembled pluton. Trace element analyses of titanite and zircon, acquired from the same mineral volume used for high precision U-Pb dating, allow us to track changes in the melt compositions as a function of time. Titanite occurs as a major host phase for the rare earth element (REE) budget during crystallization of the VFC and records trace element compositions that are distinct for each magma composition, ranging from gabbro to granodiorite. Calculated mineral equilibrium melt compositions, combined with the Zr-in-titanite thermometer reveals coeval titanite and amphibole crystallization at temperatures ranging from $\sim 700^{\circ}\text{C}$ to 750°C in the felsic melts and coeval titanite and zircon crystallization at $\sim 800^{\circ}\text{C}$ in the mafic melts. The melts in equilibrium with titanite provide insights into melt compositions at low crystallization temperatures, however they cannot be related to titanite U-Pb dates which reflect cooling below the 650°C closure temperature.

In contrast to titanite, zircon contains only small percentages ($< 10\%$) of the REE budget, despite recording prolonged periods of zircon growth over 100 – 200 ka timescales. Calculated equilibrium melt compositions for zircon reflect coeval crystallization with plagioclase and to a lesser extent amphibole. However, large variations are observed in zircon equilibrium melt compositions and show no correlation through time. We interpret the non-systematic melt variations to represent chemically distinct magma batches. During periods of rejuvenation zircon equilibrium melt batches require $\sim 50\%$ crystallization of varying proportions of plagioclase and amphibole, from melts in equilibrium with initial zircons, while other equilibrium melt batches appear to reflect different degrees of mixing with mafic melts. This study illustrates the power of applying trace element compositions from crystallizing mineral assemblages, to obtain a detailed record of magmatic evolution which is not evident in whole rock studies.

* Manuscript (Broderick, Stauffacher, Frick, Günther, Schaltegger) in preparation

4.1 Introduction

While it is common to use whole rock compositions in order to discuss differentiation within a suite of plutonic rocks (Noyes et al., 1983; Ulmer et al., 1983; Gromet and Silver, 1986; Blundy and Sparks, 1992; Glazner et al., 2008; Gray et al., 2008; Stauffacher, 2012), growing evidence supports the fact that plutons are incrementally assembled by multiple injections over 10 to 100 ka timescales (Michel et al., 2008; Schaltegger et al., 2009; Leuthold et al., 2012; Schoene et al., 2012; Broderick, Chapter 2). During periods of successive intrusions, magma temperatures and composition can fluctuate within magma batches, resulting in periods of dissolution and growth during which time the proportions of crystals and melt vary throughout a magmas evolution (Claiborne et al., 2010; Wotzlaw et al., 2013; Broderick, Chapter 2), therefore highlighting that the use of whole rock compositions are not representative of the melt composition at the time of mineral crystallization.

The growth and dissolution of accessory minerals, such as allanite, apatite, titanite and zircon, can have a strong influence on the trace element budget of magmas (Gromet and Silver, 1983; Sawka, 1988; Schaltegger and Krähenbühl, 1990; Hermann, 2002; Hoskin and Schaltegger, 2003; Bea et al., 2006; Rubatto and

Hermann, 2007; Claiborne et al., 2010; Wotzlaw et al., 2013) and are therefore often applied as tracers for magmatic processes (Glazner et al., 2008; Claiborne et al., 2010; Schoene et al., 2012; Wotzlaw et al., 2013). However our ability to reconstruct the evolution of a magma depends on the saturation and survivability of accessory phases (Hoskin et al., 2000; Hanchar and Watson, 2003) in a magma batch during periods of successive intrusions.

In this study, we utilize trace element concentrations in titanite and zircon, obtained by TIMS-TEA analysis (Schoene et al., 2010) from the same volume of titanite and zircon used for U-Pb determinations (Broderick, Chapter 2), in order to evaluate magma evolution during incremental emplacement as a function of time. We calculate trace element variations in the melt, by applying published partition coefficients to the trace element compositions of titanite and zircon. Combined with calculated equilibrium melt compositions for major crystallizing phases such as amphibole and plagioclase, we attempt to reconstruct magma evolution during incremental assembly.

The Val Fredda Complex (VFC), located in the southern tip of the Adamello batholith, N. Italy provides insights into the history of a pluton that was incrementally constructed from compositionally diverse magma compositions.

Zircon U-Pb dates record 100 – 200 ka periods of protracted growth, as the result of multiple periods of enhanced zircon crystallization (Broderick, Chapter 2). Whereas titanite U-Pb dates record the near solidus crystallization of felsic crystal mushes and mafic melts. The equilibrium melt compositions presented here highlight large variations in melt compositions in response to periods of remelting and remobilization of felsic crystal mushes, where individual magma batches record varying degrees of melting, crystallization and mixing.

4.2 Geologic setting

The Tertiary Adamello Batholith is exposed over an area of ~670 km² with ~2 km of vertical relief, in the Southern Alps, Northern Italy (Brack, 1983; Callegari and Brack, 2002). The Adamello batholith is mainly composed of tonalites, thondjemites and granodiorites with minor mafic units in the southern most part of the batholith (Brack, 1983; Callegari and Brack, 2002). The mafic rocks occur mainly in the periphery and are best exposed in the Val Fredda Complex and the Blumone Complex (Ulmer et al., 1983; Blundy and Sparks, 1992; Tiepolo et al., 2005, 2011).

Based on detailed fieldwork (Brack, 1983; Ulmer et al., 1983; Blundy and Sparks, 1992) the VFC intrusion was described as a complex system that

was constructed by a series of felsic magmas that show vertical accretion by horizontal injections of mafic sills, of variable thickness ~ 0.5 m up to 100 m, into the crystallizing roof of a larger magmatic system. High precision U-Pb zircon dates from the VFC felsic and mafic units, record protracted zircon growth over 100 – 200 ka within individual units. U-Pb probability density distribution curves, for individual units, record multiple periods of enhanced zircon crystallization. Coinciding periods of enhanced crystallization indicate that the VFC units share a common thermal history associated with cooling after episodes of rejuvenation the felsic crystal mushes by repeated mafic injections (Broderick, Chapter 2). Based on petrographic relationships, zircon saturates early within the felsic units and crystallizes throughout the evolution of the felsic magmas (Broderick, Chapter 3). However, during periods of enhanced zircon crystallization, the chemical composition of zircon record non-systematic trace element variations, which we interpret as reflecting zircon crystallization from chemical distinct magma batches (Broderick, Chapter 2).

This study focuses on the Val Fredda Complex (VFC), a small marginal intrusion exposed over ~6 km² in the southern most part of the batholith (Fig.1), that consists of five distinct, lithological units: (1) the Val Fredda tonalite (VFT) outcrops mainly in the north of the complex; (2) the

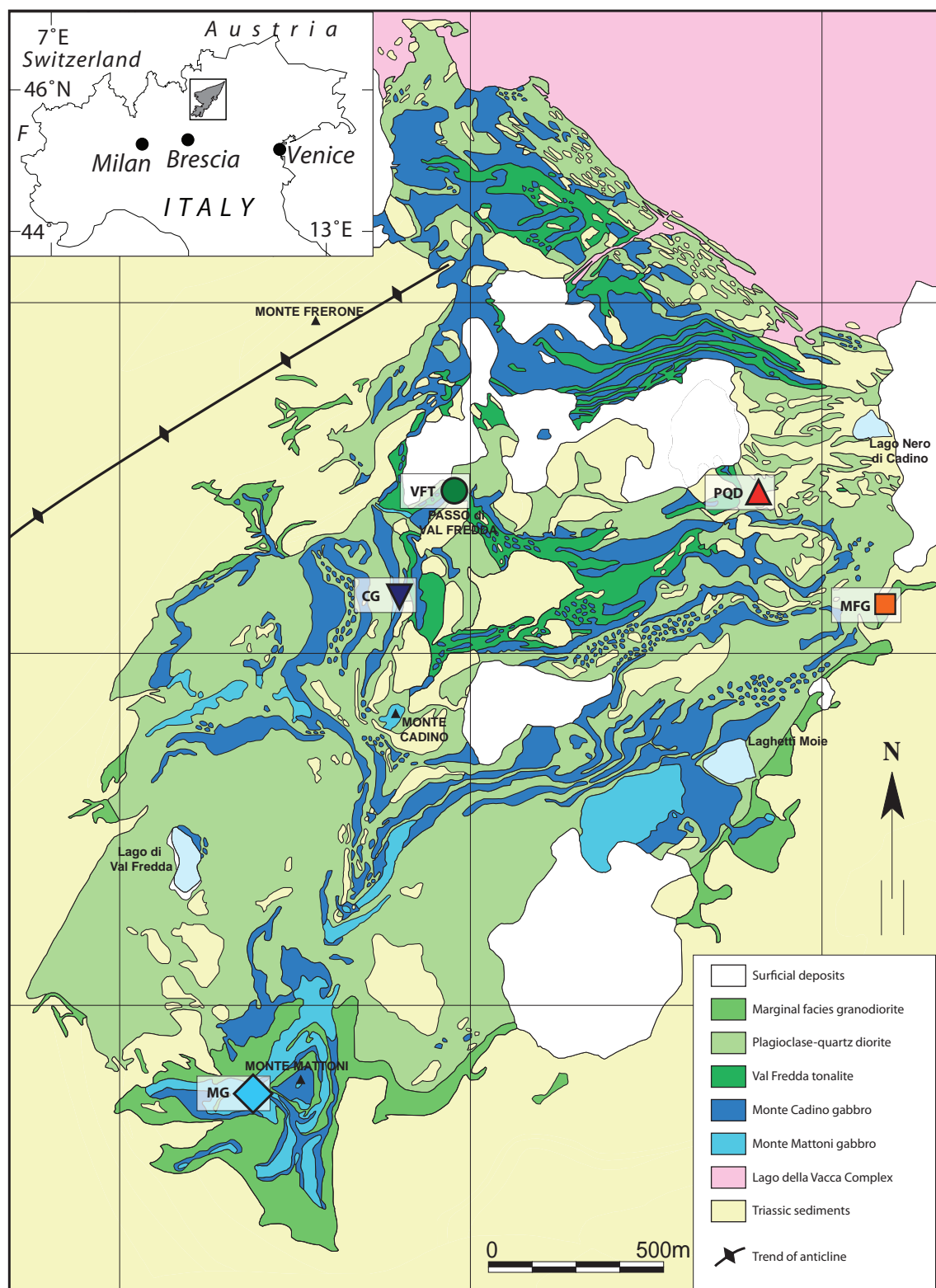


Figure 1: Simplified geologic map of the Val Fredda Complex, modified after Blundy and Sparks (1992), located in the southern most part of the Adamello batholith (see inset map for location). Sample locations for titanite and zircon data: MFG = Marginal facies granodiorite; PQT = Plagioclase quartz diorite; VFT = Val Fredda tonalite; CG = Cadino gabbro; MG = Mattoni gabbro.

plagioclase quartz diorite (PQT) outcrops mainly in the central and northern parts; (3) the marginal facies granodiorite (MFG) outcrops

mainly along the southern and eastern margins; (4) the Mattoni gabbro (MG) occurs mainly in the southern most part of the pluton near Monte

Mattoni; (5) the Cadino gabbro (CG) occurs through out the pluton as a series of horizontal sheets separated by felsic units (PQD, VFT) of variable thickness (mm to m scale) depending on the locality but outcrops most abundantly at Monte Cadino.

4.3 Petrography

Sample locations are shown in Fig. 1 and petrographic descriptions including titanite textures are given below and zircon descriptions are given in Chapter 3.

The Marginal Facies granodiorite (MFG) has a porphyritic texture and is characterized by ~ 30 % phenocrysts of euhedral plagioclase (≤ 5 mm), biotite (≤ 4 mm) and rounded quartz (≤ 4 mm) in a fine grained aplitic matrix of K-feldspar and quartz, and with minor amphibole. Plagioclase grains are oscillatory zoned and record zoned compositions from An_{72-41} in the cores to An_{24-19} in the rims (Blundy and Shimizu, 1991). Accessory minerals include titanite, zircon and apatite forming subhedral to euhedral grains and anhedral magnetite. The MFG contains titanite grains that range from ~100 μ m to ~500 μ m. MFG titanite grains are subhedral to euhedral and crystallize at grain boundaries with quartz and potassium-feldspar. However, all titanite grains identified in thin section have irregular shaped embayments that are filled with either

quartz or potassium-feldspar (Fig. 2a).

The Plagioclase quartz diorite (PQD) has an equigranular texture, composed of plagioclase (≤ 4 mm), quartz (≤ 4 mm) and lacks K-feldspar. Plagioclase grains typically contain resorbed cores and exhibit oscillatory zoning, but show weak compositional variations (e.g. An_{43-40} ; Blundy and Shimizu, 1991). Mafic minerals are euhedral biotite (≤ 4 mm), amphibole (≤ 6 mm; pargasite to Mg-hornblende; Stauffacher, 2012) and anhedral magnetite (< 1 mm). Accessory minerals are subhedral to euhedral grains of titanite, zircon and apatite. The PQD contains titanite grains that are anhedral to subhedral and are ≤ 50 μ m, interstitial titanite is more abundant, relative to grains, and is spatially associated with all PQD forming minerals (Fig. 2b).

The Val Fredda tonalite (VFT) has a weakly porphyritic texture and is characterized by euhedral plagioclase (≤ 7 mm) and rounded quartz (≤ 3 mm) phenocrysts and minor K-feldspar (< 1 mm). Plagioclase grains record variable compositions (An_{85-15} ; Blundy and Shimizu, 1991) and typically contain resorbed calcic cores with oscillatory zoned sodic rims. Mafic minerals are euhedral biotite (≤ 4 mm), amphibole (≤ 7 mm; Mg-hornblende; Stauffacher, 2012) and anhedral magnetite (< 1 mm) and accessory minerals include titanite, zircon, apatite and interstitial ilmenite. The VFT contains anhedral titanite grains that are ≤ 50

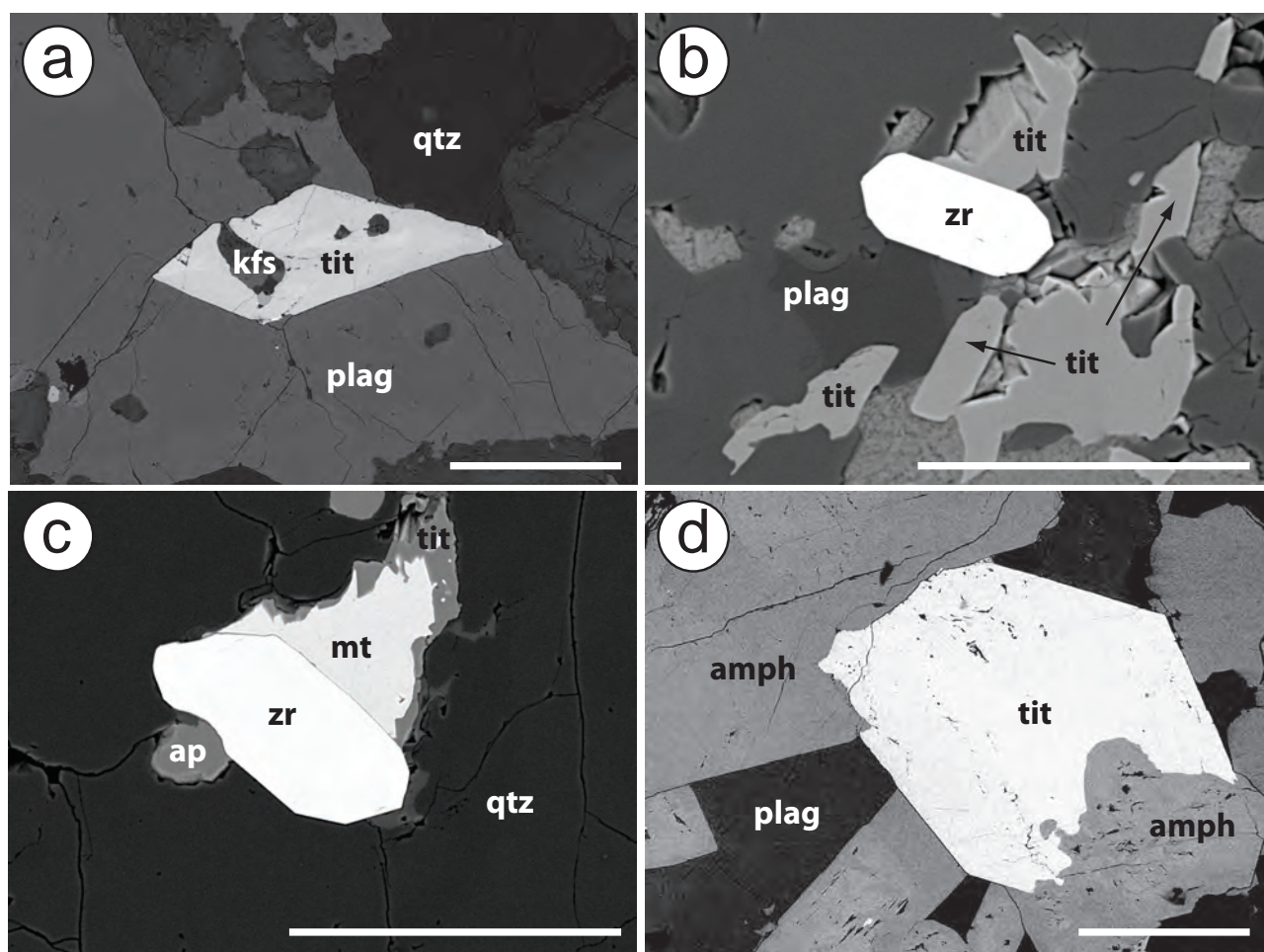


Figure 2: BSE images of representative titanite grains in thin sections from: a) MFG: euhedral titanite with irregular embayment filled with K-feldspar; b) PQD: interstitial titanite; c) VFT: titanite overgrowth on magnetite; d) MG: titanite inter-grown with matrix amphibole. amph = amphibole; ap = apatite; kfs = K-feldspar; mt = magnetite; plag = plagioclase; qtz = quartz; tit = titanite; zr = zircon. Scale bars = 100 μm

μm and interstitial titanite that mainly occurs as overgrowths on magnetite (Fig. 2c).

The Mattoni gabbro (MG) has a porphyritic texture and is characterized by large prismatic amphiboles (up to 8 mm) in a matrix mainly composed of plagioclase (≤ 4 mm), euhedral clinopyroxene (< 1 mm), green amphibole (≤ 3 mm) and minor quartz. The large amphiboles are compositionally zoned and contain brown cores (Ti-pargasite; Tiepolo et al., 2002), which contain inclusions of clinopyroxene and

olivine. Green amphibole rims (Mg-hornblende; Tiepolo et al., 2005) are compositionally similar to the matrix amphiboles. Clinopyroxene occurs as corroded, Al and Cr-rich grains in amphibole cores and as euhedral Al-poor grains in the matrix (Ulmer et al., 1983; Tiepolo et al., 2002, 2005). Plagioclase grains are poikilitic and record continuous compositional zoning, with decreasing An content towards the rim (An_{98-22} ; Blundy and Shimizu, 1991). Accessory minerals are titanite, zircon, apatite and calcite.

Calcite occurs as interstitial grains and as single rounded grains rimmed by small clinopyroxene grains (Fig. B4) referred to as “ocelli” (Ulmer et al., 1983; Blundy and Sparks, 1992). In addition to calcite, plagioclase and quartz grains also form ocelli within the Mattoni gabbro. The MG contains large titanite grains, up to 2 mm in size. MG titanites are subhedral to euhedral and crystallize at grain boundaries with matrix amphiboles and plagioclase. Some MG titanites are inter-grown with the matrix amphibole, suggesting coeval crystallization (Fig. 2d). Cadino gabbro (CG) is characterized by acicular amphiboles (≤ 5 mm) in a matrix of anhedral plagioclase (≤ 4 mm), quartz (≤ 3 mm) and biotite (< 1 mm). Plagioclase grains record zoned compositions of An_{94-71} in the cores to An_{44-35} in the rims (Blundy and Shimizu, 1991). Accessory minerals are titanite, zircon, apatite and ilmenite. No titanites were located in thin sections of the CG, even though abundant titanites were recovered by conventional separation techniques.

4.4 Analytical methods

4.4.1 Whole-rock geochemistry and modal abundances

Whole rock major element compositions of the samples were determined on fused lithium tetraborate glass discs using a Philips PW2400 X-ray fluorescence spectrometer (XRF).

Table 1:
Geochemical whole rock data (XRF and LA-ICP-MS) for the Val Fredda Complex

Sample	MFG	PQD	VFT	MG	CG
SiO ₂	70.49	62.62	59.85	47.67	53.42
TiO ₂	0.30	0.52	0.58	1.17	0.99
Al ₂ O ₃	15.81	18.32	19.08	14.78	18.29
Fe ₂ O ₃	2.60	4.52	5.12	8.29	7.69
MnO	0.10	0.11	0.11	0.13	0.13
MgO	0.98	1.85	2.19	10.45	5.24
CaO	3.39	5.92	6.87	12.60	9.69
Na ₂ O	3.59	3.67	3.66	1.82	2.28
K ₂ O	2.34	1.40	1.00	0.43	0.99
P ₂ O ₅	0.11	0.19	0.21	0.07	0.15
total	99.69	99.11	98.68	97.41	98.86
ASI	1.08	1.00	0.97	0.56	0.82
Sc	4.1	5.8	7.1	68	26.7
V	38.3	85	112.7	306.2	235.1
Cr	-	-	-	659.8	25.7
Co	3.4	8	10.1	34.7	21.2
Ni	-	-	-	94.7	10
Cu	2.8	54.3	15.7	44.1	9.2
Zn	28.4	29.1	39.7	40.9	37.1
Ga	13.2	16.2	16.9	11.8	15.3
Rb	66.3	36.5	28.4	5.7	29.9
Sr	330.6	523.3	555.6	269	353.9
Y	11.5	12.1	11.7	13.2	12.7
Zr	95.4	131.6	133.2	39	24
Nb	13.2	8.5	7.3	4.6	8.7
Cs	1.2	0.7	0.8	0.1	1.1
Ba	559.4	404.6	363.3	143.8	239.6
La	29.1	25.4	24.3	7.2	28.8
Ce	45.7	43	42.2	15.6	47.2
Pr	4.1	4.2	4	1.8	4.1
Nd	13	14.9	14.6	7.9	14.1
Sm	2.2	2.9	2.7	2.3	2.5
Eu	0.6	0.9	0.9	0.7	0.9
Gd	1.8	2.4	2.5	2.6	2.5
Tb	0.3	0.3	0.4	0.4	0.4
Dy	1.7	2.3	2.2	2.7	2.3
Ho	0.3	0.5	0.5	0.5	0.5
Er	1.4	1.4	1.3	1.3	1.3
Tm	0.2	0.2	0.2	0.2	0.2
Yb	1.4	1.4	1.5	1.3	1.4
Lu	0.3	0.2	0.2	0.2	0.2
Hf	2.6	3.3	3.2	1.4	1.1
Ta	1.3	0.4	0.4	0.3	0.6
W	0.3	0.2	0.5	0.4	0.4
Tl	0.1	0.1	0.1	-	0
Pb	13.6	5.1	6.2	2.1	3.2
Th	17	7.4	4.6	2.2	11.9
U	2.4	1.7	1	0.6	3.2

Major element oxides concentrations displayed as wt%, trace elements as ppm.

ASI: (alumina saturatin index) molar ratio of $Al_2O_3 / (Na_2O + K_2O + CaO)$.

“ - ” analysis below dection limit

Trace element abundances were analyzed on fragments from the same fused lithium tetraborate glass discs by laser ablation inductively coupled plasma mass-spectrometry (LA-ICP-MS) using an ELAN 6100 DRC quadrupole ICPMS (Perkin

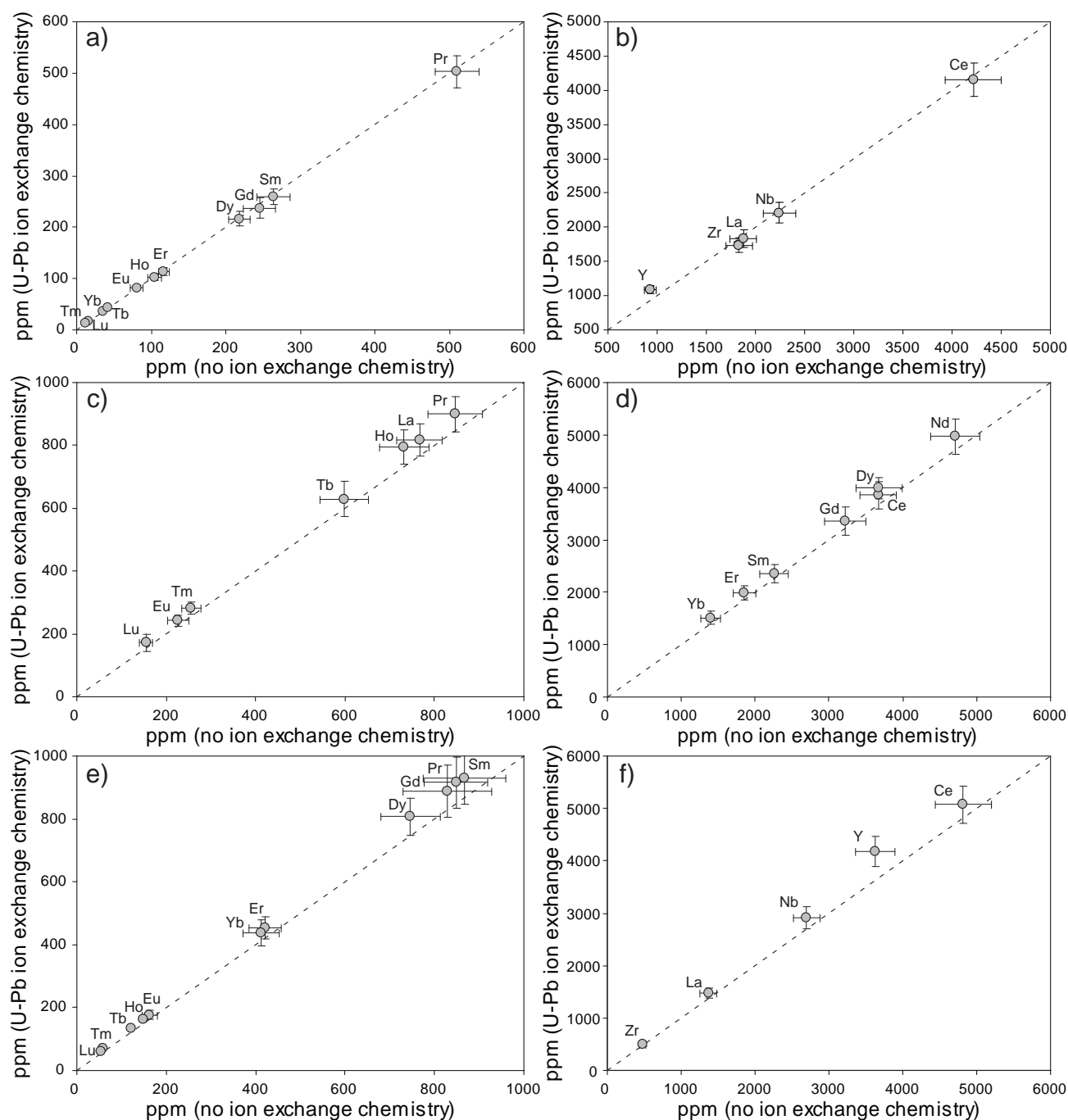


Figure 3: ICP-MS trace element data demonstrating the reproducibility for single titanite grains from which half of the dissolved grain was collected for trace element analysis, whereas the other half was collected following titanite ion exchange chemistry for U-Pb dating. a) MG-t6: 0 - 600 ppm; b) MG-t6: 500 - 5000 ppm; c) MFG-t5: 0 - 1000 ppm; d) MFG-t5: 1000 - 6000 ppm; e) PQD-t4: 0 - 1000 ppm; f) PQD-t4: 0 - 6000 ppm.

Elmer) interfaced to a GeoLas 200 M 193 nm ArF excimer laser ablation system (Lambda Physik). The laser was operating at an on-sample energy density of about 10 J/cm², a 10-Hz repetition rate and a 120- μ m pit size. Helium was used as a cell gas. The acquisition times for the background

and the ablation interval corresponded to ~ 70 and 30–35 seconds, respectively. Dwell times per isotope ranged from 10 to 20 ms, and peak hopping mode was employed. The ThO⁺/Th⁺ and Ba²⁺/Ba⁺ ratios were optimized to 0.0036 and 0.0142, respectively. The SRM 612

synthetic glass standard from NIST was used for external standardization. The average element abundances in it were taken from Pearce et al. (1997). ^{42}Ca served as an internal standard. Intensity versus time data were reduced using LAMTRACE. For each sample 3 measurements were acquired and results were then averaged. All geochemical analyses were carried out at the Institute of Mineralogy and Geochemistry, University of Lausanne. Data are presented in

Table 1.

The modal abundances of minerals for each sample are reported in Table 2 and were determined by point counting on high resolution thin section scans using the image analysis software JMicroVision (Roduit, 2002). Major mineral abundances were determined from 500 points per 3.5 x 5 cm thin section using the random grid point counting mode. Zircon and titanite modal abundances were determined by

Table 2:
Modal abundances of samples from the Val Fredda Complex

Sample	MFG	PQD	VFT	MG	CG
Plagioclase	40	55	57	27	52
Quartz	33	11	24	6	10
K-feldspar	15	-	0.5	-	-
Amphibole	0.9	13	8	35c - 20r*	30
Biotite	10	7	10	-	7
Clinopyroxene	-	-	-	10	-
Titanite	0.03	0.01	0.01	0.24	0.01
Zircon	0.1	0.02	0.02	0.01	0.01
accessories	ap, al, mag	ap, al, mag	ap, mag	ap, mag, cc	ap, mag

Representative modal data collected from point counting.

“-” not identified.

* amphibole was distinguished between cores (c) and rims (r).

ap = apatite; al = allanite; mag = magnetite; cc = calcite.

manual counting using the previously determined locations in thin section from Chapter 3.

4.4.2 TIMS-TEA (titanite trace element analyses)

The trace element fraction was collected for 16 titanite grains following ion exchange chemistry and trace elements analyzed following the TIMS-TEA method described in Schoene et al. (2010). The samples were dried down on a hot plate

and re-dissolved in 1ml of a 0.1M HF and 0.5N HNO_3 solution doped with 1ppb Ir to serve as an internal standard during ICP-MS measurements. Multi-element concentration standards were produced from a multi-element stock solution, which was diluted into nine calibration solutions of differing concentrations (REE ranging from 5 ppt to 500 ppb and Ca, Ti from 50 ppb to 10 ppm). Each calibration solution was doped with 1 ppb Ir in order to serve as an internal standard

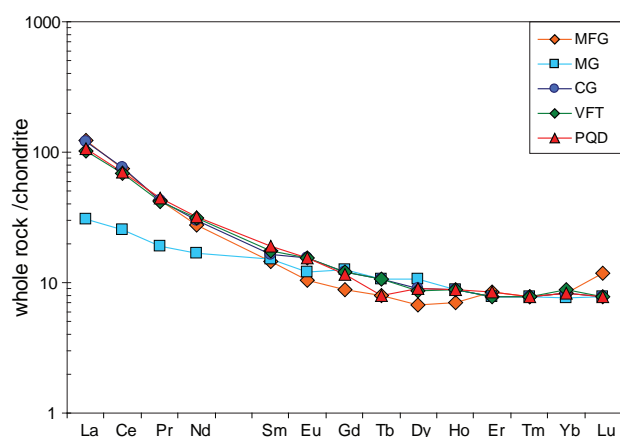


Figure 4: Chondrite normalized whole rock REE patterns for the samples from the Val Fredda Complex.

during ICP-MS measurements. Trace element concentrations were analyzed using an Element 2 SF-ICP-MS in solution mode at ETH Zürich. Solutions were introduced into the plasma using a CETAC Aridus desolvation system with an uptake rate of 100 $\mu\text{l}/\text{min}$. Measurements were carried out in medium mass resolution ($m/\Delta m = 4000$). Calibration solutions were measured prior to and during each session, and a blank solution was used to rinse the transport line in between each sample and was measured every 12 samples for background. In order to minimize the effect of plasma fluctuations or different nebulizer aspiration rates between samples, 1 ppb iridium was added to all samples and calibration solutions as an internal standard. Titanites were analyzed for Ca, Ti, Sr, Y, Zr, Hf, REEs, Nb, Ta, and Th concentrations.

Because the two-stage HBr-HCl titanite ion exchange chemistry (Krogh, 1973) is more complex, in comparison to the HCl-based

ion exchange chemistry for zircon, we tested for element fractionation during chemistry following similar methods described for zircon in Schoene et al. (2010). Three titanite grains were dissolved and the solution was split into two aliquots, where one aliquot was passed through ion exchange chemistry for U-Pb dating prior to trace element analyses, whereas the second aliquot was analyzed for trace elements only. Titanite grains were selected from different samples (MFG, PQD and MG) in order to test the reproducibility of the trace element concentrations of titanite from samples of differing magma compositions. Comparisons between aliquots are shown in Fig. 3 and Table 3.

Trace element concentrations were calculated by least squares linear interpolation based on normalization with the Ir internal standard, and on calibration curves defined from measured stock solutions described above. In order to convert the concentrations within the wash solutions to concentrations in titanite, all wash solution elemental concentrations were normalized to 26.94 wt% CaO. Concentrations are reported in ppm and in weight %, and all uncertainties are reported at the two-sigma level. Data are presented in Table 4.

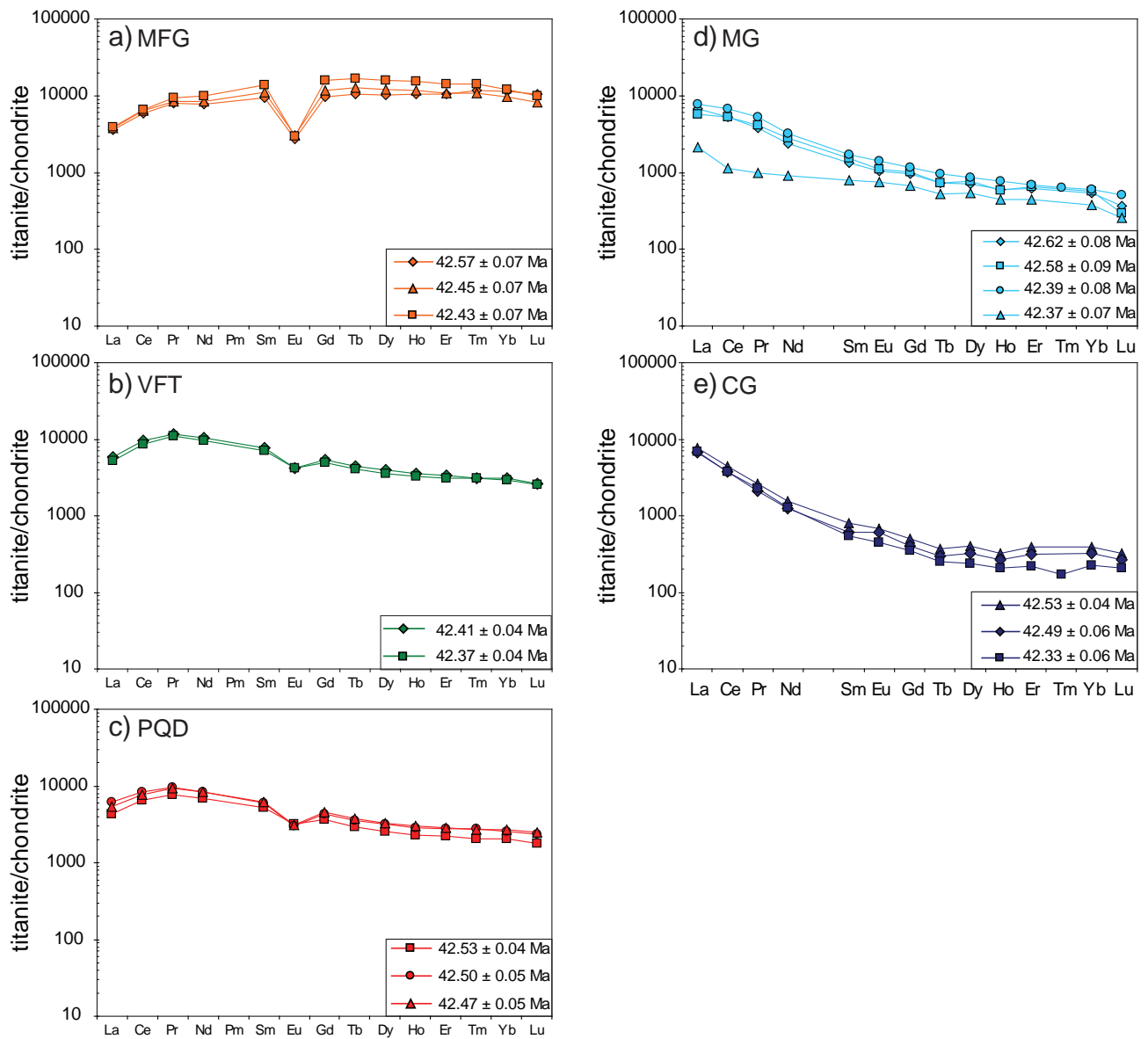


Figure 5: Variations of Chondrite normalized REE patterns for titanite through time, analyzed by TIM-TEA.

4.4.3 Trace element analysis in apatite by LA-ICP-MS

In situ trace element analyses were carried out on apatites in polished epoxy mounts by LA-ICP-MS using a Thermo Scientific Element XR mass spectrometer coupled to a New Wave Research ArF 193 nm laser ablation system at the University of Lausanne. Operating conditions of the laser include using a 50 μm ablation pit, a 12 Hz frequency and an on-sample energy density

of $\sim 5 \text{ J/cm}^2$. Helium was used as a cell gas. The acquisition times for the background and the ablation interval corresponded to 60 and 30 seconds, respectively. Dwell times per isotope ranged from 10 to 20 ms and peak hopping mode was employed. The ThO^+/Th^+ and $\text{Ba}^{2+}/\text{Ba}^+$ ratios were optimized to 0.035% and 1.5%, respectively. Measurements of unknowns were bracketed by NIST SRM-612 glass measurements which were employed for the

Table 3:
TIMS-TEA titanite trace element results for titanite aliquots from the Val Fredda Complex

	Ti	± 2s	Sr	± 2s	Y	± 2s	Zr	± 2s	Nb	± 2s	La	± 2s	Ce	± 2s	Pr	± 2s	Nd	± 2s	Sm	± 2s	Eu	± 2s
Titanite aliquots measured for trace elements																						
MG-t6_no-chem	36.5	2.4	41.7	3.5	932	58	1832	134	2242	164	1877	133	4218	284	510	29	1559	120	264	22	81	8
MFG-t5_no-chem	36.2	2.5	19.5	1.7	17564	1118	621	71	8666	535	767	51	3668	249	846	61	4712	334	2258	190	226	24
PQD-t4_no-chem	35.0	3.7	22.4	2.7	3627	265	482	44	2698	183	1367	108	4819	383	849	71	3619	319	867	92	163	16
Titanite aliquots measured for trace elements following ion exchange chemistry																						
MG-t6_U-Pb	33.6	2.7	41.8	2.6	1089	61	1733	108	2212	153	1839	129	4154	243	503	31	1508	96	260	15	81	6
MFG-t5_U-Pb	33.4	3.0	19.6	2.0	20157	1281	598	44	8510	652	817	53	3851	262	900	56	4976	340	2355	169	242	18
PQD-t4_U-Pb	38.0	2.9	21.8	2.2	4174	287	506	38	2914	203	1477	93	5073	350	916	67	3904	319	930	83	176	15
Gd	± 2s	Tb	± 2s	Dy	± 2s	Ho	± 2s	Er	± 2s	Tm	± 2s	Yb	± 2s	Lu	± 2s	Hf	± 2s	Ta	± 2s	Th	± 2s	
Titanite aliquots measured for trace elements																						
MG-t6_no-chem	245	22	35.7	3.8	218	15	42.1	3.0	116	7	15.1	1.4	105	10	12.0	1.3	91	11	261	32	395	29
MFG-t5_no-chem	3224	280	598	55	3677	314	732	56	1854	157	256	21	1395	132	155	14	99	12	1794	199	379	31
PQD-t4_no-chem	829	99	122	12	746	67	150	13	421	36	60	5	412	41	54	6	48	8	299	34	688	66
Titanite aliquots measured for trace elements following ion exchange chemistry																						
MG-t6_U-Pb	238	20	35.8	2.2	216	12	43.1	3.7	114	7	16.3	1.2	103	7	13.0	1.0	90	8	238	17	401	23
MFG-t5_U-Pb	3357	266	629	56	3986	200	795	54	1983	139	282	18	1512	120	172	16	103	13	1607	127	408	29
PQD-t4_U-Pb	888	82	133	11	807	60	163	12	453	35	70	6	438	42	60	6	52	7	224	23	736	62

no-chem indicates titanite aliquot analyzed for trace elements only.

U-Pb indicates titanite aliquot passed through ion exchange chemistry for U-Pb dating prior to trace element analyses.

Titanium is reported in wt.% and trace elements are reported in ppm.

“ - ” analysis below detection limit

Table 4:
TIMS-TEA titanite trace element results for samples from the Val Fredda Complex

	²⁰⁶ Pb/ ²³⁸ U ^a	±2σ abs	Th/U ^b	Ti	±2s	Sr	±2s	Y	±2s	Zr	±2s	Nb	±2s	La	±2s	Ce	±2s	Pr	±2s	Nd	±2s	Sm	±2s	
Marginal Facies granodiorite																								
MFG-11	42.577	0.065	1.07	33.6	2.1	12.2	0.9	19143	898	914	45	10621	501	854	40	3650	180	752	34	3588	158	1432	80	
MFG-12	42.433	0.069	1.39	38.6	3.0	15.5	1.7	24943	1730	759	56	9916	639	931	63	4037	229	893	65	4606	301	2130	153	
MFG-13	42.448	0.066	1.50	30.2	1.9	15.4	1.2	19308	911	619	40	10106	633	906	42	3896	237	803	39	3947	165	1705	87	
Mattoni gabbro																								
MG-11	42.616	0.081	6.82	37.3	2.7	43.9	3.9	616	43	1876	142	1453	100	1611	107	3248	247	356	25	1108	98	204	26	
MG-12	42.582	0.091	6.39	35.9	2.6	40.8	4.1	400	30	2011	154	1182	78	1362	107	3245	232	396	29	1301	123	236	25	
MG-13	42.365	0.070	4.78	37.1	2.7	30.5	2.5	416	31	955	74	-	-	506	35	691	51	92	7	425	50	121	11	
MG-15	42.391	0.079	6.30	33.6	2.7	41.8	2.6	1089	61	1733	108	2212	153	1839	129	4154	243	503	31	1508	96	260	15	
Cadino gabbro																								
CG-11	42.487	0.059	1.26	37.1	3.1	24.5	2.4	374	30	511	42	629	50	1583	97	2292	164	203	17	583	53	94	10	
CG-12	42.331	0.062	3.12	34.7	2.7	27.5	2.0	322	16	437	32	444	28	1626	105	2292	129	220	12	594	34	84	6	
CG-14	42.526	0.038	1.62	35.6	2.3	20.4	2.3	468	33	1005	81	861	54	1831	126	2725	176	250	19	734	53	121	23	
Val Fredda Tonalite																								
VFT-11	42.408	0.039	0.48	32.6	2.0	29.6	2.8	4774	323	878	74	4029	265	1399	94	5912	433	1120	73	4895	391	1167	75	
VFT-12	42.373	0.043	0.54	31.0	2.2	26.7	2.3	4829	284	560	32	3374	187	1235	59	5259	343	1039	61	4466	305	1071	79	
Plagioclase quartz diorite																								
POD-11	42.527	0.039	0.73	35.1	3.6	22.8	2.4	3208	192	556	38	3215	216	1034	61	3961	240	736	44	3258	257	799	74	
POD-12	42.467	0.051	0.91	33.2	2.4	18.6	1.9	4389	249	791	51	3150	172	1274	69	4675	261	885	54	3902	265	953	72	
POD-13	42.496	0.048	0.80	38.0	2.9	21.8	2.2	4174	287	506	38	2914	203	1477	93	5073	350	916	67	3904	319	930	83	
Eu	±2s	Gd	±2s	Tb	±2s	Dy	±2s	Ho	±2s	Er	±2s	Tm	±2s	Yb	±2s	Lu	±2s	Hf	±2s	Ta	±2s	Th	±2s	
Marginal Facies granodiorite																								
MFG-11	158	10	1996	122	392	32	2589	119	596	27	1752	81	301	16	1929	118	266	16	125	9	2095	180	316	13
MFG-12	173	17	3217	301	628	62	4023	203	873	60	2369	166	366	28	2067	166	251	23	161	16	1249	139	388	31
MFG-13	175	12	2408	158	471	32	3074	138	655	31	1766	78	279	13	1636	79	206	12	119	9	1801	123	350	19
Mattoni gabbro																								
MG-11	61	7	200	27	27	3	182	14	34	2	101	11	10	1	93	9	9	1	125	14	182	20	367	30
MG-12	63	16	206	18	27	9	197	16	33	4	107	10	8	1	98	10	7	1	123	14	174	20	220	19
MG-13	43	4	139	15	19	2	137	10	25	2	74	6	7	1	64	7	6	1	48	6	-	466	41	
MG-15	81	6	238	20	36	2	216	12	43	4	114	7	16	1	103	7	13	1	90	8	238	17	401	23
Cadino gabbro																								
CG-11	36	5	83	10	11	1	82	8	15	3	52	8	3	1	55	8	7	1	21	3	9	1	538	49
CG-12	26	2	71	5	10	1	61	4	12	1	37	2	4	0	38	3	5	0	21	2	22	2	686	46
CG-14	39	4	104	12	14	1	103	8	18	3	65	7	4	0	67	8	8	1	61	9	38	4	911	71
Val Fredda Tonalite																								
VFT-11	241	25	1099	103	167	17	1008	63	200	15	556	41	79	8	525	47	66	7	63	6	455	45	715	64
VFT-12	240	19	1011	88	152	13	901	44	186	12	510	32	78	6	492	40	65	4	46	6	393	43	605	45
Plagioclase quartz diorite																								
POD-11	184	15	745	69	109	10	652	44	129	9	367	27	52	7	352	30	45	4	47	6	166	20	521	38
POD-12	178	12	935	70	139	12	829	52	170	10	467	32	70	4	454	36	63	5	99	11	157	15	699	52
POD-13	176	15	888	82	133	11	807	60	163	12	453	35	70	6	438	42	60	6	52	7	224	23	736	62

^a U-Pb dates are from Broderick Chapter 2

^b Th contents calculated from radiogenic ^{208}Pb and the $^{207}\text{Pb}/^{206}\text{Pb}$ date of the sample, assuming concordance between U-Th and Pb systems.

Titanium is reported in wt.% and trace elements are reported in ppm

- “ analysis below detection limit

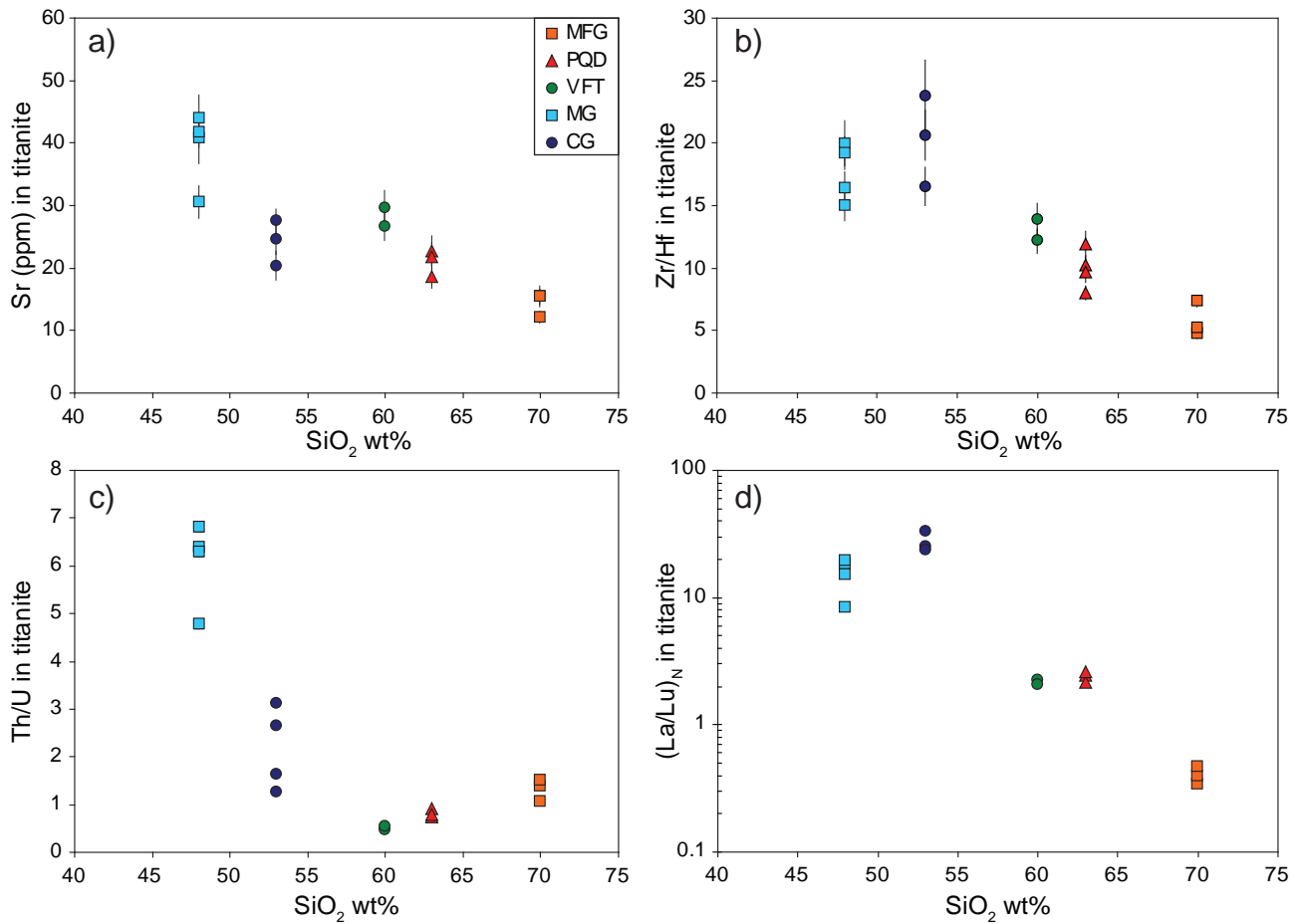


Figure 6: Variations of trace element concentrations and ratios of titanite with increasing whole rock SiO_2 content.

external standardization. Calcium was chosen as the internal standard element ($\text{CaO} = 54.02$ wt. %). Intensity versus time data were reduced in LAMTRACE. All spectra were checked for the presence of surface contamination and intensity spikes and corrected when necessary. Data are presented in Table 5 and were used for REE budgets shown in Figure 7.

4.5 Results

4.5.1 Whole-rock compositions

Whole-rock results of representative samples of each lithology of the VFC are summarized

in Table 1 and Figure 4. The felsic units (MFG, PQD and VFT) and the CG display remarkably similar rare earth element (REE) patterns are characterized by light REE enrichment relative to middle REEs and heavy REEs and lack negative Eu anomalies ($\text{Eu}/\text{Eu}^* \sim 0.9 - 1$). The depletions in MREEs to HREEs form the typical concave up pattern that is consistent with the removal of amphibole, which fractionates MREEs and HREEs from LREEs (Glazner et al., 2008; Nandedkar, 2013). Whereas the MG is depleted in LREEs, up to a factor of three lower than the other VFC units and is characterized by

Table 5:
LA-ICP-MS apatite trace element results for samples from the Val Fredda Complex

	Sc	Rb	Sr	Y	Zr	Nb	La	Ce	Pr	Nd	Sm	Eu	Gd	Tb	Dy	Ho	Er	Tm	Yb	Lu	Hf	Pb	Th	U
Marginal Facies granodiorite (MFG)																								
cb03-ap_5.2	0.19	0.06	164	411	0.39	0.01	753	1794	218	852	134	15.0	113	13.8	79	14	38	4.7	30	4.1	0.01	4.3	18	9.4
cb03-ap_4	0.46	0.25	119	946	2.49	0.37	353	1092	155	702	153	16.0	148	21.9	144	29	85	13.3	96	15.5	0.02	4.6	23	10.9
cb03-ap_3	0.26	0.08	112	772	11.29	0.04	426	1210	164	715	142	13.6	146	20.0	125	26	73	10.7	75	11.1	0.23	6.6	26	12.5
cb03-ap_1	0.28	0.04	328	339	0.40	-	834	1839	208	806	126	15.9	99	12.2	68	13	32	4.2	25	3.7	0.01	5.6	24	10.2
cb03-ap_6	0.24	0.08	184	464	0.48	0.01	658	1555	192	786	132	14.3	110	14.0	80	16	40	5.5	36	5.2	0.01	4.6	22	10.6
cb03-ap_7	0.29	0.08	119	653	0.37	0.12	342	1155	160	714	141	14.1	126	17.1	107	21	59	8.5	59	8.9	-	4.4	18	8.4
Mattoni gabbro (MG)																								
cb04-ap_2	0.21	-	162	59	1.23	-	141	223	22	89	15	3.5	15	1.8	11	2	6	0.8	5	0.8	-	3.3	8	2.7
cb04-ap_3	0.90	0.06	430	152	3.57	0.01	194	424	54	240	46	11.5	42	5.5	32	6	15	1.9	11	1.5	0.02	4.7	11	2.3
cb04-ap_6	0.36	0.37	322	131	3.39	0.01	254	450	52	215	40	9.6	37	4.6	27	5	14	1.7	10	1.5	0.02	4.2	13	3.5
cb04-ap_7	0.99	0.05	389	145	3.37	0.01	179	394	50	217	43	11.4	41	5.2	31	6	15	1.8	11	1.4	0.02	4.9	11	2.6
cb04-ap_8	0.28	-	129	50	0.42	-	96	113	11	47	10	2.6	11	1.4	9	2	5	0.6	4	0.7	-	6.6	40	27.8
cb04-ap_9	0.24	0.09	150	47	0.71	-	89	131	14	55	10	2.5	11	1.3	8	2	5	0.6	4	0.7	-	3.6	7	2.2
Val Fredda tonalite (VFT)																								
cb09-ap2	0.22	0.05	315	244	0.42	0.01	764	1573	167	615	87	12.4	68	8.2	46	9	23	3.0	19	2.7	0.01	2.2	23	10.8
cb09-ap6	0.22	0.06	221	304	0.33	0.08	173	584	84	391	76	11.2	71	9.3	56	11	29	4.0	25	3.9	0.01	1.8	27	14.3
cb09-ap7	-	0.09	305	300	0.74	0.01	837	1788	192	714	104	14.7	80	9.9	56	11	28	3.8	24	3.6	0.01	2.7	34	13.4
Plagioclase quartz diorite (PQD)																								
cb13ap-1	-	0.06	325	308	0.58	-	728	1629	187	748	121	14.4	96	11.1	65	12	30	3.8	23	3.4	0.01	3.1	27	13.0
cb13ap-2	-	0.05	360	390	1.37	0.01	983	2077	233	918	139	17.4	104	12.8	72	14	36	4.8	30	4.4	0.24	3.2	37	13.7
cb13ap-5	0.28	-	236	253	0.24	-	389	1094	138	616	99	9.4	81	9.7	53	10	24	3.1	18	2.8	-	2.1	40	21.4
cb13ap-6	0.28	0.05	212	404	0.50	0.07	293	901	126	598	112	14.3	99	12.6	77	15	40	5.4	34	5.2	0.01	1.8	32	33.4
cb13ap-7	0.23	0.06	261	232	0.32	0.01	416	928	112	468	80	9.9	67	7.9	47	9	23	2.9	18	2.8	-	2.6	26	17.1
cb13ap-10	0.32	-	217	340	0.59	0.07	394	1086	142	632	109	13.2	87	11.0	64	12	30	4.2	26	3.9	-	1.3	42	16.0

Elements are reported in ppm

“ - ” analysis below detection limit

a relatively flat REE pattern.

4.5.2 Titanite aliquots

Trace element concentrations were analyzed from three large titanite grains ($\geq 400 \mu\text{m}$) that were split into two aliquots, where one half of the dissolved sample was passed through ion exchange chemistry for U-Pb dating prior to trace element analyses (Table 3: titanite_U-Pb), whereas the second half of the dissolved sample was collected and analyzed for trace elements only (Table 3: titanite_no-chem). Titanite trace element and REE data from the two aliquots are summarized in Figure 3. For the three titanite grains we obtained REE and trace element concentrations that are reproducible between the two aliquots (Fig. 3) indicating that the trace elements were not significantly fractionated during titanite ion exchange chemistry and demonstrates the accuracy of the method.

4.5.3 Trace element composition of titanite

Trace element concentrations were analyzed from the same volume of titanite used for U-Pb age determinations in Chapter 2, described as TIMS-TEA by Schoene et al. (2010). Titanite trace and rare earth element (REE) data are summarized in Table 4 and in Figures 5 and 6. The chondrite-normalized REE patterns for titanite differ significantly between samples

(Fig. 5). Three titanite grains from the MFG are rather homogenous with LREE depleted relative to the HREE, and have large negative Eu anomalies ($\text{Eu}/\text{Eu}^* \sim 0.2$). Three titanite grains from the PQD and two titanite grains from the VFT sample have similar patterns showing weak LREE enrichment, relative to HREEs, and display negative Eu anomalies ($\text{Eu}/\text{Eu}^* \sim 0.5$ and 0.7 , respectively). Titanites from the felsic samples have chondrite-normalized REE patterns that record an overall increase in REE concentrations, within individual samples, through time (Fig. 5a-c), indicating that the melts became more enriched in REEs during the evolution of the felsic magmas. The analyzed titanites from the felsic samples are characterized by fairly homogenous concentrations of Zr (500 to 900 ppm). In contrast, titanite trace element concentrations of Sr, Y, Nb and Hf vary over a factor of three to five among the felsic samples. Titanite grains from the mafic samples (CG and MG) are enriched in LREE relative to the HREE, and lack negative Eu anomalies ($\text{Eu}/\text{Eu}^* \sim 1$ and 0.95 , respectively). Three titanites from the CG sample have chondrite-normalized REE patterns that record an overall decrease in REE concentrations through time (Fig. 5d), indicating that the melt becomes depleted in REEs. Whereas, the four titanite grains from the MG record non-systematic chondrite-normalized REE variations through time (Fig. 5e) pointing

to chemical variability in the MG melt during titanite crystallization. The analyzed titanites from the mafic samples are characterized by rather homogenous concentrations of Zr and Sr, which are distinct for each unit. In contrast, titanite trace element concentrations of Y, Nb and Hf vary over a factor of two to three among the mafic samples.

With increasing whole rock SiO_2 content, titanite trace element concentrations and ratios such as Sr, Zr/Hf and Eu/Eu* record an overall decrease from mafic to felsic samples, with the exception of the CG sample which is slightly enriched, relative to MG (Fig. 6). The decreasing Sr and Eu/Eu* in titanite suggests decreasing abundances of these elements in the melt as the result of increased plagioclase fractionation as differentiation proceeds (Fig. 6a). The observed decrease in Zr/Hf in titanite (Fig. 5b) is consistent with the removal of Zr and Hf in the melt during zircon fractionation (Bea et al., 2006; Claiborne et al., 2010). In contrast, titanite Th/U ratios record an overall decrease (~6.8 to 0.5) from 48 wt.% SiO_2 to 60 wt.% SiO_2 , followed by an increase in Th/U (~0.5 to 1.5) from 60 wt.% to 70 wt.% SiO_2 (Fig. 5c). This suggests that in the mafic samples, the decrease in Th/U in titanite is related to the crystallization of titanite, which preferentially incorporates Th, whereas, the increase in Th/U in titanite from the felsic samples is the result of zircon crystallization,

which preferentially incorporates U over Th. Titanite trace element ratios such as Nb/Ta and La/Lu record non-systematic variations with increasing SiO_2 content (Fig. 6d).

4.6 Discussion

4.6.1 Mineral contributions to whole rock REE budget

Titanite trace element compositions and REE patterns record variations that are distinct for the magma from which they are crystallizing (Fig. 5). As a major reservoir for REEs it is important to understand how titanite contributes to the whole rock REE budget in comparison to other mineral phases, in order to evaluate the potential use of titanite for geochemical modelling. Using the modal mineral abundances (Table 2) and their corresponding REE concentrations for each VFC sample (titanite and apatite: this study; zircon: TIMS-TEA from Chapter 2; MFG, PQD, VFT amphiboles and plagioclase: Stauffacher, 2012; Mattoni gabbro minerals: Tiepolo et al., 2002, 2005), we calculated the percent contribution from each mineral to the whole rock REE budget (Fig. 7).

Felsic samples

REE contributions for the felsic units (MFG, PQD, VFT) are calculated from major minerals; amphibole and plagioclase (from Stauffacher, 2012) and accessory minerals; titanite and apatite

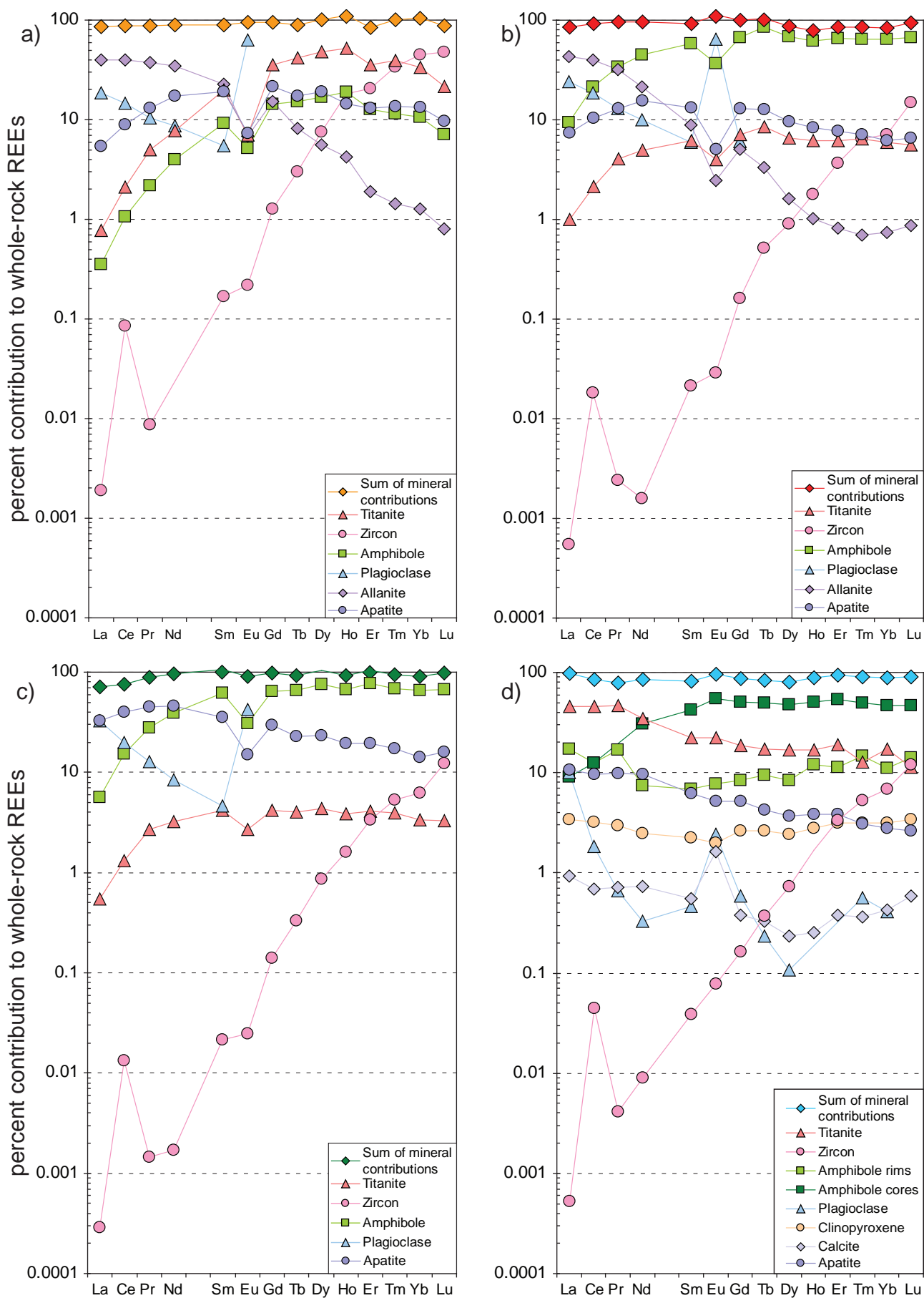


Figure 7: REE contributions of each mineral normalized to whole rock abundances for samples from the VFC. a) MFG; b) PQD; c) VFT; d) MG.

(this study), zircon (TIMS-TEA results from Chapter 2) and allanite (from Stauffacher, 2012). The MFG is the most differentiated sample (~70 wt% SiO₂) and is the only sample from the VFC in which amphibole crystallization is minimal (< 1%; Table 2). As amphibole and titanite preferentially incorporate MREE to HREEs relative to LREEs (Prowatke and Klemme, 2005; Bachmann et al., 2005; Nandedkar, 2013) the residual melt becomes depleted in MREEs and HREEs during crystallization. The lack of amphibole crystallization in the MFG results in titanite controlling the MREE budget (up to 50%), at low modal abundances (< 1%), whereas amphibole only contains ~20% at low modal abundances (Fig. 7a). The lower REE abundances in amphibole can result from titanite crystallization in a melt prior to amphibole crystallization (Sawka, 1988), which is consistent with our observed euhedral, up to 500 µm, titanite grains in the MFG (Fig. 2a). Plagioclase is the most abundant mineral in the MFG (Table 2) and is the controlling mineral for Eu (~ 60%), due the preferential incorporation of Eu²⁺ into plagioclase relative to the other minerals. The early crystallization of plagioclase in the MFG is consistent with the presence of negative Eu anomalies in the other crystallizing phases (Fig. 7a). Accessory minerals allanite and apatite contribute significantly to the whole-rock LREE and MREE totals, respectively, whereas

accessory zircon contributes significantly to the whole-rock HREE total. Zircons contribution becomes increasingly more significant from the MREEs through HREEs (e.g. Gd ~2 % and Lu ~50%), consistent with increasing partition coefficients with increasing ionic radius (Sano et al., 2002; Rubatto and Hermann, 2007). The sum of the MFG mineral contributions are slightly deficient (> 85%) which can be attributed to additional accessory minerals, for example monazite and/or thorite, which have not been detected in our thin sections.

Both the PQD and VFT samples contain amphibole (13% and 8%, respectively), resulting in amphibole controlling the MREE and HREE budget, > 65% in both the PQD and VFT (Fig. 7b-c). The higher MREE to HREE whole rock contributions from amphibole relative to titanite in the PQD (< 8%) and VFT (< 4%) is the result of earlier amphibole crystallization prior to the crystallization of often interstitial titanite (Fig. 2b-c). Plagioclase contributes significantly in both the PQD and VFT to Eu, and is considered an early crystallizing phase based on the presence of negative Eu anomalies in all other crystallizing phases (Fig. 7b-c). Allanite contributes significantly in the PQD to the LREEs (~40%) at low modal abundances (< 1%) , whereas apatite contributes up to 15% of the MREE budget. In contrast, apatite contributes significantly in the VFT to the

LREEs, up to 45%. In both the PQD and VFT, zircons contribution becomes increasing more significant in the HREEs, relative to titanite (Fig. 7). The sum of the mineral contributions in the PQD and VFT is deficient in the LREEs (~90 and 70%, respectively). The cause for the discrepancy in the LREEs is attributed to the lack of allanite data for the VFT.

The VFC felsic samples demonstrate that the whole rock REE budget for each felsic unit is controlled by the crystallization of amphibole and accessory titanite, and is more importantly controlled by the sequence in which these two minerals crystallize.

Mattoni gabbro

REE contributions for the Mattoni gabbro are calculated from major minerals, amphibole (cores and rims), clinopyroxene, calcite and plagioclase (from Tiepolo et al., 2002, 2005) and accessory minerals, titanite and apatite (this study) and zircon (TIMS-TEA results from Chapter 2). It is apparent from Figure 7d that the amphibole cores are the major reservoir of MREE to HREE, contributing > 50 % to the whole rock budget. The amphibole cores are depleted in LREEs relative to MREE and HREEs, consistent with experimental amphibole REE partition coefficient data (Nandedkar, 2013). The matrix forming minerals, amphibole, clinopyroxene, calcite and plagioclase, together contribute less than 20% for each of the REEs,

except for La (~30%). Titanite is the major host phase for the LREEs (~ 45%) and is the major contributor to the whole rock MREE to HREE budget among the matrix forming minerals (~20%). The higher REE abundances in titanite, relative to the matrix amphibole, is the result of titanites preferential incorporation of REEs over amphibole (Prowatke and Klemme, 2005; Bachmann et al., 2005) during periods of coeval titanite and amphibole crystallization, consistent with petrographic observations (Fig. 2d). The sum of the mineral contributions for each element ranges from ~ 80% in the LREEs to > 90% in the MREE to HREEs. The cause for the discrepancy in the LREEs is attributed to additional accessory minerals which have not been detected in our thin sections.

Our calculations indicate that during the evolution of the Mattoni gabbro the crystallization of amphibole and titanite are the major reservoirs for REEs (Fig. 7d). During early stages of crystallization at 0.8 – 1.0 GPa amphibole cores are the major host phase for REEs. Following subsequent magma emplacement at 0.2 – 0.3 GPa, titanite becomes the major host phase for REEs incorporating > 50% of the REEs from the residual melt. The transition from amphibole to titanite controlling the REE budget, is the result of amphiboles preferential incorporation of REEs relative to olivine, spinel and clinopyroxene (Rollinson,

1993), and the lack of titanite crystallization at depth. However, once titanite begins to crystallize it controls the REE budget even at low modal abundances (Wotzlaw et al., 2013). Titanite's ability to strongly influence the melt composition during crystallization demonstrates the potential of titanite to document changes in magma composition through time. Therefore, titanite may be a more robust accessory mineral relative to zircon, as zircon only contains a few percent of the HREE budget (e.g. Er – Lu; Fig. 7d).

Cadino gabbro

Due to the lack of textural information for titanite and zircon as well as the lack of chemical data for the major crystallizing phases (e.g. amphibole and plagioclase), we do not present mineral contributions to whole rock for the CG.

4.6.2 Calculated melt compositions

Partition coefficients applied to measured mineral compositions allow us to calculate the melt compositions in equilibrium with each crystallizing mineral assemblage. However as equilibrium partitioning between minerals and melt is a function of pressure (P), temperature (T) and melt composition (Hermann, 2002; Prowatke and Klemme, 2005; Rubatto and Hermann, 2007; Nandedkar, 2013), the selection of partition coefficients for each mineral should closely match the system being

Table 6:
REE partition coefficients

REE partition coefficients used for felsic melt calculations					
	Amphibole ^a	Plagioclase ^b	Zircon ^c	Allanite ^d	Titanite ^e
La	0.921	-	0.00046	2819	113
Ce	1.725	0.241	0.36	2245	223
Pr	-	-	0.0172	-	-
Nd	5.393	0.172	0.077	1980	639
Pm	-	-	-	-	-
Sm	10.567	0.125	0.8	1254	930
Eu	8.154	2.11	1.22	794	661
Gd	14.4	0.09	8	-	855
Tb	18.4	-	20.7	-	-
Dy	19.565	0.086	45.9	-	935
Ho	19.079	-	80	-	-
Er	17.444	0.084	136	-	636
Tm	17.168	-	197	-	-
Yb	15.299	0.077	277	-	393
Lu	12.863	0.062	325	-	-

REE partition coefficients used for mafic melt calculations (MG)					
	Amph-cores ^f	Amph-rims ^g	Plagioclase ^b	Zircon ^h	Titanite ⁱ
La	0.151	0.405	-	-	8.2
Ce	0.337	0.703	0.241	-	28.4
Pr	-	-	-	-	77
Nd	0.865	1.75	0.172	-	-
Pm	-	-	-	-	-
Sm	1.706	3.57	0.125	16	364
Eu	1.88	3.727	2.11	8.5	-
Gd	2.394	4.855	0.09	30	368
Tb	2.792	5.073	-	-	-
Dy	2.732	4.986	0.086	100	-
Ho	2.795	5.235	-	-	-
Er	2.882	4.775	0.084	214	-
Tm	2.465	4.787	-	-	-
Yb	2.284	4.328	0.077	345	-
Lu	1.903	4.026	0.062	445	50

Additional REE partition coefficients for titanite used for discussion			
	Titanite ^j	Titanite ^k	Titanite ^l
La	1.88	2.17	7.5
Ce	3.61	4.6	12.1
Pr	7.39	9.7	-
Nd	-	-	23.6
Pm	-	-	-
Sm	20.4	31.2	26.4
Eu	-	-	25.9
Gd	18.2	30.5	20.2
Tb	-	-	-
Dy	-	-	11.3
Ho	-	-	-
Er	-	-	-
Tm	-	-	-
Yb	-	-	3.31
Lu	2.38	3.65	-

Sources of data: a) Nandedkar, 2013 at 780°C; b) Rolinson, 1993; c) Sano et al., 2002; d) Klimm et al., 2008 at 800°C; e) Bachmann et al., 2005; f) Nandedkar, 2013 at 950°C; g) Nandedkar, 2013 at 890°C; h) Rubatto and Hermann, 2007 at 800°C; i) Prowatke and Klemme, 2005: ASI300; j) Prowatke and Klemme, 2005: RHY; k) Prowatke and Klemme, 2005: DAC; l) Tiepolo et al. 2002.

investigated. Since the VFC felsic units record a similar P-T history, based on Al-in-hornblende geobarometry (P = 0.2 – 0.3 GPa; Stauffacher, 2012), Ti-in-zircon temperatures (T ~ 700 -

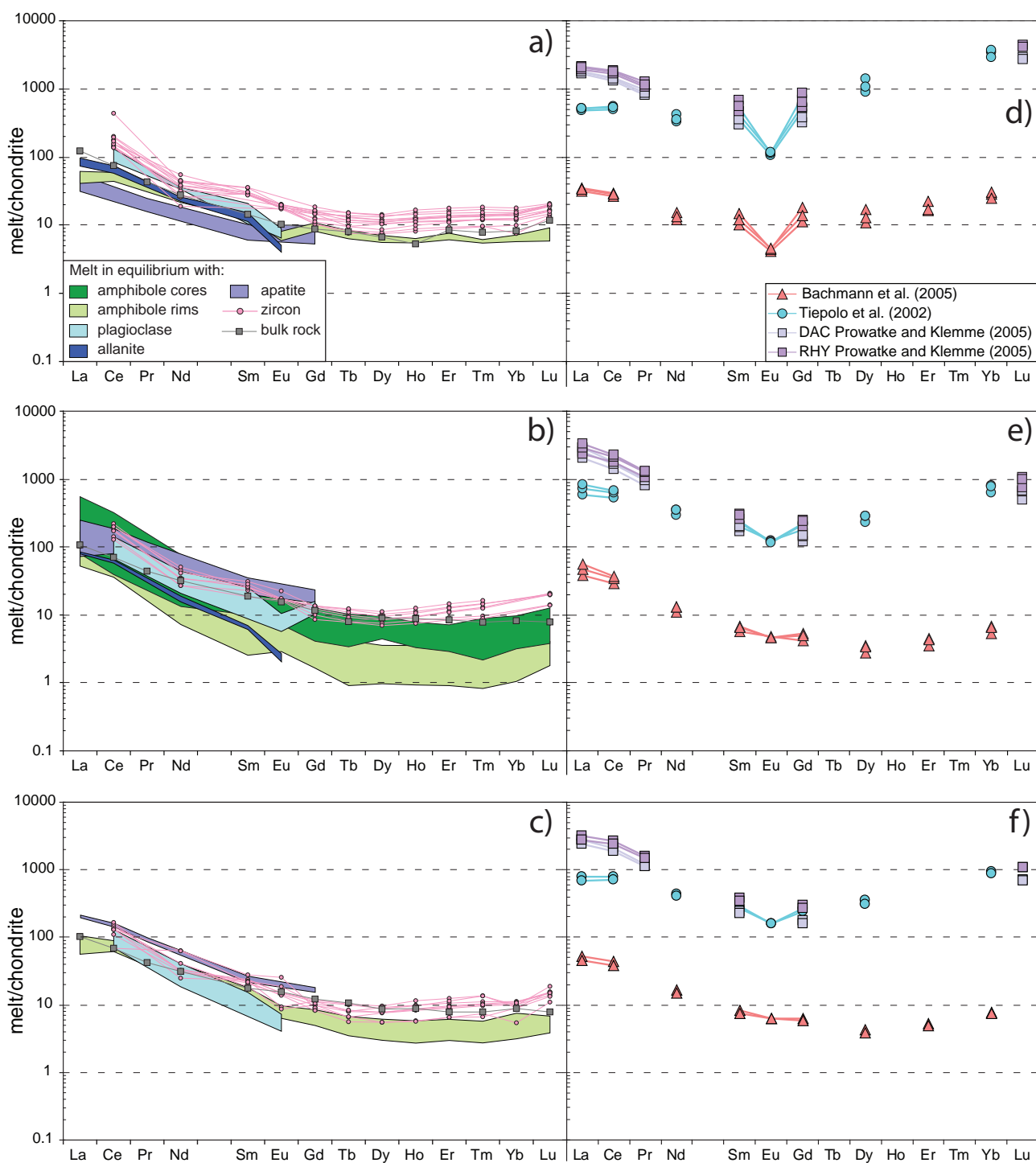


Figure 8: a-c) Calculated REE patterns of melts in equilibrium with crystallizing phases from the felsic samples: a) MFG; b) PQD; c) VFT. d-f) Calculated melts in equilibrium with titanite using different partition coefficients: d) MFG; e) PQD; f) VFT. (See text for discussion).

850°C; Broderick, Chapter 2) and amphibole-plagioclase pair temperatures ($T \sim 670 - 860^\circ\text{C}$; Stauffacher, 2012) and as bulk rock SiO_2 compositions range from 60 – 70 wt% SiO_2 we apply a single set of partition coefficients, which

have been determined for dacite compositions given in Table 5, to the minerals from the felsic units in order to calculate equilibrium melt compositions. With the exception of amphibole from the PQD for which two sets of partition

coefficients, based on temperature, 950°C and 780°C, (Nandedkar, 2013) are applied to cores and rims, respectively. In addition, we calculate allanite equilibrium melt compositions using the partition coefficients of Klimm et al. (2008) which were determined for basaltic compositions at 800°C and 2.5 GPa. While, these conditions do not closely match those of the VFC felsic units, our selection of the Klimm et al. (2008) partition coefficients for allanite are based on two factors: 1) these experimentally determined partition coefficients are similar to the partition coefficients determined from mineral/glass pairs from rhyolite compositions (Brooks et al., 1981; Mahood and Hildreth, 1983) and 2) the partition coefficients fit to the lattice strain model of Blundy and Wood (1994), which indicates equilibrium between allanite and melt in the experiments.

For the MG, based P-T changes during amphibole crystallization from 1000°C at 0.8 – 1.0 GPa to emplacement into the shallow crust, 0.2 – 0.3 GPa, at 900°C (Ulmer et al., 1983), we applied two sets of experimentally determined partition coefficients for amphibole based on temperature (950°C and 890°; Nandedkar, 2013) given in Table 6. Since petrographic observations, show that plagioclase, zircon and titanite are limited to the MG matrix (Broderick, Chapter 3), which crystallized following emplacement (0.2 – 0.3 GPa; Ulmer et al., 1983), we apply a

single set of partition coefficients to the matrix forming minerals given in Table 6. Previous results indicate that MG zircons crystallized from less evolved melts (e.g. Hf: ~7,000 ppm) and at higher temperatures (e.g. Ti-in-zircon temperatures of 750°C to 850°C; Broderick Chapter 2) in comparison the zircons from the felsic samples (e.g. Hf: 10,000 – 12,000; T: 700°C to 750°C; Broderick Chapter 2), therefore we apply the partition coefficients of Rubatto and Hermann (2007) to the MG zircons, which were determined for similar dacite compositions applied to zircons from the felsic samples (Sano et al., 2002) but for higher temperatures (e.g. 800°C).

Felsic melt compositions

Amphibole and plagioclase

The REE patterns for the melts in equilibrium with the crystallizing phases of the VFC felsic units, are slightly LREE enriched relative to the HREEs (Fig. 8) and mimic the REE patterns for the whole rock compositions. Melt REE patterns calculated for plagioclase from the PQD and VFT, based on the limited LREE data (Stauffer, 2012), are in agreement with the REE melt patterns calculated for amphibole, indicating coeval plagioclase and amphibole crystallization from similar melt compositions. However the calculated REE melt compositions in equilibrium with plagioclase for the MFG,

which is amphibole-poor ($< 1\%$), show slight LREE enrichment relative to melts in equilibrium with amphibole (Fig. 8a). This is related to two factors: 1) the lack of REE depletion due to the minor amphibole fractionation and 2) the low REE partitioning into plagioclase ($K_d < 1$), resulting in the residual melts becoming REE enriched during plagioclase fractionation (Gromet and Silver, 1986). Amphiboles from the VFC felsic units record similar melt patterns which have flat HREE slopes that vary by a factor of two within samples, however the REE abundances vary by up to a factor of five between samples (Fig. 8). Since the PQD contains amphiboles in which cores and rims can be distinguished based on compositions ranging from pargasite cores to Mg-hornblende rims (Stauffer, 2012), we applied different partition coefficients to the amphibole cores and rims which are given in Table 5. The calculated REE melts in equilibrium with the amphibole cores have higher REEs and lack negative Eu anomalies relative to the amphibole rims which display Eu anomalies (Fig. 8b). The different equilibrium melt compositions, between cores and rims, results from the early crystallization and stability of the pargasite cores at higher pressures and temperatures (Nandedkar, 2013), whereas the rims reflect in situ crystallization at lower pressures and temperatures (Stauffer, 2012) from a melt that has fractionated

amphibole, thus depleting the melt in MREE to HREEs. The melts in equilibrium with the PQD amphibole rims record variable Eu anomalies ($\sim 0.7 - 1.4$) which is the result of either changes in the proportions of crystallizing plagioclase relative to the proportions of amphibole or that amphibole rims reflect crystallization from contrasting magma compositions.

Accessory minerals

Allanite

REE melts in equilibrium with allanite from the PQD and MFG record similar melt patterns that are LREE enriched and have negative Eu anomalies (Fig. 8a-b). The allanite equilibrium melts are in agreement with the REE melt patterns calculated for amphibole, indicating coeval allanite and amphibole crystallization from similar melt compositions that have fractionated plagioclase.

Titanite

The REE partition coefficients between titanite and melt are strongly controlled by melt composition (Prowatke and Klemme, 2005) and vary over an order of magnitude between studies (Tiepolo et al., 2002; Prowatke and Klemme, 2005; Bachmann et al., 2005). The experimental work of Prowatke and Klemme (2005) show that the REE partition coefficients increase substantially (e.g. D_{Dy} varies from 1.1 to 415) with the increasing degree of melt

polymerization, for which the alumina saturation index ($ASI = \text{molar } Al_2O_3 / (Na_2O + K_2O + CaO)$) is used as a proxy. Thus, before we can relate melt compositions in equilibrium with titanite to other calculated REE equilibrium melt compositions, we must evaluate which published titanite partition coefficients are most applicable to the VFC felsic units.

The calculated REE melt compositions in equilibrium with titanite, using different partition coefficients (Fig. 8d-f) display similar melt patterns within samples; however they vary by two orders of magnitude. Titanite partition coefficients were determined experimentally by Prowatke and Klemme (2005) from dacite (DAC) and rhyolite (RHY) compositions and by Tiepolo et al. (2002) on lamproite compositions, whereas the partition coefficients of Bachmann et al. (2005) were determined from mineral/glass pairs from the Fish Canyon tuff (FCT). Because VFC titanites crystallized from felsic melt compositions, we consider the partition coefficients of Prowatke and Klemme (2005) and Bachmann et al. (2005) to be more representative of the VFC felsic units, and thus exclude Tiepolo et al. (2002) based on composition even though they are in agreement with the results of Prowatke and Klemme (2005; Fig. 8d-f). Due to the large discrepancies in the partition coefficients of similar melt compositions between the studies (Prowatke and Klemme, 2005; Bachmann et

al., 2005), we evaluate the partition coefficients based on the ASI, which has the strongest influence on titanite equilibrium partitioning. Prowatke and Klemme (2005) report for dacite compositions an $ASI = 0.66$ and for rhyolite melt compositions an $ASI = 0.63$, whereas the FCT whole rock compositions yield an $ASI = 0.97$ (Bachmann et al., 2002). As VFC whole rock compositions yield ASI values that range from 0.97 to 1.08 (Table 1), we consider the partition coefficients of Bachmann et al. (2005) the most applicable for calculating REE felsic melt compositions in equilibrium with titanite. Based on the arguments outlined above, the melt in equilibrium with titanite, using the partition coefficients of Bachmann et al. (2005), have REE melt patterns that are consistent with the removal of MREEs due to the fractionation amphibole and titanite, and overlapping REE melt patterns between amphibole and titanite indicate crystallization for similar melt compositions (Fig. 8)

Titanite equilibrium melt compositions through time

Ideally we would like to relate the melt composition in equilibrium with titanite to the near solidus crystallization of the VFC felsic crystal mushes, as recorded by our titanite U-Pb dates (Broderick, Chapter 2: Fig. 2). For the U-Pb system of titanite, Cherniak

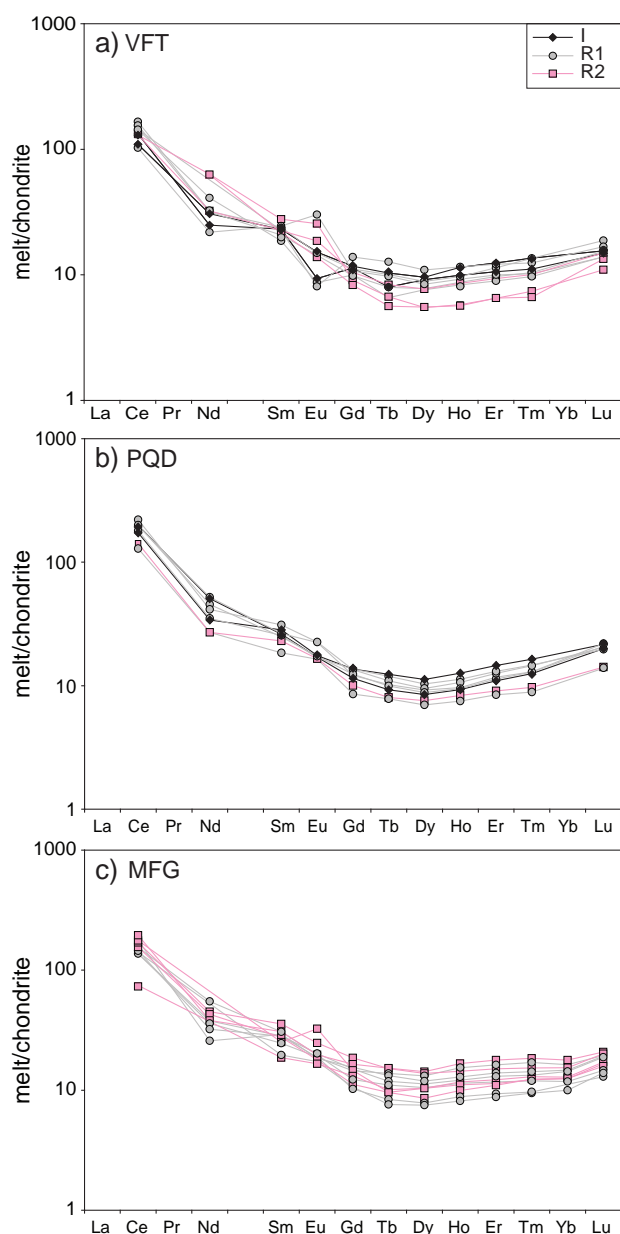


Figure 9: Calculated REE patterns of melts in equilibrium with zircon, from the felsic units, based on previously determined periods of enhanced zircon crystallization. I = initial felsic intrusions; R1, R2 = periods of rejuvenation of felsic crystal mushes. (See text for discussion)

(1993) experimentally determined the closure temperature for titanite, based on Pb diffusion, of $650 \pm 50^\circ\text{C}$ for grains with a diffusion radius of 0.05 cm and a cooling rate of $10^\circ\text{C}/\text{Ma}$. In contrast, Frost et al. (2000) calculate a closure temperature for Pb diffusion in titanite of 700°C for smaller grains with a diffusion

radius of 0.01 cm with a cooling rate of $100^\circ\text{C}/\text{Ma}$. Furthermore, Frost et al. (2000) suggest higher closure temperatures for larger grains (e.g. $> 700^\circ\text{C}$ for titanite grains with a 0.05 cm diffusion radius) based on titanite U-Pb ages, from high grade metamorphic terranes, which were not reset during metamorphism (Scott and St. Onge, 1995; Pidgeon et al., 1996; Schaerer, 1996). In contrast to Pb diffusion in titanite, experimental data (Cherniak, 1995) suggests that REE diffusion in titanite is several orders of magnitude slower than Pb diffusion in titanite (Cherniak, 1993), which corresponds to higher REE closure temperatures for titanite of $> 900^\circ\text{C}$ for grains with a diffusion radius of 0.05 cm and a cooling rate of $10^\circ\text{C}/\text{Ma}$. The $\geq 200^\circ\text{C}$ difference in closure temperatures highlights the difficulty in relating equilibrium REE melt composition recorded by titanite at the time of crystallization to the U-Pb date recorded when titanite cools below its closure temperature. Our calculated REE melt compositions indicate that titanite crystallization was coeval with amphibole crystallization (Fig. 8), which is suggestive of titanite crystallization above solidus conditions. Therefore we applied the Zr-in-sphene (titanite) thermometer of Hayden et al. (2008) to estimate the crystallization temperatures recorded by titanite. Measured Zr concentrations in titanite from the felsic units range from 500 to 900 ppm which translates to Zr-in-titanite

temperatures of $\sim 700^{\circ}\text{C}$ to 750°C (see Appendix C for details). These calculated temperatures for titanite crystallization are consistent with temperatures recorded by titanite from dacite and rhyolite compositions (Hayden et al., 2008; Colombini et al., 2011). More importantly, our titanite crystallization temperatures overlap with amphibole crystallization temperatures of $\sim 680^{\circ}\text{C}$ to 860°C (Stauffer, 2012) consistent with coeval crystallization with amphibole. Therefore, because titanite crystallized at temperatures above its closure temperature, our titanite U-Pb dates record the closure age which can be potentially younger than its magmatic age (Frost et al., 2000), thus we can not confidently link titanite equilibrium melt compositions with the U-Pb dates recorded by VFC titanite. In addition, the VFC felsic units were kept above solidus temperatures in a “crystal mush state” due to repeated thermal fluctuations, as the result of repeated mafic injections over 100 – 200 ka timescales (Broderick, Chapter 2), and because the Pb isotopes in titanite are likely to be disturbed during thermal fluctuations (Cherniak, 1993) resulting in titanite U-Pb dates being reset at higher temperatures, we are unable to link melt compositions in equilibrium with titanite crystallization to their corresponding U-Pb dates.

Zircon equilibrium melt compositions through time

Calculated REE patterns for the felsic melts in equilibrium with zircon, except La which is below the limit of detection, have higher REEs relative to amphibole and plagioclase (Fig. 8). The REE enrichment in the felsic melts may be the result of extensive plagioclase and quartz fractionation (Table 2), where REEs are incompatible ($K_d < 1$) resulting in the residual melts becoming more enriched in REEs. The calculated melt compositions in equilibrium with zircon from the felsic samples record similar melt patterns with variable negative and positive Eu anomalies (Fig. 8a-c). In order to further explore the observed variations in the REE melt compositions in equilibrium with zircon, we relate equilibrium melt compositions to the previously determined periods of enhanced zircon crystallization associated with the initial felsic intrusions, referred to as I, and periods of rejuvenation of felsic crystal mushes, referred to as R1 and R2 (see Broderick, Chapter 2).

The calculated REE melts in equilibrium with VFT zircons record Eu anomalies that vary from negative ($\text{Eu}/\text{Eu}^* = 0.5$) to positive ($\text{Eu}/\text{Eu}^* = 1.8$) and show no correlations with time (Fig. 9a). The melt compositions associated with the initial felsic intrusions (I) record rather homogenous LREEs and HREEs and slightly negative Eu anomalies ($\text{Eu}/\text{Eu}^* = 0.6 - 0.9$).

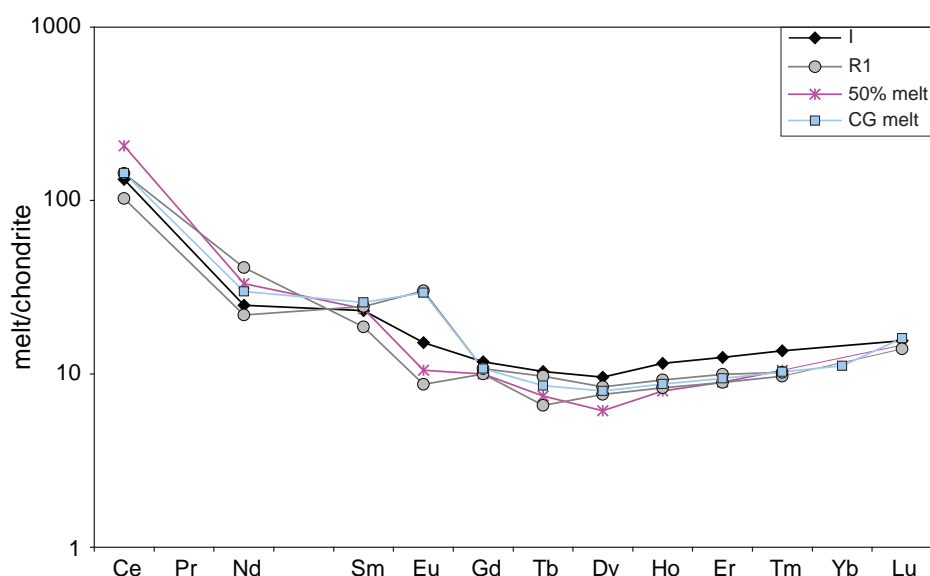


Figure 10: The calculated REE melt patterns in equilibrium with zircon during R1 show large compositional variations. After 50% crystallization of plagioclase and amphibole we can reproduce the melts with negative Eu anomalies. Whereas melts with positive Eu anomalies are consistent with equilibrium melts for the CG (see text for discussion).

Calculated melt compositions in equilibrium with zircon crystallizing during R1 record the largest variations in Eu anomalies ($\text{Eu}/\text{Eu}^* = 0.5 - 1.8$) and have HREEs similar to the melt compositions from I. Because zircon crystallization during R1 is the result of cooling following remelting and remobilization of the felsic crystal mushes due to mafic injections, we suggest that the large variations in the melt compositions in equilibrium with zircon is consistent with zircon crystallization from chemically distinct magma batches (see discussion below). The calculated REE melts in equilibrium with zircon that crystallized during R2 have positive Eu anomalies ($\text{Eu}/\text{Eu}^* = 1.0 - 1.6$) and are depleted in HREEs relative to melts from I and R1, which indicates crystallization from a melt that has fractionated amphibole and minor titanite and is consistent with overlapping equilibrium

melts from R2 zircons with amphibole (Fig. 8a), therefore they are considered to be coeval. The calculated REE melts in equilibrium with the PQD zircons follow similar trends as the melts in equilibrium for the VFT zircons (Fig. 9b) and therefore are considered to record similar histories. These results are in agreement with the core-rim REE patterns, based on trace elements in zircon, for the VFT and PQD, where zircon rims record lower abundances of REEs relative to zircon cores (see Chapter 2, Fig. 4) pointing to crystallization from REE depleted melt due to amphibole fractionation.

The calculated melt compositions in equilibrium with the MFG zircons are similar during R1 and R2 (Fig. 9c), although melts associated with R2 record mostly positive Eu anomalies ($\text{Eu}/\text{Eu}^* \sim 0.9 - 1.7$). The lack of amphibole crystallization in the MFG explains the lack

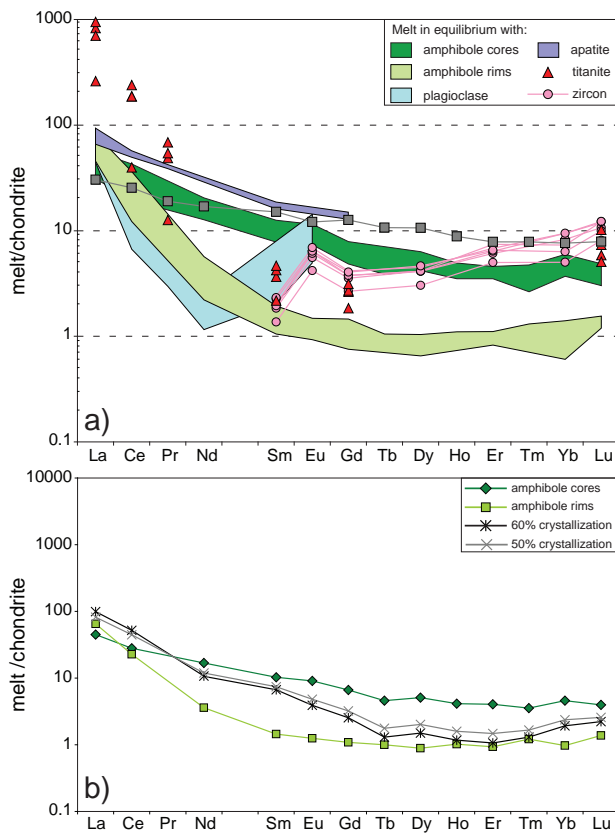


Figure 11: a) Calculated REE patterns of melts in equilibrium with the MG mineral phases. b) demonstrates that the MG equilibrium melts for the amphibole can almost be reproduced by 50 - 60% crystallization from melt in equilibrium with amphibole cores.

of REE depletion in R2 melts relative to R1. However, it does not explain the positive Eu anomalies during R2, which requires amphibole fractionation. Therefore, a plausible explanation for the positive Eu during R2 that it is the result of melting plagioclase during rejuvenation, which would enrich the melt in Eu from which zircon crystallized. This is supported by ubiquitous resorbed plagioclase grains in the felsic magmas (Blundy and Shimizu, 1991; Stauffacher, 2012). The REE equilibrium melts for R1 and R2 are in agreement with the core-rim REE data for the MFG, where zircons record overlapping REE

concentrations (see Broderick Chapter 2, Fig. 4).

A crystallization model for the VFT

In order to explain the chemical variability of the VFT melt compositions in equilibrium with zircon, we have modelled REE melt compositions based on differences in the fractionating assemblages. The starting melt composition was taken to be the melt in equilibrium with zircon crystallizing from the initial felsic intrusions (I). The lack of an Eu anomaly ($\text{Eu}/\text{Eu}^* = 0.9$) in the starting melt composition indicates that zircon crystallized early, prior to extensive plagioclase fractionation and is therefore considered to be the best approximation for the starting melt composition at ~ 42.60 Ma (Broderick, Chapter 2) prior to rejuvenation. Using the Rayleigh crystallization model with a fractionating mineral assemblage of $\text{plagioclase}_{(0.9)} + \text{amphibole}_{(0.1)}$ we can reproduce R1 equilibrium melt compositions with negative Eu anomalies at 50% crystallization (Fig. 10) consistent with the estimated crystallinity from our conceptual zircon crystallization model in Broderick Chapter 2. These results are also in agreement with the experiments on the Sierra Nevada tonalites which at $850 - 900^\circ\text{C}$ contain 55% crystals composed of plagioclase, amphibole and magnetite (Piwinski, 1968). The R1 equilibrium melt compositions with positive

Eu anomalies (Fig. 9a-b) could not be reproduced by any combination of fractionating assemblages between 50% and 80% crystallization. This could be the result of the partition coefficients used to calculate the melt may not reflect equilibrium partitioning behaviour, however due to the limited temperature range recorded by Ti-in-zircon temperatures (700 - 800°C; Broderick, Chapter 2) we argue that the use of a constant partition coefficient to calculate melt compositions during R1 should reflect equilibrium partitioning behaviour. We suggest that the R1 equilibrium melt compositions with positive Eu anomalies represent melts that can not be explained by only crystallization, thus the R1 equilibrium melts may reflect other processes such as plagioclase accumulation, melting of plagioclase, mixing or assimilation. The presence of ubiquitous resorbed plagioclase grains, in the VFT (Fig. B1), supports the melting of plagioclase as process to enrich the melt in Eu from which R1 zircons crystallize. However, figure 10 illustrates that R1 zircon equilibrium melt compositions with positive Eu anomalies are broadly consistent with the zircon equilibrium melt compositions of the CG, which points to mixing between felsic and mafic melts as a processes which contributes to enriching the melt in Eu from which R1 zircons crystallize. Additional evidence for mixing comes from zircon Hf isotopic compositions

that record large variations in ϵ_{Hf} during R1 and point to increased mixing with the CG through time (Broderick, Chapter 2). We suggest based on textural (Fig. B1) and field observations (Fig. A1), that the observed positive Eu anomalies in the equilibrium melts are the result of both melting of plagioclase and mixing with the CG. Therefore, based on the arguments outlined above combined with chemical variability record by zircon (Broderick, Chapter 2), we propose that the melts in equilibrium with zircon during R1 are consistent with zircon crystallizing from different magma batches which reflect the crystallization of plagioclase and amphibole of varying proportions among batches, combined with different degrees of plagioclase melting and/or mixing with the CG. The results presented here highlight that by using accessory minerals (e.g. zircon) we can identify distinct magma batches, which record different processes between batches, within a single unit on the hand sample scale. By using accessory zircon, we are able to look at the evolution of the VFT in greater detail, where zircon records multiple periods of dissolution and growth in distinct magma batches, details that are not evident in whole-rock geochemistry (Fig. 4).

We argue that based on the complex evolution of the VFT, that if we modeled the fractionation of the VFT from whole-rock geochemistry, the identification of distinct individual magma

batches, as well as the different processes in which the magma batches were formed would be lost.

Mattoni gabbro melt compositions

Amphibole

The REE patterns for the melts in equilibrium with the crystallizing phases of the MG are slightly LREE enriched relative to the HREEs (Fig. 11a), whereas the whole rock records a relatively flat REE pattern (Fig. 4). Melt REE patterns calculated for amphibole cores and rims have similar REE melt patterns, however the melts in equilibrium with the amphibole rims have lower REEs relative to amphibole core melt compositions. The REE depleted melt in equilibrium with the amphibole rims has the typical concave up pattern that is consistent with the removal of MREEs due to fractionation of amphibole (cores) and titanite. Our calculated REE melt compositions for the MG amphiboles are in disagreement with the calculated melt compositions of Tiepolo et al. (2002, 2005) that record contrasting melt patterns between cores and rims, which the authors suggest could not result from fractional crystallization. However, we argue that due to the variable P-T conditions in which the MG amphiboles crystallized ($P = 0.8 - 1.0$ GPa at $T = 1000^{\circ}\text{C}$ and $P = 0.2 - 0.3$ GPa at $T = 900^{\circ}\text{C}$; Ulmer et al., 1983) that the application of a single set of partition

coefficients by Tiepolo et al. (2002, 2005) to the amphibole cores and rims does not accurately estimate the melt composition from which the MG amphiboles crystallized. In addition, the partition coefficients applied by Tiepolo et al. (2002, 2005) indicate incompatible behaviour for all REEs in amphibole, except for Dy which is in disagreement with other sets of amphibole partition coefficients which record compatible behaviour for middle to heavy REEs, with the exception of La to Nd which are incompatible (Sisson, 1994; Bachmann et al., 2005; Nandedkar, 2013). Furthermore, using the melt composition in equilibrium with the amphibole cores as a starting melt composition, after 50 – 60% amphibole (core) crystallization, calculated by Rayleigh fractional crystallization, the residual melt is in agreement with the melts from which the amphibole rims crystallized, with the exception of the LREEs (Fig. 11b). We suggest that our inability to reproduce the LREEs is the result of their incompatible behavior in amphibole (Nandedkar, 2013). Therefore, based on our melt compositions in equilibrium with amphibole, we propose that the amphibole rims crystallized from a REE depleted residual melt as the result of the crystallization of the amphibole cores at depth.

Accessory minerals

Titanite

Based on the arguments outlined above, for

the felsic melt compositions, titanite partition coefficients applied to the MG titanites are from the experimental data of Prowatke and Klemme (2005) using sample ASI280 with a corresponding ASI = 0.58 which is similar to the ASI = 0.59 calculated from MG whole rock compositions (Table 1). The REE melt in equilibrium with titanite overlaps with the REE melt in equilibrium with zircon, which indicates coeval titanite and zircon crystallization from similar melt compositions. Measured Zr concentrations in the titanite from the MG range from 1700 to 2000 ppm which translates to Zr-in-titanite temperatures of $\sim 800^{\circ}\text{C}$ (see Appendix C for details). Again, based on temperature differences between crystallization and the closure of the U-Pb system in titanite, we are unable to link melt compositions in equilibrium with titanite crystallization to their corresponding U-Pb dates.

Zircon

The calculated REE melts in equilibrium with zircon record positive Eu anomalies, which are also observed in plagioclase (Fig. 11a). The positive Eu anomalies in the melts in equilibrium with zircon and plagioclase indicate that zircon and plagioclase crystallized from melts that have fractionated amphibole and titanite, which discriminates against Eu during crystallization (Gromet and Silver, 1986; Glazner et al., 2008),

and enriches the residual melt in Eu. This is consistent with our petrographic observations, where zircon saturates late in the MG evolution and is associated with the late crystallizing phases; plagioclase and quartz (Broderick, Chapter 3). The calculated equilibrium REE melts are similar between C1 and C2, which is consistent with zircon crystallizing from rather homogenous melt compositions (Broderick, Chapter 2). Whereas, the depleted melt in equilibrium with plagioclase is the result of plagioclase as the final crystallizing phase in a strongly depleted residual melt.

4.7 Conclusions

The present study has shown that the use of trace element compositions from mineral assemblages to calculate equilibrium melt compositions provides a detailed record of magmatic evolution that is not evident from whole rock studies.

Trace element concentration of titanites record distinct patterns over the range of VFC magma compositions. Calculated melt compositions in equilibrium with titanite vary of two orders of magnitude based on available partition coefficients, and requires that partition coefficients are evaluated based on the ASI of the magma composition, however there is currently no experimental data for peraluminous compositions. While titanite has an influential

role on the REE budget of the magma, due to difficulties in estimating equilibrium melt compositions combined with differences in closure temperatures between Pb and REEs (Cherniak, 1993, 1995) the estimated equilibrium melt compositions for titanite cannot be related to the U-Pb dates recorded by titanite.

Equilibrium melt compositions calculated from zircon trace element compositions, obtained by TIMS-TEA (Schoene et al., 2010), highlights changes in melt composition through time. The largest variations in equilibrium melt compositions correspond to zircon crystallization following the remelting and remobilization of the felsic crystal mushes, referred to as R1. During this period of zircon crystallization, equilibrium melt compositions reflect variable proportions of crystallizing amphibole and plagioclase combined with different degrees of melting and mixing within individual magma batches. We propose that these individual magma batches represent “small magma chambers” within a crystal mush, thus highlighting the problematics that may arise in geochemical modeling from whole-rock geochemistry.

References

- Anderson, J. L., Barth, A. P., Wooden, J. L., and Mazdab, F., 2008, Thermometers and thermobarometers in granitic systems: Reviews in Mineralogy and Geochemistry, v. 69, p. 121-142.
- Bachmann, O., Dungan, M. A., and Bussy, F., 2005, Insights into shallow magmatic processes in large silicic magma bodies: the trace element record in the Fish Canyon magma body, Colorado: Contributions to Mineralogy and Petrology, v. 149, p. 338-349.
- Bachmann, O., Dungan, M. A., and Lipman, P. W., 2002, The Fish Canyon magma body, San Juan volcanic field, Colorado: rejuvenation and eruption of an upper-crustal batholith: Journal of Petrology, v. 43, p. 1469-1503.
- Bea, F., Montero, P., and Ortega, M., 2006, A LA-ICP-MS evaluation of Zr reservoirs in common crustal rocks: Implications for Zr and Hf geochemistry, and zircon-forming processes: The Canadian Mineralogist, v. 44, p. 693-714.
- Blundy, J. D., and Shimizu, N., 1991, Trace element evidence for plagioclase recycling in calc-alkaline magmas: Earth and Planetary Science Letters, v. 102, p. 178-197.
- Blundy, J. D., and Sparks, R. S. J., 1992, Petrogenesis of mafic inclusions in granitoids of the Adamello Massif, Italy: Journal of Petrology, v. 33, p. 1039-1104.
- Blundy, J. D., and Wood, B., 2003, Partitioning of trace elements between crystals and melts: Earth and Planetary Science Letters, v. 210, p. 383-397.
- Brack, P., 1983, Multiple intrusions-examples from the Adamello batholith (Italy) and their significance on the mechanism of intrusion: Mem. Soc. Geol. Ital, v. 26, p. 145-157.
- Brooks, C.K., Henderson, P., and Ronsbo., G., 1981, Rare-earth partition between allanite and glass in the obsidian of Sandy Braes, Northern Ireland: Mineralogical Magazine, v. 4, p. 157-160.
- Callegari, E., and Brack, P., 2002, Geological map of the Tertiary Adamello Batholith (Northern Italy) Explanatory notes and legend: Mem. Sci. Geol, v. 54, p. 19-49.
- Cherniak, D. J., 1993, Lead diffusion in titanite and preliminary results on the effects of radiation damage on Pb transport: Chemical Geology, v. 110, p. 177-194.

- Cherniak, D. J., 1995, Sr and Nd diffusion in titanite: *Chemical geology*, v. 125, p. 219-232.
- Claiborne, L. L., Miller, C. F., and Wooden, J. L., 2010, Trace element composition of igneous zircon: a thermal and compositional record of the accumulation and evolution of a large silicic batholith, Spirit Mountain, Nevada: *Contributions to Mineralogy and Petrology*, v. 160, p. 511-531.
- Colombini, L. L., Miller, C. F., Gualda, G. A. R., Wooden, J. L., and Miller, J. S., 2011, Sphene and zircon in the Highland Range volcanic sequence (Miocene, southern Nevada, USA): elemental partitioning, phase relations, and influence on evolution of silicic magma: *Mineralogy and Petrology*, v. 102, p. 29-50.
- Glazner, A. F., Coleman, D. S., and Bartley, J. M., 2008, The tenuous connection between high-silica rhyolites and granodiorite plutons: *Geology*, v. 36, p. 183-186.
- Gray, W., Glazner, A. F., Coleman, D. S., and Bartley, J. M., 2008, Long-term geochemical variability of the Late Cretaceous Tuolumne intrusive suite, central Sierra Nevada, California: *Geological Society, London, Special Publications*, v. 304, p. 183-201.
- Gromet, L.P., and Silver, L.T., 1983, Rare earth element distributions among minerals in a granodiorite and their petrogenic implications: *Geochimica et Cosmochimica Acta*, v. 47, p. 925-939.
- Gromet, L.P., and Silver, L.T., 1986, REE variations across the Peninsular Ranges batholith: Implications for batholithic petrogenesis and crustal growth in magmatic arcs: *Journal of Petrology*, v. 28, p. 75-125.
- Hanchar, J. M., and Watson, E. B., 2003, Zircon saturation thermometry: *Reviews in mineralogy and geochemistry*, v. 53, p. 89-112.
- Hayden, L. A., Watson, E. B., and Wark, D. A., 2008, A thermobarometer for sphene (titanite): *Contributions to Mineralogy and Petrology*, v. 155, p. 529-540.
- Hermann, J. r., 2002, Allanite: thorium and light rare earth element carrier in subducted crust: *Chemical Geology*, v. 192, p. 289-306.
- Hoskin, P. W., Kinny, P. D., Wyborn, D., and Chappell, B. W., 2000, Identifying accessory mineral saturation during differentiation in granitoid magmas: an integrated approach: *Journal of Petrology*, v. 41, p. 1365-1396.
- Hoskin, P. W. O., and Schaltegger, U., 2003, The composition of zircon and igneous and metamorphic petrogenesis: *Reviews in mineralogy and geochemistry*, v. 53, p. 27-62.
- Klimm, K., Blundy, J.D and Green, T.H., 2008, Trace Element Partitioning and Accessory Phase Saturation during H₂O-Saturated Melting of Basalt with Implications for Subduction Zone Chemical Fluxes: *Journal of Petrology*, v. 49, p. 523-553.
- Krogh, T. E., 1973, A low-contamination method for hydrothermal decomposition of zircon and extraction of U and Pb for isotopic age determinations: *Geochimica et cosmochimica acta*, v. 37, p. 485-494.
- Leuthold, J., Müntener, O., Baumgartner, L. P., Putlitz, B., Ovtcharova, M., and Schaltegger, U., 2012, Time resolved construction of a bimodal laccolith (Torres del Paine, Patagonia): *Earth and Planetary Science Letters*, v. 325, p. 85-92.
- Mahood, G., and Hildreth, W., 1983, Large partition coefficients for trace elements in high-silica rhyolites: *Geochimica et Cosmochimica Acta*, v. 47, p. 11-30.
- Memeti, V., Paterson, S., Matzel, J., Mundil, R., and Okaya, D., 2010, Magmatic lobes as “snapshots” of magma chamber growth and evolution in large, composite batholiths: An example from the Tuolumne intrusion, Sierra Nevada, California: *Geological Society of America Bulletin*, v. 122, p. 1912-1931.
- Michel, J., Baumgartner, L., Putlitz, B., Schaltegger, U., and Ovtcharova, M., 2008, Incremental growth of the Patagonian Torres del Paine laccolith over 90 ky: *Geology*, v. 36, p. 459-462.
- Miller, J. S., Matzel, J. E. P., Miller, C. F.,

- Burgess, S. D., and Miller, R. B., 2007, Zircon growth and recycling during the assembly of large, composite arc plutons: *Journal of Volcanology and Geothermal Research*, v. 167, p. 282-299.
- Nandedkar, R., 2013, Evolution of Hydrous Mantle-Derived Calc-alkaline Liquids by Fractional Crystallisation at 0.7 and 0.4 GPa - An Experimental Study, PhD thesis, ETH Zürich.
- Noyes, H.J., Frey, F.A. and Wones, D.R., 1983, A tale of two plutons: Geochemical evidence bearing on the origin and differentiation of the Red Lake and Eagle Peak plutons, Central Sierra Nevada, California: *The Journal of Geology*, v. 91, p. 487-509.
- Pidgeon, R.T., Bosch, D., and Bruguier, O., 1996, Inherited zircon and titanite U-Pb systems in an Archaean syenite from southwestern Australia: implications for U-Pb stability of titanite: *Earth and Planetary Science Letters*, v. 141, p. 187-198.
- Piwinskii, A. J., 1968, Experimental studies of igneous rock series central Sierra Nevada batholith, California: *The Journal of Geology*, p. 548-570.
- Prowatke, S., and Klemme, S., 2005, Effect of melt composition on the partitioning of trace elements between titanite and silicate melt: *Geochimica et Cosmochimica Acta*, v. 69, p. 695-709.
- Prowatke, S., and Klemme, S., 2006, Trace element partitioning between apatite and silicate melts: *Geochimica et Cosmochimica Acta*, v. 70, p. 4513-4527.
- Roduit, N., 2006, Quantification and measurement in digital images of thin sections with JMicroVision: *Geophysical Research Abstracts*, 2006, p. 08260.
- Rollinson, H. R., and Data, U. G., 1993, Using geochemical data: Evaluation, Presentation, Interpretation.
- Rubatto, D., and Hermann, J. r., 2007, Experimental zircon/melt and zircon/garnet trace element partitioning and implications for the geochronology of crustal rocks: *Chemical Geology*, v. 241, p. 38-61.
- Sano, Y., Terada, K., and Fukuoka, T., 2002, High mass resolution ion microprobe analysis of rare earth elements in silicate glass, apatite and zircon: lack of matrix dependency: *Chemical Geology*, v. 184, p. 217-230.
- Sawka, W. N., 1988, REE and trace element variations in accessory minerals and hornblende from the strongly zoned McMurry Meadows Pluton, California: *Transactions of the Royal Society of Edinburgh: Earth Sciences*, v. 79, p. 157-168.
- Schaltegger, U., and Krähenenbühl, U., 1990, Heavy rare-earth element enrichment in grainites of the Aar Massif (Central Alps, Switzerland): *Chemical Geology*, v. 89, p. 49-63.
- Schaltegger, U., Brack, P., Ovtcharova, M., Peytcheva, I., Schoene, B., Stracke, A., Marocchi, M., and Bargossi, G. M., 2009, Zircon and titanite recording 1.5 million years of magma accretion, crystallization and initial cooling in a composite pluton (southern Adamello batholith, northern Italy): *Earth and Planetary Science Letters*, v. 286, p. 208-218.
- Schoene, B., Latkoczy, C., Schaltegger, U., and Günther, D., 2010, A new method integrating high-precision U-Pb geochronology with zircon trace element analysis (U-Pb TIMS-TEA): *Geochimica et Cosmochimica Acta*, v. 74, p. 7144-7159.
- Schoene, B., Schaltegger, U., Brack, P., Latkoczy, C., Stracke, A., and Günther, D., 2012, Rates of magma differentiation and emplacement in a ballooning pluton recorded by U-Pb TIMS-TEA, Adamello batholith, Italy: *Earth and Planetary Science Letters*, v. 355, p. 162-173.
- Scott, D. J. and St. Onge, M.R., 1995, Constraints on Pb closure temperature in titanite based on rocks from the Ungava orogen, Canada: Implications for U-Pb geochronology and P-T-t path determinations: *Geology*, v. 23 no. 12 p. 1123-1126.
- Sisson, T. W., 1994, Hornblende-melt trace-element partitioning measured by ion

- microprobe: *Chemical Geology*, v. 117, p. 331-344.
- Stauffer, A. K., 2012, Petrology and mineral chemistry of the Val Fredda Complex leucocratic units, Adamello, Italy, MSc thesis, ETH Zürich.
- Tiepolo, M., Oberti, R., and Vannucci, R., 2002, Trace-element incorporation in titanite: constraints from experimentally determined solid/liquid partition coefficients: *Chemical Geology*, v. 191, p. 105-119.
- Tiepolo, M., and Tribuzio, R., 2005, Slab-melting during Alpine orogeny: evidence from mafic cumulates of the Adamello batholith (Central Alps, Italy): *Chemical geology*, v. 216, p. 271-288.
- Tiepolo, M., Tribuzio, R., and Langone, A., 2011, High-Mg andesite petrogenesis by amphibole crystallization and ultramafic crust assimilation: Evidence from Adamello hornblendites (Central Alps, Italy): *Journal of Petrology*, v. 52, p. 1011-1045.
- Tiepolo, M., Tribuzio, R., and Vannucci, R., 2002, The compositions of mantle-derived melts developed during the Alpine continental collision: *Contributions to Mineralogy and Petrology*, v. 144, p. 1-15.
- Ulmer, P., Callegari, E., and Soderregger, U. C., 1983, Genesis of the mafic and ultramafic rocks and their genetical relations to the tonalitic-trondhjemitic granitoids of the southern part of the Adamello batholith (Northern Italy): *Mem. Soc. Geol. Ital.*, v. 26, p. 171-222.
- Wotzlaw, J.-F., Schaltegger, U., Frick, D. A., Dungan, M. A., Gerdes, A., and Günther, D., 2013, Tracking the evolution of large-volume silicic magma reservoirs from assembly to supereruption: *Geology*.

Chapter 5

Conclusions and Outlook

Integrating field observations with state of the art analytical techniques, the history of the Val Fredda Complex could be reconstructed from its initial felsic intrusions through periods of rejuvenation to the final stages of crystallization at solidus temperatures. During periods of rejuvenation as a result of repeated mafic sill injections, varying degrees of melting, crystallization and mixing with mafic melts, led to the development of chemically distinct magma batches, which have been preserved by zircon trace element and isotopic compositions. Protracted zircon growth on 100 – 200 ka timescales reflect multiple periods of enhanced zircon crystallization as the result of cooling following the rejuvenation of felsic crystal mushes by mafic melts.

The occurrence of repeated mafic sill injections resulted in repeated cycles of thermal fluctuations, causing the periods of mineral dissolution and growth and as a result highlights the difficulty in relating zircon growth to the paragenetic sequence of VFC magmas and the difficulties associated with the geochemical modeling of granitoids.

The outcomes of this study have implications on our view of magma evolution during incremental pluton assembly. The main points are summarized below.

- The high-precision dates of the VFC demonstrate the difficulty to relate zircon dates to physical processes such as the emplacement of magma, but represent repeated periods of enhanced zircon crystallization in the “crystal mush state” at temperatures closely above the solidus. In addition initial classification of zircons (e.g. autocrysts vs. antecrysts), described by Miller et al., 2007, cannot be applied to the majority of VFC zircons, indicating that the application of these terms relative to the process of physical emplacement of the magma has to be done with caution and requires additional constraints. The high precision U-Pb dates presented here highlight the timing of periods of enhanced zircon which provide the input parameters for time-resolved incremental pluton emplacement models. Future work requires the development of a thermo-mechanical model in order to evaluate the extent in which magma batches develop over 100 – 200 ka timescales of incremental assembly. For

example are magma batches inter-connected? Do they exist at the pluton scale or do occur locally with the mafic sheet intrusions?

- In addition, future work including detailed sampling of the mafic sheets for U-Pb dating may provide insights to the timing of individual sheet injections, e.g. the mafic sheets that represent the final injections contain only C2 zircons. By dating the individual mafic sheets, we can potentially identify if multiple sheets are injected at once, if the sheets are injected one at a time or do we observe numerous mafic sheets injected at same time and then slowly decreasing to the injection of one sheet at a time? Once this is constrained, we can quantify mafic magma injection rates for different identified pulses. This could be combined with melt composition estimates from zircons between sheets to establish if there is an evolution in melt composition through time. The observed compositional variations between mafic sheets could potentially provide information about fractionation processes at depth versus in situ fractionation. For example, do the youngest mafic sheets record differences in amphibole fractionation in comparison to the older mafic sheets?
- The high-precision texturally controlled zircon dates obtained from VFC units could not be related to paragenetic sequence due to periods of dissolution and growth of the crystallizing mineral assemblages associated with repeated periods of rejuvenation. However future work in the application of our method for obtaining high-precision texturally controlled zircon dates in order to relate periods of zircon growth to a crystallizing sequence, is promising for long lived magmatic systems that have not undergone periods of rejuvenation and/or mixing.
- Detailed mineral studies provide valuable information for reconstructing magma evolution, which is not evident from whole rock studies. Future work for reconstructing magma evolution requires detailed isotopic and geochemical information of crystallizing mineral assemblages, which will provide valuable information for the development of geochemical models for granitoids during incremental assembly.

- By using accessory zircon, we are able to look at the evolution of the magma in greater detail, and identify individual magma batches, which distinct evolutionary processes among batches. We propose that these individual magma batches actually represent “small magma chambers” within a crystal mush. Future work would require a detailed study of these “small magma chambers” to determine what amount of melt is required to form a magma chamber? Do these “small magma chambers” record fundamental differences from larger magma chambers?

APPENDIX A

ID-TIMS analytical details

Sample preparation

Zircons were separated from bulk samples using standard mineral separation techniques. To minimize the effects of secondary lead loss the zircons were treated by chemical abrasion prior to analysis, involving high-temperature annealing followed by a HF-HNO₃ leaching step (Mattinson, 2005). Annealing was performed by loading ~50 zircon grains of each sample in quartz crucibles and placing them into a furnace at 900 °C for 48 h. Subsequently, zircons from each sample were transferred into 3 ml screw-top Savillex vials together with ca. 120 µl of concentrated HF and 20 µl of 7N HNO₃ for the leaching step. Savillex vials were placed into a Teflon Parr vessel with 5 ml of concentrated HF, and placed in an oven at 180 °C for 15 h. After the partial dissolution step, the leachate was completely pipetted out and the remaining zircons were rinsed in ultrapure water and then fluxed in 6N HCl for several hours on a hotplate at a temperature of ca. 80 °C. After removal of the acid, the zircon grains were again rinsed several times in ultra-pure water and acetone in an ultrasonic bath. Single zircon grains were selected and loaded for dissolution into pre-cleaned miniaturized Teflon vessels. After

adding ~0.005g of ²⁰²Pb-²⁰⁵Pb-²³³U-²³⁵U spike (EARTHTIME, spike calibration described on www.earth-time.org) to each zircon, the grains were dissolved in 63 µl of concentrated HF with a trace of 7N HNO₃ at 206 °C for 7 days then evaporated and the residue was re-dissolved overnight in 36 µl of 3N HCl at 206 °C. Titanites were dissolved in HF + 7N HNO₃ at 206°C for 2 days then evaporated and the residue was re-dissolved overnight in 36 µl of 6N HCl at 206 °C, then they were dried down again and re-dissolved in HBr prior to chemistry. Lead and U were separated by HCl (zircon) and two-stage HBr-HCl (titanite) based on anion exchange chemistry (Krogh, 1973) in 50 µl columns and dried down with 3 µl of 0.06N H₃PO₄.

Mass spectrometry and procedural blank

The isotopic analyses were performed at the University of Geneva on a TRITON mass spectrometer equipped with a MasCom discrete dynode secondary electron multiplier in ion counting mode. The linearity of the MasCom multiplier was calibrated using U500, Sr SRM987, and Pb SRM982 and SRM 983. Both Pb and U were loaded with 1 µl of silica gel – phosphoric acid mixture (Gerstenberger and Haase 1997) on outgassed single Re-filaments. Pb isotope compositions were measured on the electron multiplier, whereas U (as UO₂) isotopic measurements were made in static Faraday mode

or, in case of low-U samples, in dynamic mode on the electron multiplier. Lead fractionation was corrected using the ET2535 tracer composition assuming $^{202}\text{Pb}/^{205}\text{Pb}$ ratio of 0.99924. Uranium mass fractionation was corrected online using the ^{233}U - ^{235}U double spike, assuming $^{238}\text{U}/^{235}\text{U}$ of 137.818 ± 0.0225 (1σ) for sample U (Hiess et al., 2012). Uranium was analyzed as an oxide, assuming an $^{18}\text{O}/^{16}\text{O}$ composition of 0.00205. U-Pb ratios and dates were calculated relative to $^{235}\text{U}/^{205}\text{Pb}$ ratio of 100.23. All U-Pb data were reduced using Tripoli and U-Pb_Redux (v.2.7.55) software (Bowring et al., 2011; McLean et al., 2011) and EATHTIME tracer calibration (v.3). 20 total procedural blanks were measured over the course of this study, spiked with the same tracer as the samples. All common Pb for zircon analyses was assigned to the procedural blank, and corrected with the following isotopic compositions: $^{206}\text{Pb}/^{204}\text{Pb} = 18.38 \pm 0.89$, $^{207}\text{Pb}/^{204}\text{Pb} = 15.58 \pm 0.69$, $^{208}\text{Pb}/^{204}\text{Pb} = 37.99 \pm 0.76$ (1σ %).

Five total procedural Pb blanks for titanite were measured during this study, spiked with the same tracer as the samples, yielding the following isotopic compositions: $^{206}\text{Pb}/^{204}\text{Pb} = 18.76 \pm 1.12$, $^{207}\text{Pb}/^{204}\text{Pb} = 15.65 \pm 0.31$, $^{208}\text{Pb}/^{204}\text{Pb} = 38.36 \pm 0.23$ (1σ %). Titanite can incorporate a significant amount of Pb at the time of crystallization; therefore we estimated the initial common Pb composition from

the three-dimensional Concordia approach (Ludwig, 2005). The calculated initial common Pb composition for the titanites from the felsic samples are $^{206}\text{Pb}/^{204}\text{Pb} = 18.61 \pm 0.05$ and $^{207}\text{Pb}/^{204}\text{Pb} = 15.66 \pm 0.03$ (1σ). The 3-D isochron intercept calculated for the titanites from the mafic samples yielded an initial common Pb composition of $^{206}\text{Pb}/^{204}\text{Pb} = 18.61 \pm 0.15$ and $^{207}\text{Pb}/^{204}\text{Pb} = 15.60 \pm 0.09$ (1σ).

Initial ^{230}Th disequilibrium calculations

For the initial ^{230}Th disequilibrium correction for zircon, we applied a constant $D_{\text{Th/U}} = 0.25 \pm 0.1$ (from Rubatto and Hermann, 2007) in order to calculate the Th/U of the magma at the time of zircon crystallization. The model Th/U ratio of the zircon was calculated from the measured $^{208}\text{Pb}/^{206}\text{Pb}$ assuming concordance between the $^{232}\text{Th} - ^{208}\text{Pb}$ and the $^{238}\text{U} - ^{206}\text{Pb}$ systems. For the initial ^{230}Th disequilibrium correction for titanite we use the mean Th/U of the magma calculated from the zircons of the same sample (see Table A1).

TIMS-TEA (zircon trace element analyses)

The zircon trace element fractions were dried down on a hot plate and re-dissolved in 1ml of a 0.1M HF and 0.5N HNO_3 solution doped with 1ppb Ir to serve as an internal standard during ICP-MS measurements, of which 500 μl were to be used later for Hf isotope analysis (see below).

Table A1

sample	Th/U zircon	+/-	DTh/U	+/-	Th/U magma	+/- 1s
MFGz1	0.66	0.01	0.25	0.1	2.66	0.33
MFGz2	0.74	0.01	0.25	0.1	2.98	0.35
MFGz3	0.70	0.01	0.25	0.1	2.78	0.33
MFGz4	0.58	0.01	0.25	0.1	2.31	0.30
MFGz5	0.57	0.01	0.25	0.1	2.28	0.30
MFGz6	0.65	0.01	0.25	0.1	2.62	0.32
MFGz7	0.45	0.01	0.25	0.1	1.81	0.27
MFGz8	0.58	0.01	0.25	0.1	2.33	0.31
MFGz9	0.59	0.01	0.25	0.1	2.37	0.31
MFGz10	0.42	0.01	0.25	0.1	1.69	0.26
MFGz11	0.56	0.01	0.25	0.1	2.23	0.30
MFGz12	0.49	0.01	0.25	0.1	1.97	0.28
MFGz13	0.53	0.01	0.25	0.1	2.14	0.29
average Th/U magma used for titanite					2.32	
standard deviation					0.37	
MGz1	1.02	0.01	0.25	0.1	4.08	0.40
MGz2	0.97	0.01	0.25	0.1	3.89	0.39
MGz3	1.33	0.01	0.25	0.1	5.32	0.46
MGz4	1.27	0.01	0.25	0.1	5.08	0.45
MGz5	1.36	0.01	0.25	0.1	5.43	0.47
MGz6	1.11	0.01	0.25	0.1	4.42	0.42
MGz7	1.22	0.01	0.25	0.1	4.89	0.44
MGz8	1.45	0.01	0.25	0.1	5.79	0.48
MGz9	1.38	0.01	0.25	0.1	5.51	0.47
MGz10	2.49	0.01	0.25	0.1	9.96	0.63
MGz11	1.34	0.01	0.25	0.1	5.37	0.46
average Th/U magma used for titanite					4.93	
standard deviation					0.67	
CGz1	0.88	0.01	0.25	0.1	3.52	0.38
CGz2	0.71	0.01	0.25	0.1	2.83	0.34
CGz3	0.93	0.01	0.25	0.1	3.74	0.39
CGz4	0.91	0.01	0.25	0.1	3.63	0.38
CGz5	0.83	0.01	0.25	0.1	3.30	0.36
CGz6	0.90	0.01	0.25	0.1	3.59	0.38
CGz7	0.82	0.01	0.25	0.1	3.29	0.36
CGz8	0.76	0.01	0.25	0.1	3.02	0.35
CGz9	0.84	0.01	0.25	0.1	3.35	0.37
average Th/U magma used for titanite					3.36	
standard deviation					0.30	
VFTz1	0.68	0.01	0.25	0.1	2.72	0.33
VFTz2	0.62	0.01	0.25	0.1	2.49	0.32
VFTz3	0.50	0.01	0.25	0.1	2.01	0.28
VFTz4	0.65	0.01	0.25	0.1	2.59	0.32
VFTz5	0.49	0.01	0.25	0.1	1.95	0.28
VFTz6	0.65	0.01	0.25	0.1	2.61	0.32
VFTz7	0.54	0.01	0.25	0.1	2.15	0.29
VFTz8	0.85	0.01	0.25	0.1	3.41	0.37
VFTz9	0.51	0.01	0.25	0.1	2.05	0.29
VFTz10	0.54	0.01	0.25	0.1	2.18	0.30
average Th/U magma used for titanite					2.42	
standard deviation					0.45	
PQDz1	0.64	0.01	0.25	0.1	2.56	0.32
PQDz2	0.73	0.01	0.25	0.1	2.92	0.34
PQDz3	0.68	0.01	0.25	0.1	2.73	0.33
PQDz4	0.64	0.01	0.25	0.1	2.55	0.32
PQDz5	0.69	0.01	0.25	0.1	2.75	0.33
PQDz6	0.76	0.01	0.25	0.1	3.02	0.35
PQDz7	0.53	0.01	0.25	0.1	2.10	0.29
PQDz8	0.93	0.01	0.25	0.1	3.74	0.39
average Th/U magma used for titanite					2.80	
standard deviation					0.47	
PEGz1	1.17	0.01	0.25	0.1	4.68	0.43
PEGz2	1.16	0.01	0.25	0.1	4.64	0.43
PEGz3	0.98	0.01	0.25	0.1	3.93	0.40
PEGz4	1.08	0.01	0.25	0.1	4.31	0.42
PEGz5	1.22	0.01	0.25	0.1	4.90	0.44
PEGz6	1.00	0.01	0.25	0.1	4.00	0.40
PEGz7	1.05	0.01	0.25	0.1	4.19	0.41
PEGz8	1.15	0.01	0.25	0.1	4.59	0.43
PEGz9	1.14	0.01	0.25	0.1	4.56	0.43

Multi-element concentration standards were produced from a multi-element stock solution, which was diluted into nine calibration solutions of differing concentrations (REE ranging from 5 ppt to 40 ppb and Zr from 50 ppb to 10 ppm and Hf from 25 ppt to 200 ppb). Each calibration solution was doped with 1 ppb Ir in order to serve as an internal standard during ICP-MS measurements. Solutions were introduced into the plasma using a CETAC Aridus desolvation system with an uptake rate of 100 μ l/min. Measurements were carried out in medium mass resolution ($m/\Delta m = 4000$). Calibration solutions were measured prior to and during each session, and a blank solution was used to rinse the transport line in between each sample and was measured every 12 samples for background. In order to minimize the effect of plasma fluctuations or different nebulizer aspiration rates between samples, 1 ppb iridium was added to all samples and calibration solutions as an internal standard. Zircons were analyzed for Y, Zr, Hf, REEs, Nb, Ta, and Th concentrations.

Concentrations were calculated by least squares linear interpolation based on normalization with the Ir internal standard, and on calibration curves defined from measured stock solutions described above. In order to convert the concentrations within the wash solutions to concentrations in zircon, wash solution elemental concentrations were normalized to $Zr + Hf = 497,646$ ppm,

which is the stoichiometric concentration in the Zr-site of zircon (Hoskin and Schaltegger, 2003). Concentrations are reported in ppm and in wt. %, and all uncertainties are reported at the two-sigma level.

In situ trace element analysis in zircon by LA-ICP-MS

Zircon grains were mounted in epoxy resin, polished and carbon-coated before being imaged by cathodoluminescence (CL) prior to LA-ICP-MS analysis, using a Jeol JSM- 7001F scanning electron microscope (SEM) in CL mode at the University of Geneva.

In situ trace element analyses were carried out on the polished and imaged zircons by LA-ICP-MS using a Thermo Scientific Element XR mass spectrometer coupled to a New Wave Research ArF 193 nm laser ablation system at the University of Lausanne. Operating conditions of the laser include using a 25 μm ablation pit, a 10 Hz frequency and an on-sample energy density of $\sim 6 \text{ J/cm}^2$. Helium was used as a cell gas. The acquisition times for the background and the ablation interval corresponded to 60 and 30 seconds, respectively. Dwell times per isotope ranged from 10 to 20 ms and peak hopping mode was employed. The ThO^+/Th^+ and $\text{Ba}^{2+}/\text{Ba}^+$ ratios were optimized to 0.06 – 0.08% and 1.7%, respectively. Measurements of unknowns were bracketed by NIST SRM-612

glass measurements which were employed for the external standardization. Silicon was chosen as the internal standard element ($\text{SiO}_2 = 32.8 \text{ wt. \%}$). Intensity versus time data were reduced in LAMTRACE. All spectra were checked for the presence of surface contamination and intensity spikes and corrected when necessary.

Zircon Hf isotope analysis

Hafnium isotopic compositions were analyzed from the same solution used for trace element analysis collected from zircon anion exchange column separation, using a Thermo-Fisher NEPTUNE multi collector inductively coupled plasma mass spectrometer (MC-ICP-MS) at Johann Wolfgang Goethe University, Frankfurt in solution mode. Following zircon anion exchange chemistry, the trace element fraction was dried down and re-dissolved in 1ml of $0.5 \text{ M HNO}_3 + 0.1 \text{ M HF}$ (500 μl for TEA and 500 μl for Hf isotopes). The solutions were introduced into the plasma using a CETAC Aridus desolvation nebulizer with an uptake rate of 100 $\mu\text{l/min}$. Data were collected in static mode on Faraday detectors. Data were acquired with 60 integration cycles over a period of 2 min, followed by 8 min of washout with a mixture of 2% HNO_3 –0.5 N HF. The isotopes ^{172}Yb , ^{173}Yb and ^{175}Lu were simultaneously monitored during each analysis step to allow for the correction of isobaric interferences between Lu and Yb

isotopes on mass 176 assuming a $^{176}\text{Yb}/^{173}\text{Yb}$ of 0.79502 and $^{176}\text{Lu}/^{175}\text{Lu}$ of 0.02656, following the method described by Gerdes and Zeh (2006). Yb and Hf isotope ratios were corrected for mass fractionation by normalizing to $^{172}\text{Yb}/^{173}\text{Yb}$ of 1.35351 and $^{179}\text{Hf}/^{177}\text{Hf}$ of 0.7325 using an exponential law. The mass bias behavior of Lu was assumed to follow that of Yb. Accuracy and reproducibility of this method were assessed by repeat analyses of 10 ppb JMC 475 standard solutions ($^{176}\text{Hf}/^{177}\text{Hf} = 0.282147 \pm 7$, 2σ , $n = 21$) over the period of measurements. Initial $^{176}\text{Hf}/^{177}\text{Hf}$ ratios and εHf were calculated using $^{206}\text{Pb}/^{238}\text{U}$ age of 42 Ma and the CHUR parameters of Bouvier et al. (2008); ($^{176}\text{Lu}/^{177}\text{Hf} = 0.0336$ and $^{176}\text{Hf}/^{177}\text{Hf} = 0.282785$). All uncertainties are reported at the two sigma level.

References

- Bouvier, A., Vervoort, J.D., and Patchett, P.J., 2008, The Lu-Hf and Sm-Nd isotopic composition of CHUR: constraints from unequilibrated chondrites and implications for the bulk composition of terrestrial planets: *Earth and Planetary Science Letters*, v. 273, p. 48-57.
- Bowring, J.F., McLean, N.M., and Bowring, S.A., 2011, Engineering cyber infrastructure for U-Pb geochronology: Tripoli and U-Pb_Redux: *Geochemistry Geophysics Geosystems*, v. 12, p. Q0AA19.
- Gerdes, A., and Zeh, A., 2009, Zircon formation versus zircon alteration--New insights from combined U-Pb and Lu-Hf in-situ LA-ICP-MS analyses, and consequences for the interpretation of Archean zircon from the Central Zone of the Limpopo Belt: *Chemical Geology*, v. 261, p. 230-243.
- Gerstenberger, H., and Haase, G., 1997, A highly effective emitter substance for mass spectrometric Pb isotope ratio determinations: *Chemical Geology*, v. 136, p. 309-312.
- Hiess, J., Condon, D.J., McLean, N., and Noble, S.R., 2012, $^{238}\text{U}/^{235}\text{U}$ systematics in terrestrial uranium-bearing minerals: *Science*, v. 335, p. 1610-1614.
- Hoskin, P.W.O., and Schaltegger, U., 2003, The composition of zircon and igneous and metamorphic petrogenesis: *Reviews in mineralogy and geochemistry*, v. 53, p. 27-62.
- Krough, T.E., 1973, A low contamination method for hydrothermal decomposition of zircon and extraction of U and Pb for isotope age determination: *Geochem. Cosmochim. Acta*, v. 37, p. 485-494.
- Ludwig, K.R., 2005, Isoplot/Ex Version 3.00: a geological toolkit for Microsoft Excel: Berkeley Geochronology Center Special Publication, 70pp, v. 4.
- Mattinson, J.M., 2005, Zircon U-Pb chemical abrasion ("CA-TIMS") method: combined annealing and multi-step partial dissolution analysis for improved precision and accuracy of zircon ages: *Chemical Geology*, v. 220, p. 47-66.
- McLean, N.M., Bowring, J.F., and Bowring, S.A., 2011, An algorithm for U-Pb isotope dilution data reduction and uncertainty propagation: *Geochemistry, Geophysics, Geosystems*, v. 12.
- Rubatto, D., and Hermann, J.r., 2007, Experimental zircon/melt and zircon/garnet trace element partitioning and implications for the geochronology of crustal rocks: *Chemical Geology*, v. 241, p. 38-61.
- Schoene, B., Latkoczy, C., Schaltegger, U., and Günther, D., 2010, A new method integrating high-precision U-Pb geochronology with zircon trace element analysis (U-Pb TIMS-TEA): *Geochimica et Cosmochimica Acta*, v. 74, p. 7144-7159.

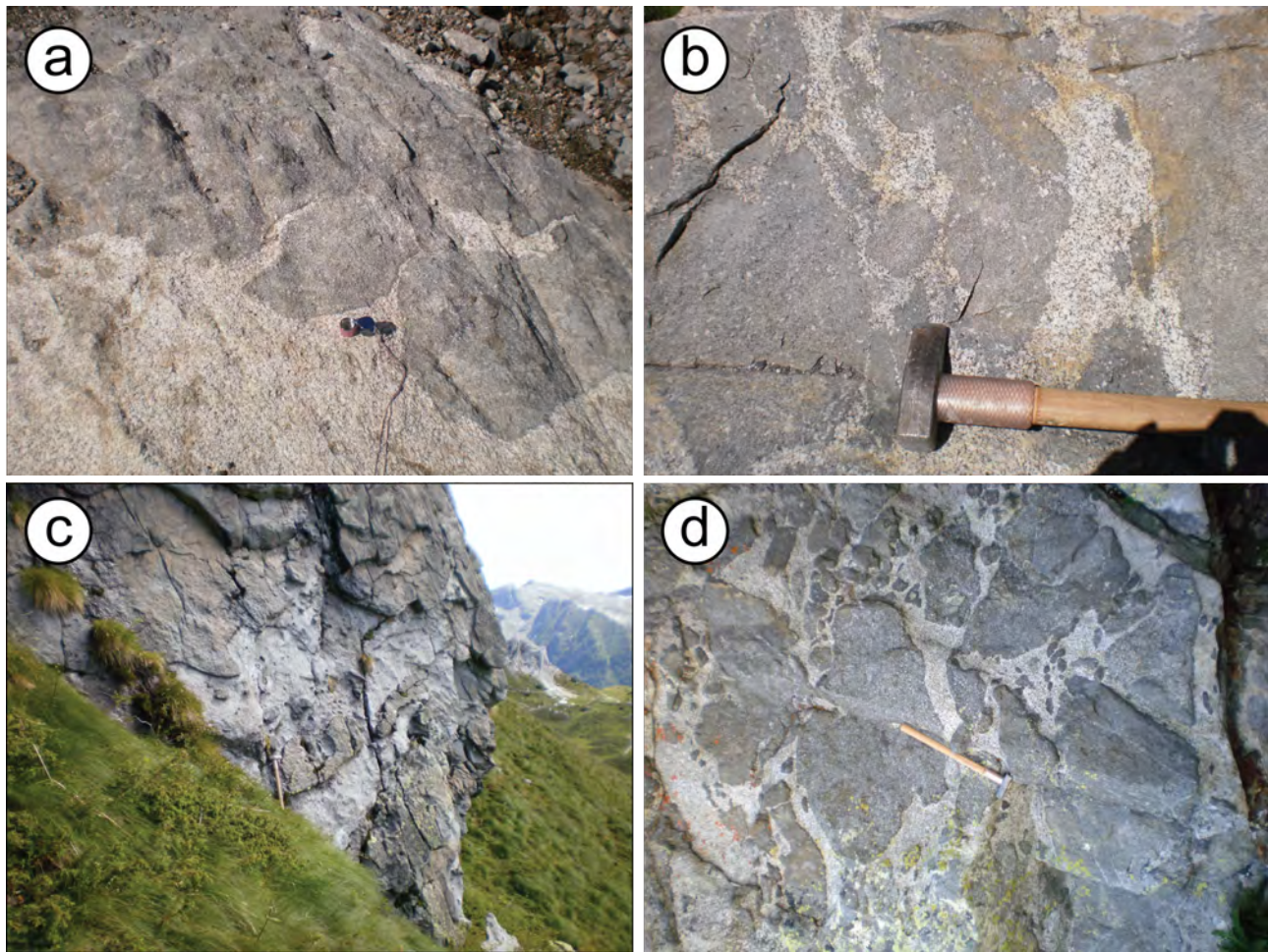


Figure A1: Field photos. a) lobate mafic sheets chilled against marginal facies granodiorite; b) various degrees of mingling between mafic melts and felsic crystal mushes ; c) Cadino mafic sheets injected laterally into crystal mush (plagioclase quartz-diorite); d) break up of mafic sheets into enclave swarms.

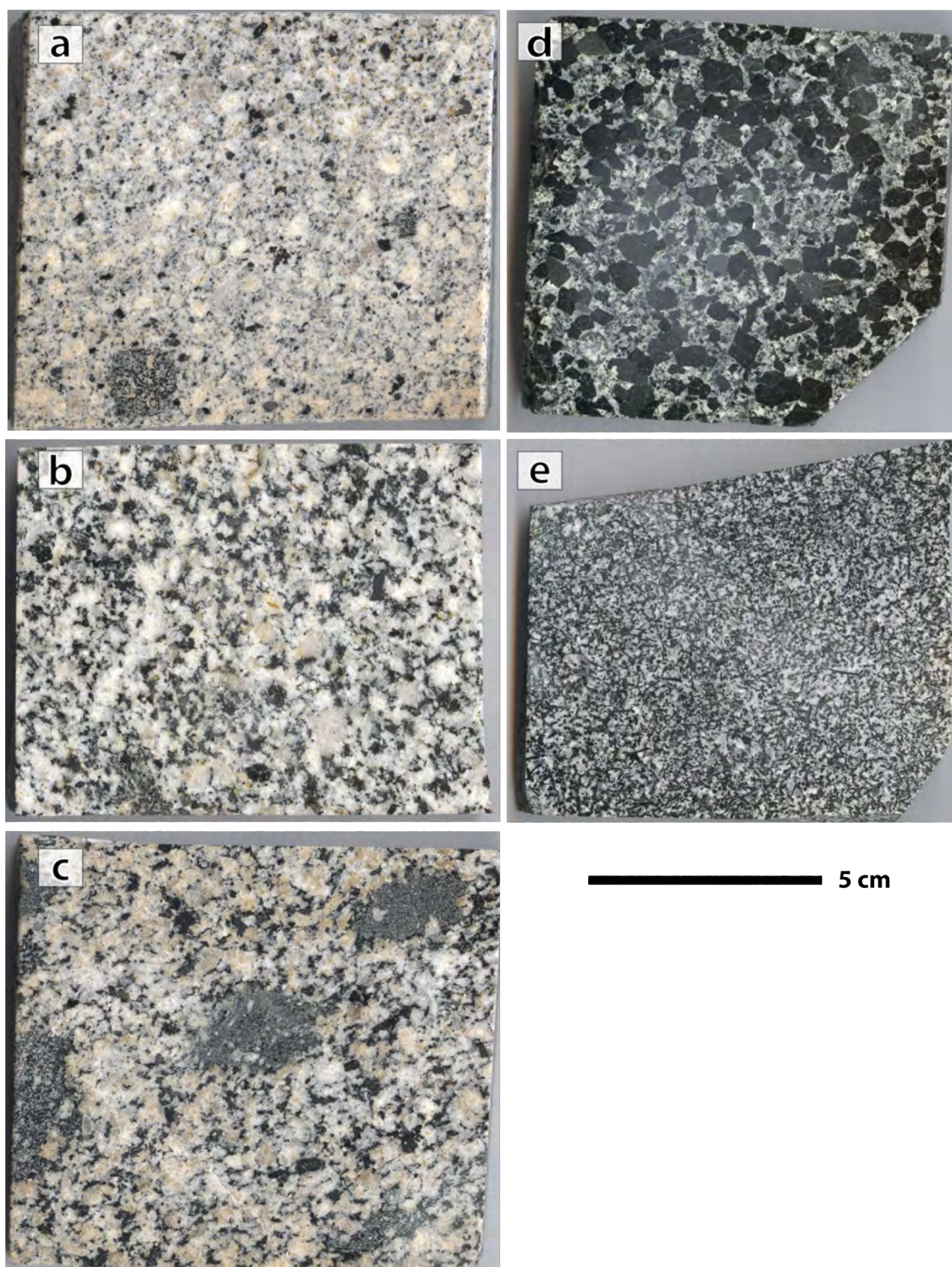
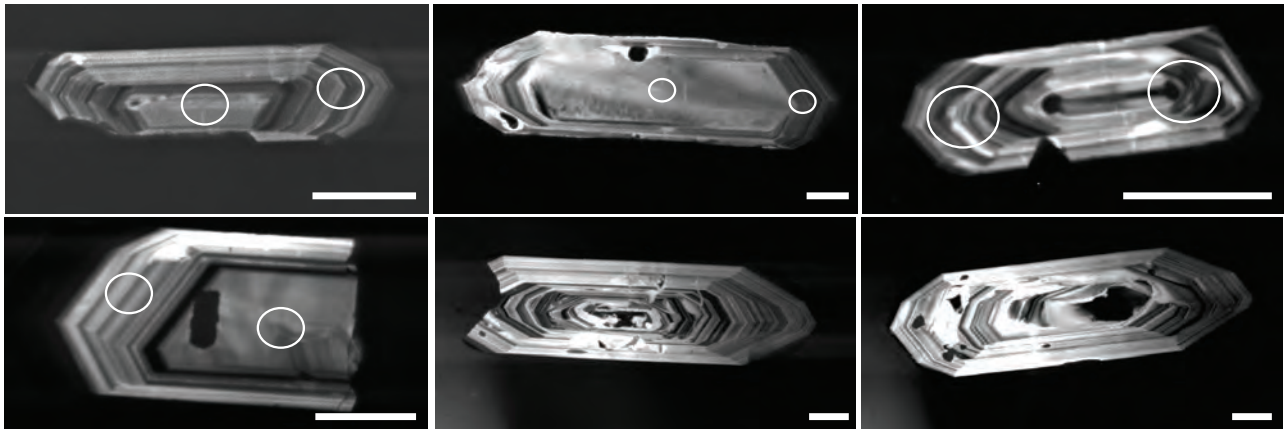


Figure A2: Polished rock slabs and map coordinates given in map datum Rome 1940 and UTM UPS zone 32 T position format.

- a) Marginal facies granodiorite (CB03): N5088131 and E0611171
- b) Plagioclase quartz diorite (CB13): N5088515 and E0610766
- c) Val Fredda tonalite (CB09): N5088392 and E0609884
- d) Mattoni gabbro (CB04): N5086734 and E0609381
- e) Cadino gabbro (CB05): N5088280 and E0609773

MFG Type 1 zircons



MFG Type 2 zircons

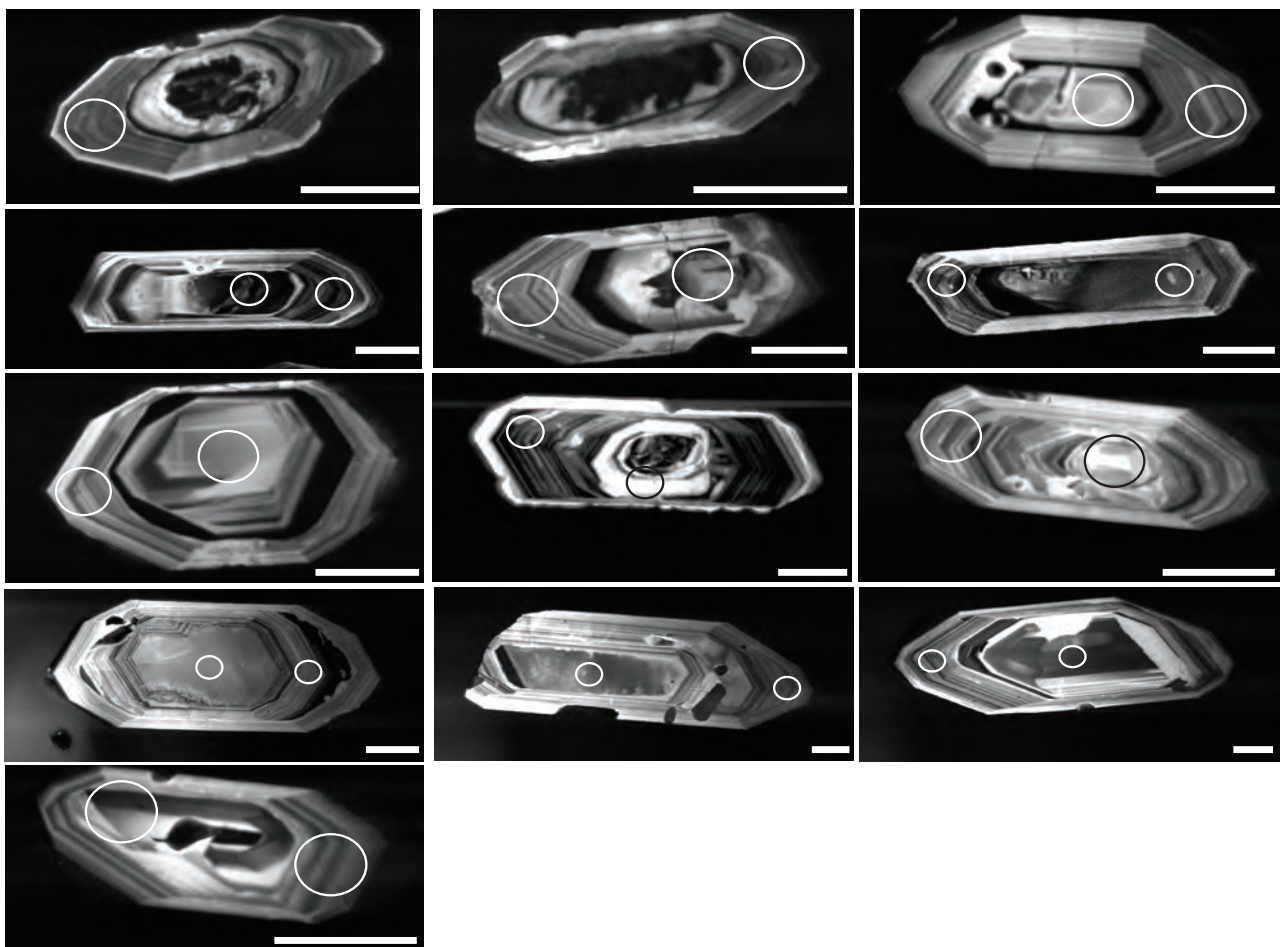
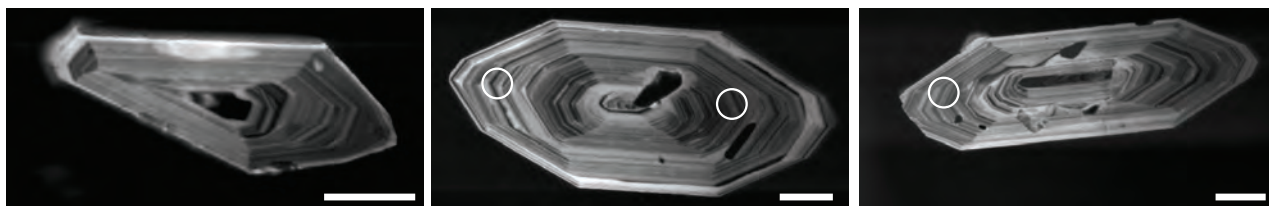


Figure A3: Cathodoluminescence images of MFG zircon showing locations of trace element analysis spots ($\sim 25\mu\text{m}$). Scale bars are $\sim 50\mu\text{m}$.

PQD Type 1 zircons



PQD Type 2 zircons

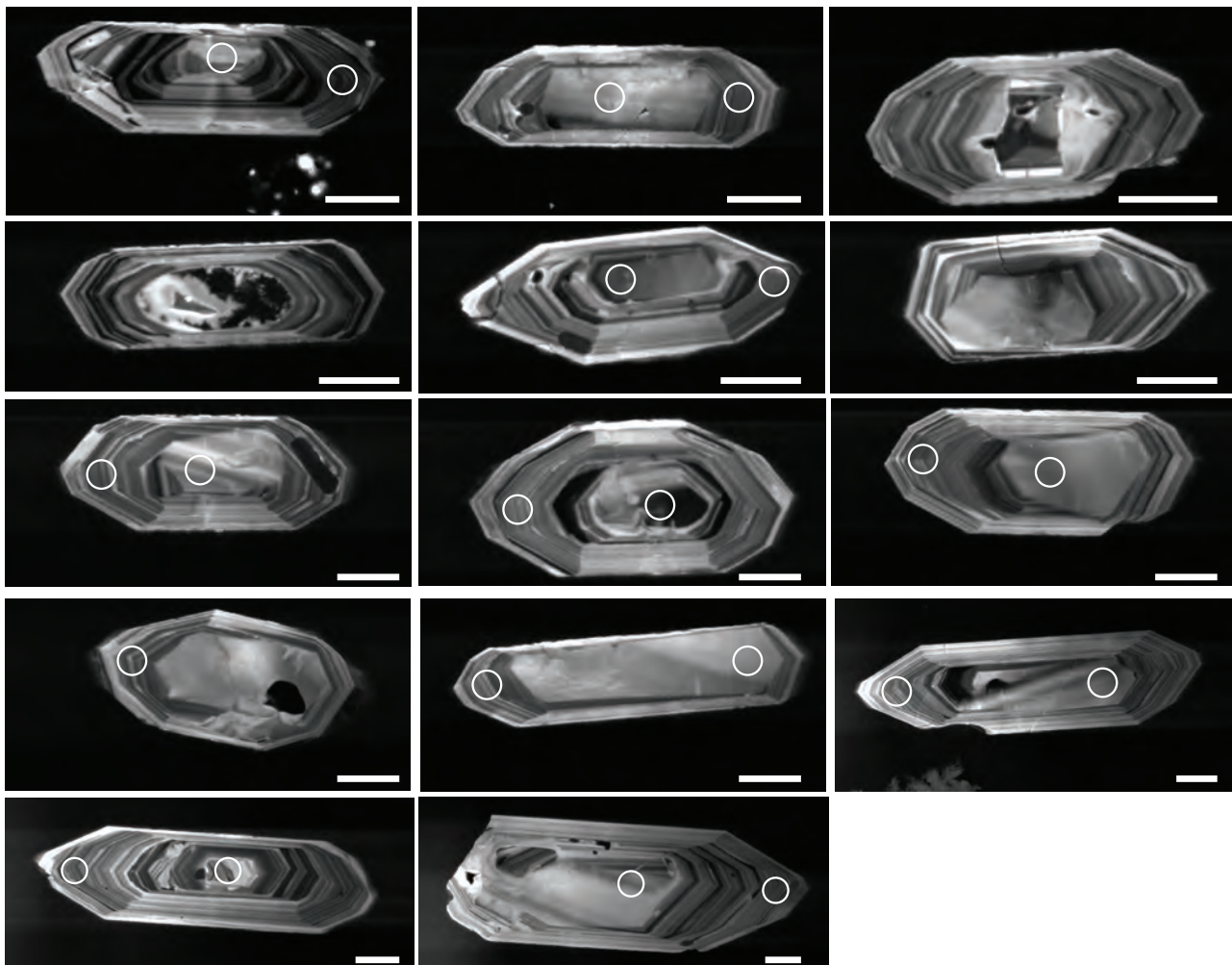
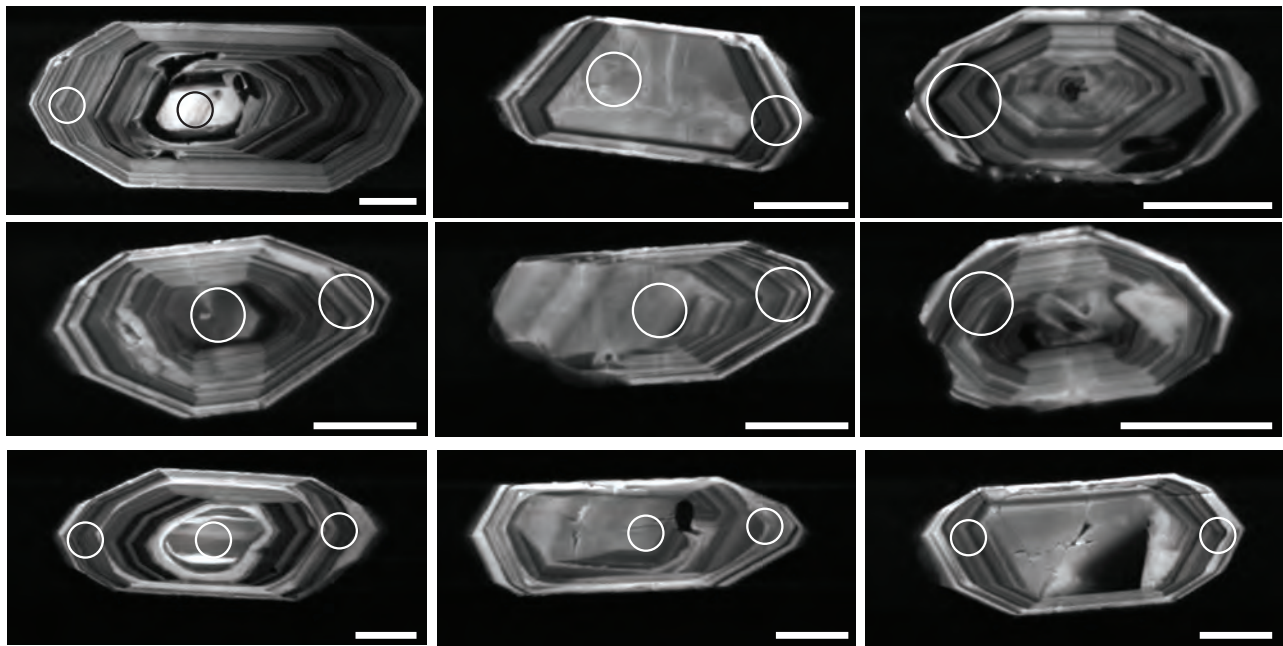


Figure A4: Cathodoluminescence images of PQD zircon showing locations of trace element analysis spots ($\sim 25\mu\text{m}$). Scale bars are $\sim 50\mu\text{m}$.

VFT Type 1 zircons



VFT Type 2 zircons

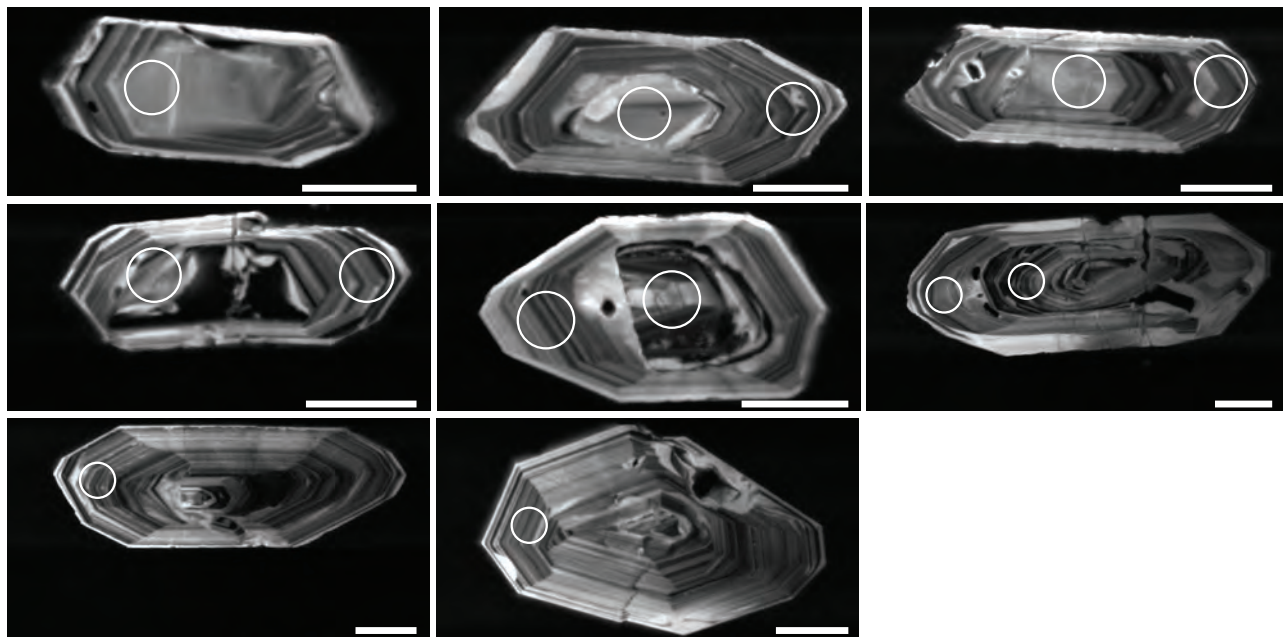
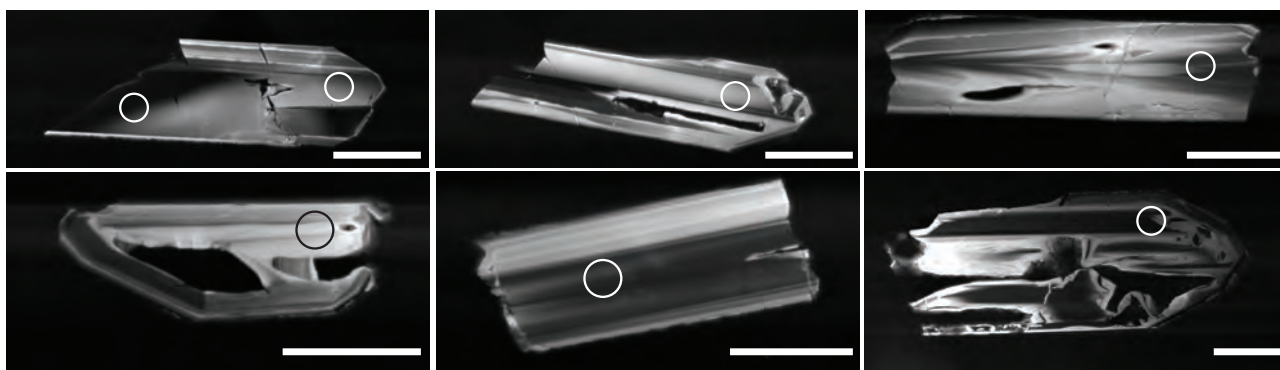


Figure A5: Cathodoluminescence images of VFT zircon showing locations of trace element analysis spots ($\sim 25\mu\text{m}$). Scale bars are $\sim 50\mu\text{m}$.

MG Type 1 zircons



MG Type 2 zircons

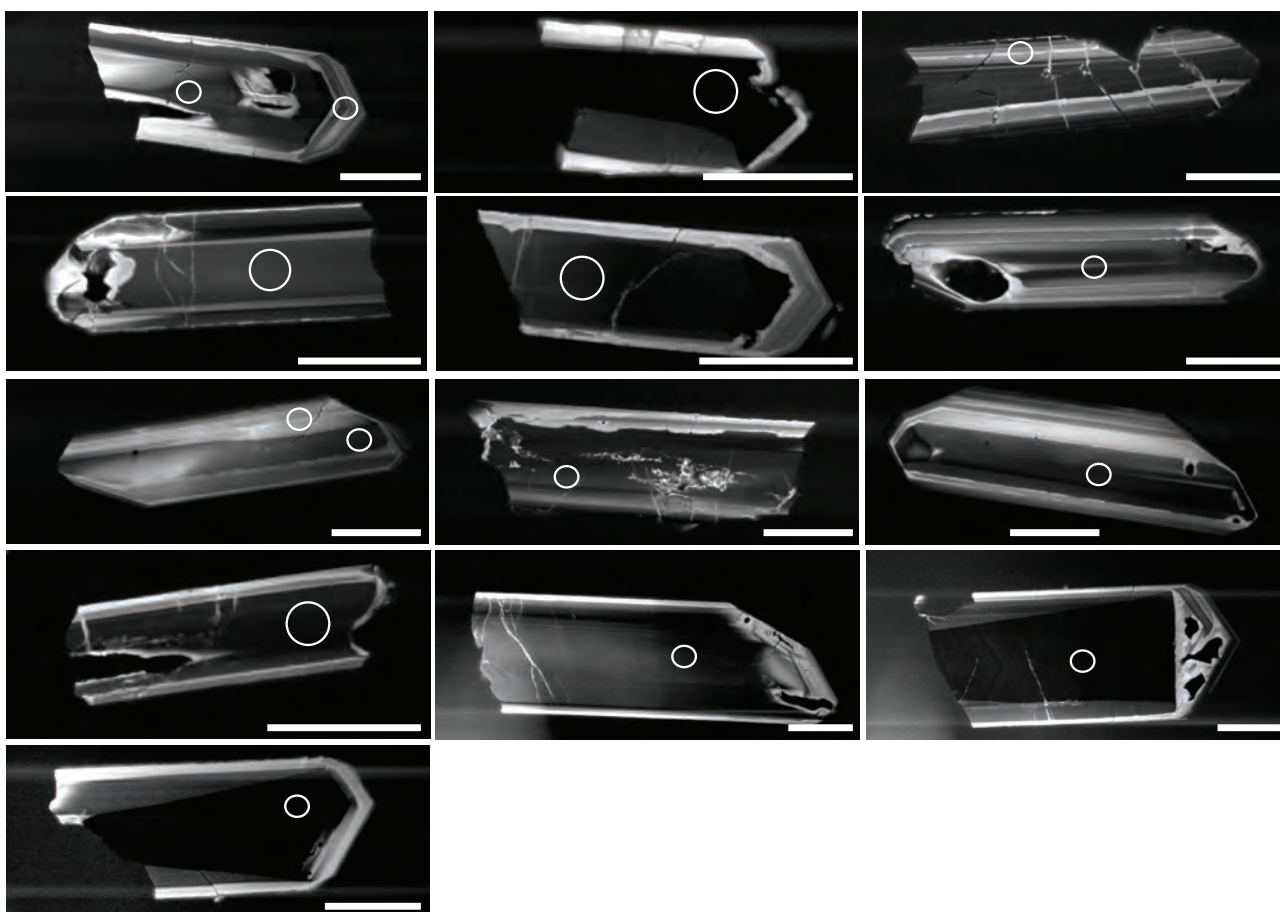
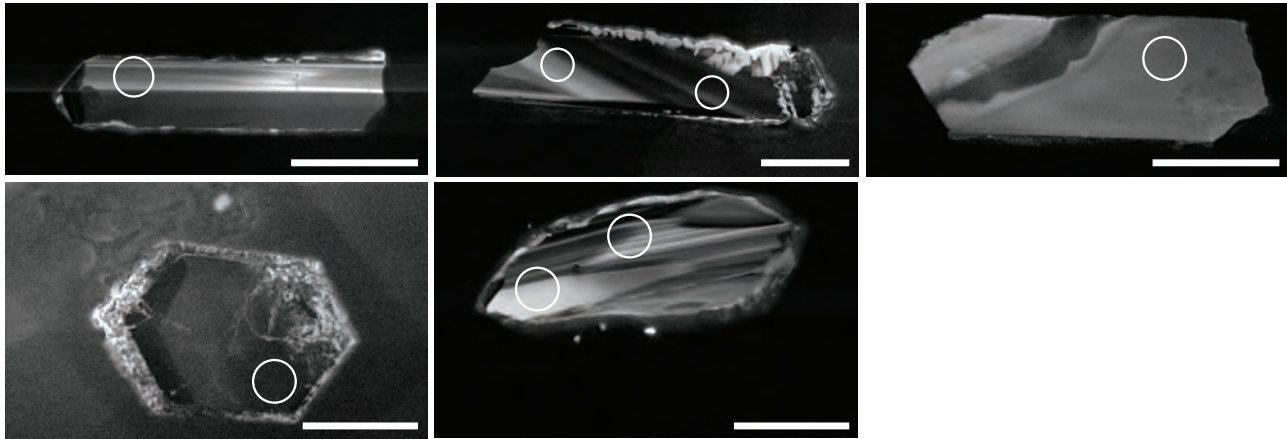


Figure A6: Cathodoluminescence images of MG zircon showing locations of trace element analysis spots ($\sim 25\mu\text{m}$). Scale bars are $\sim 100\mu\text{m}$.

CG Type 1 zircons



CG Type 2 zircons

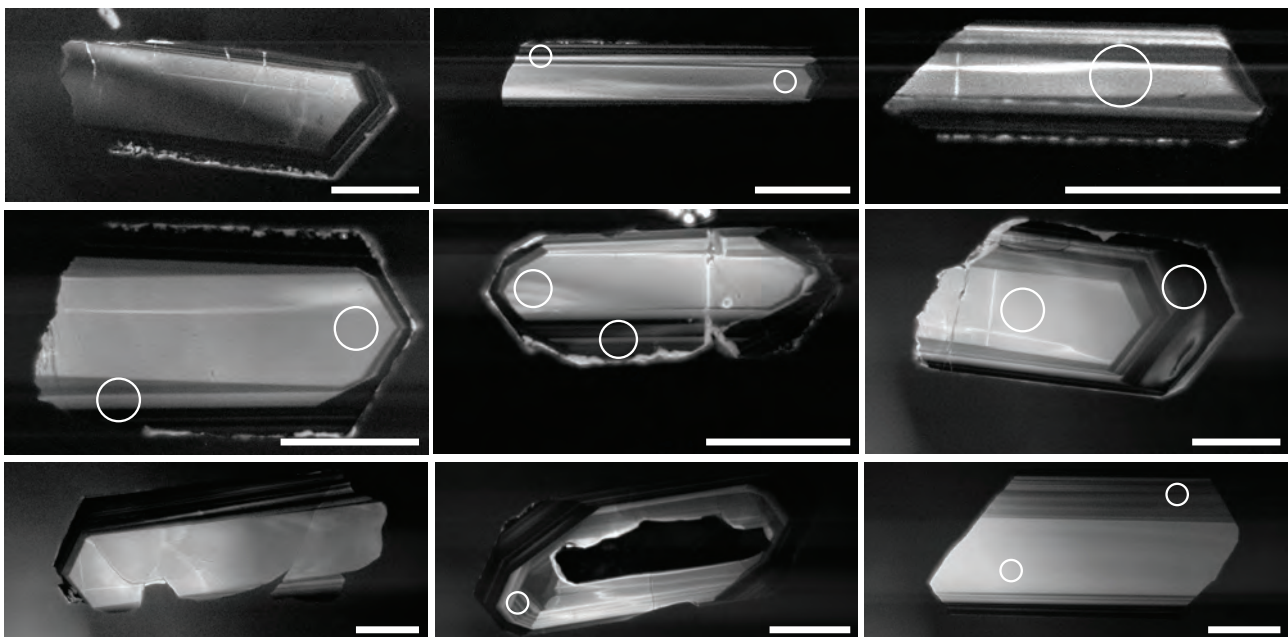


Figure A7: Cathodoluminescence images of CG zircon showing locations of trace element analysis spots ($\sim 25\mu\text{m}$). Scale bars are $\sim 100\mu\text{m}$.

APPENDIX B

ID-TIMS analytical details

Sample preparation

Zircons were extracted from thin sections using a Medenbach micro-drill. To minimize the effects of secondary lead loss the zircons were treated by chemical abrasion prior to analysis, involving high-temperature annealing followed by a HF-HNO₃ leaching step (Mattinson, 2005). Annealing was performed by loading individual zircon grains, following micro-drilling, of each sample in quartz crucibles and placing them into a furnace at 900 °C for 48 h. Subsequently, individual zircons from each sample were transferred into 3 ml screw-top Savillex vials together with ca. 120 µl of concentrated HF and 20 µl of 7N HNO₃ for the leaching step. Savillex vials were placed into a Teflon Parr vessel with 5 ml of concentrated HF, and placed in an oven at 180 °C for 8 h. After the partial dissolution step, the leachate was completely pipetted out and the individual zircons were rinsed in ultrapure water and then fluxed in 6N HCl for several hours on a hotplate at a temperature of ca. 80 °C. After removal of the acid, the zircon grains were again rinsed several times in ultra-pure water and acetone in an ultrasonic bath. Single zircon grains were selected and loaded for dissolution into pre-cleaned Teflon microcapsules. After

adding ~0.005g of ²⁰²Pb-²⁰⁵Pb-²³³U-²³⁵U spike (EARTHTIME, spike calibration described on www.earth-time.org) to each zircon, the grains were dissolved in 63 µl of concentrated HF with a trace of 7N HNO₃ at 206 °C for 48 hours inside a PARR dissolution vessel. After dissolution, samples were dried down and redissolved in 6N HCl at 180 °C overnight, dried down again and redissolved in 3N HCl. Lead and U were separated by HCl (zircon) based on anion exchange chemistry (Krogh, 1973) in 50 µl columns and dried down with 3 µl of 0.06N H₃PO₄.

Mass spectrometry and procedural blank

The isotopic analyses were performed at the University of Geneva on a TRITON mass spectrometer equipped with a MasCom discrete dynode secondary electron multiplier in ion counting mode. The linearity of the MasCom multiplier was calibrated using U500, Sr SRM987, and Pb SRM982 and SRM 983. Both Pb and U were loaded with 1 µl of silica gel – phosphoric acid mixture (Gerstenberger and Haase 1997) on outgassed single Re-filaments. Pb isotope compositions were measured on the electron multiplier, whereas U (as UO₂) isotopic measurements were made in static Faraday mode or, in case of low-U samples, in dynamic mode on the electron multiplier. Lead fractionation was corrected using the ET2535 tracer composition assuming ²⁰²Pb/²⁰⁵Pb ratio of 0.99924. Uranium

Table B1

sample	Th/U zircon	+/-	DTh/U	+/-	Th/U magma	+/- 1s
Marginal Facies granodiorite (MFG)						
03a2-z6	0.59	0.01	0.25	0.1	2.36	0.31
03-b1-z30	0.66	0.01	0.25	0.1	2.64	0.33
03b2-z8	0.60	0.01	0.25	0.1	2.40	0.31
Mattoni gabbro (MG)						
04a2-z2	0.82	0.01	0.25	0.1	3.28	0.36
04a2-z3	1.24	0.01	0.25	0.1	4.96	0.45
04b1-z2	1.20	0.01	0.25	0.1	4.80	0.44
04b1-z5a	1.03	0.01	0.25	0.1	4.12	0.41
04b1-z5b	1.02	0.01	0.25	0.1	4.08	0.40
04b2-z7	1.55	0.01	0.25	0.1	6.20	0.50
Val Fredda tonalite (VFT)						
09a1-z10	0.54	0.01	0.25	0.1	2.16	0.29
09a2-z21	1.06	0.01	0.25	0.1	4.24	0.41
09a2-z23	1.05	0.01	0.25	0.1	4.20	0.41
09a2-z24	0.78	0.01	0.25	0.1	3.12	0.35
09b1-z3	0.78	0.01	0.25	0.1	3.12	0.35
09b2-z18	0.82	0.01	0.25	0.1	3.28	0.36
Plagioclase quartz diorite (PQD)						
13c1-z8	0.27	0.01	0.25	0.1	1.08	0.21
13c1-z11	0.71	0.01	0.25	0.1	2.84	0.34
13c1-z15	0.45	0.01	0.25	0.1	1.80	0.27

mass fractionation was corrected online using the ^{233}U - ^{235}U double spike, assuming $^{238}\text{U}/^{235}\text{U}$ of 137.818 ± 0.0225 (1σ) for sample U (Hiess et al., 2012). Uranium was analyzed as an oxide, assuming an $^{18}\text{O}/^{16}\text{O}$ composition of 0.00205. U-Pb ratios and dates were calculated relative to $^{235}\text{U}/^{205}\text{Pb}$ ratio of 100.23. All U-Pb data were reduced using Tripoli and U-Pb_Redux (v.2.7.55) software (Bowring et al., 2011; McLean et al., 2011) and EATHTIME tracer calibration (v.3). 15 total procedural blanks were measured over the course of this study, spiked with the same tracer as the samples and had total Pb = 0.8 – 2.0 picograms. Therefore all common Pb for zircon analyses was assigned to the procedural blank, and corrected with the following isotopic compositions: $^{206}\text{Pb}/^{204}\text{Pb} = 18.38 \pm 0.89$, $^{207}\text{Pb}/^{204}\text{Pb} = 15.58 \pm 0.69$, $^{208}\text{Pb}/^{204}\text{Pb} = 37.99 \pm 0.76$ (1σ %).

Initial ^{230}Th disequilibrium calculations

For the initial ^{230}Th disequilibrium correction for zircon, we applied a constant $D_{\text{Th/U}} = 0.25 \pm 0.1$ (from Rubatto and Hermann, 2007) in order to calculate the Th/U of the magma at the time of zircon crystallization. The model Th/U ratio of the zircon was calculated from the measured $^{208}\text{Pb}/^{206}\text{Pb}$ assuming concordance between the $^{232}\text{Th} - ^{208}\text{Pb}$ and the $^{238}\text{U} - ^{206}\text{Pb}$ systems. See Table B1.

Zircon Hf isotope analysis

Hafnium isotopic compositions were analyzed from the same solution used for trace element analysis collected from zircon anion exchange column separation; using a Thermo-Scientific NEPTUNE Plus multi collector inductively coupled plasma mass spectrometer (MC-ICP-MS) at the University of Geneva following the methods described in Appendix A.

Zircon Hf isotope results

Hf isotope compositions in zircon were obtained from the same volume of zircon used for U-Pb age determinations. The isotopic data, including ϵHf values are presented in Table below. Eleven out of 18 zircons analyzed, had intensities below 1V on ^{180}Hf and therefore could not be measured accurately. The ϵHf values from the measured zircons range from +6.3 to +13.0.

The ϵHf values of VFT zircons scatter between +9.5 to +12.8, which is in disagreement with the

values obtained for the VFT in Broderick Chapter 2 which range from +2.2 to +7.1 (see Table 5 in Broderick Chapter 2). The ϵ_{Hf} values of MG zircons scatter between +9.2 to +13.0, which is in disagreement with the values obtained for the MG in Chapter 2 which range from +11 to +12.5 (see Table 5 in Broderick Chapter 2). Further work is required to explore the discrepancies between the two studies.

References

- Bowring, J.F., McLean, N.M., and Bowring, S.A., 2011, Engineering cyber infrastructure for U-Pb geochronology: Tripoli and U-Pb_Redux: *Geochemistry Geophysics Geosystems*, v. 12, p. Q0AA19.
- Gerstenberger, H., and Haase, G., 1997, A highly effective emitter substance for mass spectrometric Pb isotope ratio determinations: *Chemical Geology*, v. 136, p. 309-312.
- Hiess, J., Condon, D.J., McLean, N., and Noble, S.R., 2012, $^{238}\text{U}/^{235}\text{U}$ systematics in terrestrial uranium-bearing minerals: *Science*, v. 335, p. 1610-1614.
- Mattinson, J.M., 2005, Zircon U-Pb chemical abrasion ("CA-TIMS") method: combined annealing and multi-step partial dissolution analysis for improved precision and accuracy of zircon ages: *Chemical Geology*, v. 220, p. 47-66.
- McLean, N.M., Bowring, J.F., and Bowring, S.A., 2011, An algorithm for U-Pb isotope dilution data reduction and uncertainty propagation: *Geochemistry, Geophysics, Geosystems*, v. 12.
- Rubatto, D., and Hermann, J.r., 2007, Experimental zircon/melt and zircon/garnet trace element partitioning and implications for the geochronology of crustal rocks: *Chemical Geology*, v. 241, p. 38-61.

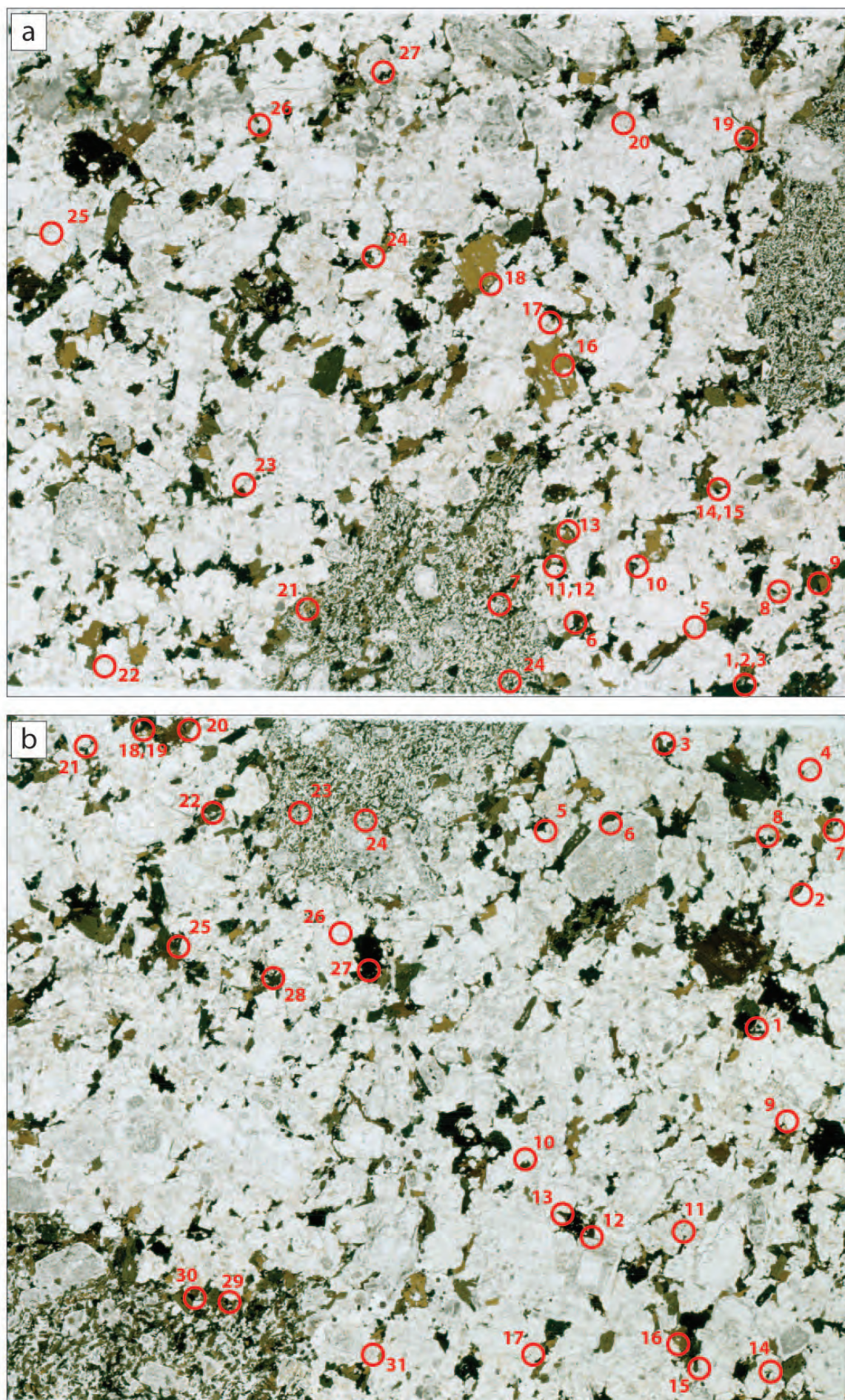


Figure B1: Zircon locations in polished thin sections from the Val Fredda tonalite (VFC09) sample.

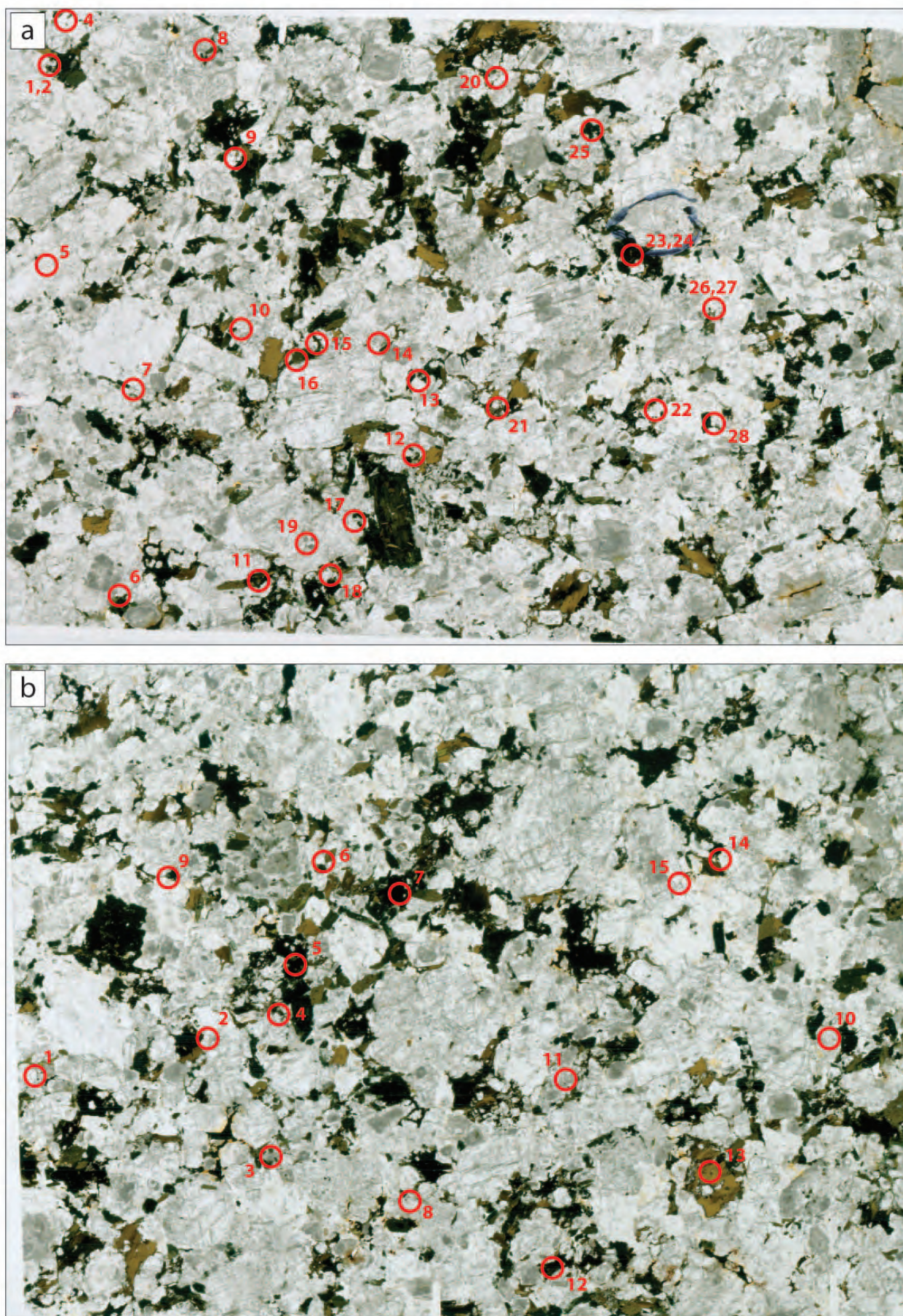


Figure B2: Zircon locations in polished thin sections from the plagioclase quartz diorite (VFC13) sample.

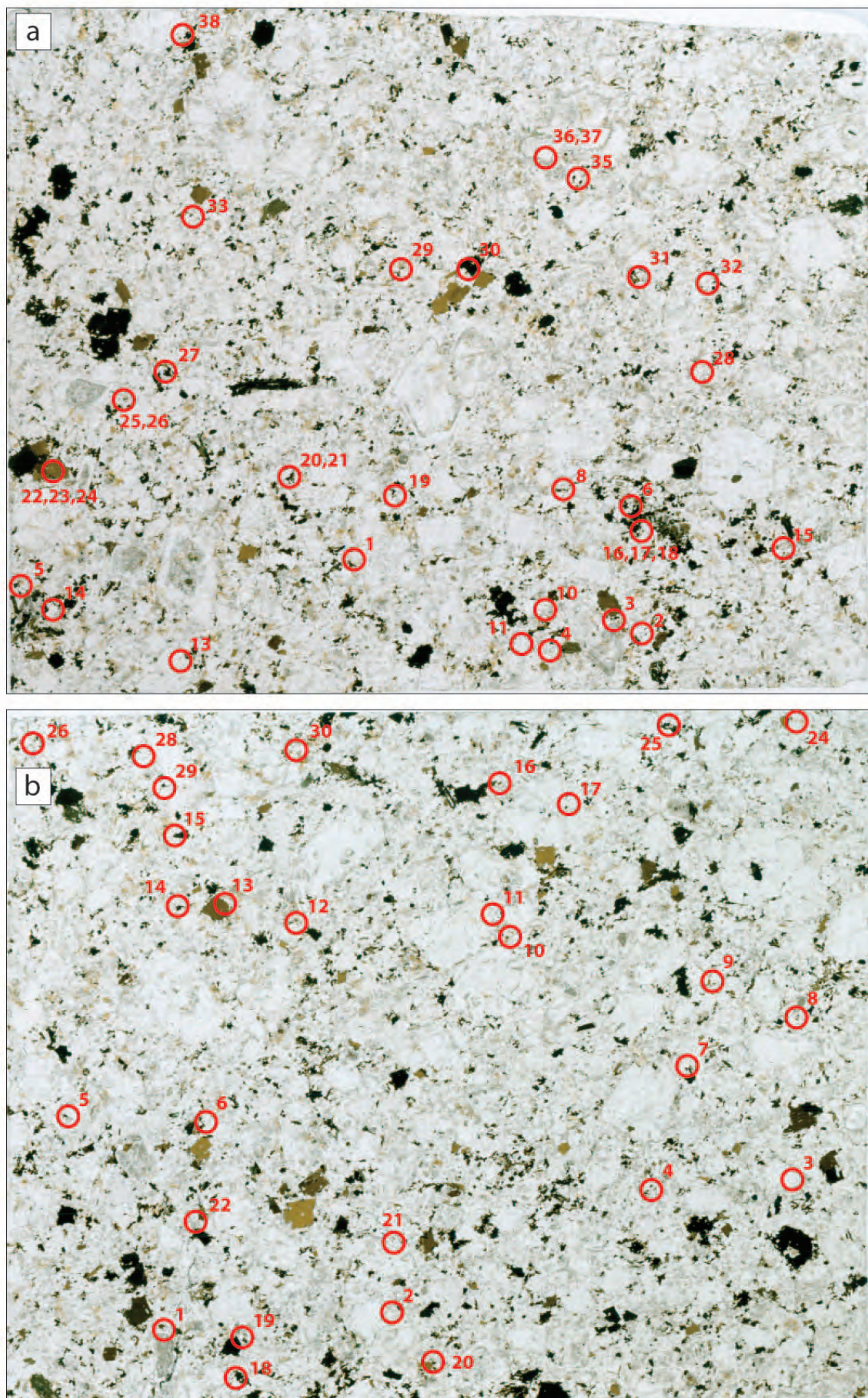


Figure B3: Zircon locations in polished thin sections from the marginal facies granodiorite (VFC03) sample.

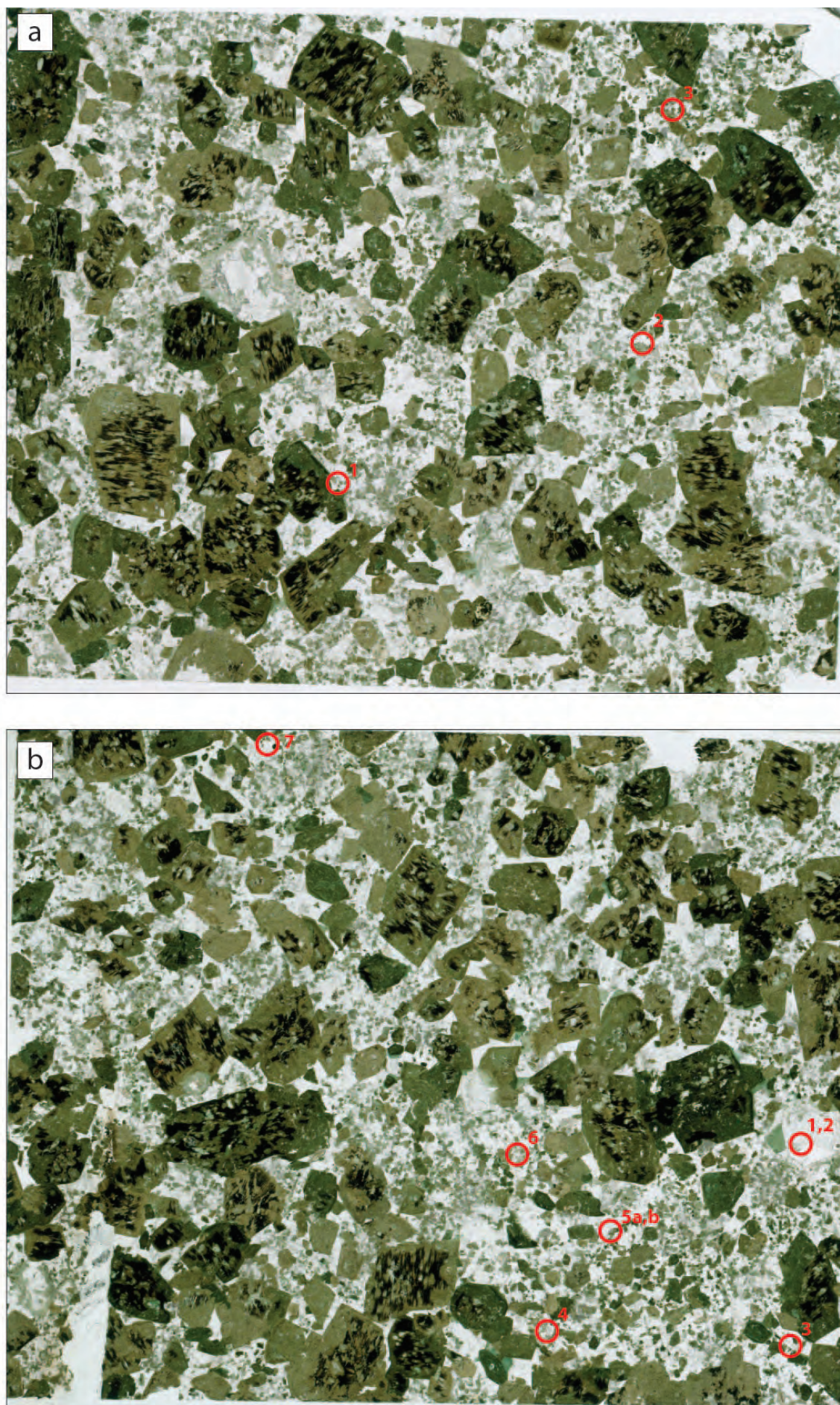


Figure B4: Zircon locations in polished thin sections from the Mattoni gabbro (VFC04) sample.

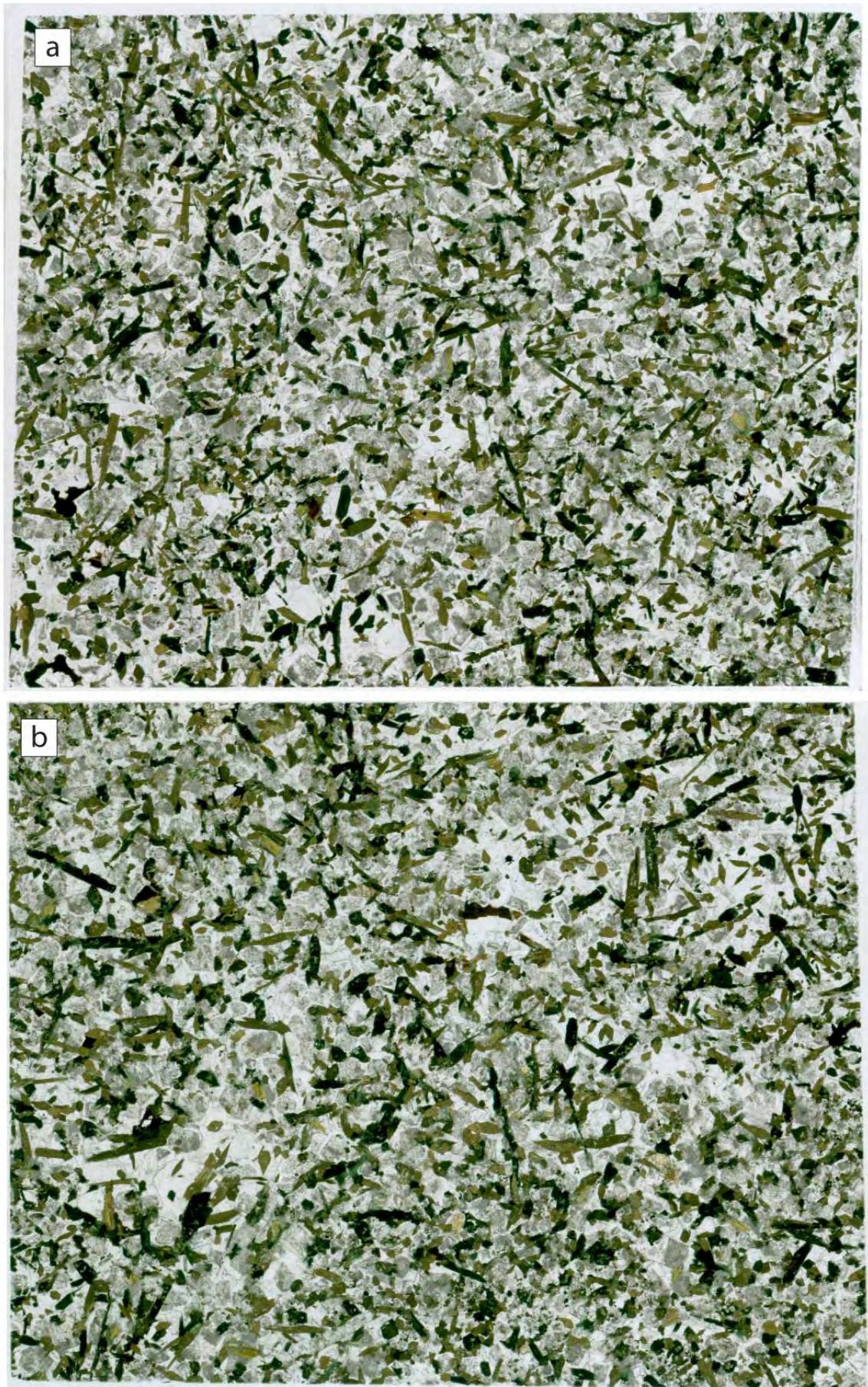


Figure B5: No zircons were located in polished thin sections from the Cadino gabbro (VFC05) sample.

APPENDIX C

Zr-in-titanite thermometry

The application of the Zr-in-sphene (titanite) thermometer (Hayden et al., 2008) has been shown to be a valuable tool in constraining the temperatures at which titanites crystallize in evolving magmas (Hayden et al., 2008; Anderson et al., 2008; Colombini et al., 2010). The thermometer, which is pressure dependent and the incorporation of Zr into titanite as a function of temperature, requires the knowledge of both SiO_2 and TiO_2 activities in the melt in order to apply the thermometer accurately. Assuming that titanite crystallization occurs at the level of emplacement, we apply independent pressure constraints obtained from Al-in-hornblende geobarometry of 0.2 GPa (Stauffer, 2012) to all titanites. Quartz is abundant in the VFC felsic samples, and is occasionally present as inclusions in zircon. In the VFC gabbros, titanites in thin section are mainly associated with plagioclase, however quartz is locally present in the gabbro. The silica activity is therefore considered to be equal to 1 for all VFC samples. Rutile is not present in any of the VFC samples; therefore the titanium activity is less than unity (< 1). Hayden and Watson (2007) have demonstrated that most magmas have a titanium activity between 0.5 and 0.9. The presence of Ti-rich minerals such as titanite and ilmenite, in all VFC samples,

suggests a rather high titanium activity, therefore an estimated titanium activity of 0.7 is applied to all samples. Using a titanium activity of 0.5 or 0.9, instead of 0.7, will change the calculated temperatures by $+13^\circ\text{C}/-17^\circ\text{C}$ at 700°C . All Zr-in-titanite temperatures calculated according to Hayden et al. (2007) using $a_{\text{TiO}_2} = 0.7$ and $a_{\text{SiO}_2} = 1$ and $P = 0.2$ GPa yield low crystallization temperatures for titanite. Measured Zr concentrations in titanite from the felsic units range from 500 to 900 ppm which translates to Zr-in-titanite temperatures of $\sim 700^\circ\text{C}$ to 750°C . Measured Zr concentrations in the titanite from the MG range from 1700 to 2000 ppm which translates to Zr-in-titanite temperatures of $\sim 800^\circ\text{C}$.

References

- Anderson, J. L., Barth, A. P., Wooden, J. L., and Mazdab, F., 2008, Thermometers and thermobarometers in granitic systems: Reviews in Mineralogy and Geochemistry, v. 69, p. 121-142.
- Colombini, L. L., Miller, C. F., Gualda, G. A. R., Wooden, J. L., and Miller, J. S., 2011, Sphene and zircon in the Highland Range volcanic sequence (Miocene, southern Nevada, USA): elemental partitioning, phase relations, and influence on evolution of silicic magma: Mineralogy and Petrology, v. 102, p. 29-50.
- Hayden, L. A., Watson, E. B., and Wark, D. A., 2008, A thermobarometer for sphene (titanite): Contributions to Mineralogy and Petrology, v. 155, p. 529-540.
- Stauffer, A. K., 2012, Petrology and mineral chemistry of the Val Fredda Complex leucocratic units, Adamello, Italy, MSc thesis, ETH Zürich.

APPENDIX D

In addition to the data collected for my thesis, I produced an additional 16 CA-ID-TIMS zircon dates for a collaboration with David Flöss within the 4D Adamello frame work. The U-Pb zircon results are presented in Table D1 and Figure D1 following methods described in Appendix A.

The ages obtained by U-Pb dating on zircon were used to constrain the emplacement style of the Western Adamello tonalite and are being prepared for publication:

“Floess, D., Baumgartner, L.P., Brack P., Broderick C., Chiaradia M., Müntener O., Putlitz B., de Saint-Blanquat M. & Schaltegger U. Anatomy of an upper-crustal pluton: evidence for incremental growth of a homogeneous intrusion (Western Adamello Tonalite, Northern Italy).”

Abstract

Large, broadly homogeneous plutons are a major component of subduction-related batholiths. The Western Adamello Tonalite (WAT) in the Italian Alps is an excellent example of a homogeneous pluton, featuring rocks with similar textures and composition over an area of 100 km². The narrow compositional range of these rocks makes it difficult to draw clear boundaries between units, which might represent coeval emplaced increments. Zones of up to a few hundred meters wide with basement xenoliths, mafic enclaves, schlieren, and hornblende-rich cumulates occur within homogeneous tonalites and are oriented parallel to the host rock contact. Forty-five igneous samples from two transects perpendicular to the host rock contact were collected and analyzed for major and trace elements, stable and radiogenic isotopes (O, Sr, Nd), Anisotropy of Magnetic Susceptibility and selected samples by U-Pb zircon geochronology.

Major and trace elements show a trend towards more SiO₂-rich (evolved) compositions for the younger, internal parts. In contrast, oxygen stable isotopes only vary in the first couple of meters close to the host rock contact, indicating wall rock assimilation. A step-like increase of ⁸⁷Sr/⁸⁶Sr (and decrease of ¹⁴³Nd/¹⁴⁴Nd) coincides with the observed heterogeneous, xenolith- and enclave-rich zones. The change in radiogenic isotopic values occurs over a few hundred meters, whereas the flat plateaus of similar isotope composition persist over areas that are a factor ~5 wider. U-Pb high precision dating on zircon yields ages of 37.62 ± 0.04 Ma, 37.15 ± 0.03 Ma, 36.66 ± 0.03 Ma and 36.42 ± 0.03 Ma (youngest zircon from each sample), indicating a total assembly time of 1.2 My and younging towards the internal parts of the pluton. The age spread within a single sample is over 200 ka, and no overlap between the four samples exists. Field structural data and Anisotropy of Magnetic Susceptibility document steeply dipping foliations and lineations in the marginal WAT (~500m), whereas the internal parts do not feature clear fabrics.

Thermal models predict that a single batch intrusion of the size of the WAT would cool ten times faster than the age span of 1.2 Ma recorded by samples. This, along with structural and chemical observations suggests incremental emplacement. The wide, homogeneous domains of tonalites have little variations in isotopic composition, suggesting that they represent batches of magma, which were rapidly isolated from the constantly evolving source. The narrow, heterogeneous zones are interpreted to result from newly formed magma pathways and incorporated feeder wall rocks. It is suggested that new conduits are rapidly established, isolating successive pulses of magma ascent from the surrounding host rocks and allowing the formation of homogeneous tonalites. Two such cycles can be seen in the WAT.

We propose that the overall geochemical evolution of the WAT and the Adamello Batholith in general, reflects changes in the deeper magma system. The step-like alternation of heterogeneous and homogenized tonalites observable at the pluton scale is the result of processes at the level of an intermediate crustal reservoir, including the establishment of new feeder pathways, reworking of older tonalites and homogenization.

Table D1:
Zircon U-Pb results for Western Adamello tonalite

Fraction		Composition			Isotopic Ratios						Dates (Ma)								
Th/U ^a	Pb ⁺ (pg)	Pb ^c (pg)	Pb ⁺ /Pb ^c	Th/U (magma) ^e	²⁰⁶ Pb/ ²⁰⁴ Pb ^f	²⁰⁶ Pb/ ²³⁸ U ^g	±2σ %	²⁰⁷ Pb/ ²³⁵ U ^g	±2σ %	²⁰⁷ Pb/ ²⁰⁶ Pb ^g	±2σ %	Corr. coef.	²⁰⁶ Pb/ ²³⁸ U ^h	±2σ abs	²⁰⁷ Pb/ ²³⁵ U ⁱ	±2σ abs	²⁰⁷ Pb/ ²⁰⁶ Pb ^h	±2σ abs	
DF336a - WAD ~ 150 m from the contact																			
DF336a-z1	0.41	28.95	1.02	28.2	1.64	1776	0.00586	0.05	0.03782	0.38	0.04683	0.35	0.65	37.75	0.02	37.69	0.14	33.26	8.38
DF336a-z2	0.43	27.87	1.43	19.5	1.72	1225	0.00587	0.11	0.03796	0.46	0.04694	0.44	0.25	37.80	0.04	37.83	0.17	38.87	10.66
DF336a-z3	0.35	24.26	1.08	22.5	1.40	1444	0.00584	0.09	0.03775	0.42	0.04690	0.40	0.33	37.62	0.04	37.62	0.15	36.57	9.55
DF336a-z4	0.36	37.03	2.57	14.4	1.44	926	0.00586	0.06	0.03795	0.55	0.04702	0.55	0.07	37.72	0.03	37.82	0.20	42.96	13.07
DF336a-z5	0.44	18.01	1.09	16.6	1.76	1042	0.00588	0.04	0.03797	0.47	0.04689	0.47	0.08	37.85	0.02	37.84	0.17	36.61	11.28
DF371b - CP ~ 5200 m from the contact																			
DF371b-z1	0.40	30.77	1.59	19.4	1.60	1226	0.00567	0.08	0.03672	0.46	0.04703	0.44	0.31	36.50	0.03	36.62	0.17	43.40	10.62
DF371b-z2	0.30	29.68	1.49	20.0	1.20	1298	0.00565	0.07	0.03666	0.43	0.04705	0.41	0.43	36.42	0.03	36.56	0.16	44.21	9.76
DF371b-z3	0.37	70.68	1.20	59.1	1.48	3737	0.00566	0.06	0.03664	0.18	0.04694	0.16	0.49	36.49	0.03	36.54	0.06	38.51	3.81
DF376c - WAD ~ 3500 m from the contact																			
DF376c-z1	0.40	35.13	1.03	34.1	1.60	2144	0.00570	0.09	0.03683	0.31	0.04686	0.29	0.39	36.74	0.03	36.73	0.11	34.83	6.89
DF376c-z2	0.43	19.39	1.30	15.0	1.72	943	0.00571	0.07	0.03694	0.57	0.04691	0.55	0.23	36.81	0.03	36.83	0.20	37.35	13.26
DF376c-z3	0.36	21.78	0.94	23.2	1.44	1483	0.00569	0.07	0.03674	0.40	0.04684	0.39	0.21	36.66	0.03	36.63	0.14	33.51	9.36
DF386d - WAD ~ 2000 m from the contact																			
DF386d-z1	0.42	50.28	1.62	31.1	1.68	1949	0.00577	0.06	0.03734	0.30	0.04693	0.29	0.36	37.20	0.02	37.23	0.11	38.32	6.92
DF386d-z2	0.38	144.87	1.52	95.0	1.52	5982	0.00579	0.06	0.03749	0.16	0.04700	0.13	0.46	37.29	0.02	37.37	0.06	41.76	3.32
DF386d-z3	0.30	33.35	1.49	22.4	1.20	1456	0.00577	0.06	0.03744	0.37	0.04706	0.36	0.23	37.19	0.02	37.32	0.14	44.82	8.74
DF386d-z4	0.33	40.79	1.67	24.4	1.32	1571	0.00577	0.07	0.03744	0.38	0.04710	0.37	0.17	37.15	0.03	37.32	0.14	46.75	8.84

a Th contents calculated from radiogenic ²⁰⁸Pb and the ²⁰⁷Pb/²⁰⁶Pb date of the sample, assuming concordance between U-Th and Pb systems.

b Total mass of radiogenic Pb.

c Total mass of common Pb.

d Ratio of radiogenic Pb (including ²⁰⁸Pb) to common Pb.

e Th/U ratio of magma from which mineral crystallized calculated from $D_{Th/U} = 0.25$ (from Rubatto and Hermann, 2007).

f Measured ratio corrected for fractionation and spike contribution only.

g Measured ratios corrected for fractionation, tracer and blank.

h Corrected for initial Th/U disequilibrium using radiogenic ²⁰⁸Pb and Th/U[magma] specified by e.

i Isotopic dates calculated using the decay constants $\lambda_{238} = 1.55125E-10$ and $\lambda_{235} = 9.8485E-10$ (Jaffey et al. 1971).

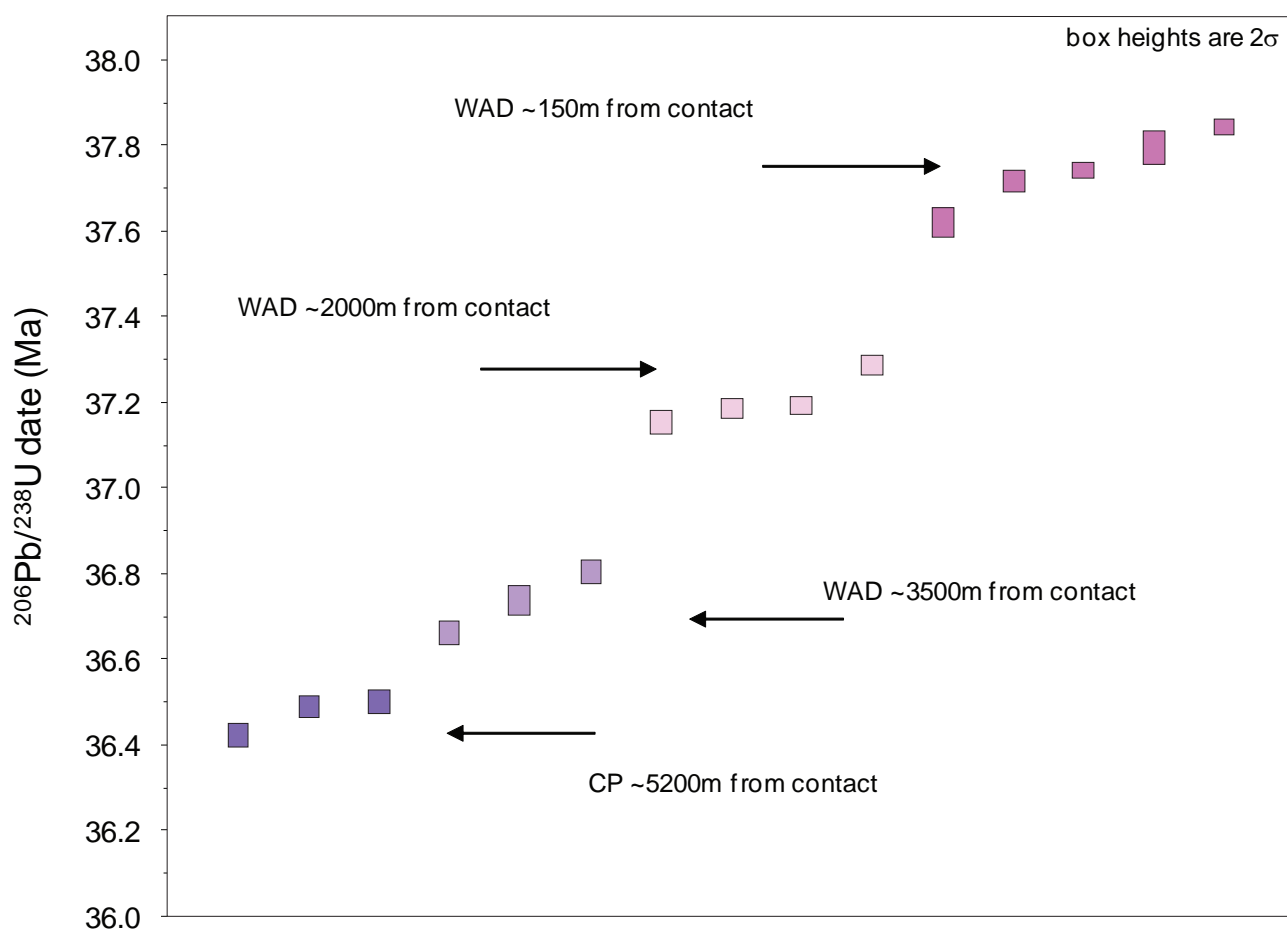


Figure D1: Age ranked $^{206}\text{Pb}/^{238}\text{U}$ dates for individual zircons from the Western Adamello tonalite.

APPENDIX E

In addition to the data collected for my thesis, I produced an additional 45 CA-ID-TIMS zircon dates for a collaboration with Roel Verberne within the 4D Adamello frame work. The U-Pb zircon results are presented in Table E1 and Figure E1 following methods described in Appendix A.

The ages obtained by U-Pb dating on zircon were used to constrain the emplacement style of the Listino Suite and are presented in the thesis chapter of Roel Verberne titled: “*Time resolved emplacement of the Listino Suite.*” To be prepared for publication.

Introduction

There is a growing body of evidence that the emplacement and growth of plutons occurs by the sequential injection of multiple magma pulses (Pitcher and Berger, 1972; Wiebe and Collins, 1998; Coleman et al., 2004; Bacon et al., 2007; Charlier et al., 2008; Miller et al., 2011; Paterson et al., 2011; Druitt et al., 2012), yet field evidence for the multiple injections can be difficult to recognize. A pluton wherein subsequent pulses are emplaced into a melt-bearing but crystal-rich host, rather than either solid or crystal-poor material would consist of zones with very different thermal histories and thus melt fraction and strength (Hildreth, 2004; Miller et al., 2011). Replenishments of varying size, composition, temperature and injection velocity undoubtedly lead to various forms of interaction between pulses, and can therefore be expected to exhibit a myriad of contrasting contact relationships in the field (Yoshinobu et al., 1998). Depending on the deformation behavior of the host in response to injection, intruding magmas may propagate as dikes, spread to form sheets, breakup into enclaves or mix with the host magma (Wiebe and Collins, 1998; Jellinek and Kerr, 1999; Snyder and Tait, 1995; Sparks et al., 1984; Sparks and Marshall, 1986). However, each of these interaction modes is not only dependent on the physical state of the magmas involved, but also the timescale over which interaction takes place. The contact relationships observed between pulses, therefore reflect the physical state of the magmas during interaction, as well as the timescale over which interaction took place, and can be used to constrain the timescales of pluton emplacement.

Recent advances in high-precision U-Pb ID-TIMS geochronology provide a tool that can possibly re- solve the timescales over which interaction between subsequent pulses occurs. Such high-precision ages have been a central argument that supports the idea that upper-crustal plutons are emplaced incrementally over timescales of up to several million years by the amalgamation of small pulses. However, with the increased precision comes the added complication of interpreting what the spread of ages obtained from a single hand specimen means in terms of geological processes. Leading to the question whether such a spread of ages represents crystallization during emplacement, transport or inheritance. A key assumption made in the argument that upper-crustal plutons are emplaced incrementally for instance, is that a U-Pb zircon age represents in situ crystal growth. This study focusses on the Listino Suite, which consists of the Listino Ring Complex and the magmatic units forming the inner and outer contact on the eastern side of the complex. These units are comprised of gabbro, tonalite, granodiorite and leucogranite, and exhibit a diverse array of super-solidus elastic to ductile interaction between sequentially emplaced magma pulses (Brack, 1984; Blundy and Sparks, 1992). As such, it provides an ideal case study on the timescales over which subsequent magma pulses can interact.

Table E1:
Zircon U-Pb results for Listino suite

Fraction	Composition			Isotopic Ratios					Dates (Ma)							
	Th/U ^a	Pb* (pg)	Pbc (pg)	^c Pb*/Pbc ^d	Th/U (magma) ^e	²⁰⁶ Pb/ ²³⁸ U ^f	²⁰⁶ Pb/ ²³⁵ U ^g	^{±2σ} %	²⁰⁷ Pb/ ²⁰⁶ Pb ^g	^{±2σ} %	Corr. coef.	²⁰⁶ Pb/ ²³⁸ U ^h	²⁰⁷ Pb/ ²³⁵ U ⁱ	^{±2σ} abs	²⁰⁷ Pb/ ²⁰⁶ Pb ^h	^{±2σ} abs
Tonalite of Malga Listino (TML)																
TML-z1	0.59	35.50	2.38	14.9	2.36	902	0.00642	0.07	0.04146	0.57	0.24	41.36	41.25	0.03	33.92	13.32
TML-z2	0.60	25.06	2.23	11.2	2.38	684	0.00640	0.08	0.04143	0.74	0.13	41.23	41.21	0.04	39.57	17.59
TML-z3	0.63	54.82	2.85	19.2	2.50	1147	0.00643	0.05	0.04167	0.43	0.08	41.37	41.45	0.02	45.57	10.21
TML-z4	0.62	30.09	1.92	15.7	2.49	942	0.00643	0.08	0.04164	0.55	0.12	41.40	41.43	0.03	42.73	12.95
TML-z5	0.64	12.67	2.32	5.5	2.55	339	0.00640	0.13	0.04139	1.55	0.10	41.20	41.18	0.05	39.47	36.98
TML-z6	0.61	25.50	1.86	13.7	2.44	826	0.00643	0.11	0.04153	0.66	0.27	41.42	41.31	0.05	34.85	15.20
TML-z8	0.60	15.71	1.09	14.4	2.39	872	0.00662	0.12	0.04274	0.96	0.43	42.62	42.50	0.05	34.63	21.90
TML-z9	0.62	8.71	1.13	7.7	2.49	470	0.00640	0.14	0.04097	1.58	0.67	41.22	40.77	0.06	13.71	35.86
Leucogranite dikes (LD)																
LD-z1	0.69	54.59	1.21	45.2	2.77	2626	0.00642	0.06	0.04142	0.24	0.17	41.31	41.21	0.03	34.80	5.64
LD-z2	0.62	113.07	1.08	104.3	2.49	6147	0.00644	0.08	0.04171	0.14	0.60	41.47	41.49	0.03	41.65	2.69
LD-z3	0.57	41.12	0.95	43.3	2.27	2600	0.00643	0.12	0.04159	0.30	0.15	41.40	41.38	0.05	39.27	7.32
LD-z4	0.67	94.49	1.13	83.7	2.68	4881	0.00644	0.05	0.04171	0.13	0.05	41.44	41.50	0.02	44.51	3.23
LD-z5	0.59	27.18	0.79	34.4	2.35	2059	0.00643	0.06	0.04154	0.27	0.12	41.40	41.33	0.03	36.64	6.50
LD-z6	0.65	22.83	1.02	22.3	2.60	1321	0.00644	0.11	0.04174	0.45	0.30	41.45	41.52	0.04	45.47	10.27
LD-z7	0.58	87.61	0.89	98.7	2.31	5893	0.00643	0.11	0.04164	0.23	0.50	41.38	41.42	0.04	43.21	4.72
LD-z8	0.65	13.19	0.69	19.0	2.62	1127	0.00643	0.13	0.04153	0.78	0.63	41.39	41.32	0.05	36.64	17.01
Listino ring gabbro (gab)																
gab-z1	1.19	56.65	5.05	11.2	4.77	593	0.00646	0.13	0.04189	0.86	0.15	41.57	41.67	0.05	47.70	20.21
gab-z2	0.85	69.44	1.55	44.9	3.39	2514	0.00646	0.10	0.04166	0.33	0.15	41.57	41.45	0.04	34.30	7.89
gab-z3	0.88	47.31	1.22	38.7	3.50	2151	0.00646	0.07	0.04182	0.28	0.43	41.56	41.60	0.03	43.72	6.18
gab-z4	0.78	130.74	1.23	106.1	3.11	6015	0.00647	0.12	0.04187	0.18	0.51	41.63	41.65	0.05	42.61	3.81
gab-z5	1.16	26.19	1.37	19.2	4.62	1001	0.00646	0.09	0.04160	0.74	0.46	41.59	41.38	0.04	29.60	16.76
gab-z6	0.98	80.20	1.28	62.9	3.92	3400	0.00646	0.09	0.04194	0.22	0.34	41.61	41.72	0.04	48.12	4.98
Laione porphyritic dikes (LPD)																
LPD-z1	0.64	96.40	1.11	86.8	2.56	5098	0.00646	0.13	0.04187	0.21	0.68	41.62	41.65	0.06	42.70	3.63
LPD-z2	0.62	96.71	0.93	103.6	2.47	6119	0.00647	0.06	0.04189	0.15	0.53	41.66	41.67	0.02	41.59	3.04
LPD-z3	0.58	27.76	0.95	29.3	2.33	1760	0.00648	0.06	0.04200	0.31	0.03	41.72	41.77	0.13	44.25	7.47
LPD-z4	0.61	50.66	0.93	54.3	2.45	3219	0.00728	0.07	0.04789	0.18	0.44	46.86	47.50	0.03	79.01	3.92
LPD-z5	0.57	65.29	1.05	62.0	2.26	3715	0.00646	0.26	0.04193	0.31	0.84	41.61	41.71	0.11	46.59	4.01
LPD-z6	0.55	42.45	1.04	41.0	2.19	2474	0.00710	0.11	0.04674	0.31	0.08	45.71	46.38	0.05	80.20	7.58
LPD-z7	0.46	44.34	1.36	32.6	1.83	2023	0.00648	0.05	0.04204	0.29	0.18	41.72	41.82	0.02	46.57	6.72
LPD-z8	0.78	19.04	1.29	14.7	3.13	850	0.00646	0.09	0.04177	0.67	0.43	41.58	41.55	0.04	39.71	15.24
LPD-z9	0.67	12.95	1.07	12.1	2.68	718	0.00650	0.15	0.04186	1.10	0.65	41.82	41.64	0.06	30.81	24.09
Listino Ring tonalite (RT)																
RT-z2	0.70	82.83	0.97	85.3	2.79	4940	0.00648	0.06	0.04194	0.17	0.52	41.72	41.71	0.02	41.09	4.91
RT-z3	1.01	44.10	0.94	47.1	4.05	2531	0.00646	0.06	0.04179	0.23	0.28	41.58	41.57	0.02	41.23	5.36
RT-z4	0.58	42.52	0.67	63.5	2.31	3797	0.00647	0.04	0.04190	0.18	0.51	41.66	41.67	0.02	41.52	3.96
RT-z5	0.66	48.96	1.10	44.4	2.66	2598	0.00647	0.04	0.04199	0.22	0.39	41.64	41.76	0.02	48.34	5.03
RT-z6	0.59	38.47	1.26	30.5	2.36	1828	0.00648	0.06	0.04195	0.30	0.14	41.74	41.73	0.03	40.17	7.15
RT-z7	0.78	31.62	0.88	35.8	3.13	2041	0.00647	0.07	0.04178	0.45	0.68	41.64	41.56	0.04	36.64	9.78
RT-z8	0.62	87.18	0.91	96.0	2.47	5672	0.00648	0.15	0.04198	0.24	0.74	41.69	41.76	0.06	44.95	3.85

Table E1:
continued

Fraction	Composition			Isotopic Ratios					Dates (Ma)										
	Th/U ^a	Pb* (pg) ^b	Pbc (pg) ^c	Pb*/Pbc ^d	Th/U (magma) ^e	²⁰⁶ Pb/ ²⁰⁴ Pb ^f	²⁰⁶ Pb/ ²³⁸ U ^g	±2σ %	²⁰⁷ Pb/ ²³⁵ U ^g	±2σ %	²⁰⁷ Pb/ ²⁰⁶ Pb ^g	±2σ %	Corr. coef.	²⁰⁶ Pb/ ²³⁸ U ^h	±2σ abs	²⁰⁷ Pb/ ²³⁵ U ⁱ	±2σ abs	²⁰⁷ Pb/ ²⁰⁶ Pb ^h	±2σ abs
Monoccola granodiorite (MT)																			
MT-z1	0.52	34.68	2.61	13.3	2.09	820	0.00681	0.07	0.04414	0.63	0.04702	0.03	0.18	43.84	0.03	43.86	0.27	44.26	14.95
MT-z2	0.59	62.99	3.23	19.5	2.35	1175	0.00648	0.09	0.04195	0.47	0.04698	0.04	0.07	41.72	0.04	41.73	0.19	41.70	11.31
MT-z3	0.64	31.92	3.60	8.9	2.57	537	0.00648	0.11	0.04211	0.96	0.04715	0.05	0.10	41.72	0.05	41.88	0.39	50.68	22.85
MT-z4	0.58	22.86	3.79	6.0	2.32	377	0.00648	0.11	0.04154	1.37	0.04654	0.06	0.14	41.70	0.06	41.33	0.56	19.31	32.66
MT-z5	0.77	24.19	2.40	10.1	3.07	590	0.00672	0.13	0.04402	0.89	0.04752	0.06	0.18	43.27	0.06	43.74	0.38	69.59	20.89
MT-z6	0.65	23.07	2.50	9.2	2.61	558	0.00649	0.10	0.04203	0.95	0.04697	0.04	0.39	41.80	0.04	41.80	0.39	41.41	22.16
MT-z7	0.57	44.04	2.84	15.5	2.28	942	0.00649	0.09	0.04192	0.62	0.04685	0.04	0.07	41.80	0.04	41.70	0.25	35.10	14.92
MT-z8	0.56	21.40	1.31	16.4	2.24	994	0.00737	0.11	0.05032	0.64	0.04952	0.05	0.49	47.43	0.05	49.85	0.31	167.08	13.89

^a Th contents calculated from radiogenic ²⁰⁸Pb and the ²⁰⁷Pb/²⁰⁶Pb date of the sample, assuming concordance between U-Th and Pb systems.

^b Total mass of radiogenic Pb.

^c Total mass of common Pb.

^d Ratio of radiogenic Pb (including ²⁰⁸Pb) to common Pb.

^e Th/U ratio of magma from which mineral crystallized calculated from $D_{Th/U} = 0.25$ (from Rubatto and Hermann, 2007).

^f Measured ratio corrected for fractionation and spike contribution only.

^g Measured ratios corrected for fractionation, tracer and blank.

^h Corrected for initial Th/U disequilibrium using radiogenic ²⁰⁸Pb and Th/U[magma] specified by ^e.

ⁱ Isotopic dates calculated using the decay constants $\lambda_{238} = 1.55125E-10$ and $\lambda_{235} = 9.8485E-10$ (Jaffey et al. 1971).

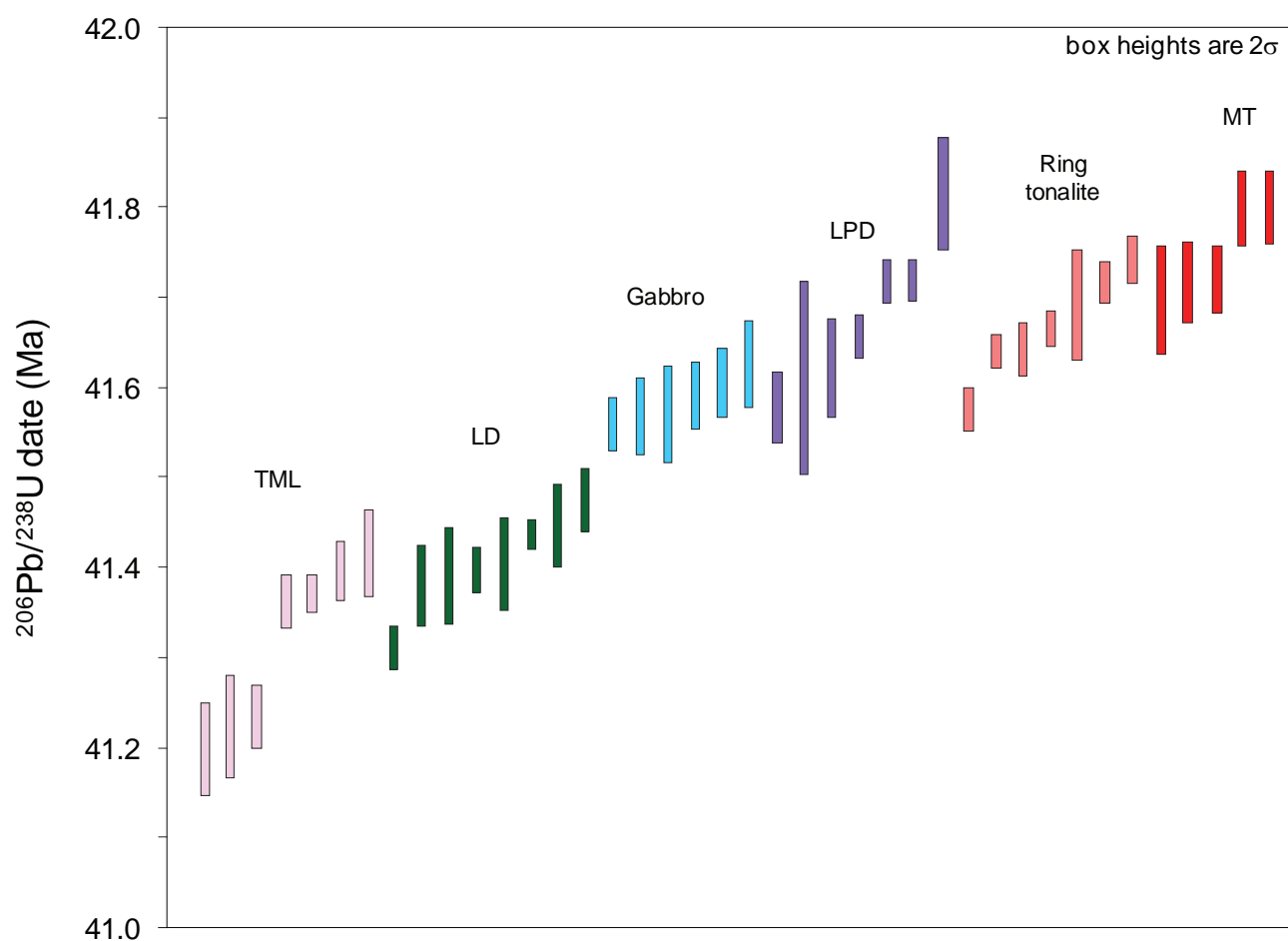


Figure E1: Age ranked $^{206}\text{Pb}/^{238}\text{U}$ dates for individual zircons from the Listino suite

APPENDIX F

In addition to the data collected for my thesis, I produced an additional 16 CA-ID-TIMS zircon dates for the Bruffione granodiorite. The Monte Bruffione granodiorite (Fig. 1a: Broderick Chapter 2) is mapped as a single homogenous pluton (Callegari and Brack 2002). Two samples were selected, from a north - south transect, for ID-TIMS analysis: 1) CB19 was collected from the center of the pluton and; 2) CB21 was collected ~ 2 m from the contact with the host Triassic sediments. Zircon U-Pb results, following methods described in Appendix A, are summarized in Table F1 and Figure F1.

$^{206}\text{Pb}/^{238}\text{U}$ dates of five zircon grains from the CB19 range from 39.80 ± 0.02 Ma to 40.24 ± 0.01 Ma (Fig. F1). The PQD zircon dates scatter over 440 ka and do not overlap at the two-sigma level (MSWD = 6) therefore excluding a calculated weighted mean age. $^{206}\text{Pb}/^{238}\text{U}$ dates of four zircon grains from the CB21 range from 40.20 ± 0.03 Ma to 40.36 ± 0.03 Ma (Fig. F1). The PQD zircon dates scatter over 160 ka and do not overlap at the two-sigma level (MSWD = 22) therefore excluding a calculated weighted mean age. Both samples contain older grains (CB19: z5, z6, z10; CB21: z1, z2, z4, z10) which are considered to be xenocrystic based on age and proximity to the contact. $^{206}\text{Pb}/^{238}\text{U}$ dates from Bruffione zircons record continuous

crystallization between samples.

Hafnium isotopic compositions were analyzed from the same volume of zircon used for ID-TIMS dating, following the methods described in Appendix A. The Hf isotopic data are presented in Table F2 and Figure F2.

Zircon grains from sample CB19 have initial Hf isotopic compositions that record little variation in ϵHf values ranging from + 0.2 to + 1.3. In contrast zircon grains from sample CB21 show considerable variations in Hf isotopic compositions with ϵHf varying from + 1.6 to + 7.3 (Fig. F2).

References

- Callegari, E., and Brack, P., 2002, Geological map of the Tertiary Adamello Batholith (Northern Italy) Explanatory notes and legend: Mem. Sci. Geol, v. 54, p. 19-49.

Table F1:
Zircon U-Pb results for the Bruffione granodiorite

Fraction	Composition				Isotopic Ratios				Dates (Ma)			
	Th/U ^a	Pb* (pg) ^b	Pbc (pg) ^c	Pb*/Pbc ^d	Th/U (magma) ^e	²⁰⁶ Pb/ ²⁰⁴ Pb ^f	²⁰⁶ Pb/ ²³⁸ U ^g	²⁰⁷ Pb/ ²³⁵ U ^g	²⁰⁷ Pb/ ²⁰⁶ Pb ^g	²⁰⁷ Pb/ ²³⁵ U ^h	²⁰⁷ Pb/ ²³⁵ U ⁱ	²⁰⁷ Pb/ ²⁰⁶ Pb ^h
Bruffione granodiorite (cb19)												
cb19-z1	0.48	15.3	2.20	7.0	1.92	445	0.00623	0.10	0.04030	1.20	0.09	40.10
cb19-z3	0.53	4.49	3.04	1.0	2.12	107	0.00618	0.40	0.04000	5.50	0.08	39.80
cb19-z4	0.72	16.2	1.24	13.0	2.88	769	0.00625	0.26	0.04044	0.94	0.36	40.24
cb19-z5	0.43	41.2	2.94	14.0	1.72	868	0.00824	0.39	0.07766	0.77	0.58	52.96
cb19-z6	0.57	15	1.33	11.0	2.28	692	0.00811	0.12	0.05425	1.00	0.04	53.64
cb19-z10	0.45	12.8	1.39	9.0	1.80	582	0.01222	0.08	0.09405	0.78	0.20	78.36
cb19-z11	0.45	18.8	1.30	14.0	1.80	910	0.00623	0.09	0.04030	0.58	0.17	40.11
cb19-z12	0.61	22.6	1.01	22.0	2.44	1340	0.00622	0.09	0.04022	0.44	0.08	40.07
Bruffione granodiorite (cb21)												
cb21-z1	0.22	53.2	2.45	22.0	0.88	1431	0.01809	0.68	0.14230	1.30	0.71	115.65
cb21-z2	0.51	14.8	1.24	12.0	2.04	743	0.00634	0.13	0.04091	1.10	0.06	40.84
cb21-z3	0.76	20.3	0.95	21.0	3.04	1233	0.00624	0.08	0.04060	0.51	0.41	40.20
cb21-z4	0.65	25.5	0.78	33.0	2.60	1926	0.00857	0.10	0.05737	0.47	0.42	55.10
cb21-z8	0.54	8.52	0.70	12.0	2.16	753	0.00624	0.12	0.04052	0.88	0.49	40.21
cb21-z10	0.14	7.76	0.94	8.0	0.56	576	0.00642	0.08	0.04180	1.10	0.21	41.31
cb21-z11	0.6	19.4	0.66	30.0	2.40	1772	0.00625	0.07	0.04033	0.36	0.44	40.15
cb21-z12	0.47	5.28	0.66	8.0	1.88	510	0.00627	0.07	0.03986	1.10	0.02	40.36

a Th contents calculated from radiogenic ²⁰⁸Pb and the ²⁰⁷Pb/²⁰⁶Pb date of the sample, assuming concordance between U-Th and Pb systems.

b Total mass of radiogenic Pb.

c Total mass of common Pb.

d Ratio of radiogenic Pb (including ²⁰⁸Pb) to common Pb.

e Th/U ratio of magma from which mineral crystallized calculated from $D_{Th/U} = 0.25$ (from Rubatto and Hermann, 2007).

f Measured ratio corrected for fractionation and spike contribution only.

g Measured ratios corrected for fractionation, tracer and blank.

h Corrected for initial Th/U disequilibrium using radiogenic ²⁰⁸Pb and Th/U[magma] specified by e.

i Isotopic dates calculated using the decay constants $\lambda_{238} = 1.55125E-10$ and $\lambda_{235} = 9.8485E-10$ (Jaffey et al. 1971).

Table F2:

Solution MC-ICPMS Lu-Hf isotope data of U-Pb dated zircons from the Bruffione granodiorite

	$^{176}\text{Yb}/^{177}\text{Hf}$ ^a	$\pm 2\sigma$	$^{176}\text{Lu}/^{177}\text{Hf}$ ^a	$\pm 2\sigma$	$^{178}\text{Hf}/^{177}\text{Hf}$	$^{180}\text{Hf}/^{177}\text{Hf}$	$\text{Hf Sig}_{\text{Hf}}(\text{V})$ ^b	$^{176}\text{Hf}/^{177}\text{Hf}$	$\pm 2\sigma$	$^{c176}\text{Hf}/^{177}\text{Hf}_{(t)}$	$\varepsilon\text{Hf}(t)$ ^d	$\pm 2\sigma$ ^c	$T_{\text{NC}}(\text{Ga})$ ^e
Bruffione granodiorite (CB19)													
cb19-z1	0.0536	43	0.00161	10	1.46720	1.88674	18	0.282766	9	0.282765	0.2	0.3	0.72
cb19-z3	0.0586	47	0.00174	10	1.46721	1.88672	8	0.282796	12	0.282795	1.2	0.4	0.66
cb19-z4	0.0533	43	0.00155	9	1.46721	1.88676	23	0.282797	10	0.282796	1.3	0.3	0.66
cb19-z5	0.0742	59	0.00238	14	1.46719	1.88670	7	0.282765	13	0.282762	0.4	0.5	0.72
cb19-z6	0.0602	48	0.00183	11	1.46722	1.88674	13	0.282738	10	0.282737	-0.6	0.3	0.77
cb19-z10	0.0458	37	0.00140	8	1.46721	1.88675	13	0.282745	11	0.282743	0.3	0.4	0.75
cb19-z11	0.0606	49	0.00185	11	1.46721	1.88664	7	0.282781	11	0.282779	0.7	0.4	0.69
cb19-z12	0.0501	40	0.00148	9	1.46722	1.88675	20	0.282771	10	0.282770	0.3	0.3	0.71
Bruffione granodiorite (CB21)													
cb21-z1	0.0978	78	0.00270	16	1.46723	1.88677	19	0.282686	10	0.282680	-1.1	0.4	0.86
cb21-z2	0.0509	41	0.00158	9	1.46720	1.88677	11	0.282805	12	0.282804	1.6	0.4	0.64
cb21-z3	0.0915	73	0.00270	16	1.46721	1.88672	17	0.282919	9	0.282917	5.6	0.3	0.42
cb21-z4	0.0847	68	0.00252	15	1.46721	1.88673	12	0.282885	11	0.282882	4.7	0.4	0.49
cb21-z8	0.0897	72	0.00330	20	1.46723	1.88670	8	0.282927	13	0.282925	5.8	0.5	0.41
cb21-z10	0.0383	31	0.00119	7	1.46719	1.88673	8	0.282825	13	0.282824	2.3	0.5	0.60
cb21-z11	0.1046	84	0.00293	18	1.46722	1.88675	15	0.282967	10	0.282965	7.3	0.4	0.33
cb21-z12	0.0853	68	0.00328	20	1.46719	1.88667	6	0.282963	12	0.282961	7.1	0.4	0.34

Quoted uncertainties (absolute) relate to the last quoted figure. Accuracy and reproducibility was checked by repeated analyses ($n = 21$) of 10 ppb solutions of JMC475.

(a) $^{176}\text{Yb}/^{177}\text{Hf} = (^{176}\text{Yb}/^{177}\text{Hf})_{\text{true}} \times (M^{173}(\text{Yb})/M^{177}(\text{Hf}))_{\text{meas}} / \ln(M^{179}\text{Hf}/^{177}\text{Hf}_{\text{true}} / ^{179}\text{Hf}/^{177}\text{Hf}_{\text{measured}}) / \ln(M^{179}(\text{Hf})/M^{177}(\text{Hf}))$, M =mass of respective isotope. The $^{176}\text{Lu}/^{177}\text{Hf}$ were calculated in a similar way by using the $^{175}\text{Lu}/^{177}\text{Hf}$ and $b(\text{Yb})$.

(b) Mean Hf signal in volt.

(c) Uncertainties are quadratic additions of the within-run precision and the daily reproducibility of the 10ppb-JMC475 solution. Uncertainties for the JMC475 quoted at 2SD (2 standard deviation).

(d) Initial $^{176}\text{Hf}/^{177}\text{Hf}$ and eHf calculated using the apparent U-Pb age determined by ID-TIMS, and the CHUR parameters: $^{176}\text{Lu}/^{177}\text{Hf} = 0.0336$, and $^{176}\text{Hf}/^{177}\text{Hf} = 0.282785$ (Bouvier et al., 2008).

(e) Two stage model age in billion years using the measured $^{176}\text{Lu}/^{177}\text{Lu}$ of each spot (first stage = age of zircon), a value of 0.0113 for the average continental crust (second stage), and a juvenile crust (NC) $^{176}\text{Lu}/^{177}\text{Lu}$ and $^{176}\text{Hf}/^{177}\text{Hf}$ of 0.0384 and 0.2

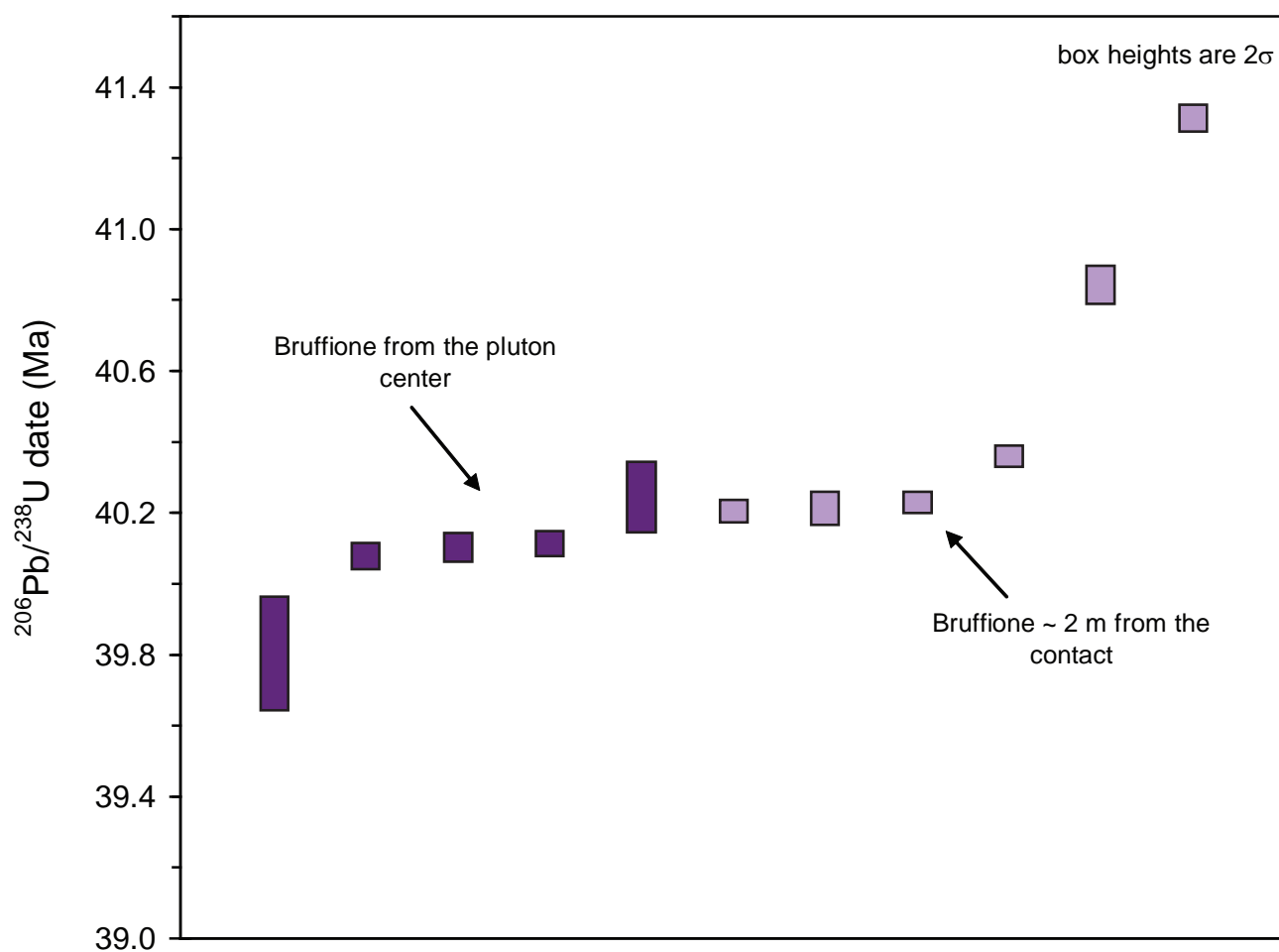


Figure F1: Age ranked $^{206}\text{Pb}/^{238}\text{U}$ dates for individual zircons from the Bruffione granodiorite

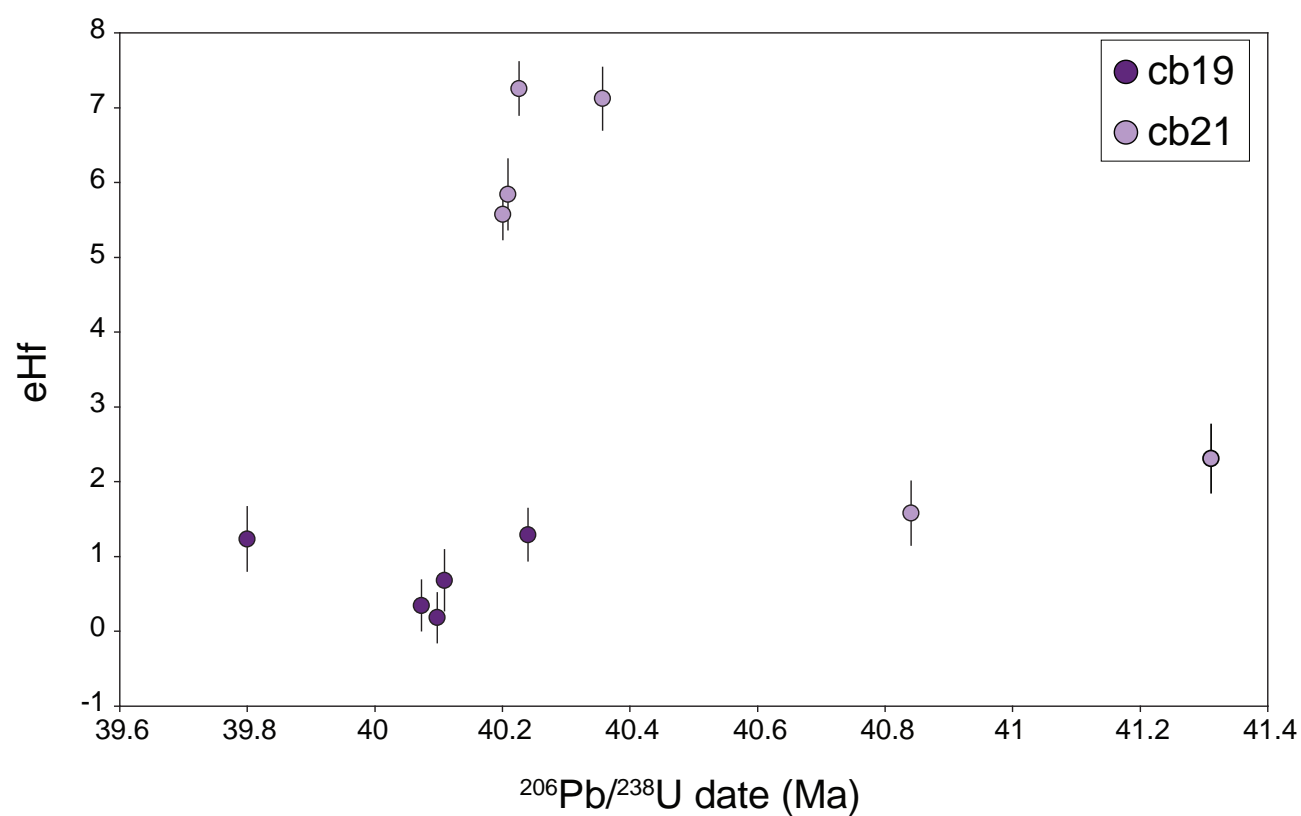


Figure F2: ϵHf values vs time for the Bruffione granodiorite

